Current sheet formation in uniformly twisted magnetic flux tubes

A thesis presented to

The University of Waikato

in fulfilment of the thesis requirement

for the degree of

Doctor of Philosophy

by

Farhad Ali

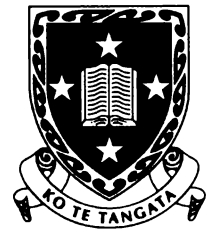

The University of Waikato
Te Whare Wānanga o Waikato

The University of Waikato

2001

Abstract

A viable mechanism for coronal heating is conversion of magnetic field energy into heat through magnetic reconnection in current sheets. Two processes capable of generating current sheets in the solar corona are studied here. The corkscrew kink instability of an axisymmetric magnetic flux tube, as a result of uniform twisting, is addressed first. Linear growth rates of the instability due to a helical perturbation are calculated for a variety of tubes. It is shown that plasma pressure and tube radius reduction are stabilising.

The helically symmetric geometry allows us to use an effectively two-dimensional formulation. A magneto-frictional code is developed to simulate relaxation to a second helical equilibrium of the tubes. Lower energy equilibria resulting from the kink are studied. Only one tube, whose twist decays with radius, is shown to result in a true field singularity or a current sheet. The Gold-Hoyle tube relaxes to a smooth kinked equilibrium. Tubes having reversal of a field component result in current concentrations as they kink and relax to a neighboring equilibrium. Plasma pressure reduces the strength of the kink in all cases.

The second process resulting in current sheet formation is the interaction of multiple flux tubes. The same frictional code is used to show that repelling tubes move away from each other as the superposed field relaxes to equilibrium. Twisting them together results in current concentrations. Attracting tubes with no neutral point also give rise to current concentrations when they are twisted together and relax to equilibrium. Current sheets are formed when attracting flux tubes, whose initial combined field have a neutral point, coalesce in the absence of plasma pressure. Introducing plasma pressure prevents current sheet formation when the tubes are not twisted together. In case the tubes are twisted together we again see current sheets, the lack of symmetry permitting plasma to flow out from between approaching flux surfaces, allowing them to come into contact. Interaction of unequal attracting tubes results in curved current sheets.

Acknowledgements

I would like to thank my chief supervisor Assoc. Prof. Alfred Sneyd for providing me the opportunity to work under his guidance, and for his continuous support and encouragement throughout my stay. Thanks also to my second supervisor Assoc. Prof. Ian Craig for his availability to help, useful discussions and suggestions, all the time. Without the support of these two pillars the structure of this thesis would have been without firm foundation. During this period I have benefited immensely from collaboration and assistance of Dr Paul Watson. Helpful discussions with Jacob Heerikhuisen and the ready computer fix-ups of Dr Stephen Joe are highly appreciated.

Complete support of my family and friends, which kept me fully devoted to this work, needs special mention. Young Saad's demand "come back or take me with you" provided me the impetus for sustained effort. I would also like to record my admiration of the friendly and home like environment provided by flatmates and friends at the university and Hamilton city. This work was financed by the Royal Society of New Zealand through Marsden Fund, Grant no. 96-UOW-MIS-0006.

Contents

Chapter 1

Introduction

1.1 Temperature in the solar atmosphere

Our Sun, a fire ball having a diameter of 1,392,000 km, a mass of 1.989×10^{30} kg and at a distance of 149,600,000 kilometers from Earth, is the main energy source for life on Earth. Most of this energy is generated by fusion of hydrogen nuclei into helium nuclei in the deep interior where the temperature approaches 15 million Kelvin (K) falling to a mere 5800 K at its surface, the photosphere, from which the bulk of solar radiation originates. The energy is carried outward in about 10^7 years, first by radiation from the center to about 70 percent of the Sun's radius, then to the surface primarily via large-scale convective motion. In most of the interior the physical conditions (density, temperature, etc.) are such that energy travels outwards very slowly, so that the temperature gradient remains rather small. In the outermost layers, the density is low enough for radiation to escape more easily into interplanetary space, leading to a much more rapid drop of the temperature as a function of radius. This trend however, changes once we reach the solar atmosphere, the region extending upward from and including the photosphere. Normally the temperature in the atmosphere should drop with radius. However, after falling from about 6600 K at the bottom of the photosphere to a

minimum value of about 4300 K at the top of the photosphere, the temperature starts rising slowly through the lower chromosphere and then more rapidly through the transition region to reach more than 10^6 K. Thereafter, the temperature falls slowly with height in the outer corona.

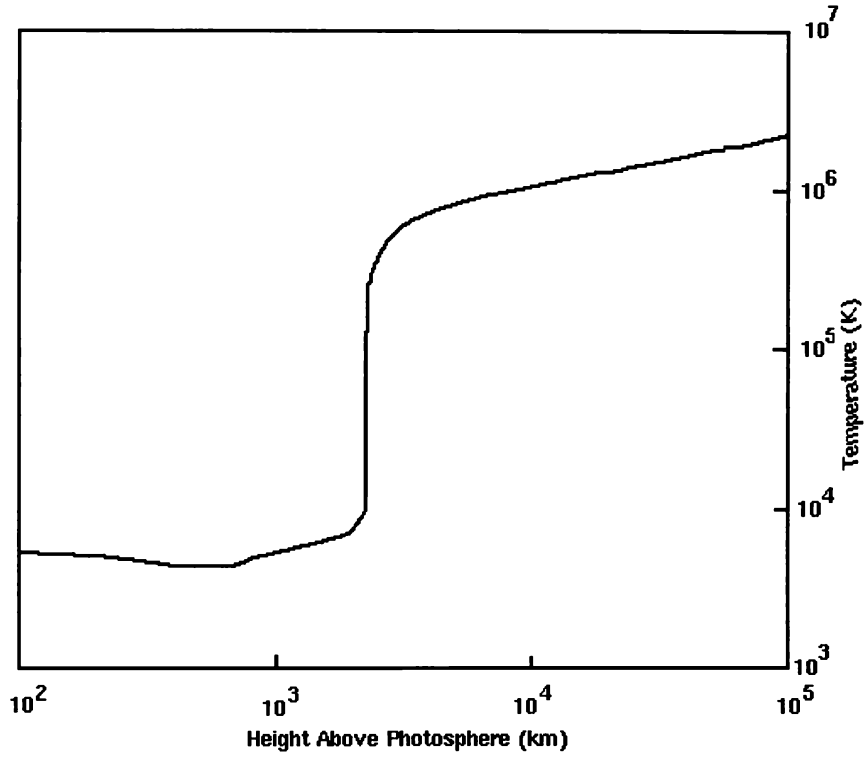

Figure 1.1: Temperature variation with height in solar atmosphere. (From Daw *et al.* [25]).

Understanding the temperature rise above the photosphere, plotted in figure 1.1 (from Daw *et al.* [25]), has been a major problem in solar physics [68] and is not yet fully resolved. A possible cause is solar atmospheric activities like sunspots, prominences and flares, all of which owe their existence to magnetic field on the Sun. The activity reaches its peak during solar maximums which are periodic sunspot events with a period of about 11 years. During the solar maximum of 1989 a flood of charged particles hitting the Earth's magnetosphere produced induced currents that disrupted the Hydro-Quebec transformers in Canada and the radio transmissions of the U.S. Coast Guard Loran navigation systems. Eleven years later, in the present

cycle, intense flare activity was observed on January 18 and July 15, 2000. Figure 1.2 is the picture of the 18th January flare from the Solar and Heliospheric Observatory (SOHO). Such large flares release magnetic energy, heat the overlying region to tens of millions of degrees and eject billions of tons of high energy plasma. Apart from these occasional large blasts smaller eruptions, called nano-flares, can be observed all the time in different active regions of the solar atmosphere.

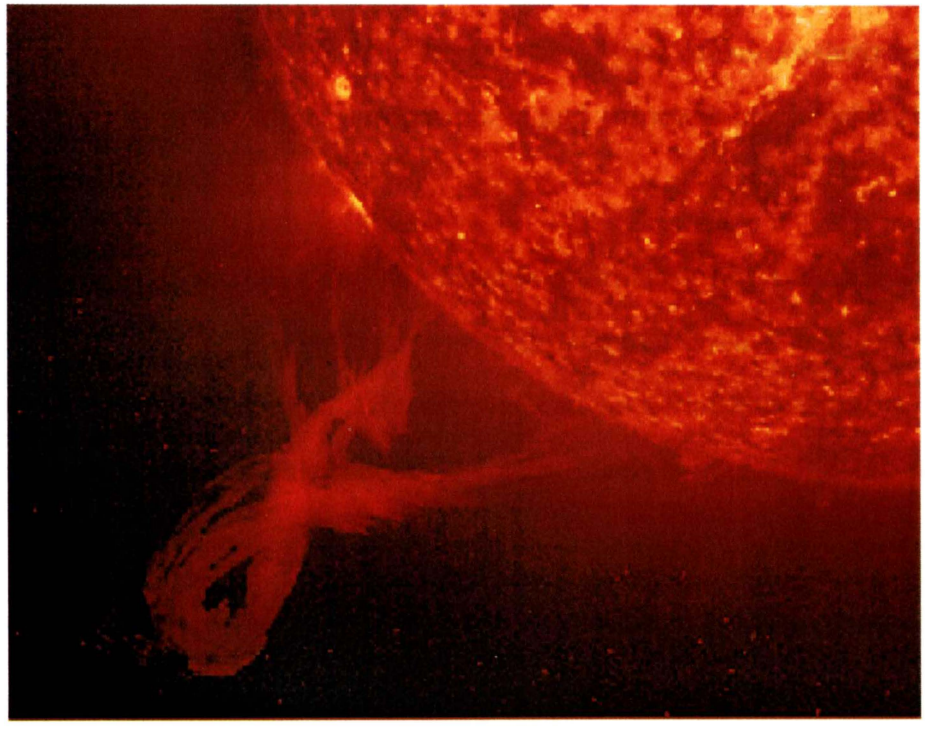

Figure 1.2: Flare of 18 January, 2000, from SOHO (courtesy B. Fleck, NASA).

1.2 Magnetic field and coronal heating

Magnetic field is produced by motion in the convection zone and the Sun's differential rotation. The magnetized plasma moves upward due to magnetic buoyancy. Because of the Coriolis force, the rising fluid cell, as it moves upward and expands horizontally, rotates slightly clockwise in the north and counterclockwise in the south.

Thus, although the motions are mainly radial, the rising fluid elements move in a corkscrew fashion twisting the accompanying magnetic fields as they come to the surface.

Heating of the solar atmosphere could be due to numerous phenomena but acoustic waves generated by turbulence in the convection zone and steepening to form shock waves in the upward propagation were previously considered to be the major cause. Now it is believed that this mechanism can heat only the low chromosphere and when the upper chromosphere is reached the flux is reduced and coherence destroyed. The heating mechanism in the upper chromosphere and corona is now considered to be magnetic in nature [68].

Heating by magnetic waves is another feasible alternative but they are scattered and refracted as the Alfvén speed increases with altitude. Even if enough wave flux reaches the corona, short period Alfvén waves can be a viable heating mechanism only in magnetic fields less than about 20 Gauss. Their energy dissipates slowly in stronger field regions [68].

A more likely mechanism is the storage of energy by photospheric motion in large scale equilibria and conversion of this energy into heat by ohmic dissipation. A major difficulty is, however, the large conductivity of the corona. Because the magnetic Reynolds number R_m in the corona is of order 10^{12}, such heating is negligibly small. The only way that ohmic dissipation can release the necessary energy is development of small-scale structures in which magnetic field varies rapidly, so that the effective local value of R_m is much reduced. On the global length scale such abrupt changes in the magnetic field $\mathbf{B}$ would appear as discontinuities, associated with large currents, or current sheets. The value of the magnetic Reynolds number in the vicinity of these sheets is reduced to a level such that the field $\mathbf{B}$ is decoupled from the plasma flow. Magnetic field lines slip through the plasma and regions of opposite polarity can meet, resulting in reconnection of field lines. A rapid conversion of magnetic energy into heat and kinetic energy, such as accompanying a solar flare is now possible.

A current sheet is a true field discontinuity and so the current density $|\mathbf{J}| \longrightarrow \infty$. In a current concentration, on the other hand, the field is continuous and $|\mathbf{J}|$ has a large but finite local maximum. While magnetic dissipation can occur in a current concentration if the current density is strong enough, it is the true current sheet that could produce the violent heating observed in solar flares.

Current sheets can form by a number of processes. Their formation at neutral points have been studied extensively [52, 23, 70, 17, 16, 53] but continuous footpoint motion of flux tubes as a cause of current sheet formation has been contentious. Parker [63] argues that a current sheet forms when an equilibrium field is disturbed continuously by a change in the boundary conditions. Van Ballegooijen [82] and Antiochos [3] argue that sheets will not form in a smoothly deformed field with no initial neutral point. Low [51] presents two analytical examples to illustrate the formation of current sheets in a magnetic field without neutral points, as a result of continuous displacement of the magnetic footpoints. Sneyd [76] furthered these findings by establishing general methods for identifying photospheric compressions which will result in current sheet formation. Several numerical studies like [12] have explored this process, but current sheet formation as a result of kinking of a flux tube is reported by few groups and needs further numerical investigation. Similarly current sheet formation as a result of flux tube interactions was mentioned quite early by Gold and Hoyle [31] but numerical evidence is still lacking.

1.3 Twisted flux tubes

Twisted magnetic flux tubes in the solar corona, or *coronal loops*, have been observed by the High Altitude Observatory (HAO) of the National Center for Atmospheric Research (NCAR) [43], the Big Bear Solar Observatory, Skylab solar observatory, the Naval Research Laboratory (NRL) [79], the Yohkoh satellite, the Solar and Heliospheric Observatory (SOHO) [73, 60], the Solar Maximum Mission (SMM)

[36, 24], the Doomless Solar Telescope (DST) [37] at Hida, Kyoto University and the Transition Region and Coronal Explorer (TRACE) [44]. A spectacular example is the prominence of 4 June, 1946, shown in figure 1.3. In fact no magnetic flux structure appearing in turbulent astrophysical environments is entirely free of twisting [64] because of differential rotation. Such structures are therefore referred to as *flux ropes, loops* or *tubes.* Twisted loop-like structures are also found in toroidal z-pinches and tokamaks [29].

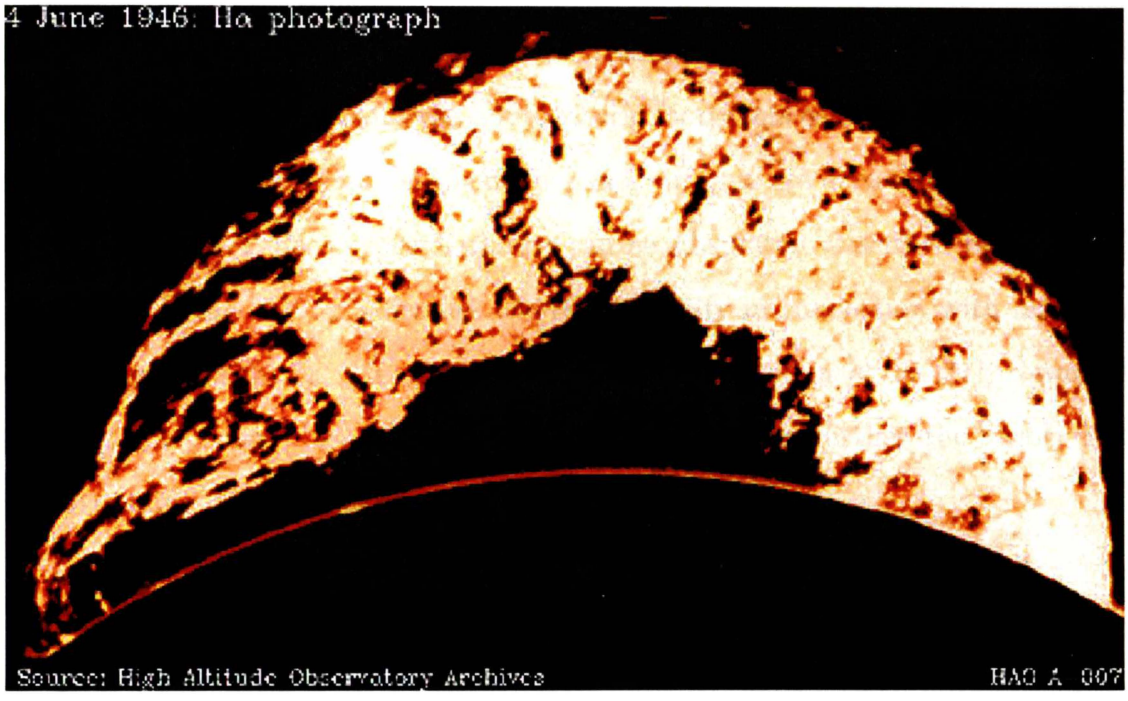

Figure 1.3: Prominence of 4 June, 1946, from HAO.

Typically large loop-like structures such as prominences may remain stable for many days and then erupt suddenly within a few minutes as flares releasing plasma and energy bursts. The field configuration before eruption must be close to static equilibrium. Since magnetic forces in the corona are much larger than plasma pressure, this implies $\mathbf{J} \times \mathbf{B} = 0$ where $\mathbf{B}$ is the magnetic field and $\mathbf{J}$ the current density. Thus the magnetic field and current are approximately parallel and the static form of Ampère's law implies

$$\nabla \times \mathbf{B} = \alpha \mathbf{B},$$

where α is some scalar function of position. Magnetic fields obeying this relation are referred to as force-free fields. The divergence of this equation shows that α is constant along a field line and the special case $\alpha = 0$ corresponds to an untwisted vacuum field.

Twisted fields have currents and free energy compared to their untwisted counterparts satisfying the same boundary conditions. The sudden loss of equilibrium by solar prominences, and twisted flux tubes in general, has received great attention as one of the possible causes of current concentrations and sheets and hence solar flares. In coronal plasma currents are continuously built up by motions beneath the solar surface that displace the photospheric footpoints of coronal magnetic field lines. In laboratory plasma, on the other hand, currents are driven by electric fields along circuits. Yet, both types of plasma can be adequately described by the MHD equations. Hence the early studies of MHD stability in connection with magnetic confinement and fusion, like the classical works of Bernstein *et al.* [11], Newcomb [58] and Kadomtsev [38] etc., provided a sound base to further the theory and understanding on the solar front.

1.4 The kink instability

Instabilities disrupting a plasma equilibrium are numerous. Of particular interest here is the kink instability that distorts an initially straight flux tube into a helix [38], see figure 1.4, so that oppositely oriented field lines may come into contact resulting in a current sheet. Work devoted to the study of this instability includes linear computations of stability bounds and growth rates, as well as detailed nonlinear time evolutions in line-tied finite and infinite configurations. Some examples are the works of Anzer [4], Raadu [69], Park *et al.* [62], Craig and co-workers [18, 19, 22], Mikić and co-workers [54, 55, 46, 48], Velli and co-workers [85, 47], Baty and co-workers [10, 9, 8], Rust [73] and Linton *et al.* [45].

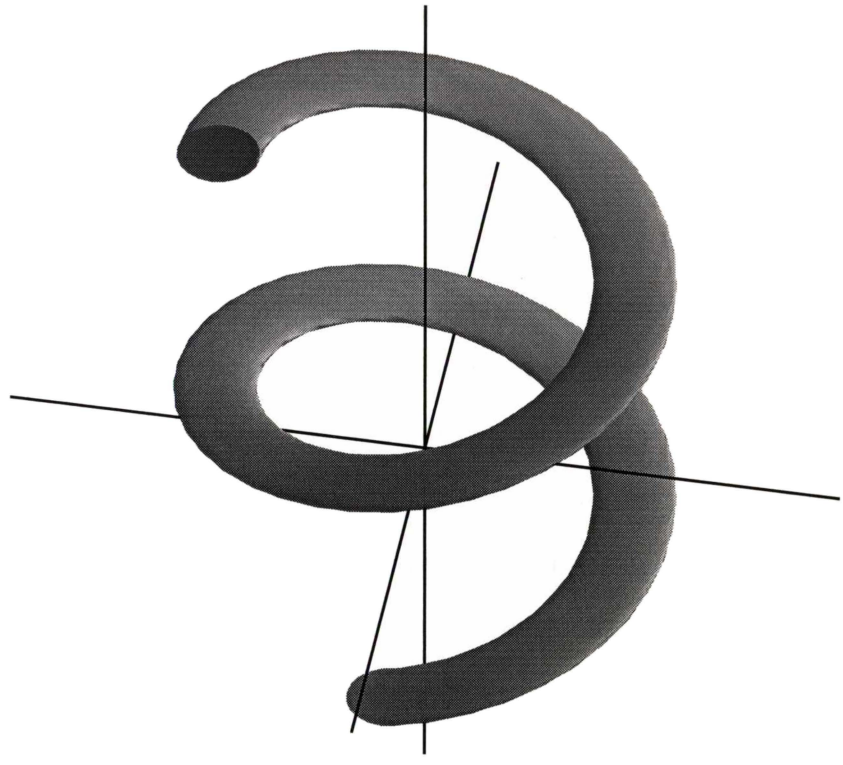

Figure 1.4: A kinked flux tube.

Some of these works report the formation of high current concentrations or current sheets accompanying this instability. Most evolution models claiming to observe current sheets include (a small) resistivity either at the outset or at a later stage in the computations. Only Park *et al.* [62] and Arber *et al.* [5] claim to see the formation of current sheets with the $m = 1$ kink in the ideal phase and so the Parker-Van Ballegooijen dispute [82] on the relaxation of an ideal plasma in an initial equilibrium to a second smooth equilibrium containing singularities by smooth footpoint motion seems reaching some settlement at last. Further numerical studies are needed to verify these findings.

It is generally believed [75, 68] that footpoint motion of flux tubes feeds energy into the tubes by twisting the field lines. This twisting can result in a kink instability (and possible current sheet) when a certain twist limit is exceeded. On the other hand, Pevtsov *et al.* [67] on the basis of observations argue reconnection as a

possible cause of the kink instability. We present here detailed simulations of an axially symmetric magneto-frictional plasma as it evolves from a state of initial equilibrium to a kinked equilibrium due to continuous helical displacements. We plot time evolution of the maximum force and current to give a clear picture of the kink and the second equilibrium.

Van der Linden and Hood [83] have shown the $m = 1$ kink mode to be always the first to go unstable in a force-free (or nearly force-free) line-tied cylindrical flux tube and Anzer [4] has showed that an idealized infinitely long magnetic flux tube is always unstable to the $m = 1$ kink mode. Since line-tying has a stabilising effect, an infinitely long tube is more prone to the kink instability. Hence we consider only infinitely long tubes. This seems justified due to the usually observed large lengths of the solar prominences. The prominence shown in Figure 1.3, for example, has a height of 200,000 kilometers above the Sun's surface. The length of this prominence can be estimated to have a value 5-6 times larger.

Solar prominences are normally arches of large aspect ratio θ = (global radius of curvature)/(transverse radius) and MHD stability is affected only to second order in $1/\theta$ by the toroidal curvature [29]. It therefore seems reasonable to approximate coronal loops as axially uniform infinite cylinders.

Analysis of prominences before, during, and after eruption by Vrsnak *et al.* [86] and Pevtsov *et al.* [67] show that prominences tend to erupt when the pitch angle of the twisted magnetic field exceeds a threshold value. Most of the above mentioned works on the kink instability (see e.g. [78, 5]) show that during the linear phase an unstable tube evolves predominantly in the "$m = 1$" mode - i.e. in the form of a helix of constant pitch τ. We simulate relaxation of the kink under the assumption of helical symmetry with a constant pitch. The problem then becomes effectively two-dimensional and sufficiently high resolution can be achieved with moderate computing power such as the recent pentium chips.

While helical flows can conveniently be represented using helical coordinates [42, 26], we use the usual Cartesian coordinates to utilize an alternating direction implicit (ADI) scheme on a rectangular grid. Since we are interested only in a final helically symmetric equilibrium we use the magneto-frictional formulation of the momentum equation (see [15, 20, 88, 50]) in a Lagrangian description simplifying our mathematical model further using the Cauchy solution [57].

1.5 Interaction of flux tubes

Apart from kinking of individual flux tubes, photospheric footpoint motion may result in moving adjacent tubes away from each other or in bringing them closer together. Gold and Hoyle, in their seminal paper "On the origin of solar flares" [31], pointed out that twisted flux tubes of opposite sense and opposite twist attract each other, leading to a sudden constriction of the current and through this to a dissipation of the energy associated with that current.

As mentioned earlier, existence of X-type and O-type nulls as a site of current sheet formation has been explored by many authors but mutual interaction of flux tubes has received less attention. Recently reconnection between two flux tubes has been studied by Kondrashov *et. al* [40] and Milano *et. al* [56], but reconnection requires the existence of current sheets. Parker [63] states that a complex topology, such as two or more flux tubes wrapped around each other, is without equilibrium and in [66] he shows that current sheets form due to juxtaposition of two different field topologies. Sneyd [77] proved that current sheet formation may occur when two flux tubes are twisted together. To date current sheet formation due to nonlinear evolution of interacting tubes has not been widely studied, so here we will attempt a detailed investigation of the interaction of twisted (attracting and repelling) tubes as they coalesce and are twisted together.

1.6 Outline

The first objective of this thesis is to explore the magnetic equilibria resulting from the kink instability in cylindrical magnetic flux tubes, and to investigate the possibility of current sheet formation. Another plausible scenario for current sheet formation is the interaction of multiple flux tubes and we study this phenomena in the latter part of this thesis. Both these phenomena have attracted the attention of many researchers, detailed above. Much work, however, is still needed to understand the required physical conditions and devise a mathematical framework compatible with observational data. Progress has been made on all fronts but more work is still needed to understand details of these processes.

As mentioned earlier, current sheet formation as a result of the kink instability and magnetic field interactions has been reported by many authors but the distinction between a true field singularity and a simple current concentration has not been stressed before. We show that successive computations on systematically refined grids are necessary to prove the existence of a current sheet.

A brief outline of this thesis is as follows. In chapter 2, we give the basic MHD equations and mention the corresponding assumptions, briefly citing their merits and drawbacks. Conditions for force-free equilibrium, such as exist in the solar corona, and simple flux tube models satisfying these conditions are presented. A few such tubes whose kink instability will be studied in detail are described here. The Gold-Hoyle flux tube is included, for comparison of our results with published data, and to build confidence in our analysis and calculations.

Linear stability analysis of the aforementioned cylindrical flux tubes, in line with Sneyd and Craig [78], is carried out in chapter 3. The numerical algorithm is described and growth rates for various flux tubes are computed. Conformity of our analysis with published results is discussed. The effect of plasma pressure and tube radius on stability of flux tubes is studied.

In chapter 4, helical symmetry relations and salient features of the magneto-frictional formulation are elaborated. Details of the corresponding numerical code are given and the method of current sheet diagnostics is described here. A few simple tests are carried out to illustrate usage and validity of the code.

Kinked helical equilibria of the Gold-Hoyle tube and a tube with oscillatory pitch are studied in chapter 5. Conformity of our simulations with our linear analysis and published results is assessed. The stabilising effect of plasma pressure and tube radius reduction is illustrated. Helical kinks resulting in current sheets and fields containing a current discontinuity are studied in chapter 6. Here also conformity with previous work and linear theory is illustrated. Refined mesh calculations are carried out to clarify the difference between current concentrations and true current sheets.

Chapters 7 and 8 deal with interactions of parallel twisted flux tubes. Repelling and attracting tubes having equal field magnitudes, whose combined initial field does not have a neutral point, are studied in chapter 7. The effect of a constant twist on the current growth is illustrated in both cases. Attracting tubes whose combined field contains a neutral point are dealt with in chapter 8. Effect of plasma pressure and tubes having unequal field magnitudes are addressed here. Concluding remarks are given in chapter 9.

Chapter 2

Basic Equations

Plasma, whether in the solar atmosphere or in laboratory devices, is composed of ionized gases and can be studied using two approaches. A particle dynamics approach is adopted when the objective of the study is internal microscopic phenomena but when macroscopic portions or bulk behavior of the plasma are under investigation, a continuous magnetohydrodynamic approximation is more suitable. Our objective here is to study macroscopic phenomena due to changes in the bulk properties like density, pressure and velocity of the solar corona, so we adopt here the magnetohydrodynamic (MHD) approach. The plasma is considered a single conducting fluid continuum and the governing equations are a combination of electrodynamic and hydrodynamic laws. Detailed descriptions of these equations can be found in any standard text such as Roberts [71] and Priest [68].

In the first section we present the basic assumptions reducing Maxwell's equations and the hydrodynamic conservation laws to a simple set of magnetohydrodynamics equations that will be used in this thesis. In the second section we describe equilibrium fields and derive the expression for an axially symmetric equilibrium field. In the third section four special forms of tubes are introduced. Linear growth rates of the kink instability in these tubes will be calculated in chapter 3 and nonlinear development of their kinks will be dealt with in chapters 5 and 6.

2.1 The ideal magnetohydrodynamics equations

Maxwell's equations (in MKSA units) are given by

$$\begin{aligned}
\nabla \times \mathbf{B} &= \mu_0 \mathbf{J} + \frac{1}{c^2}\frac{\partial \mathbf{E}}{\partial t}, && \text{(Ampère's law)},\\
\nabla \cdot \mathbf{B} &= 0, && \text{(Divergence-free condition)},\\
\nabla \times \mathbf{E} &= -\frac{\partial \mathbf{B}}{\partial t} && \text{(Faraday's law)},\\
\epsilon_0 \nabla \cdot \mathbf{E} &= \rho' && \text{(Gauss's theorem)}.
\end{aligned} \tag{2.1}$$

Here $\mathbf{B}$ is the magnetic flux density loosely referred to as the magnetic field in an astrophysical context (T or $\mathrm{Wb/m^2}$), $\mathbf{E}$ is the electric field strength (V/m), $\mathbf{J}$ is the electric current density ($\mathrm{A/m^2}$) and ρ' is the charge density ($\mathrm{C/m^3}$). Solar plasma is normally treated as isotropic so that the permeability μ and permittivity ϵ are approximated by their vacuum values $\mu_0 = 4\pi \times 10^{-7}$ H/m and $\epsilon_0 \approx 8.854 \times 10^{-12}$ F/m. The constant $c = 1/\sqrt{\epsilon_0 \mu_0} \approx 2.998 \times 10^8$ m/s is the speed of light in vacuum.

In magnetohydrodynamics the flow speed v, *sound speed* $c_s = (\gamma P/\rho)^{1/2}$ and *Alfvén speed* $v_A = B/(\mu_0 \rho)^{1/2}$, with ρ and P denoting the fluid density and pressure, are considered much smaller than the speed of light c. Thus the displacement current $\frac{1}{c^2}\frac{\partial \mathbf{E}}{\partial t}$ in Ampère's law can be neglected and we get

$$\mathbf{J} = \frac{1}{\mu_0} \nabla \times \mathbf{B}.$$

Plasma moving at a velocity $\mathbf{v}$ in the presence of a magnetic field $\mathbf{B}$ is subject to an electric field $(\mathbf{v} \times \mathbf{B})$ in addition to the electric field $\mathbf{E}$ which would act on material at rest, and Ohm's law gives

$$\mathbf{J} = \sigma(\mathbf{E} + \mathbf{v} \times \mathbf{B}). \tag{2.2}$$

Here σ is the conductivity of the plasma (mho/m). When $\mathbf{E}$ is eliminated from Faraday's law using Ohm's law and $\mathbf{J}$ is eliminated using Ampère's law we get

$$\begin{aligned}
\frac{\partial \mathbf{B}}{\partial t} &= -\nabla \times (-\mathbf{v} \times \mathbf{B} + \mathbf{J}/\sigma)\\
&= \nabla \times (\mathbf{v} \times \mathbf{B}) - \eta \nabla \times (\nabla \times \mathbf{B}).
\end{aligned}$$

Here $\eta = 1/(\mu_0\sigma)$ is called the magnetic diffusivity. Now using the divergence-free condition we get

$$\frac{\partial \mathbf{B}}{\partial t} = \nabla \times (\mathbf{v} \times \mathbf{B}) + \eta \nabla^2 \mathbf{B},$$

which is called the induction equation.

In astrophysical plasmas the length scales ℓ are very large and so the large magnetic Reynolds number $R_m = \ell v/\eta$, sometimes referred to as the infinite conductivity limit, implies that the magnetic field is effectively frozen in to the plasma. In such cases the last term in the induction equation can be neglected.

The evolution of the velocity field $\mathbf{v}$ is governed by the momentum equation

$$\rho \frac{D\mathbf{v}}{Dt} = -\nabla P + \mathbf{J} \times \mathbf{B} + \boldsymbol{f},$$

and density ρ by the continuity equation

$$\frac{D\rho}{Dt} + \rho \nabla \cdot \mathbf{v} = 0,$$

where

$$\frac{D}{Dt} \equiv \frac{\partial}{\partial t} + \mathbf{v} \cdot \nabla$$

is the material derivative for time variations following the motion and $\boldsymbol{f}$ represents other body forces acting on the plasma such as gravity and viscosity.

Normally Ampère's law, rather than Ohm's law, is used to determine the current density $\mathbf{J}$. The divergence-free condition negates the existence of sources and sinks of magnetic field i.e. monopoles [6]. It constrains individual lines of force either to form closed loops within a confining volume of space or to extend to infinity [64]. The induction equation governs time evolution of the magnetic field $\mathbf{B}$ that results from fluid motions.

The momentum equation determines the acceleration of the fluid in response to local forces. The term ∇P represents the hydrodynamic force due to pressure gradients and $\mathbf{J} \times \mathbf{B}$, the *Lorentz force* per unit volume, represents the action of magnetic field

on the conducting fluid. The Lorentz force is normally very large compared to the pressure gradient or gravity and viscosity.

The continuity equation gives the density change as a result of fluid motion, which in turn gives the change in pressure through the equation of state

$$P = g_p \rho^\gamma,$$

where γ is the ratio of specific heats and g_p a constant. This equation assumes that heat changes by conduction and Joule heating are negligible and that the pressure variation is adiabatic.

Normally the weak gravity (buoyancy) and viscous effects are also neglected and the equations are normalized using:

$$\begin{aligned} \rho &\longrightarrow \frac{\rho}{\rho_0}, \quad t \longrightarrow \frac{t}{t_A}, \quad \mathbf{r} \longrightarrow \frac{\mathbf{r}}{\ell}, \\ \mathbf{B} &\longrightarrow \frac{\mathbf{B}}{B_0}, \quad \mathbf{v} \longrightarrow \frac{\mathbf{v}}{v_A}, \quad P \longrightarrow \frac{P}{B_0^2/\mu_0}, \end{aligned} \tag{2.3}$$

with $\ell = O(10^7)$ m a typical length scale, $v_A = O(10^6)$ m/s the Alfvén speed, $t_A = \ell/v_A = O(10)$ s, $\rho_0 = O(10^{-9})$ kg/m^3 and $B_0 = O(10^{-2})$ T (= 100 G).

The resulting dimensionless ideal MHD equations are then given by

$$\rho \frac{D\mathbf{v}}{Dt} = -\nabla P + \mathbf{J} \times \mathbf{B}, \tag{2.4}$$

$$\frac{\partial \mathbf{B}}{\partial t} = \nabla \times (\mathbf{v} \times \mathbf{B}), \tag{2.5}$$

$$\frac{D\rho}{Dt} + \rho \nabla \cdot \mathbf{v} = 0, \tag{2.6}$$

$$P = g_p \rho^\gamma, \tag{2.7}$$

$$\mathbf{J} = \nabla \times \mathbf{B} \tag{2.8}$$

and

$$\nabla \cdot \mathbf{B} = 0. \tag{2.9}$$

The important effects neglected by the ideal MHD equations include heat conductivity, viscosity and resistivity.

Both extended and reduced forms of these equations have been used extensively to study plasma dynamics in the astrophysical domain. Extended versions, like those including relativistic effects or using a frame of reference rotating with the Sun, are normally cumbersome to handle computationally and necessitate other simplifying assumptions. On the other hand, models which are too simplified such as the one-dimensional thin tube approximations, or those assuming incompressibility, may suppress important effects. Three-dimensional calculations using equations (2.4) - (2.9) or their extensions including resistivity [9, 5, 2, 8], require high computational power and fine tuning of the codes to deal with numerous instabilities, disparate time scales and conservation requirements. Conservation of mass, momentum, and energy simultaneously using numerical approximations, in itself, is a highly challenging task and has not been satisfactorily achieved in simple (non-magnetic) compressible flows, while the MHD equations require conservation of magnetic flux also.

Apart from resolution of physical instabilities, a numerical code needs to take care of numerical stability, dispersion and time-step limitations. Most of the three-dimensional calculations cited above use artificial diffusion either explicitly or implicitly in the form of frequent averaging or grid stretching etc. Some employ special treatments such as spectral methods and Fourier expansions or Fast Fourier Transforms, in specific coordinate directions depending on the geometry of the domain. Some introduce Laplace smoothers that sometimes kill small scale phenomena indiscriminately to keep the computational cost within sustainable limits. While three-dimensional calculations are necessary to study detailed evolution of the complex topology of kinked tubes, the high computational and coding costs encourage simpler formulations capable of exploring salient features of the phenomena, yet requiring modest computational resources for good resolution. With these requirements and limitations in view we present our approach in the next section and the following two chapters.

2.2 Axisymmetric flux tubes

As noted earlier, twisted magnetic flux tubes have been observed to remain in a state of quasi-static equilibrium for many days before eruption. During this long period, energy may be stored due to slow twisting of the tube by photospheric motion, until a certain threshold value is reached where the tube kinks or interacts with other magnetic structures in its vicinity resulting in magnetic reconnection and hence release of magnetic energy. To understand the mechanism of eruption numerous theoretical models of the initial equilibrium field have been proposed and studied. These studies include calculation of stability bounds, linear growth rates and nonlinear evolution of different instabilities. Parker [64] asserts that there is no equilibrium in the absence of symmetry and Tsinganos in a series of papers has investigated possible equilibrium configurations in detail with emphasis on helically symmetric fields in [80]. We describe in the following a simple axisymmetric flux tube some forms of which have received great attention in the past.

For a magnetic field in equilibrium the momentum equation (2.4) gives $\mathbf{J}\times\mathbf{B} = \nabla P$. In coronal loops the field is nearly force-free so that the pressure gradient can be neglected to give

$$\mathbf{J} \times \mathbf{B} = 0. \tag{2.10}$$

Thus the current and magnetic field are parallel and we have

$$\mathbf{J} = \alpha\mathbf{B},$$

where α is some function of position. The divergence of this equation implies

$$\nabla\alpha \cdot \mathbf{B} = 0,$$

showing that α is constant along each field line. When α has the same constant value on each field line, $\mathbf{B}$ is a linear force-free field and

$$\nabla \times (\nabla \times \mathbf{B}) = \nabla(\nabla \cdot \mathbf{B}) - \nabla^2\mathbf{B} = \alpha\nabla \times \mathbf{B}.$$

This on using $\mathbf{J} = \alpha\mathbf{B}$ and the divergence-free condition gives

$$(\nabla^2 + \alpha^2)\mathbf{B} = 0.$$

In this case numerous analytic solutions are available, see for example Priest [68]. If $\alpha = 0$, the magnetic field is an untwisted potential field,

$$\mathbf{B} = \nabla\phi,$$

having scalar potential ϕ. It is the twisted flux tubes that have currents and free energy compared to their untwisted counterparts satisfying the same boundary conditions. Moreover, as already mentioned, there is observational evidence of twisted flux tubes in the solar corona in the form of newly emerging loops and long-lived prominences. Thus we will consider the case of a non-zero α in which the magnetic field lines are twisted and magnetic tension balances the internal magnetic pressure. A preliminary discussion of twisted flux tubes can be found in Parker [64] and Priest [68].

The axial uniformity and large aspect ratio of observed coronal flux tubes suggests that we may represent a typical flux tube as an axisymmetric infinitely long uniform circular cylinder. In this case

$$\frac{\partial \mathbf{B}}{\partial \theta} = \frac{\partial \mathbf{B}}{\partial z} = 0.$$

Then $\nabla \cdot \mathbf{B} = 0$ in cylindrical coordinates gives $\frac{\partial B_r}{\partial r} = 0$. Thus $B_r =$ constant and since $B_r \to 0$ as $r \to \infty$, we have $B_r = 0$ throughout. Hence we can take our field as

$$\mathbf{B} = B_\theta(r)\widehat{\boldsymbol{\theta}} + B_z(r)\widehat{\mathbf{z}}. \tag{2.11}$$

This gives $B^2 = B_\theta^2 + B_z^2$ and $\nabla B^2 = \frac{\partial}{\partial r}(B_\theta^2 + B_z^2)\,\widehat{\mathbf{r}}$, whilst

$$(\mathbf{B}\cdot\nabla)\mathbf{B} = \left(B_\theta \frac{1}{r}\frac{\partial}{\partial\theta} + B_z\frac{\partial}{\partial z}\right)(B_\theta\widehat{\theta} + B_z\widehat{\mathbf{z}}) = \frac{B_\theta^2}{r}\frac{\partial\widehat{\theta}}{\partial\theta}$$

and $\widehat{\theta} = -\sin\theta\widehat{\mathbf{x}} + \cos\theta\widehat{\mathbf{y}}$ so that $\frac{\partial\widehat{\theta}}{\partial\theta} = -\widehat{\mathbf{r}}$. Hence equation (2.10) written as

$$(\nabla\times\mathbf{B})\times\mathbf{B} = (\mathbf{B}\cdot\nabla)\mathbf{B} - \frac{1}{2}\nabla B^2 = 0,$$

gives

$$\frac{1}{2}\frac{\partial}{\partial r}(B_\theta^2 + B_z^2) + \frac{1}{r}B_\theta^2 = 0. \tag{2.12}$$

The term $(\mathbf{B}\cdot\nabla)\mathbf{B}$ represents the magnetic tension due to curvature of field lines and $\frac{1}{2}\nabla B^2$ the magnetic pressure.

As shown in figure 2.1, field lines in a twisted flux tube form helices at constant radial distances from the axis. A convenient specification of this field is in terms of the *twist function*

$$k(r) = \frac{B_\theta(r)}{rB_z(r)}. \tag{2.13}$$

The pitch of the field is $2\pi/k$ and gives the axial displacement of a field line that encircles the axis once.

Figure 2.1: A schematic sketch of field lines in a twisted flux tube.

Writing (2.12) in terms of $k(r)$ we obtain,

$$\frac{1}{2}\frac{\partial}{\partial r}\left\{B_z^2(1+r^2k^2)\right\} + rk^2B_z^2 = 0,$$

or

$$\frac{B_z'}{B_z} + \frac{(1+r^2k^2)'}{2(1+r^2k^2)} + \frac{rk^2}{1+r^2k^2} = 0.$$

Integration, with $B_z = 1$ at $r = 0$, gives

$$B_z = \frac{1}{\sqrt{1+r^2k^2}} \exp\left(-\int_0^r \frac{rk^2}{1+r^2k^2}dr\right). \tag{2.14}$$

Alternatively we can add $B_z^2 r^2 k k'$ to both sides of (2.12) to get

$$\frac{B_z'}{B_z} + \frac{(1+r^2k^2)'}{(1+r^2k^2)} = \frac{r^2kk'}{1+r^2k^2}.$$

Then integration, with $B_z = 1$ at $r = 0$, gives [78]

$$B_z = \frac{1}{1+r^2k^2} \exp\left(\int_0^r \frac{r^2kk'}{1+r^2k^2} dr\right). \tag{2.15}$$

These fields are non-planar yet depend on the planar Cartesian coordinates x and y only. Such fields are some times called two-and-a-half dimensional and can be expressed in terms of a flux function $\psi(x,y)$ as

$$\mathbf{B} = \nabla\psi(x,y) \times \widehat{\mathbf{z}} + B_z(x,y)\widehat{\mathbf{z}}. \tag{2.16}$$

2.3 Flux tubes to be studied

Cylindrical equilibrium fields can be generated using the above equations by specifying either B_z or B_θ. Equilibrium fields can also be obtained by numerical relaxation of a non-force-free field [10] but in some cases classification by the twist function k has received more attention (see for example [72, 19, 14, 9]). Here we define four different types of fields and will study their kink instability in chapters 3, 5 and 6.

Our first class of flux tubes, which we refer to as $\mathsf{B}_1(\nu)$, is obtained by taking the twist proportional to a power of the radius r,

$$k(r) = r^\nu, \tag{2.17}$$

where ν is a positive real number. In this case (2.14) gives

$$B_z = (1+r^{2\nu+2})^{-(\nu+2)/(2\nu+2)}, \qquad B_\theta = krB_z = r^{\nu+1}B_z. \tag{2.18}$$

The case $\nu = 0$, $k = 1$ represents the popular Gold-Hoyle field, and the linear stability of general $\nu \geq 0$ (the *power-law twist*) fields is studied in detail by Craig *et al.* [19]. Figure 2.2 shows plots of the twist $k(r)$ and axial field $B_z(r)$ for a few tubes of this class.

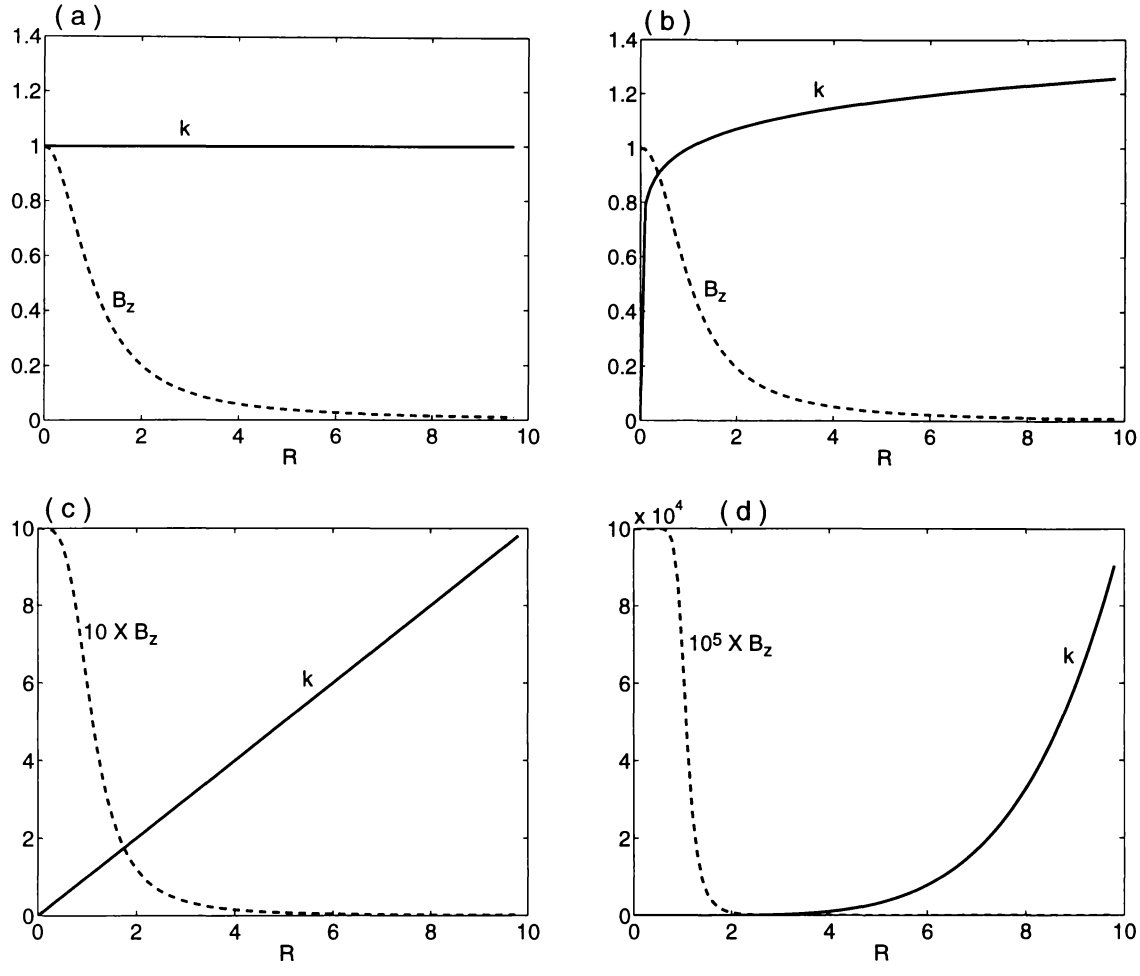

Figure 2.2: Twist k (solid lines) and B_z (dashed lines) versus r of $B_1(0)$ in (a), $B_1(0.1)$ in (b), $B_1(1)$ in (c) and $B_1(5)$ in (d).

Craig *et al.* [19] give linear growth rates for all these tubes and we will use them as a validity test of our linear stability analysis in the next chapter. The Gold-Hoyle field will be used for comparison of results both in the linear and nonlinear studies.

The $B_1(\nu)$ fields are somewhat unrealistic in that the twist increases monotonically with r (although both field components tend to zero for large r). Robinson [72], after analyzing stability bounds of numerous field configurations, concludes that a plasma with appreciable hydrodynamic pressure and a vacuum region outside will always be kink unstable if the pitch of the field lines possesses a minimum at finite r. We define another field whose twist reverses sign at $r = \pi$ and has both a maximum

and a minimum. We set

$$k(r) = \begin{cases} \sin(r) & \text{if } r \leq \frac{3}{2}\pi, \\ \sin(\frac{3}{2}\pi) & \text{if } r > \frac{3}{2}\pi. \end{cases} \tag{2.19}$$

This field is labeled B_2. Here B_z and B_θ are to be calculated numerically using (2.14). Figure 2.3 shows $k(r)$ and $B_z(r)$ for this tube. The minimum of the pitch occurs at $r = \frac{\pi}{2}$.

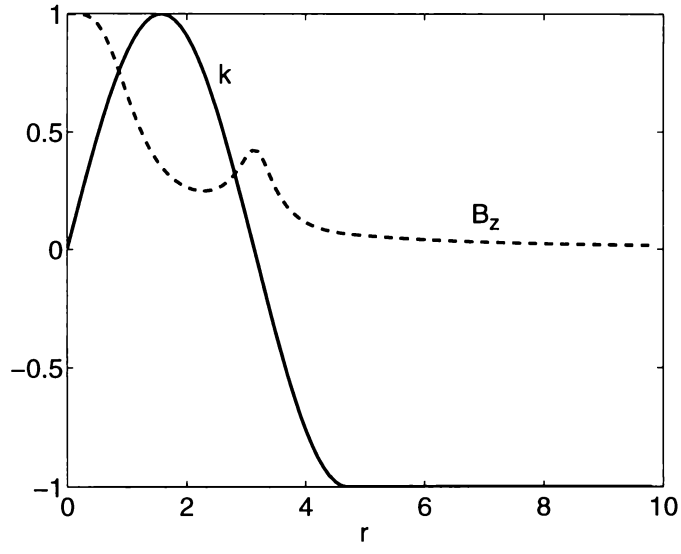

Figure 2.3: Twist k (solid line) and B_z (dashed line) versus r of B_2.

Robinson [72] also mentions that for stability it is necessary for the pitch to decrease with r. We define our third field to have $k(r)$ constant, for $0 \leq r \leq \frac{3}{2}$, then falling off rapidly to zero. We set

$$k(r) = \begin{cases} 1 & \text{if } r \leq \frac{3}{2}, \\ \\ \exp[-(r - \frac{3}{2})^2] & \text{if } r > \frac{3}{2}. \end{cases} \tag{2.20}$$

As before $B_z(r)$ and $B_\theta(r)$ can be obtained from (2.14) using numerical integration. We denote this field by B_3. Figure 2.4 shows $k(r)$ and $B_z(r)$ for this tube. A similar tube has recently been studied by Arber *et al.* [5] who find current sheet formation as the tube kinks.

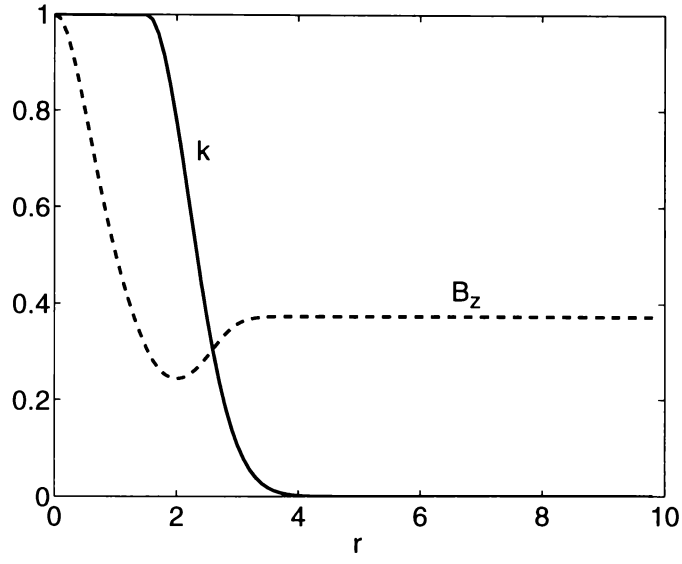

Figure 2.4: Twist k (solid line) and B_z (dashed line) versus r of B_3.

According to Robinson [72] stability requires that the axial field must reverse and the axial flux must not. If there is a central core region to the configuration where B_θ is negligible and the pitch becomes infinite the configuration is stable for a given wall position, however such a situation may only be transient because of field diffusion. We take our fourth class to have axial field reversal; it is conveniently specified by

$$B_z(r) = \begin{cases} \cos(r/2) & \text{if } r \leq 4, \\ \cos(2) & \text{if } r > 4. \end{cases} \tag{2.21}$$

This tube is denoted by B_4. Its azimuthal component can be obtained using

$$\frac{\partial}{\partial r} B_z^2 = -\frac{1}{2}\sin(r)$$

to get

$$\frac{\partial}{\partial r}(r^2 B_\theta^2) = \frac{1}{2} r^2 \sin(r),$$

when $r \leq 4$. Then

$$B_\theta^2 = \frac{\sin(r)}{r} - \frac{1}{2}\cos(r) + \frac{\cos(r)}{r^2} + \frac{1}{r^2} C,$$

with the constant of integration $C = -1$, to avoid a singularity at $r = 0$, gives

$$B_\theta(r) = \begin{cases} \left[\frac{\sin(r)}{r} - \frac{1}{2}\cos(r) - \frac{1-\cos(r)}{r^2}\right]^{\frac{1}{2}} & \text{if } r \leq 4, \\ \frac{4}{r} B_\theta(4) & \text{if } r > 4. \end{cases} \tag{2.22}$$

The twist and axial field for this tube are plotted in figure 2.5. Here B_z vanishes at $r = \pi$ and changes sign while k becomes infinite and changes sign.

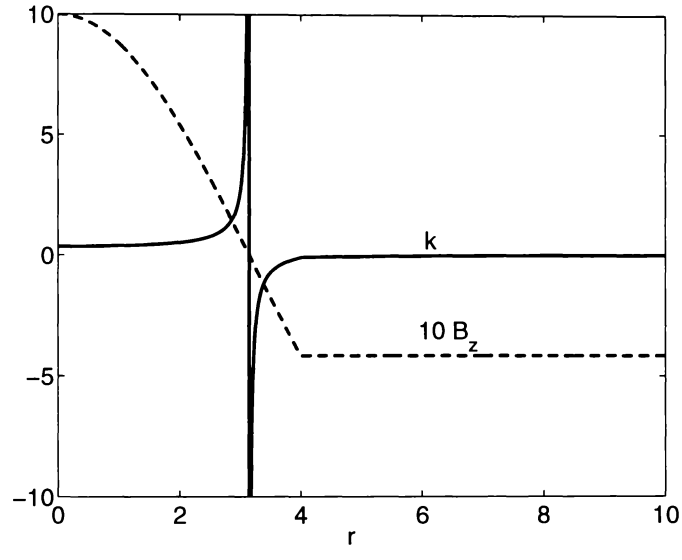

Figure 2.5: Twist k (solid line) and B_z (dashed line) versus r of B_4.

Chapter 3

Linear stability of twisted flux tubes

It has been long recognized that the kink instability provides a key destabilizing mechanism for the magnetically dominated coronal plasma and this instability may lead to current sheet formation. It is therefore very important to know what sort of magnetic structures, found in the solar corona, are susceptible to the kink instability. It is usually difficult to show that a system is stable, because this requires a general proof that there is no perturbation of any form under which the system is unstable. On the other hand, instability is the tendency of a system to move away from equilibrium by a small velocity perturbation (or a small displacement) and may be established by demonstrating the existence of a single unstable mode.

Stability analysis of plasma columns using the linearized form of the MHD equations has received great attention in the past (see e.g. [41, 58, 4, 72, 7, 30, 74, 33, 34, 35, 27, 18, 78, 19, 28, 85, 14]). The earlier studies like [41, 58, 72, 7] were concerned with pinched laboratory fields but Anzer [4] emphasized that all infinite cylindrical coronal magnetic structures are kink unstable and that conversion of magnetic to kinetic energy may be triggered by the helical kink instability. Later on substantial work on the stability analysis of magnetic flux tubes, like [33, 34, 35, 27, 18],

has appeared in the astrophysical literature. Most of these studies use the energy principle of Bernstein *et al.* [11] and either calculate bounds following Newcomb [58] or the full eigenvalue spectrum as in Bateman [6].

In this chapter we calculate linear growth rates of the four flux tubes B_1 – B_4, introduced in chapter 2, following Sneyd and Craig [78]. First we describe our method of calculating growth rates, for axisymmetric flux tubes. We then carry out calculation of the growth rates emphasizing the effect of plasma pressure and tube radius. This provides us the pitch ranges for the kink instability of these tubes, as well as an indication of the size of the computational domain necessary for the nonlinear kink simulations. We check the validity of our linear analysis by comparing our results with published work on growth rates of the Gold-Hoyle field and checking the conformity of our results with the nonlinear calculations in the next two chapters.

3.1 Linear stability analysis

Following Bernstein *et al.* [11], we consider the effect of a small plasma displacement $\boldsymbol{\xi}(\mathbf{x})$ on the equilibrium field $\mathbf{B}$. If $\delta\mathbf{v}$ represents the velocity perturbation, due to this small displacement, then the induction equation (2.5) gives

$$\frac{\partial}{\partial t}(\mathbf{B}+\delta\mathbf{B}) = \nabla\times\big(\delta\mathbf{v}\times(\mathbf{B}+\delta\mathbf{B})\big).$$

Neglecting second order terms, such as, $\delta\mathbf{v}\times\delta\mathbf{B}$, we get

$$\frac{\partial}{\partial t}\delta\mathbf{B} = \nabla\times(\delta\mathbf{v}\times\mathbf{B}),$$

which on integration with respect to time gives

$$\delta\mathbf{B} = \nabla\times(\boldsymbol{\xi}\times\mathbf{B}). \tag{3.1}$$

The continuity equation (2.6), on neglecting second order terms, gives

$$\frac{\partial}{\partial t}\delta\rho \;=\; -\nabla\cdot(\rho\,\delta\mathbf{v}),$$

which on integration implies $\delta\rho = -\nabla\cdot(\rho\boldsymbol{\xi})$, or

$$\delta\rho = -\rho\nabla\cdot\boldsymbol{\xi},$$

taking $\nabla\rho = 0$ in the initial equilibrium. The equation of state (2.7) gives

$$P + \delta P = g_p(\rho^\gamma + \gamma\rho^{\gamma-1}\delta\rho + \cdots), \text{ or } \delta P = g_p\gamma\rho^{\gamma-1}\delta\rho\,.$$

Thus $\delta P = -g_p\,\gamma\,\rho^\gamma\,\nabla\cdot\boldsymbol{\xi} = -\gamma\,P\,\nabla\cdot\boldsymbol{\xi}$, on neglecting second order terms yields

$$-\nabla(\delta P) = \gamma\,P\,\nabla(\nabla\cdot\boldsymbol{\xi}).$$

Hence to first order the Lorentz force perturbation $\mathbf{F}_b$ is given by

$$\mathbf{F}_b = [(\nabla\times\delta\mathbf{B})\times\mathbf{B} + (\nabla\times\mathbf{B})\times\delta\mathbf{B}], \tag{3.2}$$

and the pressure perturbation force $\mathbf{F}_p$ is given by

$$\mathbf{F}_p = \gamma P\nabla(\nabla\cdot\boldsymbol{\xi}). \tag{3.3}$$

Since the field is in equilibrium the magnetic energy E_M is minimum or maximum and a change in E_M due to a small displacement $\boldsymbol{\xi}$ must vanish to leading order, i.e. $\delta E_M = 0$. Instability occurs when a $\boldsymbol{\xi}$ can be found that gives a negative second order variation $\delta^2 E_M$. This decrease in E_M is equal to the work done by $\mathbf{F}$ i.e.

$$-\delta^2 E_M = \frac{1}{2}\langle\mathbf{F}\,,\,\boldsymbol{\xi}\rangle, \tag{3.4}$$

where the factor $\frac{1}{2}$ arises because the mean force during the displacement from $\mathbf{0}$ to $\boldsymbol{\xi}$ is $\frac{1}{2}\mathbf{F}$ (see, e.g., [68]) and the inner product $\langle\mathbf{a},\mathbf{b}\rangle$ denotes the integral of $\mathbf{a}\cdot\mathbf{b}$ over the fluid volume [78].

Bernstein *et al.* (1958) show that the operator

$$\mathbf{F}(\boldsymbol{\xi}) = \mathbf{F}_b(\boldsymbol{\xi}) + \mathbf{F}_p(\boldsymbol{\xi})$$

is self-adjoint, so the eigenvalues are real. Thus for an eigenvalue λ with corresponding eigenvector $\boldsymbol{\xi}$, substitution of $\mathbf{F} = \lambda\boldsymbol{\xi}$ into (3.4) gives

$$-\delta^2 E_M = \frac{1}{2}\lambda\|\boldsymbol{\xi}\|^2.$$

Hence the condition for instability is the existence of a positive eigenvalue λ. The magnitude of λ then gives a measure of the strength of the instability or the amount of energy released, since $\delta^2 E_M$ is proportional to λ.

Following Newcomb [58] we may take ξ_r to be real and ξ_θ, ξ_z purely imaginary, due to the invariance of $\mathbf{F}$ under rotations about and translations along the z-axis. The simplification used by Sneyd and Craig [78] of neglecting the component of $\boldsymbol{\xi}$ parallel to $\mathbf{B}$ is not applicable here, since this component affects $\mathbf{F}_p(\boldsymbol{\xi})$. Also the $m = 1$ mode is usually the first to go unstable [83], distorting the tube into a corkscrew helical structure. Hence we take a helical displacement of the form

$$\boldsymbol{\xi} = [f(r)\cos\psi,\ g(r)\sin\psi,\ h(r)\sin\psi],\quad \psi = m\theta - \tau z, \tag{3.5}$$

where m and τ are the azimuthal and axial mode numbers respectively. This displacement along with the equilibrium field

$$\mathbf{B} = [0,\ rkB_z,\ B_z]$$

gives

$$\boldsymbol{\xi}\times\mathbf{B} = [(g - rkh)B_z\sin\psi,\ -fB_z\cos\psi,\ rkfB_z\cos\psi],$$

so that

$$\begin{aligned}\delta\mathbf{B} = \ & [(\tau - mk)fB_z\sin\psi,\ \{(rkh - g)\tau B_z - (rkfB_z)'\}\cos\psi,\\ & \tfrac{1}{r}\{(rkh - g)mB_z - (rfB_z)'\}\cos\psi],\end{aligned} \tag{3.6}$$

with prime representing derivative with respect to r.

Then

$$\begin{aligned}\nabla\times\delta\mathbf{B} = \Bigg[&\frac{1}{r^2}\Big\{m(rfB_z)' - (rkh - g)\left(m^2 + r^2\tau^2\right)B_z + \tau(rkfB_z)'\Big\}\sin\psi,\\ &\left\{m(gB_z/r)' - m(khB_z)' + ((rfB_z)'/r)'\right\}\cos\psi,\\ &\Big\{\tau\Big(2khB_z + r(khB_z)' - (rgB_z)'/r\Big) - \frac{1}{r}(rkfB_z)' - (rkfB_z)'' +\\ &\frac{m}{r}(mk - \tau)fB_z\Big\}\cos\psi\Bigg],\end{aligned} \tag{3.7}$$

and

$$(\nabla\times\delta\mathbf{B})\times\mathbf{B} = \Big[\Big\{ (mk-\tau)^2 f B_z + ((rfB_z)'/r)' - m(khB_z)' + m\left(\frac{gB_z}{r}\right)' +$$

$$k\left(\tau(rgB_z)' - r\tau khB_z - rt(rkhB_z)' + (rkfB - z)' + r(rkfB_z)''\right)\Big\} B_z\cos\psi,$$

$$-\left\{\frac{m}{r^2}(rfB_z)' + \frac{1}{r^2}B_z(g-rkh)(m^2+r^2\tau^2) + \tau(rfkB_z)'\right\} B_z\sin\psi,$$

$$rk\left\{\frac{m}{r^2}(rfB_z)' + \frac{1}{r^2}B_z(g-rkh)(m^2+r^2\tau^2) + \tau(rfkB_z)'\right\} B_z\sin\psi\Big]. \qquad (3.8)$$

Also

$$\nabla\times\mathbf{B} = \left[0,\ -B_z',\ \left(r^2kB_z\right)'/r\right],$$

implies

$$(\nabla\times\mathbf{B})\times\delta\mathbf{B} = \Big[\frac{1}{r}\Big\{\big((rfB_z)' + mB_z(g-rkh)\big)B_z' +$$

$$\left(r^2kB_z\right)'\left(\tau B_z(g-rkh) + (rkfB_z)'\right)\Big\}\cos\psi,$$

$$\frac{1}{r}\left(r^2kB_z\right)'(\tau-mk)fB_z\sin\psi,\ \ (\tau-mk)fB_zB_z'\sin\psi\Big]. \qquad (3.9)$$

Similarly

$$\nabla\cdot\boldsymbol{\xi} = \frac{1}{r}\left[(rf)' + mg - rkh\right]\cos\psi\ ,$$

implies

$$\nabla(\nabla\cdot\boldsymbol{\xi}) = \Big[\Big\{\frac{1}{r}\big((rf)' + mg - rkh\big)\Big\}'\cos\psi,\ -\frac{m}{r^2}\big((rf)' + mg - rkh\big)\sin\psi,$$

$$\frac{k}{r}\big((rf)' + mg - rkh\big)\sin\psi\Big]. \qquad (3.10)$$

Hence the components of $\mathbf{F}$ are given by

$$\begin{aligned}
F_r(\boldsymbol{\xi}) &= [P_{r2}f'' + P_{r1}f' + P_{r0}f + Q_{r1}g' + Q_{r0}g + R_{r1}h' + R_{r0}h]\cos\psi,\\
F_\theta(\boldsymbol{\xi}) &= [P_{t1}f' + P_{t0}f + Q_{t0}g + R_{t0}h]\sin\psi,\\
F_z(\boldsymbol{\xi}) &= [P_{z1}f' + P_{z0}f + Q_{z0}g + R_{z0}h]\sin\psi, \qquad (3.11)
\end{aligned}$$

where

$$
\begin{aligned}
P_{r2} &= (1+r^2k^2)B_z^2+\gamma P,\\
P_{r1} &= \frac{1}{r}\left[(1-r^2k^2)B_z^2+\gamma P\right],\\
P_{r0} &= \left[\frac{r^4k^4-4r^2k^2-2r^3kk'-1}{r^2(1+r^2k^2)}-(mk-\tau)^2\right]B_z^2-\frac{\gamma P}{r^2},\\
Q_{r1} &= -P_{t1}=\frac{1}{r}\left[(m+r^2k\tau)B_z^2+m\gamma P\right],\\
Q_{r0} &= \left[\tau(rk'-r^3k^2k'+3k-r^2k^3)-\frac{m}{r^2}\left\{1+5r^2k^2+2r^3kk'\right\}\right]\frac{B_z^2}{1+r^2k^2}-\frac{m\gamma P}{r^2},\\
R_{r1} &= -P_{z1}=-(r^2k\tau+m)kB_z^2-\tau\gamma P,\\
R_{r0} &= \left[m(r^2k^2k'+4rk^3-k')-2rk\tau(2k+rk')\right]\frac{B_z^2}{1+r^2k^2},\\
P_{t0} &= (r^2k\tau-m)\frac{B_z^2}{r^2}-\frac{m\gamma P}{r^2},\\
Q_{t0} &= -(r^2\tau^2+m^2)\frac{B_z^2}{r^2}-\frac{m^2\gamma P}{r^2},\\
R_{t0} &= Q_{z0}=(r^2\tau^2+m^2)\frac{kB_z^2}{r}+\frac{m\tau\gamma P}{r},\\
P_{z0} &= -(r^2k\tau-m)\frac{kB_z^2}{r}+\frac{\tau\gamma P}{r},\\
R_{z0} &= -(r^2\tau^2+m^2)k^2B_z^2-\tau^2\gamma P.
\end{aligned}
\tag{3.12}
$$

Now $\mathbf{F}=\lambda\boldsymbol{\xi}$ gives three linear differential equations

$$
\begin{aligned}
F_r(\boldsymbol{\xi}) &= \lambda f\cos\psi,\\
F_\theta(\boldsymbol{\xi}) &= \lambda g\sin\psi,\\
F_z(\boldsymbol{\xi}) &= \lambda h\sin\psi.
\end{aligned}
$$

Backward substitution, for h and g from the last two equations, yields a second-order ordinary differential equation in $f(r)$,

$$
f''+a(r,\lambda,\tau)f'+b(r,\lambda,\tau)f=0, \tag{3.13}
$$

where the coefficients a and b are rather complicated functions of the given arguments that are calculated with *Maple* and are given in the Appendix. To require physical variables (and hence the gradient of $\boldsymbol{\xi}$) to be finite at the coordinate singularity $r=0$, Sneyd and Craig (1989) show that initial conditions can be taken

as

$$f(0) = 1, \qquad f'(0) = 0. \tag{3.14}$$

If we imagine that the flux tube is confined within a rigid cylinder $0 \leq r \leq r_0$ say, the radial displacement $f(r)$ must vanish on the outer boundary;

$$f(r_0) = 0. \tag{3.15}$$

To determine an eigenvalue we use the technique, of Sneyd and Craig [78], illustrated in figure 3.1. We choose a value of λ then integrate (3.13) numerically as an initial-value problem from $r = 0$ using the initial conditions (3.14). If the solution graph

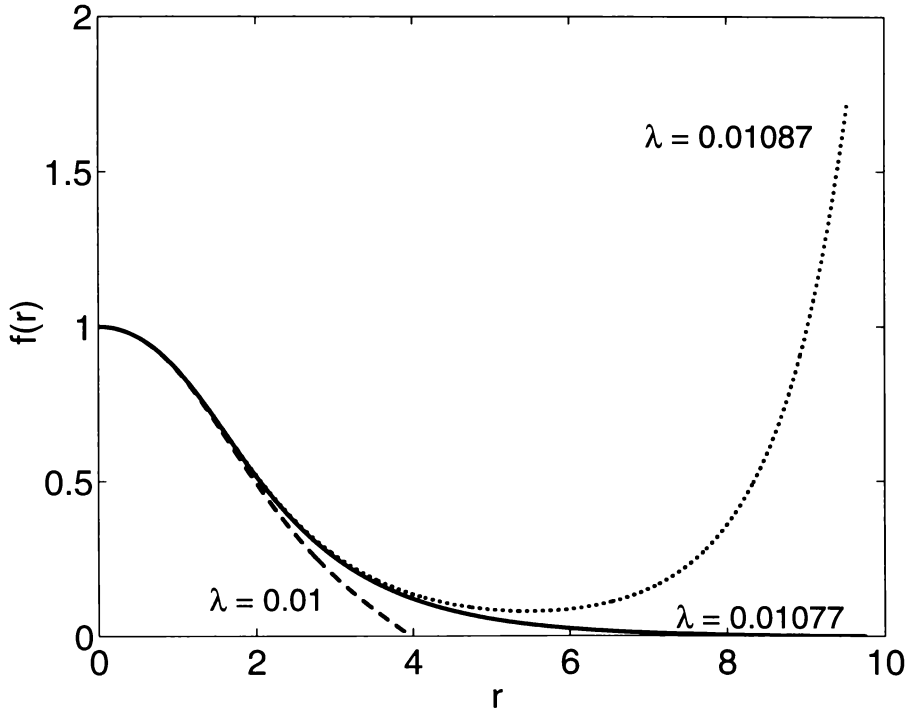

Figure 3.1: Illustration of the method in case of Gold-Hoyle tube when $\tau = 0.5$, $m = 1$, and $P = 0$. The dashed curve $\lambda = 0.01$ represents the eigenfunction for a tube of radius 3.97; the solid curve $\lambda = 0.01077$ the eigenfunction for a tube of radius 9.75. The dotted curve $\lambda = 0.01087$ illustrates the effect of choosing λ greater than the maximum growth rate.

crosses the axis at $r = r_a$ say, then the function f satisfies $f(r_a) = 0$ and therefore represents the eigenfunction for a tube of radius r_a, with our initially-chosen λ as the corresponding eigenvalue. If the initial choice of λ is greater than the growth

rate for an unconfined tube, we find that the graph of $f(r)$ eventually increases rapidly, not crossing the axis.

The behavior of the curve is extremely sensitive to the choice of λ when we are close to the maximum growth rate. For integration of (3.13) we use the fourth order Runge-Kutta routine D02BJF of the NAG library and use a bisection method to determine λ for a given tube radius.

3.2 Growth rates

The energy principle of Bernstein *et al.* [11] provided the foundation for stability analysis of magnetic fields and Newcomb's approach [58] received wide acceptance in calculating stability bounds of magnetic field configurations in the early sixties. Since then numerous modifications and variants (see references cited in the preceding section) have appeared, and been used in different contexts but Anzer [4] emphasized the importance of the kink instability in the context of solar flares. Hood [33, 34, 35, 32, 85, 14, 83] and Craig [18, 78, 19, 28] with different co-workers have kept pushing the boundary on the solar front continuously. To validate our calculations we will refer to relevant results of the latter group as our approach is similar and some of the tests reproduce their earlier results which gives us confidence in our algorithm.

In the following we present results of growth rate calculations for the tubes defined in section 2.3 using the algorithm described in the preceding section and study the effect of twist τ (i.e. pitch of the kink), radius r_a of the tube, and plasma pressure P on stability of these tubes. We plot growth rate λ versus τ for various r_a and P values to demonstrate their effect on stability. The effect of twist and tube radius on the stability of Gold-Hoyle tube has been studied in detail by Sneyd and Craig [78] and we find complete agreement in this case. For tubes $\mathsf{B}_1(\nu)$ previous results are available for comparison and we find the behavior of tubes B_2, B_3 and B_4 is also roughly similar.

Plotted in figure 3.2 are our calculated growth rates for the Gold-Hoyle tube as the solid line, when $P = 0$ and $r_a = 20$. The left hand curve corresponds to the $m = 1$ mode, the center to $m = 2$ and the right hand to $m = 3$. These curves match accurately with Fig. 1 of Sneyd and Craig's [78] infinite radius tube. The dash-dotted and dashed lines in figure 3.2 represent the corresponding curves for our tubes B_2 and B_3 respectively.

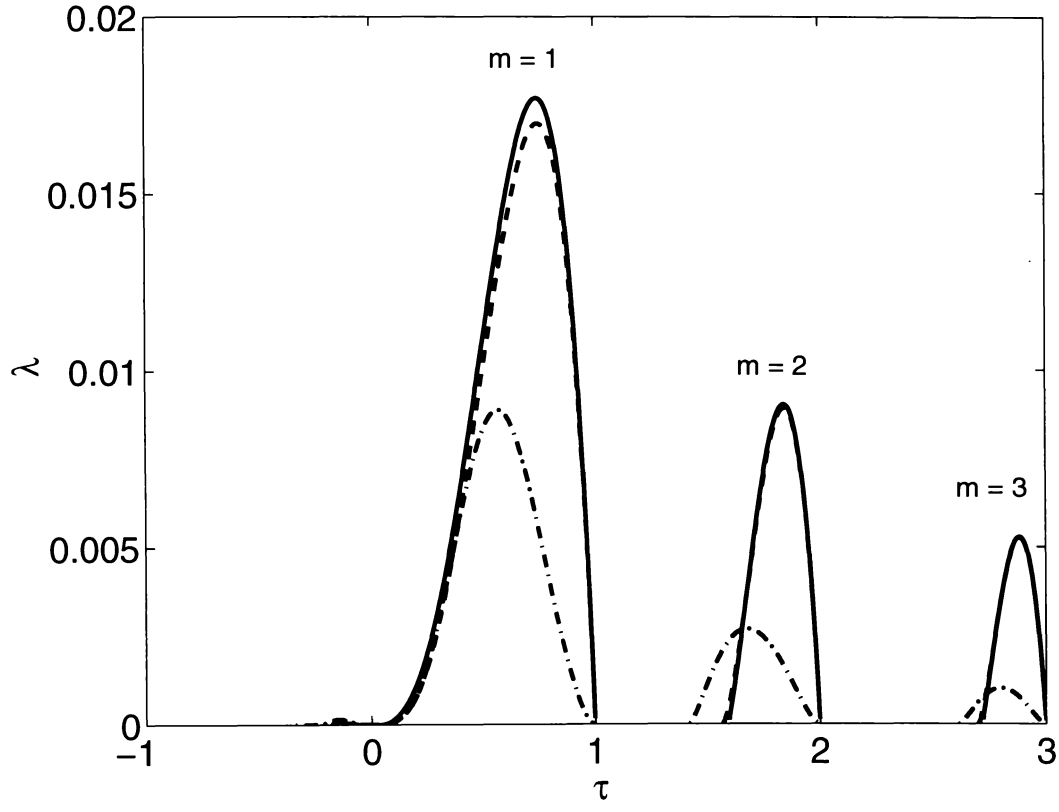

Figure 3.2: Growth rates versus pitch τ of $\mathsf{B}_1(0)$ (solid), B_2 (dash-dotted) and B_3 (dashed) for $m = 1, 2, 3$ when $r_a = 20$ and $P = 0$.

The $m = 1$ kink mode is the most unstable mode in all the cases. B_3 is slightly more stable than the Gold-Hoyle tube as is clear from its maximum growth rate, $\lambda = 0.016977$, compared to $\lambda = 0.017698$ for the Gold-Hoyle tube, both maxima occurring at $\tau = 0.75$. The maximum growth rate of B_2 is the smallest of the three, having a value of 0.008795 at $\tau = 0.575$ for the $m = 1$ mode, almost half that of the Gold-Hoyle tube.

For the weaker $m = 2$ mode the maximum growth rates are $\lambda = 0.009027$ at $\tau = 1.845$, $\lambda = 0.008927$ at $\tau = 1.845$ and $\lambda = 0.00268$ at $\tau = 1.675$ for Gold-Hoyle, B_3 and B_2 respectively. The corresponding values for the weakest mode $m = 3$ are $\lambda = 0.005275$ at $\tau = 2.885$, $\lambda = 0.005258$ at $\tau = 2.885$ and $\lambda = 0.001016$ at $\tau = 2.8$ respectively. A very weak reverse-pitch kink instability ($\tau < 0$) is noticeable for the Gold-Hoyle tube and B_2.

We plot the growth rate of B_4 for $m = 1$ separately in figure 3.3 because it is extremely weak for negative τ while for $\tau > 0$ the tube is completely stable. Hence Robinson's [72] remark, that axial field reversal makes the configuration stable, is validated here. He studies such a field (see [72] Fig. 6) and shows that a positive τ value (his negative k) is more stabilising but there is a possibility of instability for negative τ.

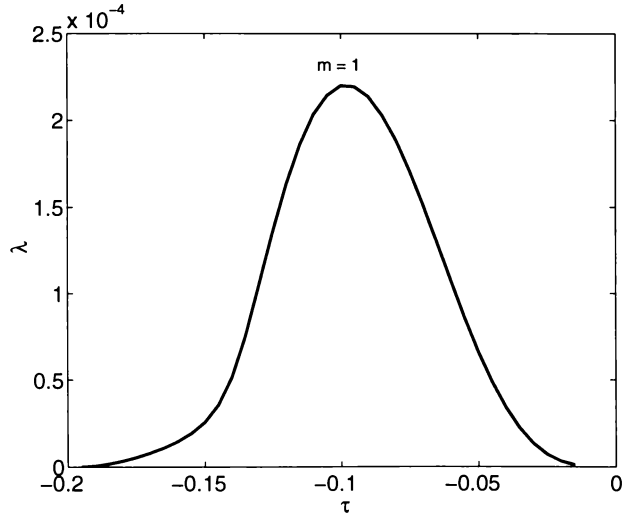

Figure 3.3: Growth rate versus pitch τ of B_4 for $m = 1$ when $r_a = 20$.

All of the above results are in full agreement with those of Robinson [72], Sneyd and Craig [78] and Van der Lindon and Hood [83]. Van der Lindon and Hood [83] uses the WKB method for stability analysis of a force-free cylindrical line-tied tube and conclude that the $m = 1$ mode is always the first to become unstable. The $m = 0$ sausage mode is always stable in axially symmetric flux tubes [78] and $m \geq 4$ kink modes seem to be more stable than $m = 1$, as is clear from the trend of growth

rates in figure 3.2. Hence in the following we will concentrate only on the $m = 1$ kink mode when investigating the effects of tube radius and hydrodynamic pressure on stability.

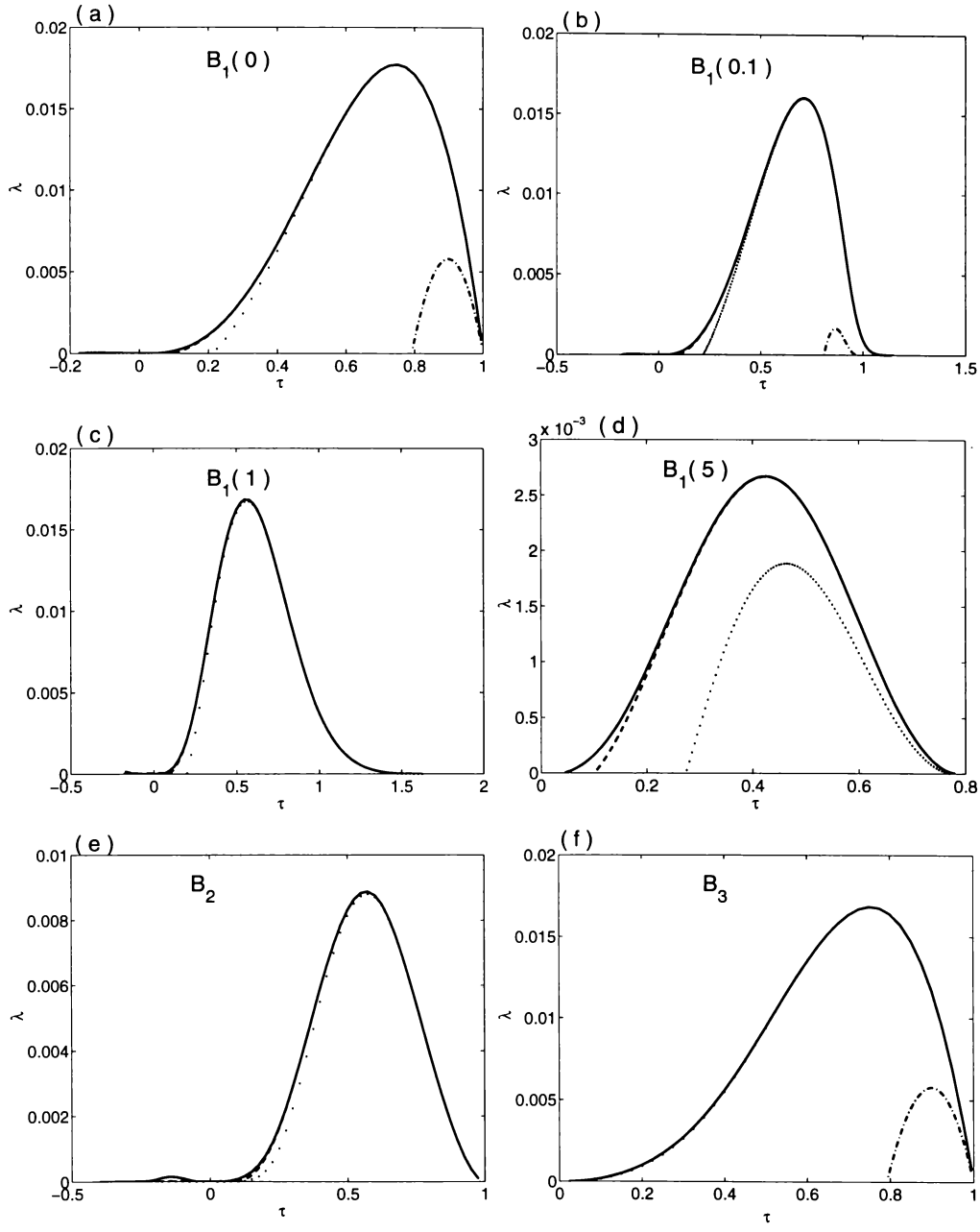

Figure 3.4: Effect of tube radius on stability. $r_a = 20$ (solid), $r_a = 10$ (dashed), $r_a = 5$ (dotted) and $r_a = 1$ (dash-dotted) when $m = 1$ and $P = 0$.

Figure 3.4 shows the effect of tube radius on growth rates for various tubes. Here $P = 0$, $m = 1$ and the solid line represents a tube of radius $r_a = 20$, the dashed $r_a = 10$, the dotted $r_a = 5$ and the dash-dotted a tube of radius $r_a = 1$. The

solid and dash-dotted curves in (a) exactly match Fig. 1 of Sneyd and Craig [78], while solid curves in (a) - (d) exactly match Fig. 1 of Craig *et al.* [19]. In most of the plots the dashed curve almost overlies the solid one, but when the radius is reduced to 1, the reduction in growth rates is quite dramatic. For $\mathsf{B}_1(1)$, $\mathsf{B}_1(5)$ and B_2 non-existence of the dash-dotted curves indicates complete stability of these tubes when $r_a = 1$.

It is clear that taking $r_a = 5$ will reduce the computational domain substantially but have negligible effect on stability for almost all tubes. Also the accuracy of the results for $\mathsf{B}_1(\nu)$, $\nu = 0$, 0.1, 1 and 5, indicates reliability of the procedure in other cases. Hence from now onward we take $r_a = 5$ and concentrate only on tubes $\mathsf{B}_1(0)$, B_2, B_3 and B_4 throughout.

With finite plasma pressure the growth rates are somewhat reduced since the initial uniform pressure distribution has a stabilizing influence. Pressure is described by the ratio of plasma to magnetic pressure,

$$\beta = \frac{P}{\frac{1}{2} B_z^2(0)}$$

where P is the initial pressure. In the solar corona $\beta \approx 0.01$ and, so, we perform calculations with this value of β both here and in the nonlinear studies. The value $\beta = 0.02$ in the following calculations is used to clarify the picture.

Plotted in figure 3.5 are the growth rates versus twist τ of our four tubes for the $m = 1$ kink mode with different plasma pressures. The solid lines are for zero gas pressure, $\beta = 0$, the dashed lines correspond to $\beta = 0.01$ and the dotted ones to $\beta = 0.02$ respectively. In each case pressure damps the instability significantly in both magnitude and twist range. The lower twist limit remains only marginally affected but the reduction in the upper limit is more pronounced. It is interesting to note that while the negative τ instability of the tube B_4 is extremely weak and has a very small range, it persists even after radius reduction from $r_a = 20$ (in figure 3.3) to $r_a = 5$ and after plasma pressure inclusion. The increase in plasma pressure has affected the maximum λ only in 6th decimal place and so no clear reduction in

λ is noticeable in the dotted curve. In practical computations such a feeble kink will be very difficult to capture and might get smoothed away by small numerical diffusion or truncation errors. The other tube having a reverse-pitch kink is the oscillating twist tube B_2 whose growth rate $\lambda = 2 \times 10^{-4}$ at $\tau = -0.125$ is affected only in the 8th decimal place by pressure.

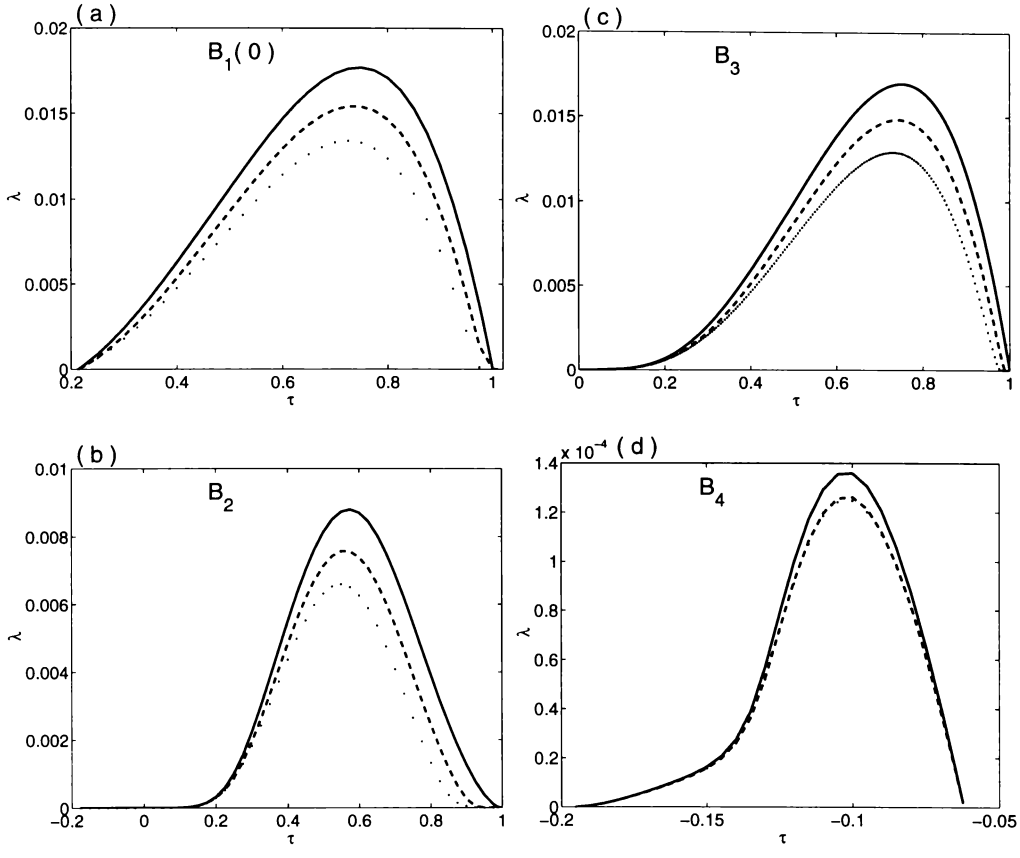

Figure 3.5: Effect of plasma pressure on stability. $\beta = 0$, (solid), $\beta = 0.01$ (dashed) and $\beta = 0.02$ (dotted) when $m = 1$.

In short, the Gold-Hoyle tube is the most unstable and B_4 the most stable amongst the four tubes B_1 - B_4 studied in this chapter. Reduction of tube radius and inclusion of plasma pressure damps the instability significantly in both magnitude and twist range. In chapters 5 and 6, we will study relaxation to a second helically symmetric equilibrium of these tubes after a small perturbation is applied.

Chapter 4

Helical symmetry and magnetofrictional plasma

Having determined that an equilibrium is unstable, the next important question is: do current sheets form when the equilibrium relaxes to a lower energy state? There have been numerous observational, theoretical and computational attempts to address this problem but no general answer is available. Possible consequences of the kink instability have not been fully explored and continue to receive much attention. Apart from rotational motions of flux-tube endpoints as the cause of twist and instability [68], Pevtsov *et al.* [67] state: "Our observations imply that an unstable coronal loop was created because of reconnection and the consequent formation of a loop whose twist exceeded 2.4π". They suggest further nonlinear studies to resolve the problem and fully understand the phenomena. A number of nonlinear MHD studies have been carried out recently to capture the kink and explore the behavior of the field during and after the development of the instability yet rigorous proof of current sheet formation is still awaited.

As stated earlier one objective of this study is to develop a mathematical model, based on the ideal MHD equations, to find lower energy equilibria in a variety of cylindrical flux tubes that requires few computational resources yet gives an accurate

picture of the process. As discussed in the first chapter, the $m = 1$ kink instability deforms a flux tube in to the shape of a helix (figure 1.4). Such deformation can be dealt with using helical coordinates (r, ϕ, e) with $\widehat{\mathbf{e}} = \widehat{\mathbf{r}} \times \widehat{\boldsymbol{\phi}}$, $\phi = \theta - \tau z$ and τ a constant representing the twist, which is inversely proportional to the pitch angle of the helix on which r and ϕ are constant. Park, Monticello and White [61] have derived and used the incompressible MHD equations using these coordinates. Landman [42] and Dritschel [26] have also used them in hydrodynamics and MHD. However, we find it more straightforward to use Cartesian coordinates (x, y, z) since we use an ADI method in our code.

A helically symmetric function f is invariant under a combined rotation about and a translation along the axis, i.e.

$$f(r, \theta, z) = f(r, \theta - \tau z, 0) \tag{4.1}$$

where τ is a constant pitch parameter. Geometrically $\tan^{-1}(\frac{1}{r\tau})$ represents the pitch angle of the helix on which r and $\phi = \theta - \tau z$ are constant, see figure 4.1.

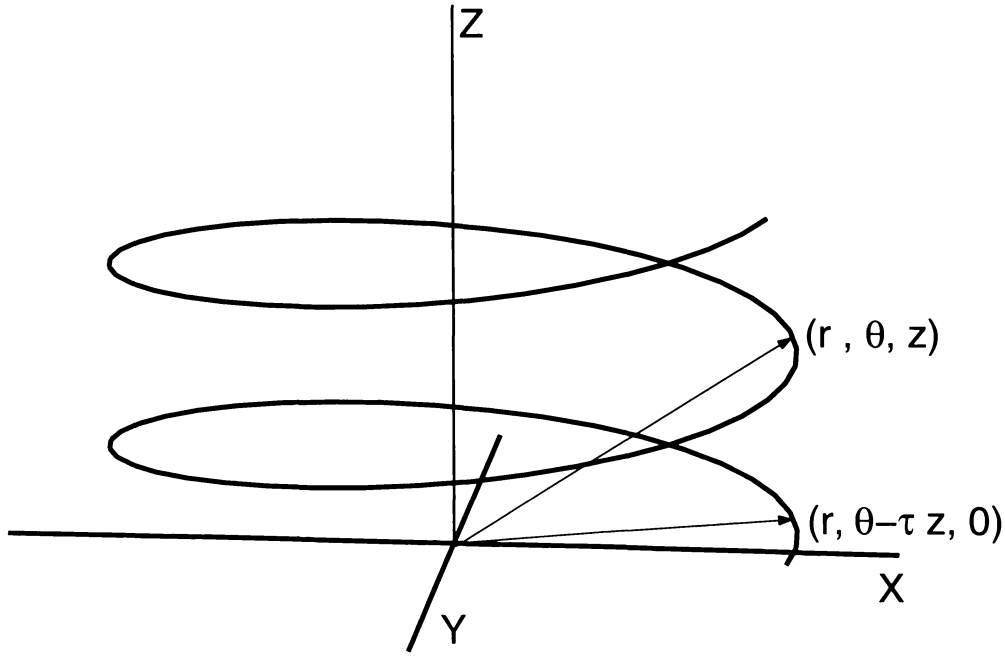

Figure 4.1: A helically symmetric function.

The helical symmetry relation (4.1) can be expressed in Cartesian coordinates as follows:

$$f(\mathbf{x}_p, z) = f\big[L(-\tau z)\mathbf{x}_p,\, 0\big], \tag{4.2}$$

where $\mathbf{x}_p = (x, y)$ or (x_1, x_2) represents position in the (x, y)-plane and L is the rotation matrix

$$L(\alpha) = \begin{pmatrix} \cos\alpha & -\sin\alpha \\ \sin\alpha & \cos\alpha \end{pmatrix}. \tag{4.3}$$

The values of a helically symmetric function in any plane $z =$ constant provide a complete specification, and in particular enable us to calculate $\partial f/\partial z$. Using suffix notation we can write,

$$f(x, y, z) = f\big[L_{1j}x_j,\, L_{2j}x_j,\, 0\big]$$

where the L_{ij} are elements of the rotation matrix (4.3) and the repeated suffix j is summed from 1-2. Differentiating with respect to z we find,

$$\frac{\partial f}{\partial z} = \frac{\partial f}{\partial x}\frac{\partial L_{1j}}{\partial z}x_j + \frac{\partial f}{\partial y}\frac{\partial L_{2j}}{\partial z}x_j.$$

Since

$$\left(\frac{\partial}{\partial z}L(-\tau z)\right)_{z=0} = \begin{pmatrix} 0 & \tau \\ -\tau & 0 \end{pmatrix},$$

it follows that

$$\left(\frac{\partial f}{\partial z}\right)_{z=0} = \tau y\frac{\partial f}{\partial x} - \tau x\frac{\partial f}{\partial y} = \frac{\partial_h f}{\partial z}, \quad \text{say} \tag{4.4}$$

where the subscript h indicates a "helical derivative".

Similarly a helically symmetric vector field $\mathbf{B}$ in the plane $z = z_0$ is a copy of the field in the plane $z = 0$ but rotated through an angle τz_0, i.e.

$$\mathbf{B}(r, \theta, z) = B_r(r, \theta - \tau z, 0)\widehat{\mathbf{r}} + B_\theta(r, \theta - \tau z, 0)\widehat{\boldsymbol{\theta}} + B_z(r, \theta - \tau z, 0)\widehat{\mathbf{z}}.$$

Since B_r now points in the rotated direction, see figure 4.2, a backward rotation is needed to relate the plane Cartesian components of $\mathbf{B}$. Thus in Cartesian coordinates we have

$$\mathbf{B}_p(\mathbf{x}_p, z) = L(\tau z)\mathbf{B}_p\big[L(-\tau z)\mathbf{x}_p,\, 0\big],$$

$$B_z(\mathbf{x}_p, z) = B_z\big[L(-\tau z)\mathbf{x}_p,\, 0\big],$$

where the subscript p denotes the component of the field lying in the (x, y)-plane.

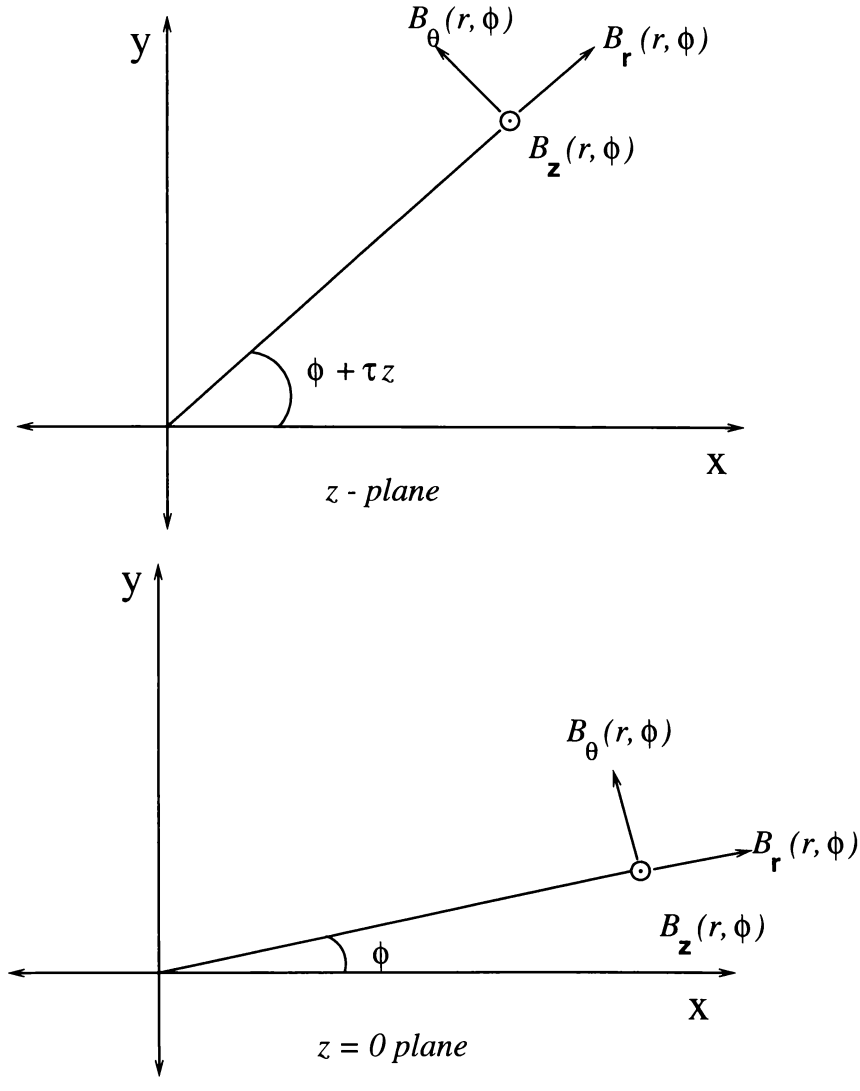

Figure 4.2: Components of a helically symmetric field in different planes.

Differentiation with respect to z then setting $z = 0$ gives,

$$\frac{\partial \mathbf{B}_p}{\partial z} = \begin{pmatrix} 0 & -\tau \\ \tau & 0 \end{pmatrix} \mathbf{B}_p\big[\mathbf{x}_p,\, 0\big] + \frac{\partial_h \mathbf{B}_p}{\partial z}.$$

To summarize:

$$\frac{\partial_h \mathbf{B}}{\partial z} = \tau \begin{pmatrix} -B_y \\ B_x \\ 0 \end{pmatrix} + \tau \left(y\frac{\partial}{\partial x} - x\frac{\partial}{\partial y} \right) \begin{pmatrix} B_x \\ B_y \\ B_z \end{pmatrix}. \tag{4.5}$$

Now we can define

$$\nabla_h \times \mathbf{B} = \begin{vmatrix} \widehat{\mathbf{x}} & \widehat{\mathbf{y}} & \widehat{\mathbf{z}} \\ \frac{\partial}{\partial x} & \frac{\partial}{\partial y} & \frac{\partial_h}{\partial z} \\ B_x & B_y & B_z \end{vmatrix}, \tag{4.6}$$

so that the electric current is given by $\mathbf{J} = \nabla_h \times \mathbf{B}$, or

$$\mathbf{J} = \begin{pmatrix} \dfrac{\partial B_z}{\partial y} - \tau \left(B_x + y\dfrac{\partial B_y}{\partial x} - x\dfrac{\partial B_y}{\partial y} \right) \\ -\dfrac{\partial B_z}{\partial x} - \tau \left(B_y - y\dfrac{\partial B_x}{\partial x} + x\dfrac{\partial B_x}{\partial y} \right) \\ \dfrac{\partial B_y}{\partial x} - \dfrac{\partial B_x}{\partial y} \end{pmatrix} \tag{4.7}$$

and the Lorentz force, $\mathbf{F_b} = \mathbf{J} \times \mathbf{B}$, is given by

$$\begin{aligned} \mathbf{F_b} = \quad & \left[B_z \left\{ \tau \left(y\tfrac{\partial B_x}{\partial x} - x\tfrac{\partial B_x}{\partial y} - B_y \right) - \tfrac{\partial B_z}{\partial x} \right\} - B_y \left\{ \tfrac{\partial B_y}{\partial x} - \tfrac{\partial B_x}{\partial y} \right\} \right] \widehat{\mathbf{x}} \\ & + \left[B_z \left\{ \tau \left(y\tfrac{\partial B_y}{\partial x} - x\tfrac{\partial B_y}{\partial y} + B_x \right) - \tfrac{\partial B_z}{\partial y} \right\} + B_x \left\{ \tfrac{\partial B_y}{\partial x} - \tfrac{\partial B_x}{\partial y} \right\} \right] \widehat{\mathbf{y}}. \end{aligned} \tag{4.8}$$

Axisymmetric fields can be treated as a particular case of helical symmetry with pitch $\tau = 0$. The assumption of helical symmetry means that variables need to be specified in the plane $z = 0$ only, z-derivatives being calculated using the above formulae. Our domain is therefore effectively the plane $z = 0$.

4.1 The frictional path to equilibrium

Since field lines are frozen-in to the plasma, a suitable numerical framework will be a Lagrangian description in which case grid points will accumulate at places of high compression automatically and no re-meshing or special techniques will be necessary to cater for current concentrations. Craig and Sneyd [20] have developed a simple

Lagrangian relaxation technique (see also [50, 22]) that we restrict to our helical geometry.

The first step in this direction is the magneto-frictional plasma approximation of Chodura and Schlüter [15] which ignores the inertia of the plasma and replaces the momentum equation (2.4) by

$$\mathbf{v} = -\nabla P + \mathbf{J} \times \mathbf{B} = \mathbf{F}_p + \mathbf{F}_b. \tag{4.9}$$

This way an energy dissipation mechanism is incorporated into the ideal MHD formulation, which comes from resistance experienced by each particle equal to its velocity. The rate of energy dissipation, $\mathbf{v} \cdot \mathbf{F} = F^2$, is always positive and an equilibrium attained using this formulation will be a true stable equilibrium. The resulting equations of motion are parabolic, rather than hyperbolic, and hence shock wave formation is eliminated [20]. As stated earlier, in chapter 3, existence of a positive eigenvalue λ of $\mathbf{F}$ corresponding to a small eigen-displacement $\boldsymbol{\xi}$ is an indicator of instability. Time evolution of $\boldsymbol{\xi}$ in the real plasma case, using (2.4), is governed by

$$\rho \frac{D^2\boldsymbol{\xi}}{Dt^2} = \lambda \boldsymbol{\xi}.$$

Thus $\boldsymbol{\xi}$ grows as $\exp(\sqrt{\lambda/\rho}\, t)$ showing that a $\boldsymbol{\xi}$ corresponding to a negative eigenvalue (-λ, say) will oscillate with angular frequency $\sqrt{\lambda/\rho}$. On the other hand for a frictional plasma (4.9) gives

$$\frac{D\boldsymbol{\xi}}{Dt} = \lambda \boldsymbol{\xi}$$

implying that $\boldsymbol{\xi}$ grows as $\exp(\lambda t)$. Thus a disturbance corresponding to a negative eigenvalue -λ will die away as $\exp(-\lambda t)$. Hence the only effect of equation (4.9) on stability is damping super critically all oscillations about a stable equilibrium. Since our only aim is to find the final equilibrium such falsification of the momentum equation is justifiable, and any final equilibrium attained will be stable [22].

We constrain the flow to lie in the $z = 0$ plane. When plasma motion ceases we know the in-plane force vanishes, so

$$\mathbf{J} \times \mathbf{B} - \nabla P = R\widehat{\mathbf{z}},$$

where R is the residual force in the z-direction. Taking the inner product of this equation with $\mathbf{B}$ gives,

$$R = -\mathbf{B} \cdot \nabla P / B_z$$

so that R must be of the order of the plasma pressure P. Since we take $\beta \ll 1$ this ensures that an equilibrium has been achieved to a high degree of approximation. We find moreover that our conclusions regarding the type of equilibrium achieved are insensitive to the choice of β. Essentially the magnetic forces determine the type of equilibrium.

In the Lagrangian formulation the position of a fluid particle is represented by the two-dimensional vector $\mathbf{x}(a_1, a_2)$ where the a_i are the coordinates of the particle at time $t = 0$. This position is updated, to $\mathbf{x} = (x_1, x_2)$, with time according to equation (4.9). The induction equation can be solved analytically by exploiting the fact that $\mathbf{B}/\rho$ evolves as a fluid line element $d\mathbf{x}$. For $\mathbf{B}/\rho$ we have

$$\begin{aligned} \frac{D}{Dt}\left(\frac{\mathbf{B}}{\rho}\right) &= \frac{1}{\rho}\frac{D\mathbf{B}}{Dt} - \frac{\mathbf{B}}{\rho^2}\frac{D\rho}{Dt} \\ &= \frac{1}{\rho}\left[\frac{D\mathbf{B}}{Dt} - \frac{\mathbf{B}}{\rho}[-\rho(\nabla \cdot \mathbf{v})]\right], \quad \text{using (2.6)}, \\ &= \left(\frac{\mathbf{B}}{\rho} \cdot \nabla\right)\mathbf{v}, \quad \text{using (2.5)}, \end{aligned} \tag{4.10}$$

while for $d\mathbf{x}$ we have

$$dx_i = \frac{\partial x_i}{\partial a_1} da_1 + \frac{\partial x_i}{\partial a_2} da_2$$

which implies

$$d\mathbf{x} = W d\mathbf{a}, \tag{4.11}$$

where

$$W = \begin{pmatrix} \frac{\partial x_1}{\partial a_1} & \frac{\partial x_1}{\partial a_2} \\ \frac{\partial x_2}{\partial a_1} & \frac{\partial x_2}{\partial a_2} \end{pmatrix}.$$

Using suffix notation, differentiation of this expression with respect to time gives

$$\begin{aligned}\frac{D}{Dt}(d\mathbf{x}) &= \frac{D}{Dt}\left(\frac{\partial x_i}{\partial a_j}da_j\right)\\ &= \frac{\partial v_i}{\partial a_j}da_j\\ &= \frac{\partial v_i}{\partial x_l}\frac{\partial x_l}{\partial a_j}da_j\\ &= \frac{\partial v_i}{\partial x_l}dx_l\\ &= (d\mathbf{x}\cdot\nabla)\mathbf{v}. \qquad (4.12)\end{aligned}$$

Since $d\mathbf{x}$ and $\mathbf{B}/\rho$ satisfy identical evolution equations, namely (4.12) and (4.10), $\mathbf{B}/\rho$ must satisfy an equation similar to (4.11). Thus, with $\rho(\mathbf{a})$ and $\mathbf{B}(\mathbf{a})$ denoting values at time $t = 0$, the values at position $\mathbf{x}(t)$ satisfy

$$\frac{\mathbf{B}(\mathbf{x})}{\rho(\mathbf{x})} = W\frac{\mathbf{B}(\mathbf{a})}{\rho(\mathbf{a})}.$$

This solution is known as the Cauchy solution (see e.g. Moffatt [57]). Now mass conservation implies

$$\rho(\mathbf{x})dx_1dx_2 = \rho(\mathbf{a})da_1da_2,$$

and

$$dx_1dx_2 = \Delta da_1da_2 \quad \text{with} \quad \Delta = \frac{\partial(x_1,x_2)}{\partial(a_1,a_2)}.$$

Thus

$$\rho(\mathbf{x}) = \rho(\mathbf{a})/\Delta. \qquad (4.13)$$

Similarly flux conservation gives the evolution of B_z as

$$B_z(\mathbf{x}) = B_z(\mathbf{a})/\Delta. \qquad (4.14)$$

Substitution for $\rho(\mathbf{x})$ in the Cauchy solution gives the relation for evolution of horizontal field components

$$B_i(\mathbf{x}) = \frac{1}{\Delta}\frac{\partial x_i}{\partial a_p}B_p(\mathbf{a}), \quad i,p = 1,2. \qquad (4.15)$$

Similarly, using the equation of state (2.7), the plasma pressure force $\mathbf{F_p} = -\nabla P$ can be obtained as

$$\mathbf{F_p} = -g_p\gamma(\rho(\mathbf{a})/\Delta)^{\gamma-1}\nabla\rho(\mathbf{x}). \qquad (4.16)$$

Now (4.11) implies

$$d\mathbf{a} = W^{-1} d\mathbf{x}$$

and

$$da_i = \frac{\partial a_i}{\partial x_1} dx_1 + \frac{\partial a_i}{\partial x_2} dx_2$$

implies

$$d\mathbf{a} = O d\mathbf{x},$$

with $O_{ij} = \frac{\partial a_i}{\partial x_j}$. That is $O = W^{-1}$, and using the chain rule we have

$$\frac{\partial}{\partial x_i} = \frac{\partial a_1}{\partial x_i}\frac{\partial}{\partial a_1} + \frac{\partial a_2}{\partial x_i}\frac{\partial}{\partial a_2} = \frac{\partial a_j}{\partial x_i}\frac{\partial}{\partial a_j} = O_{ji}\frac{\partial}{\partial a_j}.$$

Thus if we define an array M by

$$M = (W^{-1})^T = \frac{1}{\Delta}\begin{pmatrix} \frac{\partial x_2}{\partial a_2} & -\frac{\partial x_2}{\partial a_1} \\ -\frac{\partial x_1}{\partial a_2} & \frac{\partial x_1}{\partial a_1} \end{pmatrix}$$

then local derivatives obtained with respect to $\mathbf{a}$ can be utilized as

$$\frac{\partial}{\partial x_i} = M_{ij}\frac{\partial}{\partial a_j}, \tag{4.17}$$

to get

$$\begin{aligned} \frac{\partial \rho(\mathbf{x})}{\partial x_i} &= \frac{1}{\Delta} M_{ij}\left(\frac{\partial \rho(\mathbf{a})}{\partial a_j} - \frac{\rho(\mathbf{a})}{\Delta}\frac{\partial \Delta}{\partial a_j}\right) \\ &= -\frac{\rho(\mathbf{a}) M_{ij}}{\Delta^2}\frac{\partial \Delta}{\partial a_j}, \end{aligned} \tag{4.18}$$

$$\frac{\partial B_z(\mathbf{x})}{\partial x_i} = \frac{1}{\Delta} M_{ij}\left(\frac{\partial B_z(\mathbf{a})}{\partial a_j} - \frac{B_z(\mathbf{a})}{\Delta}\frac{\partial \Delta}{\partial a_j}\right), \tag{4.19}$$

and

$$\frac{\partial B_i(\mathbf{x})}{\partial x_j} = \frac{1}{\Delta} M_{jq}\left(\frac{\partial^2 x_i}{\partial a_p \partial a_q} B_p(\mathbf{a}) + \frac{\partial x_i}{\partial a_p}\frac{\partial B_p(\mathbf{a})}{\partial a_q} - \frac{B_p(\mathbf{a})}{\Delta}\frac{\partial x_i}{\partial a_p}\frac{\partial \Delta}{\partial a_q}\right). \tag{4.20}$$

This way, the only equations to be solved for frictional evolution are the two components of

$$\frac{D\mathbf{x}}{Dt} = \mathbf{F}_p + \mathbf{F}_b, \tag{4.21}$$

with $\mathbf{F}_p$ and $\mathbf{F}_b$ given by (4.16) and (4.8) respectively. Equations (4.13 - 4.15) and (4.18 - 4.20) provide all that is needed for force, $\mathbf{F} = \mathbf{F}_p + \mathbf{F}_b$, update.

After a uniform twist τ we get $B_x(\mathbf{x}) = B_x(\mathbf{a}) - \tau a_2 B_z(\mathbf{a})$ and $B_y(\mathbf{x}) = B_y(\mathbf{a}) + \tau a_1 B_z(\mathbf{a})$. These substitutions in the expressions for $\mathbf{J}$ and $\mathbf{F}$ give the extra rotation that needs subtraction when defining the initial field and its gradient.

4.2 The helical code

We take a rectangular computational domain $[-r_a\,,\,r_a] \times [-r_a\,,\,r_a]$ enclosing the tube (tubes), with a square mesh and super conducting boundaries. Thus the three-dimensional box enclosing the cylindrical tube (tubes) also twists with the field and nodes on the boundaries remain fixed. Local field values $B_z(\mathbf{a})$ are calculated at the fixed grid points (a_1, a_2) once at the start of the calculations and stored for use in the field updating for the rest of the calculations. The initial equilibrium tubes are axially symmetric, $\mathbf{B} = B_\theta(r)\widehat{\boldsymbol{\theta}} + B_z(r)\widehat{\mathbf{z}}$ with $B_\theta = rkB_z$. For a kink of pitch τ the field component B_θ goes through a rigid body rotation, as explained in the preceding section. Thus we subtract the extra rotation to have $B_\theta = r(k-\tau)B_z$ and so the horizontal components of field B_x and B_y are given by

$$B_x\widehat{\mathbf{x}} + B_y\widehat{\mathbf{y}} = r(k-\tau)B_z\widehat{\boldsymbol{\theta}}.$$

With $\widehat{\boldsymbol{\theta}} = -\sin\theta\widehat{\mathbf{x}} + \cos\theta\widehat{\mathbf{y}}$ this gives

$$B_x = -a_2(k-\tau)B_z \quad \text{and} \quad B_y = a_1(k-\tau)B_z.$$

Denoting $\frac{\partial B_z}{\partial r}$ by B'_z, local gradients are now given by the analytic expressions

$$\begin{aligned}
\frac{\partial B_z}{\partial a_1} &= \frac{a_1}{r}B'_z, & \frac{\partial B_z}{\partial a_2} &= \frac{a_2}{r}B'_z,\\
\frac{\partial B_x}{\partial a_1} &= -\frac{a_1 a_2}{r}Q, & \frac{\partial B_y}{\partial a_2} &= \frac{a_1 a_2}{r}Q,\\
\frac{\partial B_x}{\partial a_2} &= -(k-\tau)B_z - \frac{a_2^2}{r}Q, & \frac{\partial B_y}{\partial a_1} &= (k-\tau)B_z + \frac{a_1^2}{r}Q
\end{aligned}$$

$$\text{with} \quad Q = (k-\tau)B'_z + B_z k' \quad \text{and} \quad B'_z = \frac{-rkB_z(2k+rk')}{1+r^2k^2}.$$

Updating of field and gradients to the deformed grid now takes place through equations (4.14 - 4.15) and (4.19 - 4.20) to give new values of $\mathbf{F}$ using (4.8) and (4.16).

Second-order centered differences are used for spatial derivatives throughout. For initial equilibrium fields, a small displacement $\boldsymbol{\xi}$ is applied to the grid $\mathbf{x}(\mathbf{a}, 0)$ to perturb the equilibrium and the resulting force is calculated using (4.16) and (4.8). Instantaneous nodal positions $\mathbf{x}(\mathbf{a}, t)$ are calculated by solving (4.21) numerically using an alternating direction implicit (ADI) scheme, detailed in Sneyd and Craig [21], and derivatives $\frac{\partial x_i}{\partial a_p}$ and $\frac{\partial^2 x_i}{\partial a_p \partial a_q}$ are calculated to obtain updated values of the matrix M, the Jacobian Δ and its derivatives. The next cycle starts again with field and force updates, to calculate new positions of the nodes.

The ADI scheme [21] adopted here has one explicit predictor step

$$X_i^{n+1(0)} = X_i^n + \Delta t F_i^n, \tag{4.22}$$

where X_i^n represents the approximation of $x_i(n\Delta t)$ and Δt the time step. This step is followed by two corrective ADI steps

$$\begin{aligned} \left(1 - \Theta\,\zeta\, q_{11}\, \delta a_1^2\right) X_i^{n+1(1)} &= X_i^{n+1(0)} - \Theta\,\zeta\, q_{11}\, \delta a_1^2 X_i^n, \\ \left(1 - \Theta\,\zeta\, q_{22}\, \delta a_2^2\right) X_i^{n+1} &= X_i^{n+1(1)} - \Theta\,\zeta\, q_{22}\, \delta a_2^2 X_i^n. \end{aligned} \tag{4.23}$$

Here $\Theta \geq 0$ is the implicitness parameter giving a fully explicit scheme when $\Theta = 0$ and a fully implicit scheme when $\Theta = 1$. With mesh size Δa, ζ is the ratio $\Delta t/(\Delta a)^2$ and q_{jj} is the coefficient of the diagonal term $\frac{\partial^2 x_j}{\partial a_j^2}$ in F_i^n. Standard centered difference operators of the form

$$\begin{aligned} \delta a_1^2 X_i^n(l,m) &= X_i^n(l+1,m) - 2X_i^n(l,m) + X_i^n(l-1,m), \\ \delta a_1 a_2 X_i^n(l,m) &= X_i^n(l+1,m+1) - X_i^n(l+1,m-1) - X_i^n(l-1,m+1) \\ &\quad + X_i^n(l-1,m-1) \end{aligned}$$

are used as follows, in the approximation of 2nd-order derivatives,

$$\begin{aligned} \frac{\partial^2 x_i}{\partial a_1^2} &= \frac{\delta a_1^2 X_i^n(l,m)}{\Delta a^2}, \\ \frac{\partial^2 x_i}{\partial a_1 a_2} &= \frac{\delta a_1 a_2 X_i^n(l,m)}{4\Delta a}, \end{aligned}$$

at a mesh point (l, m) and time level n. The coefficients q_{jj} of the diagonal term

$\frac{\partial^2 x_j}{\partial a_j^2}$ in F_i^n are given by

$$q_{11} = \frac{1}{\Delta^2}\Bigg[(1+r^2\tau^2)\left(B_z(\mathbf{x})\frac{\partial x_{3-i}}{\partial a_2}\right)^2 + B_{3-i}^2(\mathbf{x})\left((\frac{\partial x_2}{\partial a_2})^2 + (\frac{\partial x_1}{\partial a_2})^2\right) + 2\tau B_z(\mathbf{x})B_{3-i}(\mathbf{x})\frac{\partial x_{3-i}}{\partial a_2}\left(x_1\frac{\partial x_2}{\partial a_2} - x_2\frac{\partial x_1}{\partial a_2}\right) + g_p\left(\frac{\partial x_{3-i}}{\partial a_2}\right)^2\Bigg]$$

and

$$q_{22} = \frac{1}{\Delta^2}\Bigg[(1+r^2\tau^2)\left(B_z(\mathbf{x})\frac{\partial x_{3-i}}{\partial a_1}\right)^2 + B_{3-i}^2(\mathbf{x})\left((\frac{\partial x_2}{\partial a_1})^2 + (\frac{\partial x_1}{\partial a_1})^2\right) + 2\tau B_z(\mathbf{x})B_{3-i}(\mathbf{x})\frac{\partial x_{3-i}}{\partial a_1}\left(x_1\frac{\partial x_2}{\partial a_1} - x_2\frac{\partial x_1}{\partial a_1}\right) + g_p\left(\frac{\partial x_{3-i}}{\partial a_1}\right)^2\Bigg].$$

In all our calculations we use the fully implicit option $\Theta = 1$ in (4.23) and the resulting tri-diagonal linear system is solved using the Thomas algorithm. The time step Δt remains constant throughout and grid compression is monitored by evaluating $\Delta_{\min}$, the minimum value of the Jacobian Δ. To avoid node crossings (negative element area) the program is stopped when Δ becomes very small or negative. When necessary, the program is restarted with a smaller value of ζ. The implicit choice allows the use of quite large time steps when the field is smooth, e.g. $\zeta = 80$ for a nonlinear kink simulation of $\mathsf{B}_1(0)$ and B_2 in the next chapter. In the presence of high current concentrations and current sheets very small time steps are needed to keep Δ positive. We also monitor the maximum values of current $|\mathbf{J}|$ and force $|\mathbf{F}|$ (J_{max}, $F_{\max}$) throughout the evolution. $F_{\max}$ gives a measure of the strength of the kink and J_{max} that of current concentration. $J_{\max}$ is monitored for any growth representing a current concentration or sheet. The current sheet diagnostics described in the next section are used to distinguish between a current concentration and a sheet.

Magnetic energy before the kink E_{M0} and after the kink E_{M1} are calculated to estimate the percent decrease $\Delta E_M = 100(E_{M0} - E_{M1})/E_{M0}$ in E_M. This needs integration to be carried out on the distorted Lagrangian grid. The method adopted here is to divide each mesh quadrilateral into two triangles, interpolate the magnetic field linearly over each triangle, then integrate. A mesh quadrilateral can be divided

into triangles in two ways, depending on the choice of diagonal; results of the two possible triangular subdivisions are then averaged. For a function w with values w_i, $i = 1 \cdots 4$ at the four vertices of the quadrilateral, the integral $I(w)$ over the quadrilateral is approximated by the following formula:

$$I(w) = \frac{1}{6}\left[w_1(2A_1 + A_3) + w_2(2A_2 + A_4) + w_3(2A_3 + A_1) + w_4(2A_4 + A_2)\right] \quad (4.24)$$

where A_j is the area of the triangle with apex at the vertex j , as illustrated in figure 4.3.

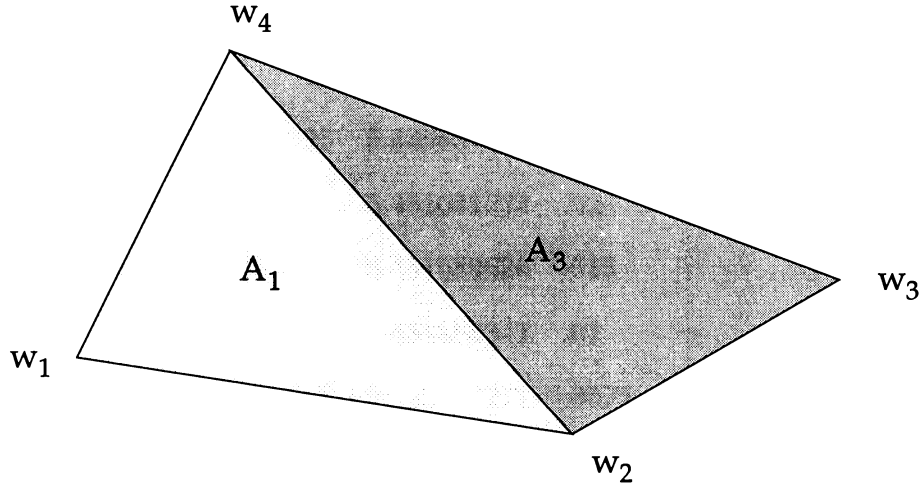

Figure 4.3: Diagram illustrating magnetic energy integration method.

With (x_i, y_i) denoting the coordinates of the ith vertex, area is calculated using

$$A_1 = \frac{1}{2}|(x_4 - x_1)(y_4 - y_2) - (y_4 - y_1)(x_4 - x_2)|,$$

and $w = \frac{1}{2}B^2$ here. The Magnetic energy is now given by

$$E_M = \sum_{\text{over grid}} I(w).$$

Table 4.1 illustrates the accuracy of this algorithm. Here the first column shows the number N of grid points; the second the calculated magnetic energy E_M of the Gold-Hoyle tube, and the third the percentage error. The error is about $O(\Delta a^2)$.

The last row lists the exact value of E_M given by

$$E_M = \frac{1}{2}\int_{-5}^{5}\int_{-5}^{5}\frac{1}{1+x^2+y^2}\,dxdy$$
$$= \int_{-5}^{5}\frac{\tan^{-1}\left(\frac{5}{\sqrt{1+y^2}}\right)}{\sqrt{1+y^2}}\,dy.$$

The last integral is evaluated using NAG routine D01DAF.

Table 4.1: E_M accuracy as function of N.

N	E_M	% Error
15	5.445070484	.13
25	5.449637699	.05
35	5.451031223	.025
45	5.451589626	.015
55	5.451868341	.01
65	5.452026211	.0072
75	5.452124592	.0054
85	5.452190649	.0042
101	5.452257295	.0029
exact	5.452417636	

For simulations of the kink in equilibrium fields the initial uniform mesh is displaced using the perturbation $\boldsymbol{\xi}$ plotted in figure 4.4. This is actually a small (0.1) multiple of the eigenvector corresponding to maximum eigenvalue $\lambda = 0.75$ of our B_3 field numerically calculated using the shifted power method described by Craig and Sneyd [78]. While this perturbation is most commonly used for kink calculations in the next chapters, the kink may also be excited by almost any perturbation. In test calculations we find that the final helical equilibrium is independent of this initial disturbance.

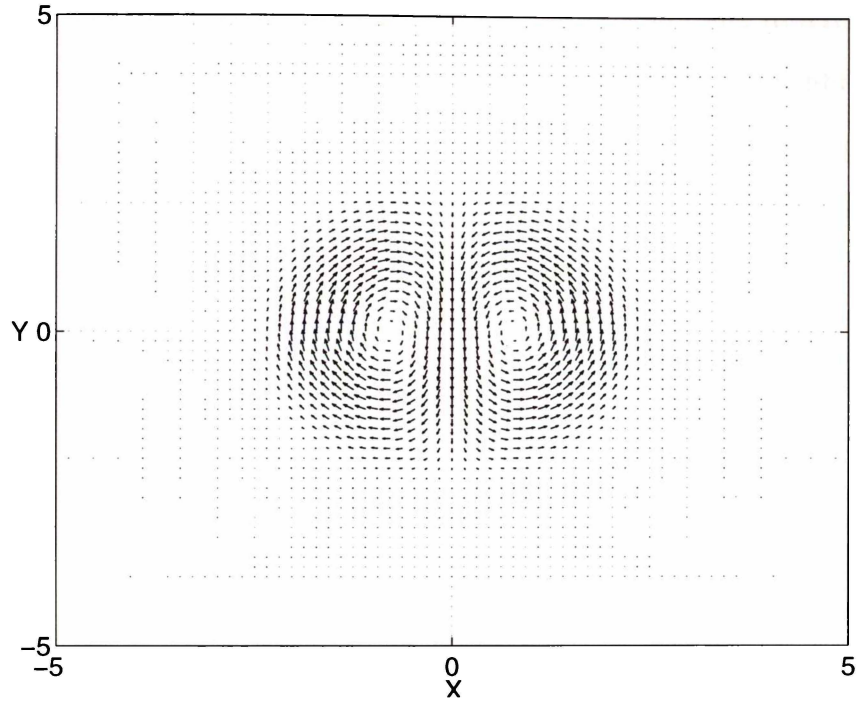

Figure 4.4: Perturbation $\boldsymbol{\xi}$ used for kink simulation. Max $|\boldsymbol{\xi}| = 0.0018$.

Computations are continued till either the disturbance dies out restoring the initial equilibrium, or the perturbation starts growing and a kink evolves. The onset of a kink is accompanied by growth of $F_{\max}$, decrease of $\Delta_{\min}$ and asymmetry in current density contours and surfaces.

4.3 Current sheet diagnostics

The distinction between a region of high current density and a current sheet has not always made clear in the literature. Current sheet formation with kink development has been reported in many papers (see next chapter for details) but rigorous distinction between current concentrations which represent steep local field gradients and current sheets which are true field discontinuities (in ideal MHD) requires a series of calculations on systematically refined grids.

In a numerical scheme it may be difficult to detect a discontinuity. In the case of the discontinuous function $y(x)$ sketched in figure 4.5, a central finite difference formula on an Eulerian mesh would estimate y' at P as $(y_2 - y_1)/(2\delta)$. To confirm the presence of a discontinuity one must perform a series of calculations, decreasing the grid spacing δ. The maximum value of y' will then be found to be proportional to δ^{-1}.

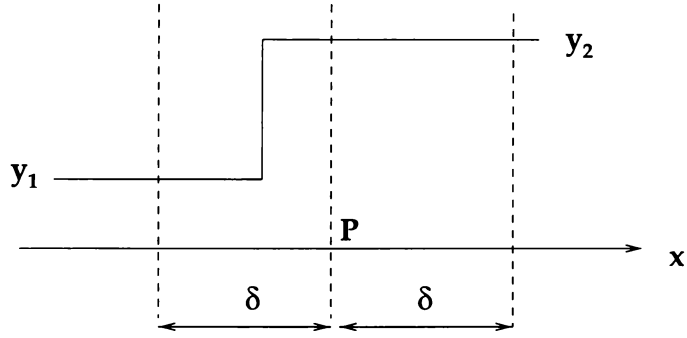

Figure 4.5: Effect of a discontinuity on a finite-difference scheme

In a Lagrangian MHD code however mesh compression may occur in the vicinity of a magnetic neutral point, which will alter this simple scaling. Consider the magnetic field $B(x)\hat{\mathbf{y}}$ contained between $x = \pm L$. We assume that B is an odd function of x. This field shown schematically in figure 4.6(a) is not in equilibrium, and will relax to the field shown in figure 4.6(b) which has uniform intensity B_E in the interval $[0, L]$ and $-B_E$ in $[-L, 0]$. There is a discontinuity in $\mathbf{B}$ and hence a current sheet at the origin. During the relaxation process, the Lagrangian mesh is advected with the fluid and compressed in the vicinity of the origin. We use a simple flux conservation argument to calculate the compression.

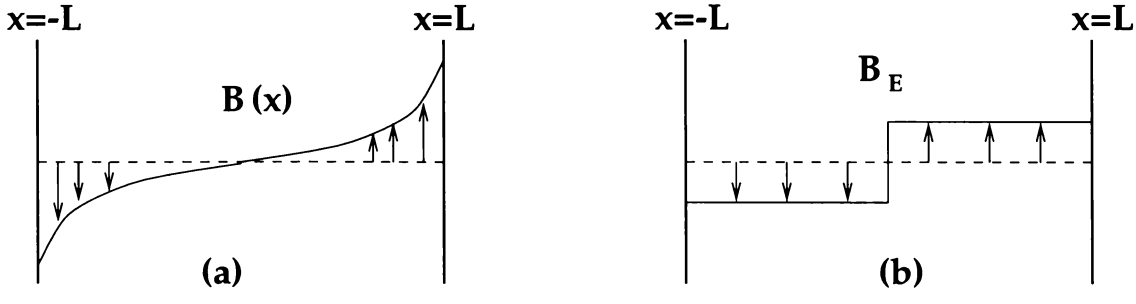

Figure 4.6: Formation of a current sheet at a neutral point

During the relaxation process flux must be conserved in the interval $[0, L]$, so

$$B_E L = \int_0^L B(x)\mathrm{d}x.$$

Also, flux must be conserved over the grid interval $[0, \delta]$, so

$$B_E \delta' = \int_0^\delta B(x)\mathrm{d}x,$$

where δ is the initial uniform grid spacing and $[0, \delta']$ the corresponding compressed interval. It follows that

$$\delta' = \frac{L \int_0^\delta B(x)\mathrm{d}x}{\int_0^L B(x)\mathrm{d}x}.$$

For example if $B(x)$ has a power-law dependence, say $B(x) \propto x^m$ (m odd) it follows from the above equation that $\delta' \propto N^{-(m+1)}$ where N is the number of grid points spanning the interval [0, L], so that

$$J_{\max} \propto N^{m+1}.$$

In particular if $B(x)$ is linear ($m = 1$) one would find $J_{\max} \propto N^2$. However, for current sheets which form in regions of positive $|\mathbf{B}|$ i.e. where $B(x) \neq 0$, such mesh compression does not take place and one expects

$$J_{\max} \propto N.$$

4.4 Preliminary tests

To ascertain the capabilities and limitations of our code we perform a few simple test calculations. In view of equations (4.13)-(4.20) the Jacobian Δ plays a major role in the approximation of all the important terms. To check the algorithm, coding and use of Δ we check numerical values of several terms containing Δ. Also it is important that our code be able to detect and diagnose current sheets properly. We use simple test problems to check this capability.

4.4.1 Accuracy

We see in equations (4.13 - 4.21) that the Jacobian Δ and its gradient occur frequently in the equations for updating the field $\mathbf{B}$ and the force operator $\mathbf{F}$. To test the accuracy of our approximation of Δ and its derivatives we calculate the pressure gradient after application of the mesh displacement

$$x_1 = a_1 + \alpha_1 a_2^3 \text{ and } x_2 = a_2 + \alpha_2 a_1^3.$$

Taking uniform density, $\rho(a) = 1.0$, and $g_p = 0.005$, analytic expressions for pressure gradient can be obtained using

$$\frac{\partial x_1}{\partial a_1} = 1, \quad \frac{\partial x_1}{\partial a_2} = 3\alpha_1 a_2^2, \quad \frac{\partial x_2}{\partial a_1} = 3\alpha_2 a_1^2, \quad \frac{\partial x_2}{\partial a_2} = 1,$$

$$\Delta = 1 - 9\alpha_1\alpha_2 a_1^2 a_2^2, \quad \frac{\partial \Delta}{\partial a_1} = -18\alpha_1\alpha_2 a_1 a_2^2 \quad \text{and} \quad \frac{\partial \Delta}{\partial a_2} = -18\alpha_1\alpha_2 a_1^2 a_2.$$

Now substitution from (4.18) in (4.16) gives

$$-\frac{\partial P}{\partial x_i} = \frac{g_p \gamma}{\Delta}\left(\frac{\rho(\mathbf{a})}{\Delta}\right)^{\gamma} M_{ij}\frac{\partial \Delta}{\partial a_j}$$

so that

$$-\frac{\partial P}{\partial x_1} = \frac{18 g_p \gamma \alpha_1\alpha_2 a_1 a_2}{\Delta^2}\left(\frac{\rho(\mathbf{a})}{\Delta}\right)^{\gamma}\left(3\alpha_2 a_1^3 - a_2\right)$$

and

$$-\frac{\partial P}{\partial x_2} = \frac{18 g_p \gamma \alpha_1\alpha_2 a_1 a_2}{\Delta^2}\left(\frac{\rho(\mathbf{a})}{\Delta}\right)^{\gamma}\left(3\alpha_1 a_2^3 - a_1\right).$$

Choosing $\alpha_1 = 0.25$ and $\alpha_2 = 0.4$ deforms the original rectangular grid in such a way that the Jacobian remains positive but the lower left and the top right corners are highly compressed resulting in a high pressure gradient. Table 4.2 shows values calculated at several mesh points using the above expressions together with their numerical approximation when $\Delta a = 0.1$ and $\gamma = 5/3$. The overall accuracy is $O(\Delta a)^2$, as expected.

Table 4.2: Numerical approximation of $\frac{\partial P}{\partial x_i}$ at several nodes.

a_1	a_2	$\frac{\partial P}{\partial x_1}$	Approx.	Error	$\frac{\partial P}{\partial x_2}$	Approx.	Error
0.2	0.3	0.027	0.026	0.0009	0.018	0.016	0.0014
0.3	0.5	0.115	0.113	0.0015	0.052	0.05	0.0023
0.5	0.5	0.164	0.162	0.0022	0.191	0.188	0.003
0.6	0.6	0.293	0.289	0.0033	0.378	0.373	0.0056
0.7	0.7	0.523	0.518	0.0056	0.808	0.795	0.0133
0.8	0.7	0.242	0.243	-0.0005	1.567	1.538	0.0289
0.8	0.8	0.972	0.962	0.0099	2.206	2.156	0.0497

4.4.2 Current sheet detection

A simple test for the formation of a current sheet is the planar 2-D case, when $\mathbf{B} = (0,\ x,\ 0)$ relaxes to equilibrium. In a square region $[-1\,,\ 1] \times [-1\,,\ 1]$ with no restriction on boundary-node movement and no plasma pressure, under ideal MHD, this field experiences a one-dimensional motion and relaxes to a step function

$$B_y = \begin{cases} \frac{1}{2}, & x \geq 0 \\ -\frac{1}{2}, & x \leq 0. \end{cases}$$

Hence $|\mathbf{J}|$ is infinite at $x = 0$ but the finite grid limitation means that the numerically calculated value of $J_{\max}$ is bounded. We therefore expect $\mathbf{J}$ to be maximum at the origin and decay towards the boundaries $y = \pm a$ because of our fixed boundary conditions. According to our analysis in the preceding section, we expect $J_{\max} \propto N^2$ approximately.

To simulate development of the current sheet at $x = 0$ we take $\Delta a = 0.05$, $\zeta = 1$; $\boldsymbol{\xi}$, τ and β all equal to zero. The initial uniform current of magnitude $|\mathbf{J}| = |\frac{\partial B_y}{\partial x}| = 1$, evolves to a thin sheet at $x = 0$, as is clear from the surface plots of $|\mathbf{J}|$ in figure 4.7. Figure 4.7(a) shows the current at $t = 0.25$ and (b) at $t = 25$. The force $F_{\max}$ is reduced to 0.35 and 10^{-12} respectively (from its initial value 1). The growth and

sharpness of the sheet are spectacular. The rounding of sheet is the effect of rigid boundaries with no node movement.

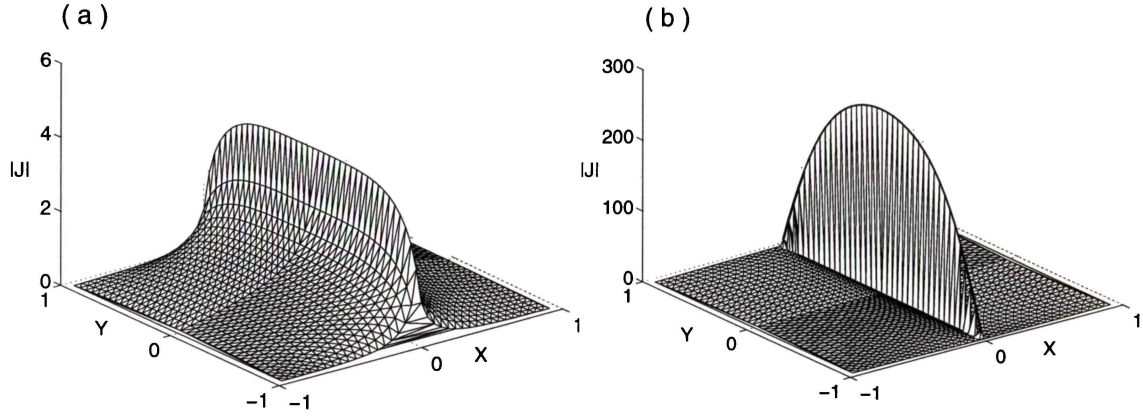

Figure 4.7: $|\mathbf{J}|$ at $t = 0.25$ and 25.

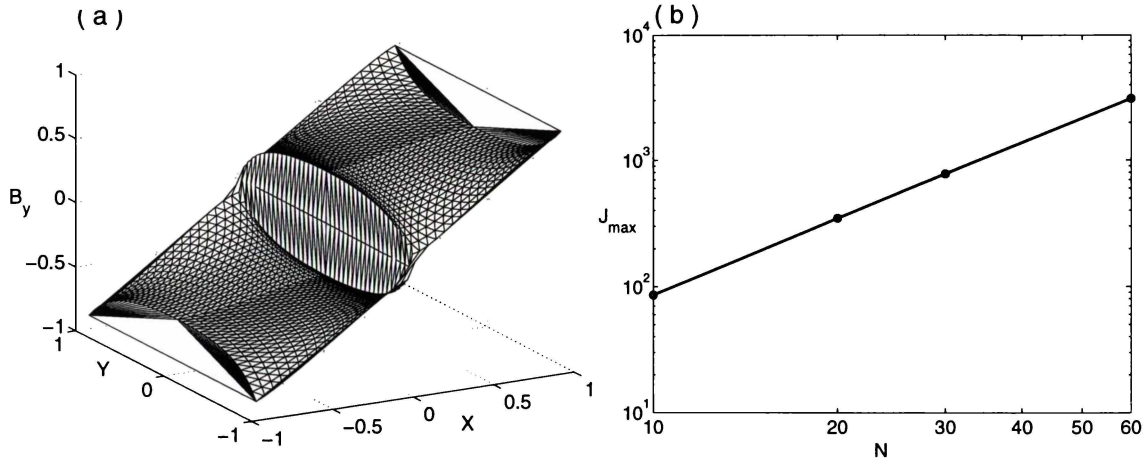

Figure 4.8: B_y corresponding to 4.7(b) and $J_{\max}$ growth with N using a log – log scale.

The corresponding B_y is plotted in figure 4.8(a) showing the development of the steep step at $x = 0$. Figure 4.8(b) shows the growth of $J_{\max}$ with N, the number of cells in $[0, 1]$. Logarithmic scales are used to show that $\log(J_{\max})$ versus $\log(N)$ is approximately a straight line having slope 2.0024, implying almost quadratic growth of $J_{\max}$ with mesh refinement. In view of our arguments in the preceding section, this is a true signature of a current sheet.

A more realistic form of this problem will include plasma pressure. However, when flux surfaces having oppositely oriented **B** are pressed against each other due to magnetic attraction or magnetic pressure, the plasma between the surfaces is compressed and pressure increases. This will tend to oppose the meeting of the flux surfaces unless the plasma can be squeezed out from between them. Hence current sheet formation may be difficult in the presence of plasma pressure.

Confirmation of current sheet formation requires continuous $J_{\max}$ growth with successive mesh refinements. In equilibrium with plasma pressure we expect length scales of $O(L\beta)$ in a domain of length L. Thus to differentiate between a current concentration and a current sheet we need initial mesh spacing $\Delta a < L\beta$. We carried out successive calculations with a large plasma pressure, $\beta = 0.2$. The results are plotted in figure 4.9. Figure 4.9(a) shows a surface plot of the current after

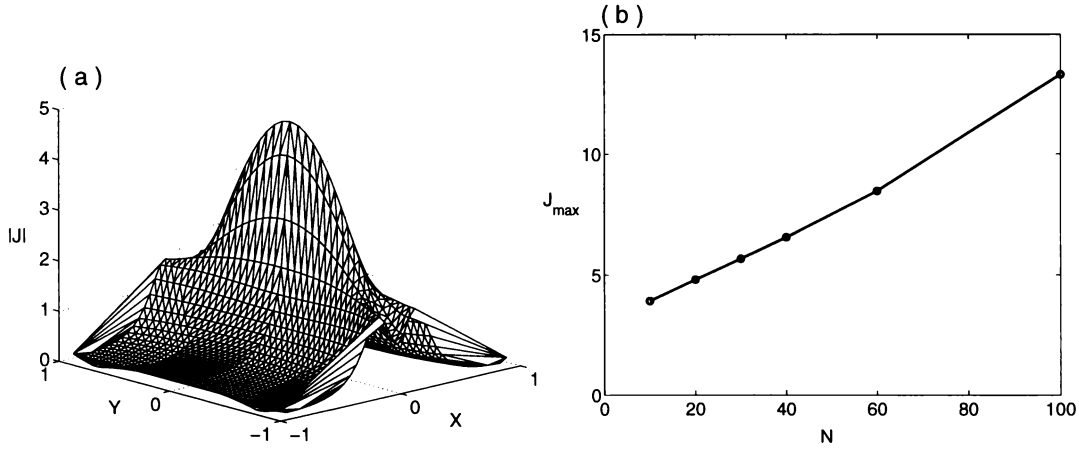

Figure 4.9: $|\mathbf{J}|$ and $J_{\max}$ growth with N when $\beta = 0.2$.

relaxation and (b) the growth of $J_{\max}$ with mesh refinement. Continuous $J_{\max}$ growth with successive mesh refinement confirms the current layer to be a sheet.

These findings are interesting because for the corresponding one-dimensional problem, it can be shown analytically that no current sheet can form (Sneyd private communication, 2001). Independent calculations by Craig and Watson (private communication, 2001) using a three-dimensional code agree with our findings. We

will see in chapter 8 that plasma pressure does prevent current sheet formation in certain cases.

In the absence of plasma pressure a problem may arise whenever a neutral line of $\mathbf{B}$, on which a current sheet forms, coincides with a grid line away from the origin. Due to unequal magnetic pressures on either side of the neutral line and fixed nodes at the boundaries, one would expect a curved sheet. But since $\mathbf{B} = 0$ at the neutral line the force $\mathbf{F}_b = \mathbf{J} \times \mathbf{B}$ is approximated as zero in the code, allowing no movement. In reality $\mathbf{B}$ is zero but $\mathbf{J}$ is infinite and one would expect a finite $\mathbf{F}_b$.

For this problem we also tested an Eulerian code and found that second-order differencing spreads the discontinuity while one-sided upwind differencing destroys the symmetry of the resulting sheet. Simple remedies for this problem using our Lagrangian code are to choose a different mesh size, so that the neutral line no longer coincides with a grid line, or to include plasma pressure. Curved sheets will be encountered in chapter 8 when we deal with unequal tube interactions. For sheets having circular shapes (as those resulting from kink) the problem of a neutral line falling on a grid line does not arise.

These preliminary tests show our code second order accurate in approximating even cubic terms in Δ, such as pressure gradient. Current sheets resulting from kinks and tube interactions can be detected and diagnosed rigorously. Applications in this thesis will include finding helical equilibria resulting from the kink instability, and the twisting together of parallel flux tubes.

Chapter 5

Kinked equilibria

Single flaring loops have been observed in the Skylab images and Priest [24] estimates an excess energy of 7×10^{23} J for a loop of field strength 500 G, radius 5 Mm, length 100 Mm, and total twist 2π, sufficient for a small flare. Emergence of already twisted flux tubes has been observed by Kejun and Shuhua [39], and Ishii *et al.* [37] (see also section 1.2) so that a small steady increase in the twist by footpoint motions might prove sufficient to trigger the kink instability.

While stability limits or eigenvalue calculations have received great attention in the past and results can be validated easily against earlier work, the nonlinear evolution varies slightly from model to model depending on the physics included, simplifications made, and the numerical procedures adopted. Formation of current sheets with continuous footpoint motion has been reported and contended by different studies in the recent past.

Parker [63] suggests that equilibrium is possible only for small scale uniform twisting and that any complicated topology contains current sheets, no smooth equilibrium being possible. Park *et al.* [62] studied numerically the nonlinear evolution of the $m = 1$ kink mode in a cylindrical tokamak using incompressible ideal MHD equations. They find the kink to develop nonlinearly into a neighboring helically

symmetric equilibrium containing a current sheet. The local maximum in their current plots is very small and they do not rigorously prove it to be a current sheet. Van Ballegooijen [82] and Antiochos [3] argue that sheets will not form in a smoothly deformed field with no initial neutral point.

With the accessibility of better computational power, 3-D numerical calculations of the nonlinear kink evolution started to appear in the literature with varying degrees of resolution and physical limitations. Craig and Sneyd [22] presented 3-D frictional plasma results of the kink evolution in a Gold-Hoyle tube and found high current concentration but due to limited resolution they could not rigorously prove formation of a current sheet. Lionello *et al.* [46] repeated the Gold-Hoyle kink evolution with a 3-D ideal MHD code and found no current sheets. Similarly Baty and Heyvaerts [10] report no "fine-scale current structure" in the kink evolution of the Gold-Hoyle field with a 3-D ideal MHD code. They also study ideal MHD evolution of a non force-free field towards a kinked equilibrium in which a non-singular (having non-zero thickness) current concentration is generated. Similarly current concentrations are reported in [9] and in the resistive MHD case by Lionello *et al.* [48, 47] but no rigorous argument is given to show that these are true current sheets or reconnection sites. Amari and Luciani [1] still consider the existence of a current sheet as a true singularity of the ideal MHD equations controversial.

Based on a reduced form of the MHD equations, Ng and Bhattacharjee [59] try to prove that there is at most one smooth equilibrium for each smooth footpoint mapping. They further deduce that "if there exists a smooth but unstable equilibrium for a given smooth footpoint mapping, there is no other smooth equilibrium that the unstable plasma can relax to. Thus non-equilibrium with current sheets must develop". They mention some numerical simulations to get an unstable current layer evolving towards a non-equilibrium state with current density growing much faster in the middle than near the end plates. They admit limitations of their spatial resolution, and an inability to distinguish between a current sheet and a current

concentration. Our calculations in this chapter (and those of Lionello *et al.* [46]) contradict their claim by producing second smooth equilibria after kinking of the tubes $\mathsf{B}_1(0)$ and B_2.

Only the recent 3-D computations by Arber *et al.* [5] rigorously show current sheet formation with development of a kink in a flux tube that closely resembles our tube B_3. They initially use an ideal MHD Lagrangian code, until the appearance of a current sheet, manifested by fast growth of maximum current density. Afterwards they continue the process with a current-dependent resistive Eulerian code arguing that nonlinear saturation of the instability in a purely ideal MHD description is not possible. With our nonlinear calculations we achieve a second equilibrium after development of the kink in almost all cases. $J_{\max}$ varies with mesh size when a current sheet develops due to a kink, as found by Arber *et al.* [5]. Calculations of Arber *et al.* [5] illustrate formation of a current sheet as a result of an ideal MHD kink instability but they do not see relaxation to a second helical equilibrium after development of the kink due to inclusion of resistivity and consequent reconnection.

In view of such a controversial state of the problem, we carry out our study of the kinked equilibrium in greater detail, testing several pitch cases and plotting time histories of $J_{\max}$, $F_{\max}$ and Δ_{min}. Sparse calculated values of E_M (and $J_{\max}$) are shown as thick dots on smooth fitted splines. Initially we have an equally spaced uniform square grid with $\Delta_{min} = 1$, and the fields being in equilibrium have $F_{\max} = 0$.

Our linear analysis, in chapter 3, shows that taking tube radius $r_a = 5$ and varying the twist τ in the range $(0\,,\,1)$ will be sufficient to get an almost complete picture of the kinking process. Hence we restrict our computational domain to $[-5\,,\,5]\times[-5\,,\,5]$ covered by a 65×65 grid which gives sufficient accuracy in view of table 4.1. Multiple resolution tests will be performed when current concentrations are encountered. We study the kink development for values of τ outside the mentioned range to verify that a kink develops only when instability is predicted by the linear theory. Here and in the next chapter we study the nonlinear development of the kink under the

constraint of helical symmetry for the four fields introduced in chapter 2, using the frictional MHD code described in chapter 4.

5.1 Helical kink and the Gold-Hoyle field

As mentioned earlier this field has been used by different groups in both the linear stability studies and nonlinear time evolution simulations due to its simplicity and because results can be easily validated against published work. As we did in the linear study, we start with this simple solar coronal field model to ensure the reliable performance of our nonlinear code. Current density surface plots and contours, before any perturbation has been applied, are given in figure 5.1. Initially $J_{\max} = 2$ and $E_M = 5.45$ for this field. Development of any asymmetry in the current plots will indicate the onset of a kink in the following calculations. This is normally accompanied by rise in the force and decrease in the value of the Jacobian.

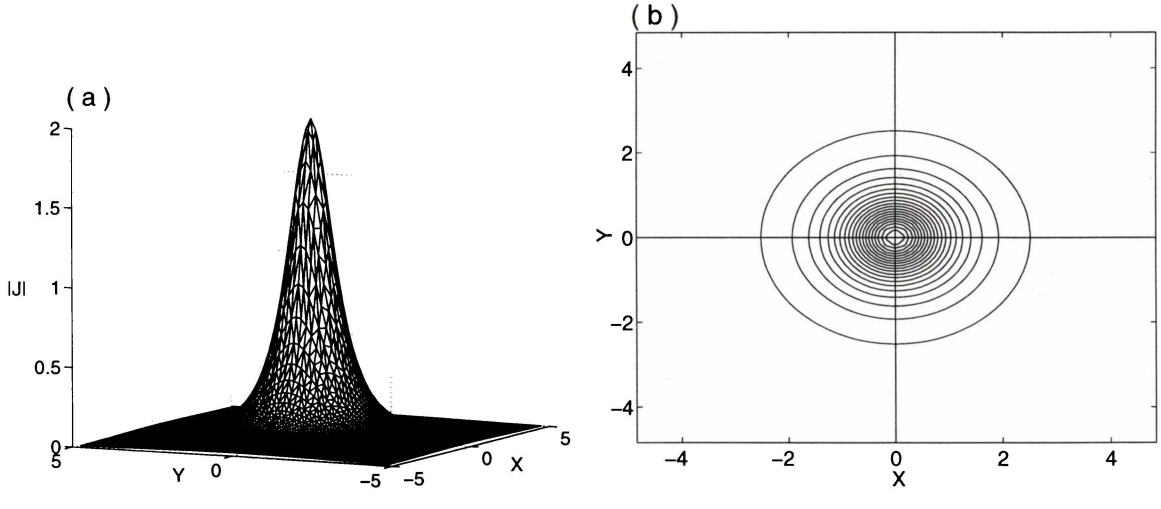

Figure 5.1: Initial |**J**| profile of Gold-Hoyle field.

For $\tau = 1.01$ and 1.5 the linear analysis, figure 3.4(a), shows this field stable to any perturbation. Figure 5.2 shows results when calculations are carried out with these pitch values after a small perturbation (shown in figure 4.4). Plasma pressure

(i.e. β) is zero. Plots in figure 5.2(a) correspond to $\tau = 1.01$ and in 5.2(b) to 1.5. Graphs are scaled for clarity. The perturbation has died out quickly and the initial equilibrium is restored in both the cases confirming the linear results.

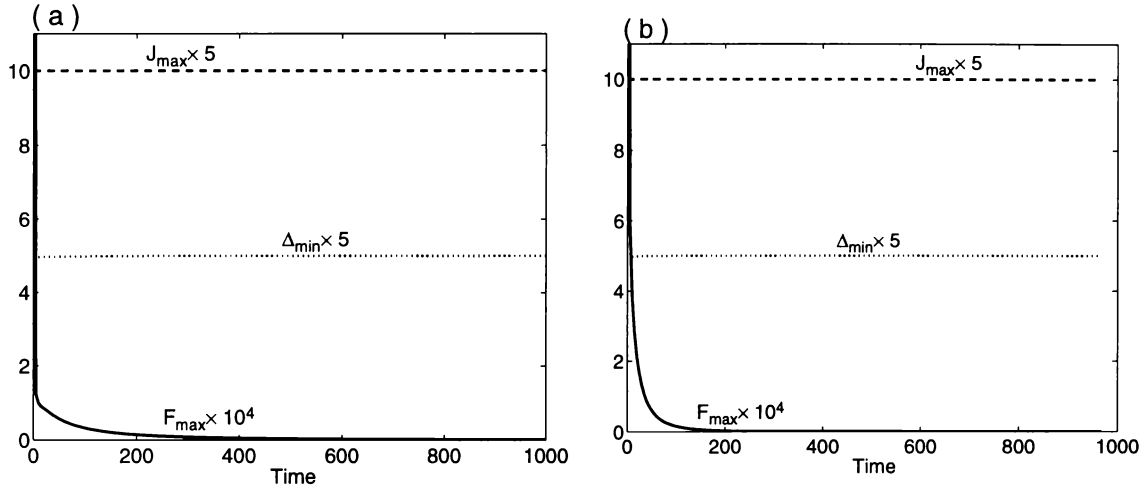

Figure 5.2: Gold-Hoyle field's relaxation when $\tau = 1.01$ and 1.5.

Calculations with pitch values having small linear growths (see chapter 3) are presented next. When $\beta = 0.0$ the growth rate is $\lambda \approx 0.0009$ for $\tau = 0.25$ and for $\tau = 0.95$ we have $\lambda \approx 0.00705$. For these pitch values our nonlinear computations produce a weak kink in both the cases as depicted in figure 5.3. The $\tau = 0.25$ kink (left column) is weaker and relaxes to a second helical equilibrium smoothly while that of $\tau = 0.95$ generates chaotic spikes confined to a narrow region. These spikes cannot be attributed to current sheet formation because they are easily smoothed out by a small plasma pressure. We do not experience such behavior with any of the other fields we study here and so suspect them either to be a feature of the Gold-Hoyle field or numerical noise due to some small scale phenomena not resolved by the code.

The spiky behavior of $J_{\max}$ can also be seen in the results of Lionello *et al.* [48], for a slightly different field configuration. They interpret this behavior as manifestation of current sheets. Their absence in the 3-D results of Lionello *et al.* [46] (our figure 5.6) could be due to nonzero β. Our calculations with different values of pitch show

that for strong kinks of the Gold Hoyle field, a small gas pressure is necessary to ensure convergence.

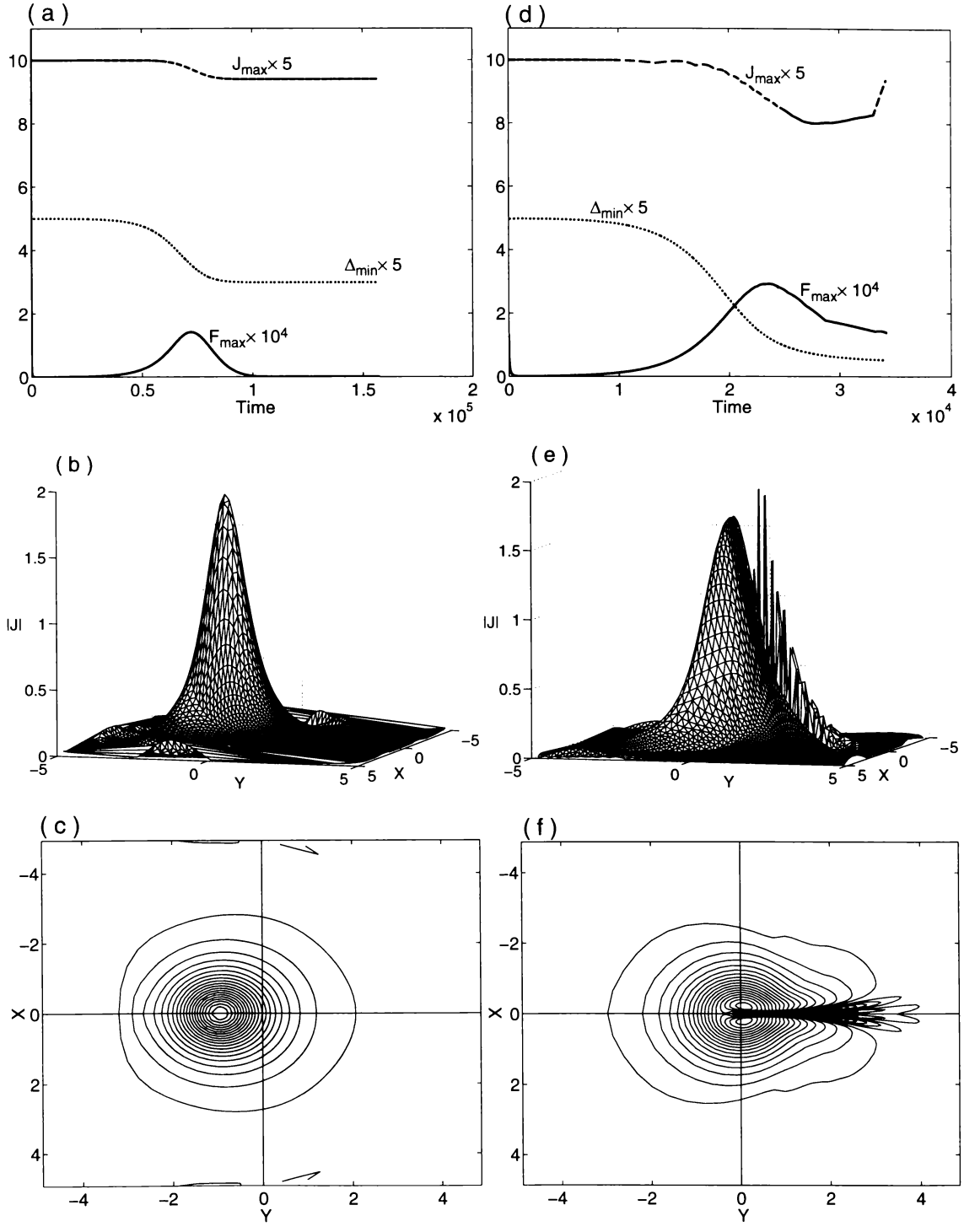

Figure 5.3: Kink of the Gold-Hoyle field with $\beta = 0.0$ when $\tau = 0.25$ (left) and 0.95 (right).

In figure 5.3(a), the initial decay in the perturbation force, stops at about $t = 4500$ with $F_{\max} = 2.09 \times 10^{-5}$. At this time the start of $F_{\max}$ growth indicates the onset of the kink which continues to rise until $t = 72000$ when $F_{\max}$ attains its maximum, 0.00014, and starts descending towards another equilibrium. The $|\mathbf{J}|$ plots in (b) and (c) are at time $t = 140000$ when $F_{\max} = 1.5 \times 10^{-8}$. At this time the magnetic energy is decreased very little, by $\Delta E_M = .059\%$, and $J_{\max} = 1.88$.

Surface and contour plots of the axial field B_z after the $\tau = 0.25$ kink (when $\beta = 0.0$) are given together with the final shape of the distorted grid in figure 5.4. The effect

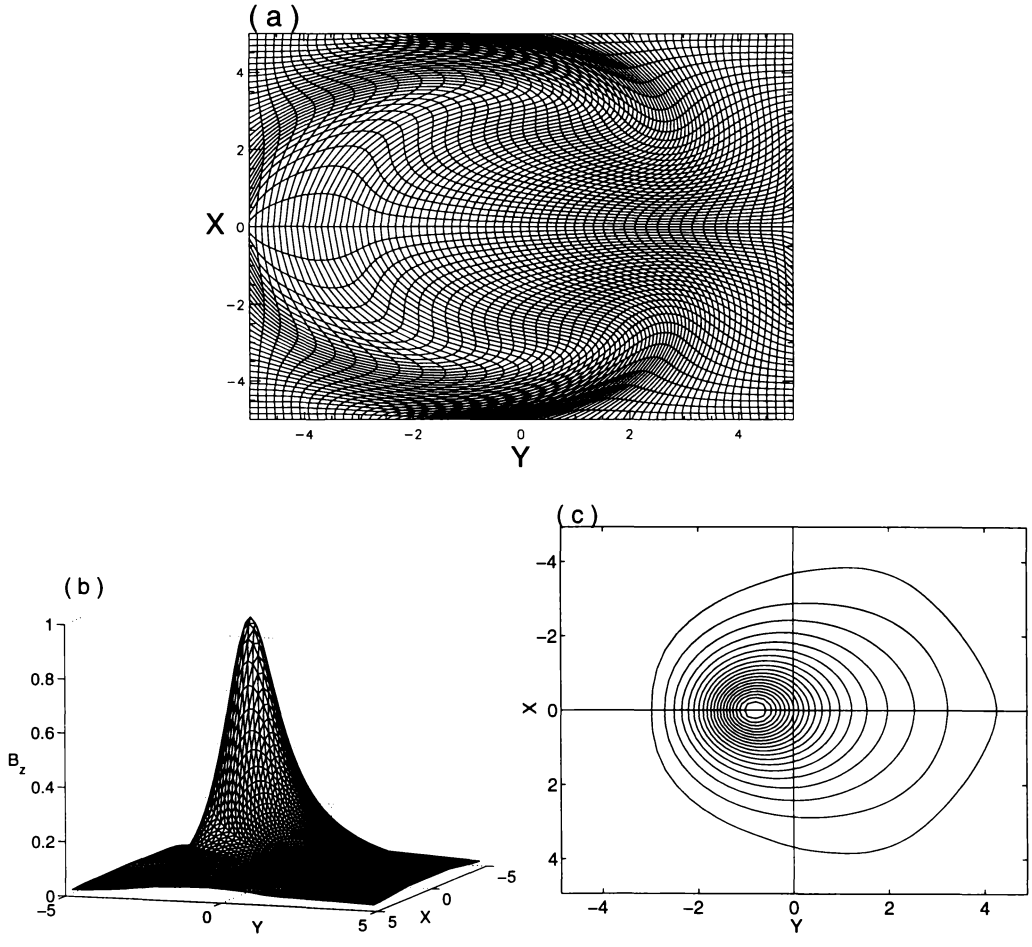

Figure 5.4: Grid and B_z of the Gold-Hoyle field after the $\tau = 0.25$ kink when $\beta = 0.0$.

of mesh refinement and tube radius on the $\tau = 0.25$ kink (with no plasma pressure) is illustrated in figure 5.5. Plots in the left hand column correspond to a 101×101 grid with tube radius $r_a = 5$ while those in the right to a 101×101 grid with tube

radius $r_a = 10$. Hence the mesh is finer in the left and coarser in the right hand plots, as compared to the 65×65 mesh of figure 5.4. The fine mesh process is extremely slow and has no significant difference with figure 5.3 (the same calculations on a 65×65 grid) while the kink of the tube with the large radius is stronger having

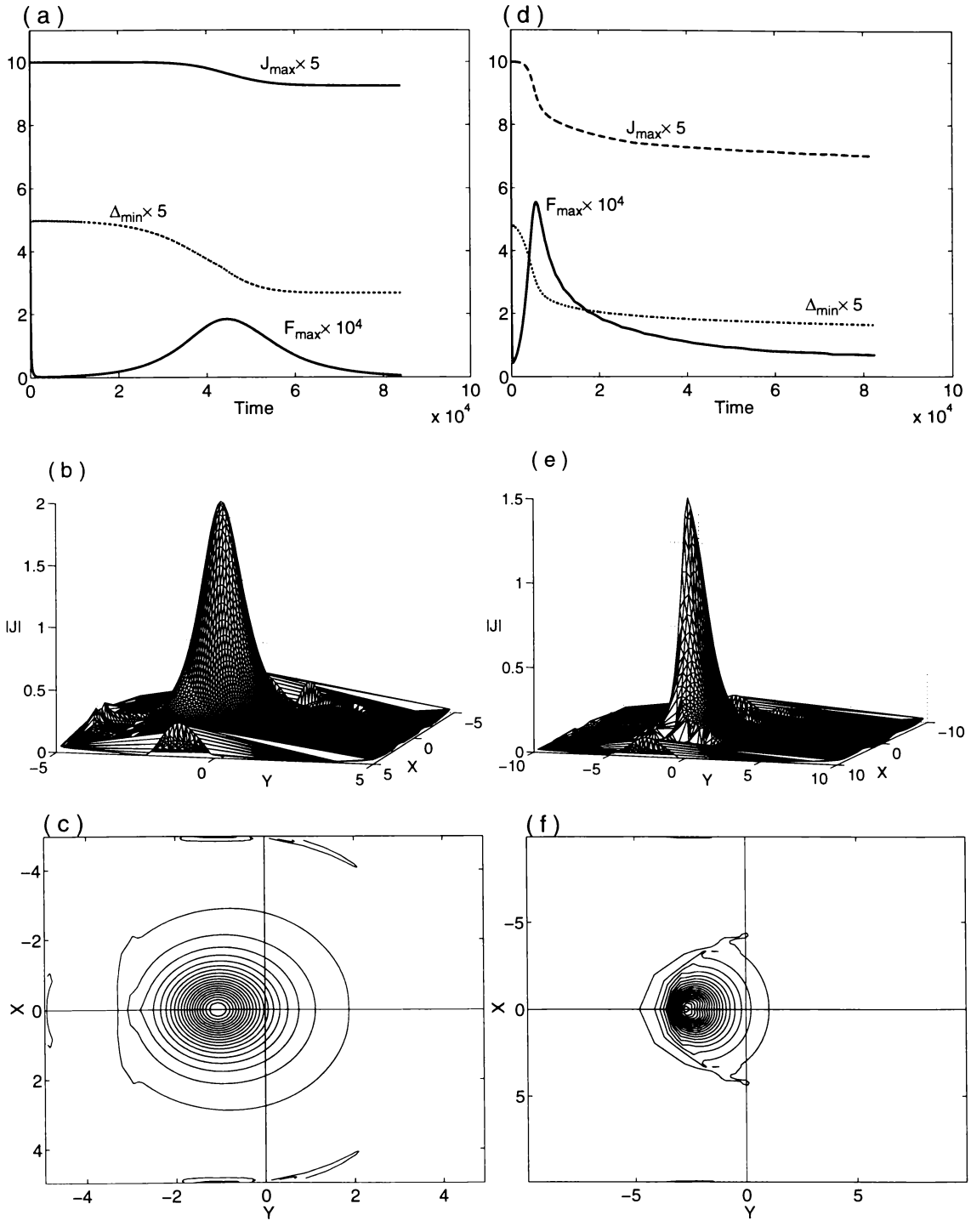

Figure 5.5: Kink of the Gold-Hoyle field with $\beta = 0.0$ when $\tau = 0.25$. Refined mesh and double radius cases.

larger growth rate in conformity with the linear analysis but relaxation to the second equilibrium is very slow. Presence of the small ripples in all the current plots show that the phenomena is inherent to the field and not an artifact of mesh resolution or boundaries.

Figure 5.6 shows |**J**| contours of the kinked equilibrium of Gold-Hoyle field as computed by Lionello *et al.* [46] with their 3-D code. As noted earlier they notice no current sheet formation as a result of this kink. They take a tube of length $L = kl$

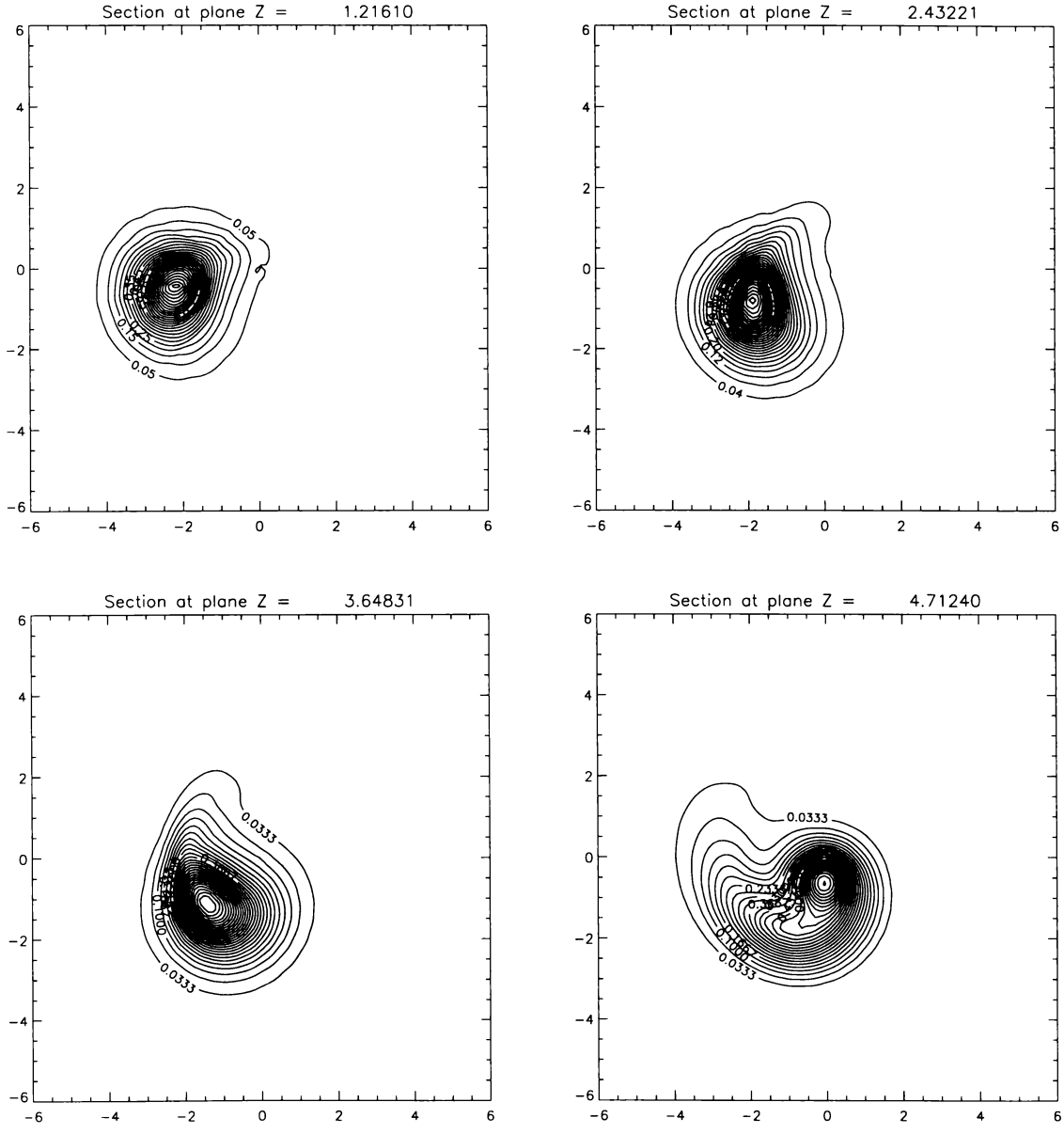

Figure 5.6: |**J**| contours of the kinked Gold-Hoyle field by Lionello *et al.* [46]. Courtesy R. Lionello.

and radius $20l$ with $k = 3\pi$. The tube being line-tied is unstable to the $m = 1$ kink when k is greater than a threshold value (say) k_0. The value of k_0 has been determined by different groups to lie in $[2.46\pi, 2.51\pi]$. A uniform plasma pressure is taken so that the value of the plasma β increases from 0.01 at the axis to 1.0 at $r \approx 10l$. The smooth behavior of their field can be attributed to inclusion of this plasma pressure. The contours given are in four different axial planes.

Figure 5.7 shows the kink with a maximum linear growth rate $\lambda = 0.017698$ having pitch $\tau = 0.75$ when $\beta = 0.01$. The kink develops quickly and is very strong compared to the previous cases. Relaxation to a second helical equilibrium is also very rapid. The $|\mathbf{J}|$ plots in (b) and (c) are at $t = 33700$. $J_{\max} = 0.99$ and magnetic energy is decreased by $\Delta E_M = 2.48\%$.

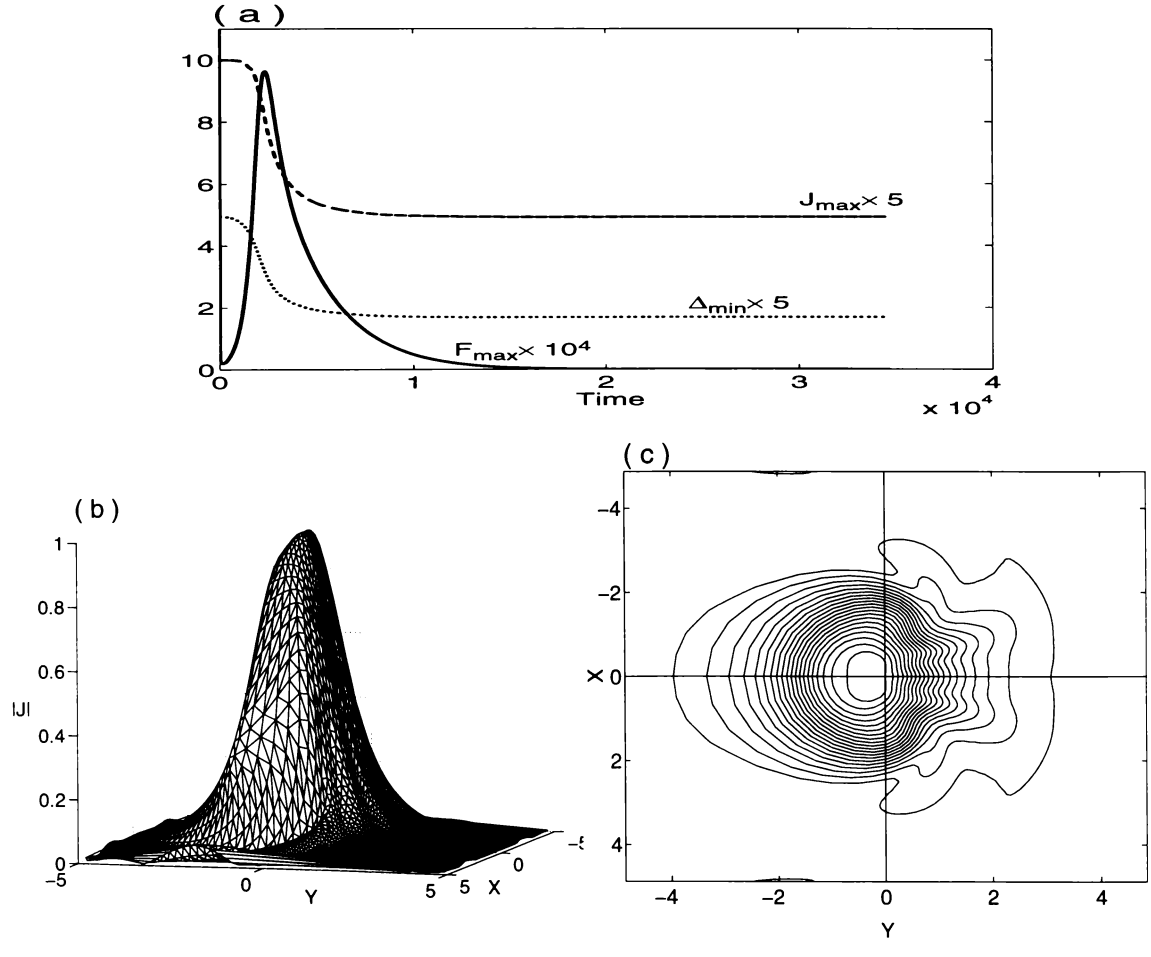

Figure 5.7: Kink of the Gold-Hoyle field with $\tau = 0.75$ when $\beta = 0.01$.

A final equilibrium attained with a given pitch τ is stable to perturbations which maintain helical symmetry with that same pitch value. In general, however, it will not be stable to a helically symmetric disturbance of *different* pitch value τ_1 say. Figure 5.8 plots magnetic energy versus relaxation pitch τ for the Gold-Hoyle flux tube with $N = 32$, as solid line. It can be seen that the maximum energy decrease occurs for a pitch value of approximately $0.63 = \tau_0$ say; quite different from the pitch value ($\tau = 0.75$) of maximum growth rate predicted by our linear analysis. The dashed and dotted curves represent calculations carried out at higher resolutions — $N = 50$ and $N = 64$ — to illustrate convergence. Although the magnetic energy decrease converges rather slowly, the twist value τ_0 which yields maximum energy decrease is not changing perceptibly.

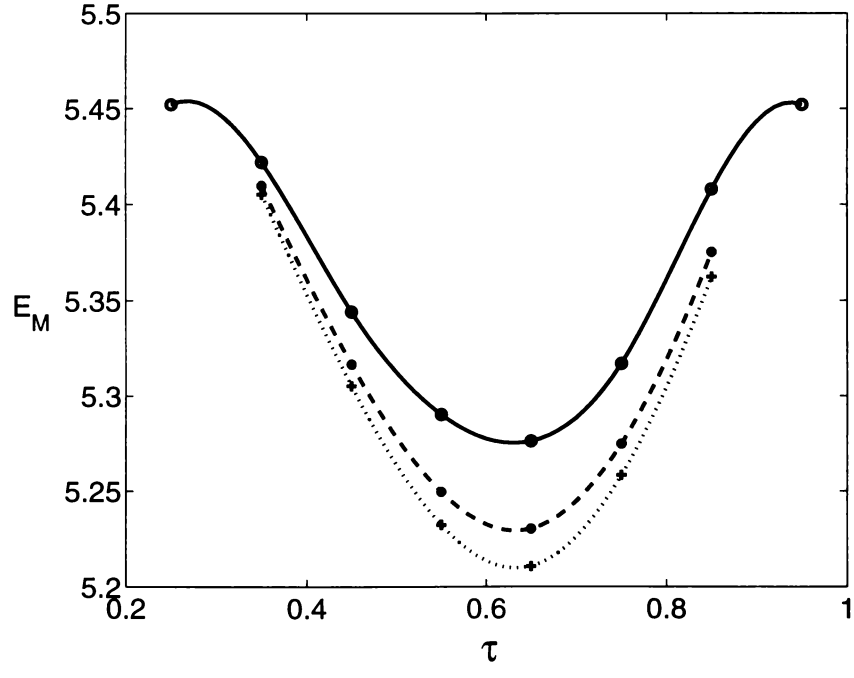

Figure 5.8: E_M versus τ in the second kinked equilibrium of the Gold-Hoyle tube. The solid, dashed and dotted lines correspond to $N = 32$, 50 and 64 respectively.

Thus if the Gold-Hoyle field were allowed to relax under helical symmetry, *but with no constraint as to the pitch of that helical symmetry* (i.e. in a pure $m = 1$ mode) a final pitch of τ_0 would be selected in order to maximize energy loss.

The resulting equilibrium would be stable to all helically-symmetric disturbances. Three-dimensional numerical experiments (Lionello *et al.*, [46]) indicate that the kink evolves predominantly in the $m = 1$ mode so the τ_0 equilibrium represents an approximation to the eventual form of an infinite Gold-Hoyle tube which kinks under no symmetry constraints whatsoever.

5.2 Helical kink of the B_2 field

This field is different from the others due to non-uniformity of its pitch in the interior and its pitch reversal. At the line where k changes sign we have $B_\theta = 0$. One may suspect that with the development of kink the field will deform in such a way that $B_z = 0$ on some point of this line giving the hope that this possible neutral point could be the site of a current sheet. The initial current density is plotted in figure 5.9. Initially $J_{\max} = 1.44$ and $E_M = 9.56$ for this field.

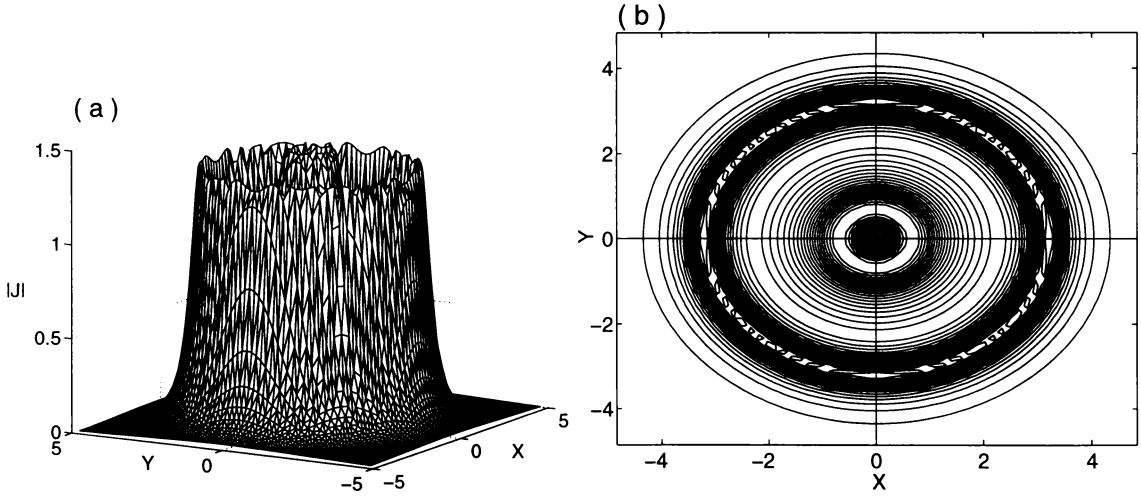

Figure 5.9: Initial current density of B_2 field.

The slight jaggedness in the layers of the surface plot is an artifact of the plotting routines else the field is smooth in these regions. These current layers are simple current concentrations as the field is continuous here. For this field also, all perturbations die out when the pitch of the kink τ is selected to lie outside the range (0 , 1).

In figure 5.10 are the results for kinks having small growth rates and a small pitch, $\tau = 0.35$, in the left column but a greater pitch, $\tau = 0.65$, in the right, when $\beta = 0.0$. Both the kinks grow very slowly and are relatively weak but the displacement of the

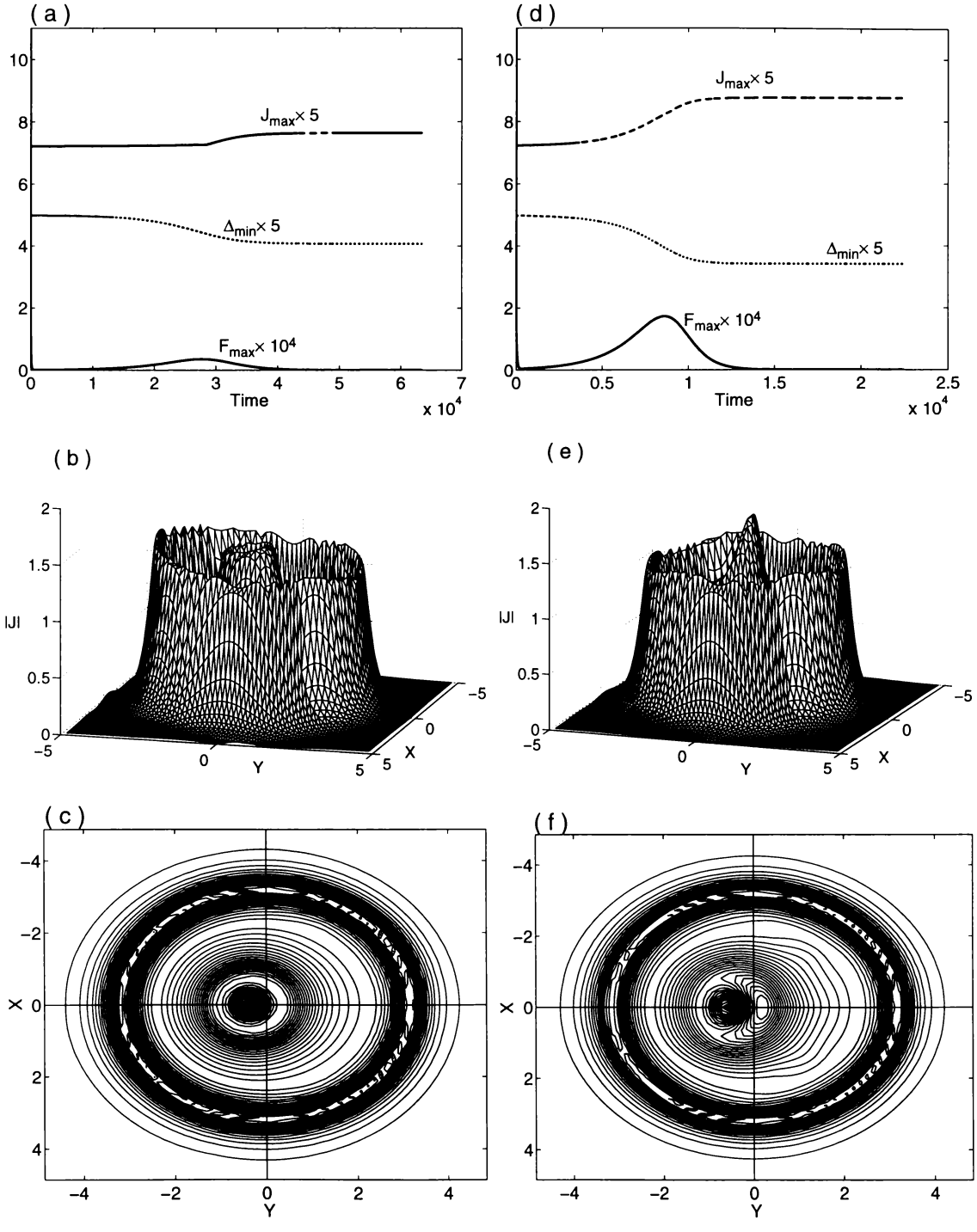

Figure 5.10: Kink of the B_2 field with $\tau = 0.35$ and 0.65 when $\beta = 0.0$.

axis is quite clear from the contour plots of $|\mathbf{J}|$. Current plots for the $\tau = 0.35$ pitch are at $t = 63400$ having E_M reduced by $\Delta E_M = 0.01\%$ and those of $\tau = 0.65$ at $t = 22000$ have E_M reduced by $\Delta E_M = 0.03\%$.

For $\tau = 0.55$ the growth rates with $\beta = 0.0$ and 0.01 respectively are $\lambda \approx 0.008729$ and 0.00756. For these values the kink formation is shown in figure 5.11 with the

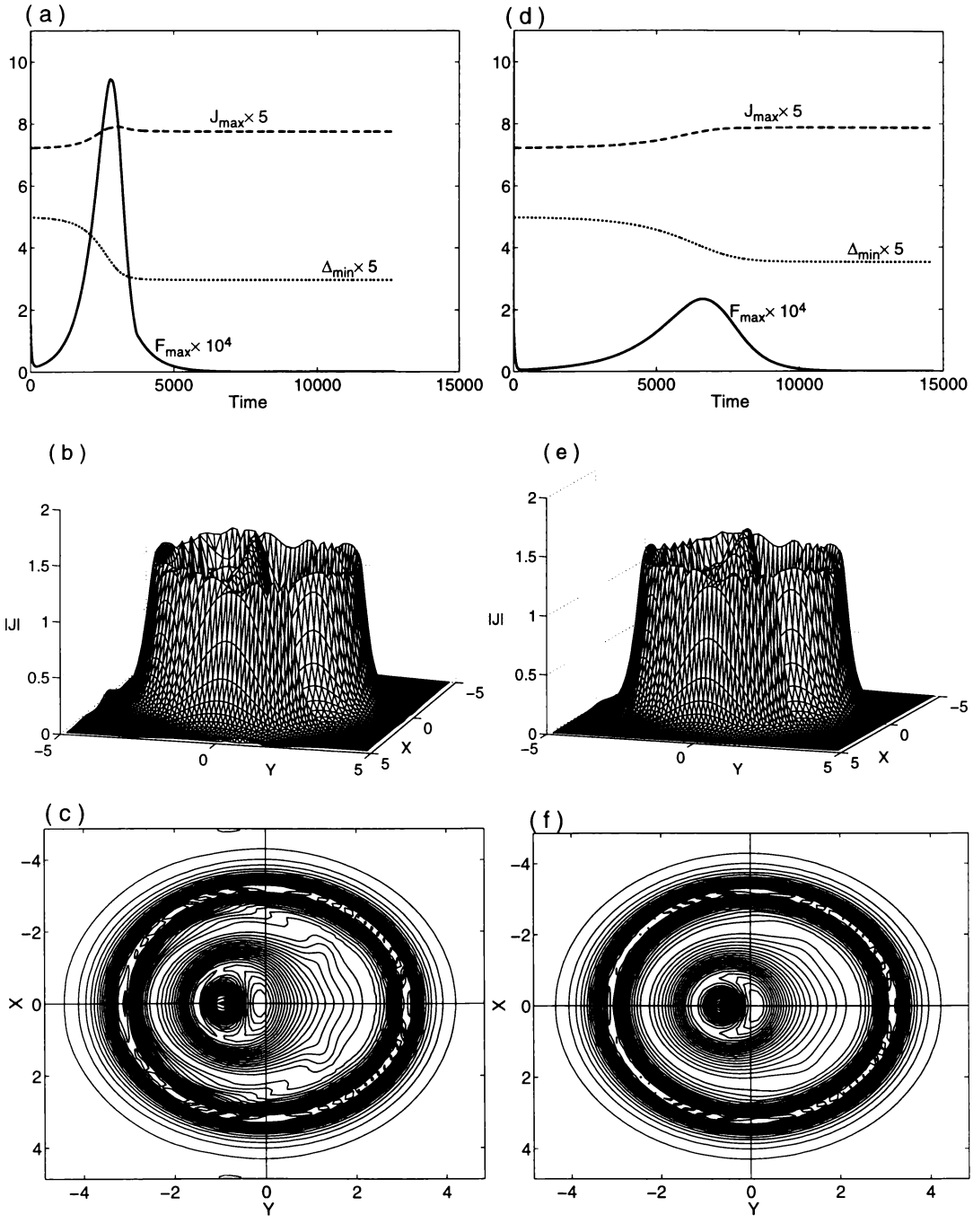

Figure 5.11: Kink of the B_2 field with $\tau = 0.55$ when $\beta = 0.0$ and 0.01.

left column representing the no pressure case and in the right $\beta = 0.01$. It is clear that plasma pressure has delayed and weakened the kink. In both cases $J_{\max}$ gets slightly increased (see (a), (d)). Current plots in (b) and (c) are at $t = 13400$ and those in (e) and (f) are at $t = 14600$. Magnetic energy is now reduced by $\Delta E_M = 0.16\%$ when $\beta = 0.0$ and $\Delta E_M = 0.073\%$ when $\beta = 0.01$.

The small increase in $J_{\max}$ does not seem to represent development of a current sheet as calculations with refined grids show no significant difference in the current structure. For this field, surface and contour plots of the axial field B_z after the $\tau = 0.55$ kink (when $\beta = 0.0$) are given together with the final shape of the distorted grid in figure 5.12.

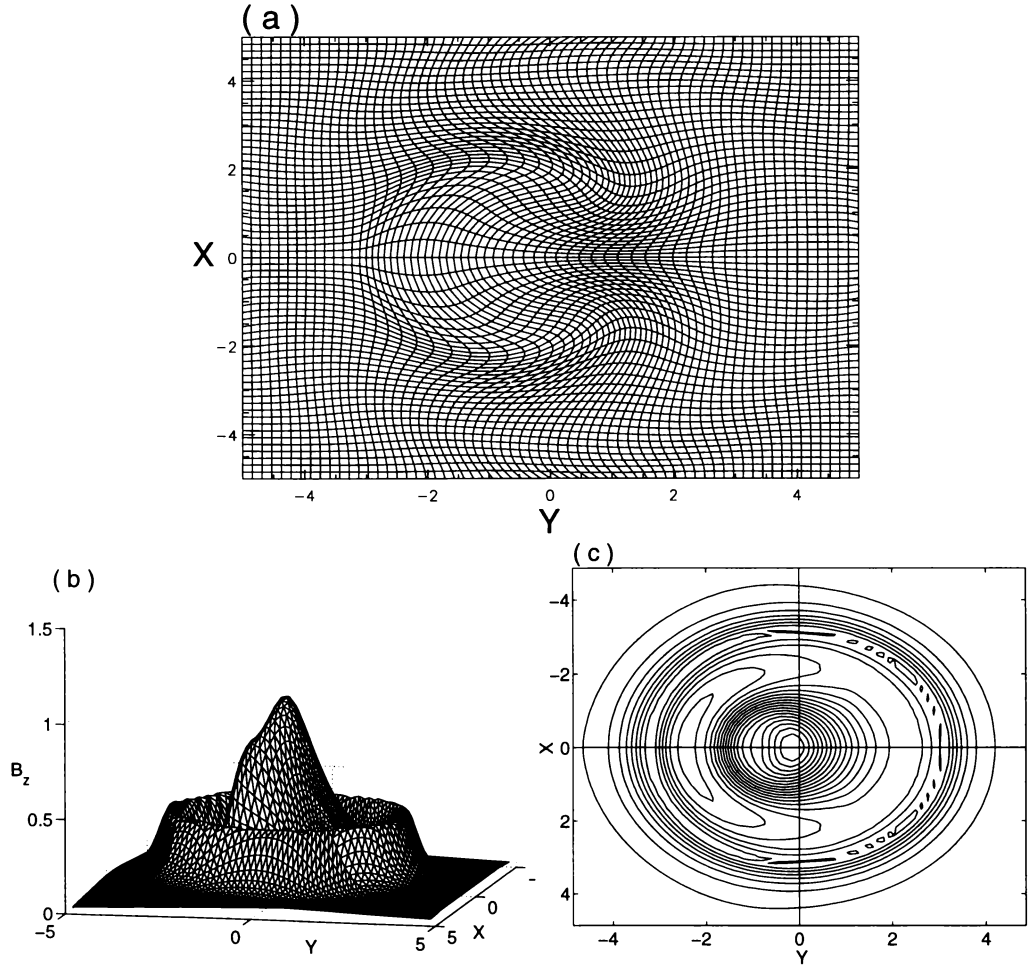

Figure 5.12: Grid and B_z of $\mathbf{B}_2$ field after the $\tau = 0.55$ kink when $\beta = 0.0$.

Figure 5.13 shows magnetic energy loss for different values of τ after kinking of this field on the standard grid. It can be noticed that the maximum energy decrease occurs for a pitch value of approximately $0.52 = \tau_0$ say, different from the pitch value of maximum growth rate predicted by our linear analysis, namely $\tau = 0.575$. Thus if this field were allowed to relax under helical symmetry in a pure $m = 1$ mode a final pitch τ_0 would be selected in order to maximise the energy loss. This equilibrium is stable to all helically-symmetric disturbances.

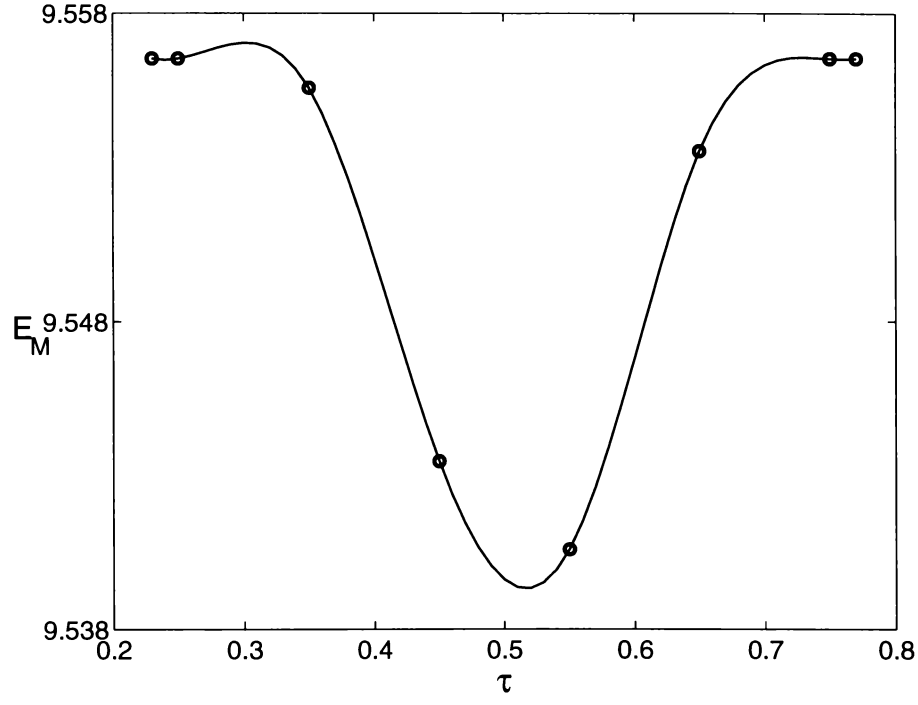

Figure 5.13: E_M versus τ for the second kinked equilibrium of the B_2 field.

These nonlinear calculations show that the B_2 field also, is unstable to the $m = 1$ helical kink in the range of τ predicted by our linear analysis and the second equilibrium is smooth. Though the surface plotting routine cannot capture the sharpness of the outer wall in the $|\mathbf{J}|$ plots, $J_{\max}$ does not increase significantly with mesh refinement or development of the kink and we get a smooth equilibrium in each case. This is in contradiction to the Ng and Bhattacharjee's claim [59] that there is no second smooth equilibrium once a smooth equilibrium is disturbed by an instability.

For both of the tubes $\mathbf{B}_1(0)$ and $\mathbf{B}_2$ once a neighboring helical equilibrium with a certain pitch τ_1 is reached, restarting the calculations from there with another pitch τ_2 relaxes to a helical equilibrium which would have been attained in case of initial calculations with τ_2. That is, the helical kink with every pitch is unique and the second equilibrium is stable to the ideal modes of the same pitch.

Chapter 6

Kinks of the B_3 and B_4 fields

Our study in the preceding chapter shows that helical kinks of Gold-Hoyle and the B_2 fields do not give rise to current sheets. This chapter is a continuation of the nonlinear calculations of the preceding chapter and here we systematically establish current sheet formation with the development of a helical kink in the field B_3. We also show that plasma pressure does not suppress formation of this current sheet. The B_4 field contains a jump discontinuity in the current and is the most stable field to kinking amongst the four fields we have studied. We modify this field to get a compressed field with high current concentration. The resulting field is more prone to the $m = 1$ kink and a kinked neighboring equilibrium can be obtained but no current sheets are formed as a result of the kink.

A current sheet being a mathematical singularity has zero thickness and cannot be adequately resolved on a finite grid, but continuous growth of a local maximum current with successive mesh refinement is a true signature of a current sheet (refer chapter 3). We present results of our nonlinear calculations using the same standard square grid 65×65 ($N = 32$) and the same tube radius $r_a = 5$. Different grid resolutions are used to detect current sheets only when we suspect their presence.

6.1 Kinking of the B_3 field

Due to its resemblance to the Gold-Hoyle field in the interior, the kink growth rates for the B_3 field are similar but generally smaller, see figure 3.4. Here also the initial current density has a maximum value $J_{max} = 2$ but the distribution shown in figure 6.1 differs that of the Gold-Hoyle field in the exterior. The field is continuous and the small current concentration does not represent a current sheet initially. The magnetic energy is 8.764944.

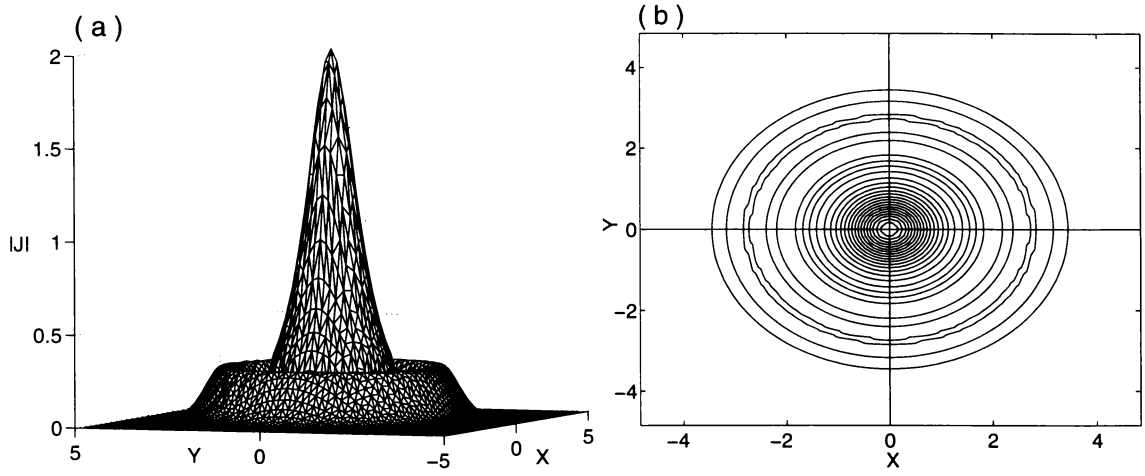

Figure 6.1: Initial $|\mathbf{J}|$ of B_3 field.

Arber *et al.* [5] have studied the initial development of the kink in a similar tube with a 3-D ideal MHD Lagrangian code. They find formation of a current sheet during the evolution of the kink, but do not show the final equilibrium. We give detailed history of the field as it kinks and relaxes to a second kinked equilibrium using our helically symmetric frictional plasma code discussed in chapter 4, to complement their findings. The effect of plasma pressure and mesh refinement on the growth of the kink and J_{max} are included for clarity.

Like the two cases of chapter 5, twisting of this field with a pitch outside the range (0 , 1) smoothes out all perturbations and the initial equilibrium is restored quickly. Plots in figure 6.2 show kinking of this field with $\tau = 0.75$. The left and right

columns correspond to $\beta = 0.0$ and 0.01 respectively. The $\tau = 0.75$ kink has the maximum growth rate $\lambda \approx 0.01697$ for this field when $\beta = 0.0$, (see figure 3.5). For $\beta = 0.01$ we have $\lambda \approx 0.01482$ when $\tau = 0.75$.

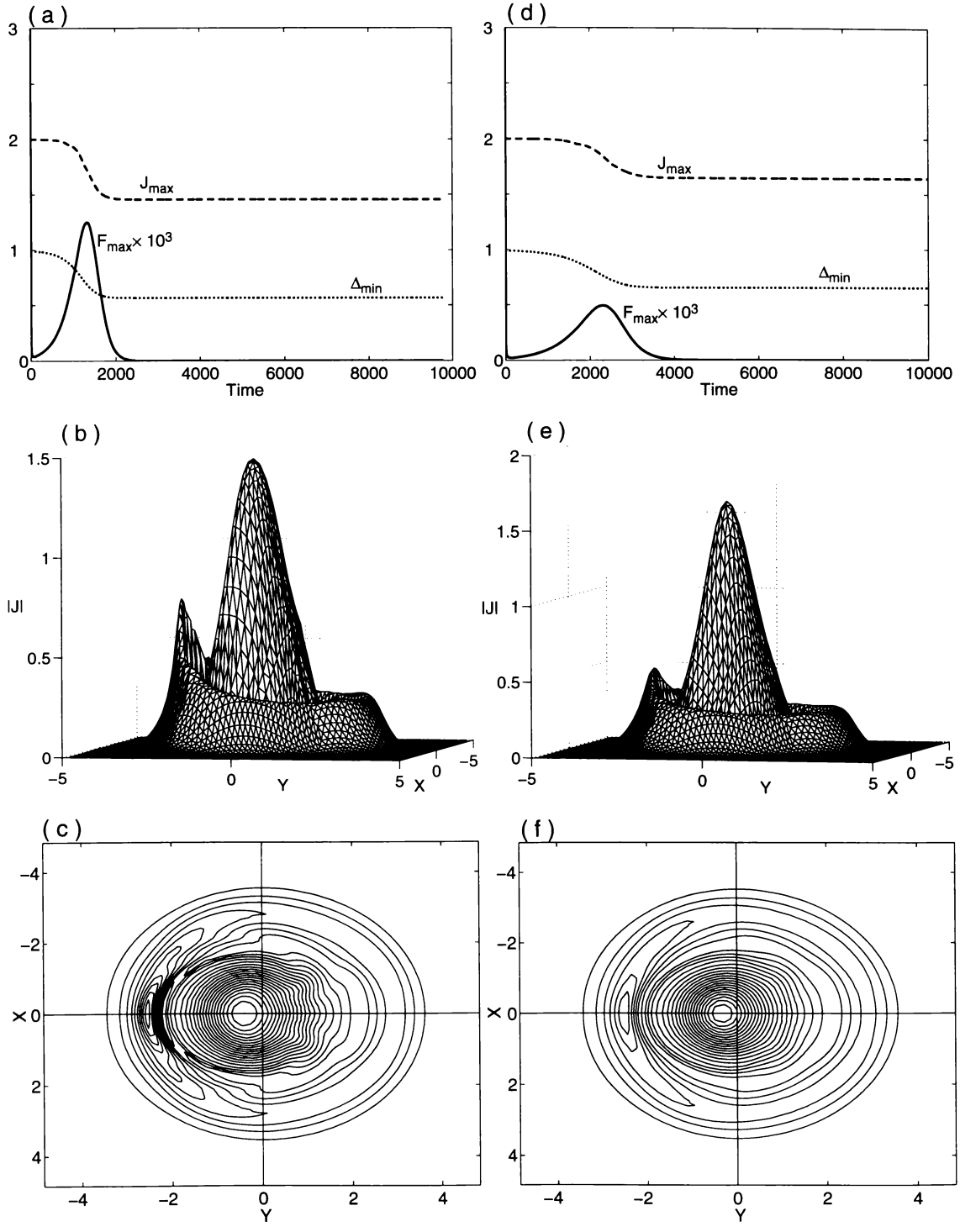

Figure 6.2: Kink of the B_3 field with $\tau = 0.75$ when $\beta = 0.0$ and 0.01.

As predicted by the linear theory, see chapter 3, plasma pressure has reduced the growth rate of the kink. Current plots are at time $t = 9800$ when the second equilibrium has been established. By this time magnetic energy is reduced by $\Delta E_M = 0.2\%$ in the zero β case and by $\Delta E_M = 0.12\%$ in the $\beta = 0.01$ case, showing that a stronger kink releases more energy. There are signs of a current concentration on the left in the $|\mathbf{J}|$ plots which, unlike the spikes of the Gold-Hoyle field, persists in the non-zero β results also, indicating the possibility of a current sheet.

To ascertain its nature we present in figure 6.3 results for three different resolutions when $\beta = 0.0$. Plots in the first and second rows correspond to $N = 25$ and 50 respectively. In the third row the resolution is increased to $N = 64$ – twice the normal. Comparison of $F_{\max}$ in (a) and (c) shows a ten-fold increase but from figure 6.2(a) to 6.3(e) there is only about a three-fold growth implying that the strength of the kink increases nonlinearly with mesh refinement. The development time of the kink varies similarly.

The surface plots of $|\mathbf{J}|$ in the first, second and third row represent the current profile after complete saturation of the kink at $t = 24000$, 4000 and 3700 respectively. There is clear indication that the layer on the left represents a current sheet.

Figure 6.4(a) shows the final distorted shape of the initially uniform 65×65 square grid and (b)-(c) the plots of axial field, B_z, in the second kinked equilibrium. Waddell *et al.* [87] in their linearized study report a skin current appearance with the development of an $m = 1$ instability in a cylindrical plasma column but it disappears soon, leaving the current in the interior fairly smooth. Here we see the persistent structure of a current layer throughout, once the kink develops. To clarify formation and nature of this layer we perform several further calculations with another τ.

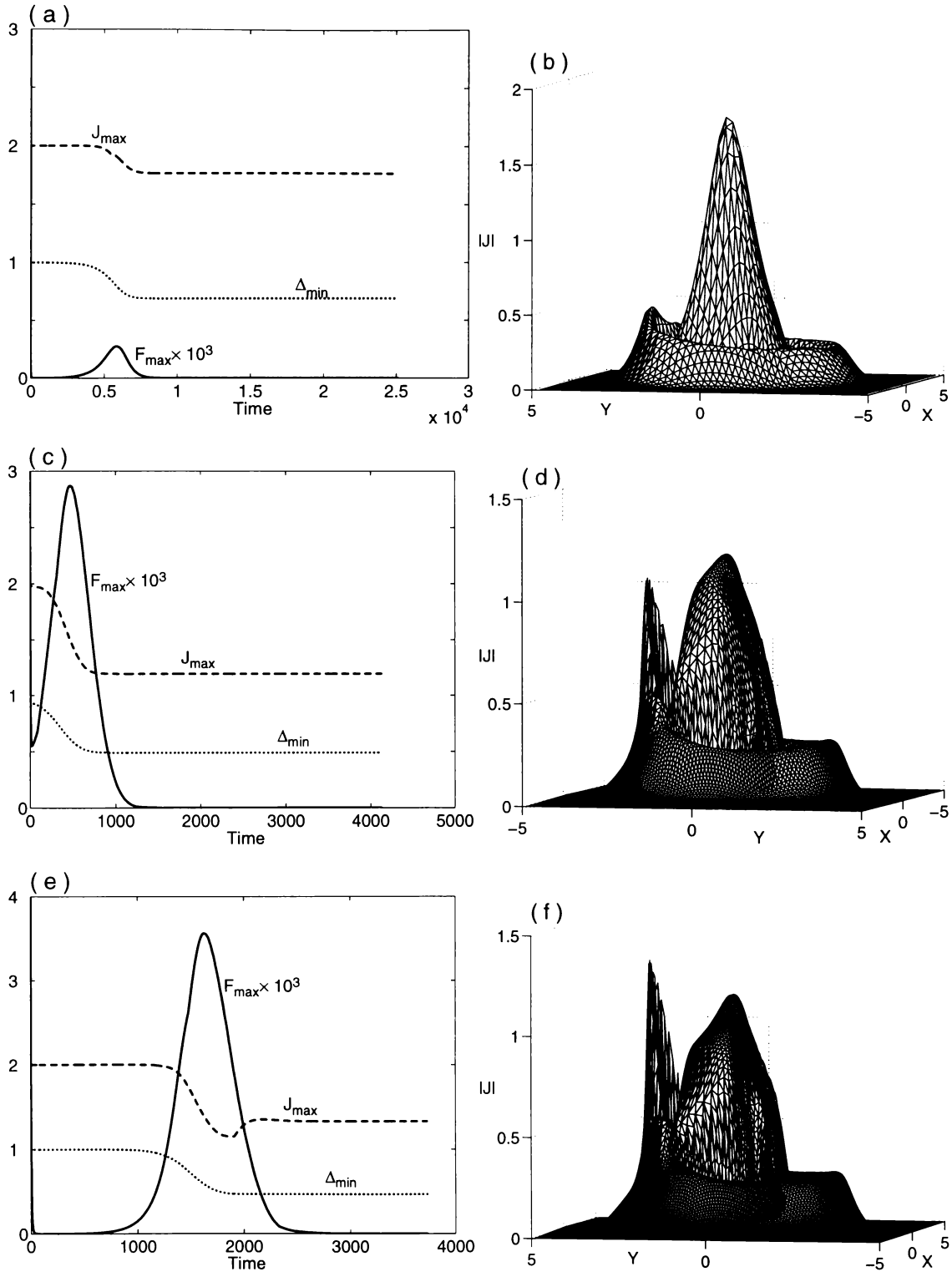

Figure 6.3: Kink of the B_3 field with $\tau = 0.75$ and $\beta = 0.0$ on different grids.

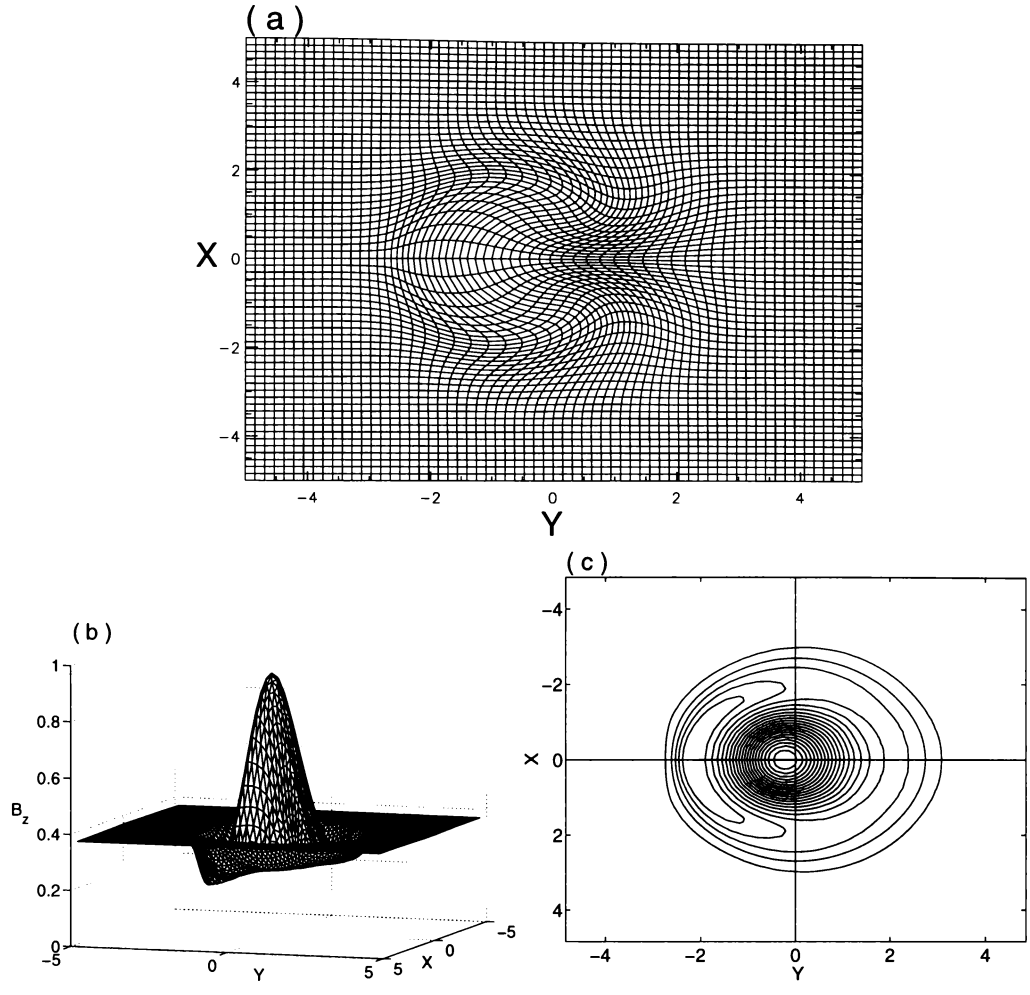

Figure 6.4: Grid and B_z of $\mathbf{B}_3$ field after the $\tau = 0.75$ kink when $\beta = 0.0$.

The kink with smaller pitch $\tau = 0.35$ on different grids is shown in figure 6.5 when $\beta = 0.0$. Results in the first row are for $N = 25$, in the second for $N = 32$, in the third for $N = 50$ and in the last row for $N = 64$. The corresponding current density is plotted at times 24000, 6100, 4000 and 8500 respectively. The current layer is more pronounced here. As before, mesh refinement increases the height of the layer. The $F_{\max}$ increase represents a stronger kink and larger ΔE_M. E_M is reduced by $\Delta E_M = 0.085\%$, 0.14%, 0.21% and 0.25% respectively.

To illustrate that the current layer is in fact a sheet the local $J_{\max}$ is plotted against N in figure 6.6 for both the $\tau = 0.75$ and 0.35 kinks. $J_{\max}$ grows approximately linearly with mesh refinement and $J_{\max} \longrightarrow \infty$ as $N \longrightarrow \infty$.

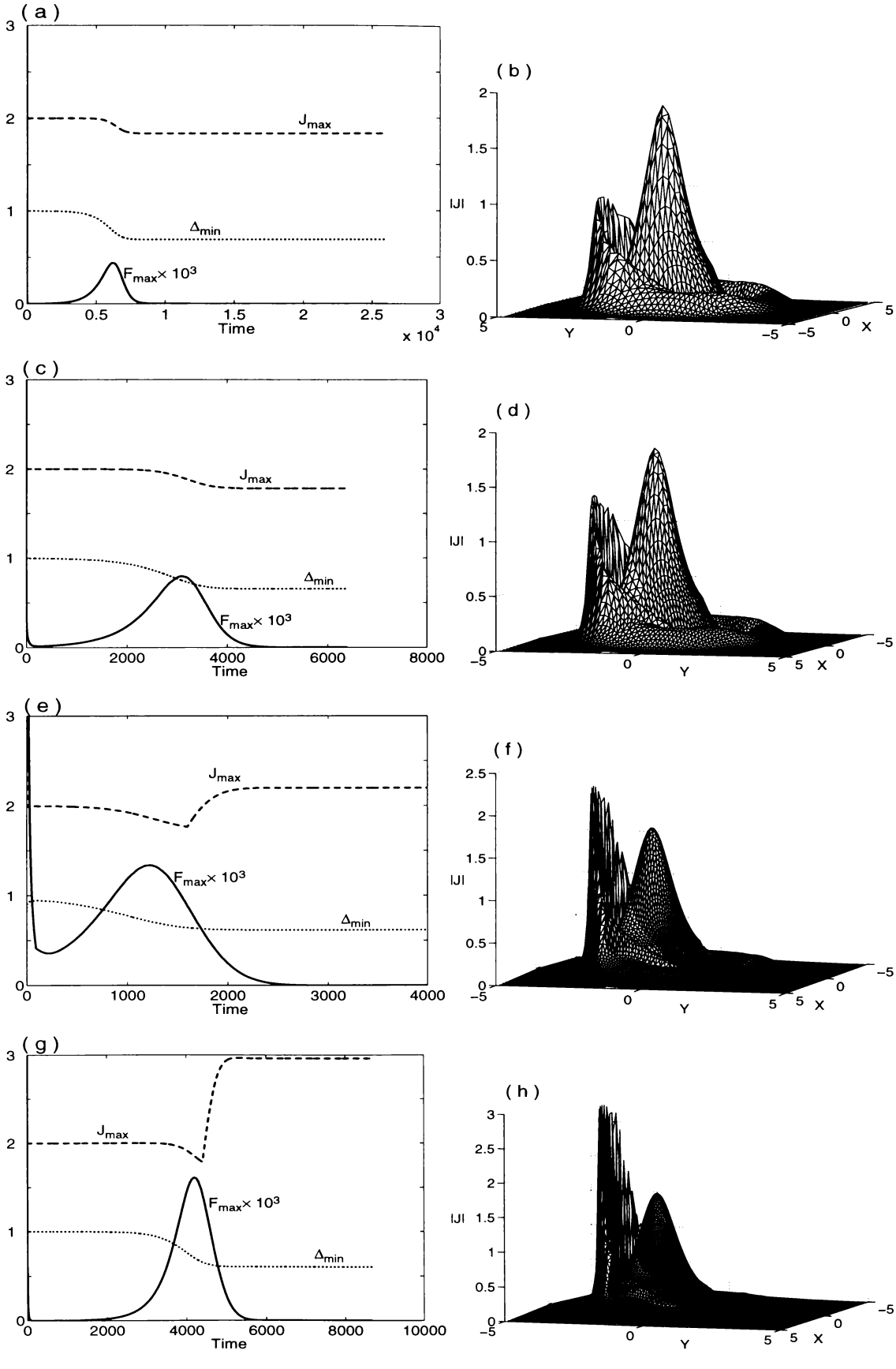

Figure 6.5: Kink of the B_3 field with $\tau = 0.35$ and $\beta = 0.0$ on different grids.

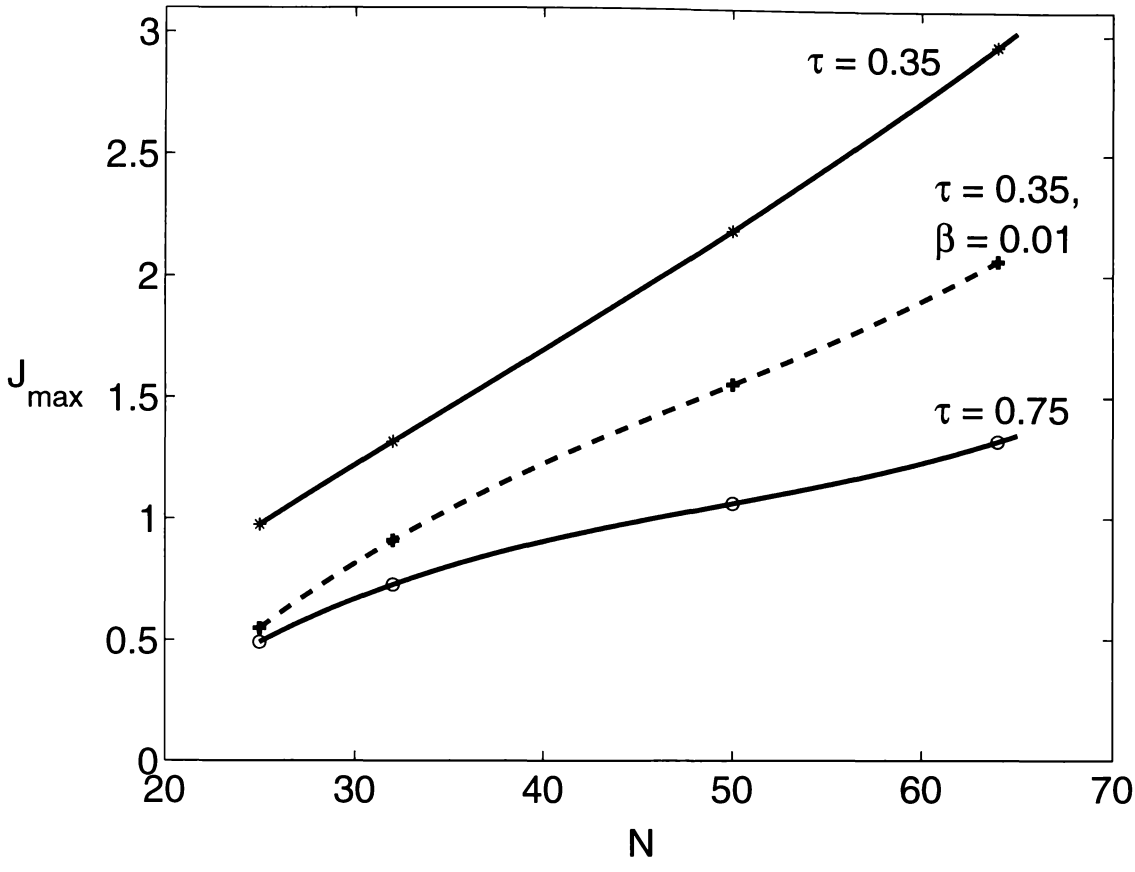

Figure 6.6: Local maximum current versus number of grid points N for the B_3 field. The solid line represents $\beta = 0$ and the dashed line $\beta = 0.01$.

As pointed out in chapter 4, in current sheets which form in regions of positive $|\mathbf{B}|$ (having no neutral point) the mesh compression is not significant and one expects $J_{\max} \propto N$ approximately.

Notice that the growth and strength of the $\tau = 0.35$ kink are smaller in the sense that $F_{\max}$ and ΔE_M are smaller than for $\tau = 0.75$ but that the current growth in the sheet is faster here. The dashed curve expresses the fact that the current sheet resulting from this kink cannot be suppressed by plasma pressure. This fact is also clear from the calculations of Arber *et al.* [5] with a similar plasma β.

For the $\tau = 0.35$ kink a contour plot of $|\mathbf{J}|$ and the corresponding distorted grid 65×65 at $t = 6100$ are given in figure 6.7(a) and (b) respectively. The corresponding surface and contour plots of B_z are given in (c) and (d). The axial drift is more pronounced compared to the $\tau = 0.75$ case (figure 6.2(c) and 6.4).

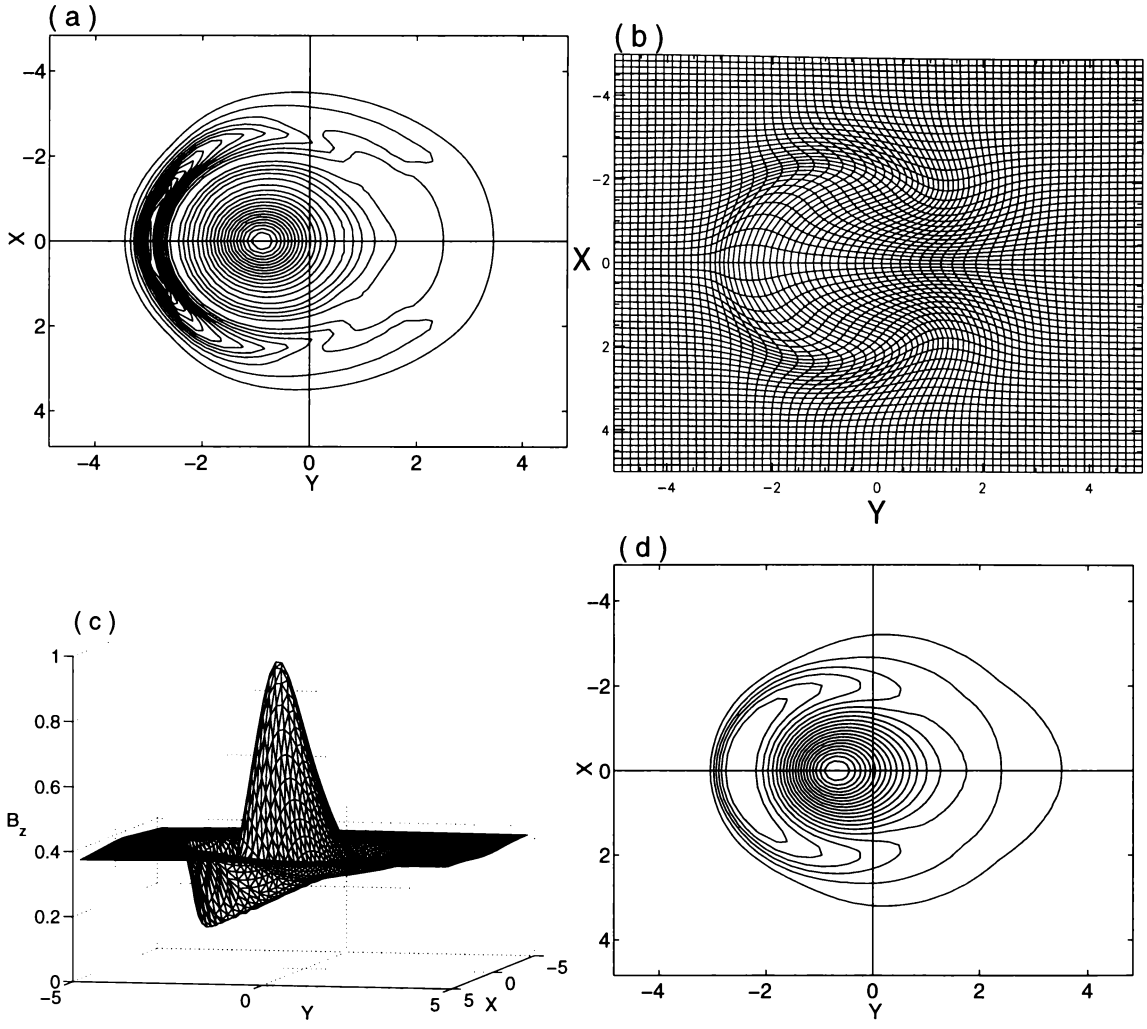

Figure 6.7: $|\mathbf{J}|$, the 65×65 grid, and B_z after the $\tau = 0.35$ kink.

Figure 6.8 shows development and saturation of the kink with a larger pitch, $\tau = 0.85$, for field B_3. The growth rate for this pitch is very small, namely $\lambda \approx 0.01482$, and we see that the field distorts very little here. Surface and contour plots of $|\mathbf{J}|$ are given at $t = 22500$ and E_M has reduced only by $\Delta E_M = 0.016\%$. The kink is very weak, and develops and saturates very slowly. Simulation of such a weak kink requires highly refined mesh in the presence of plasma pressure.

This study of the tube B_3 provides strong evidence of current sheet formation with the development of kink in this field. Plasma pressure has a stabilising effect on the kink but does not suppress current sheet formation.

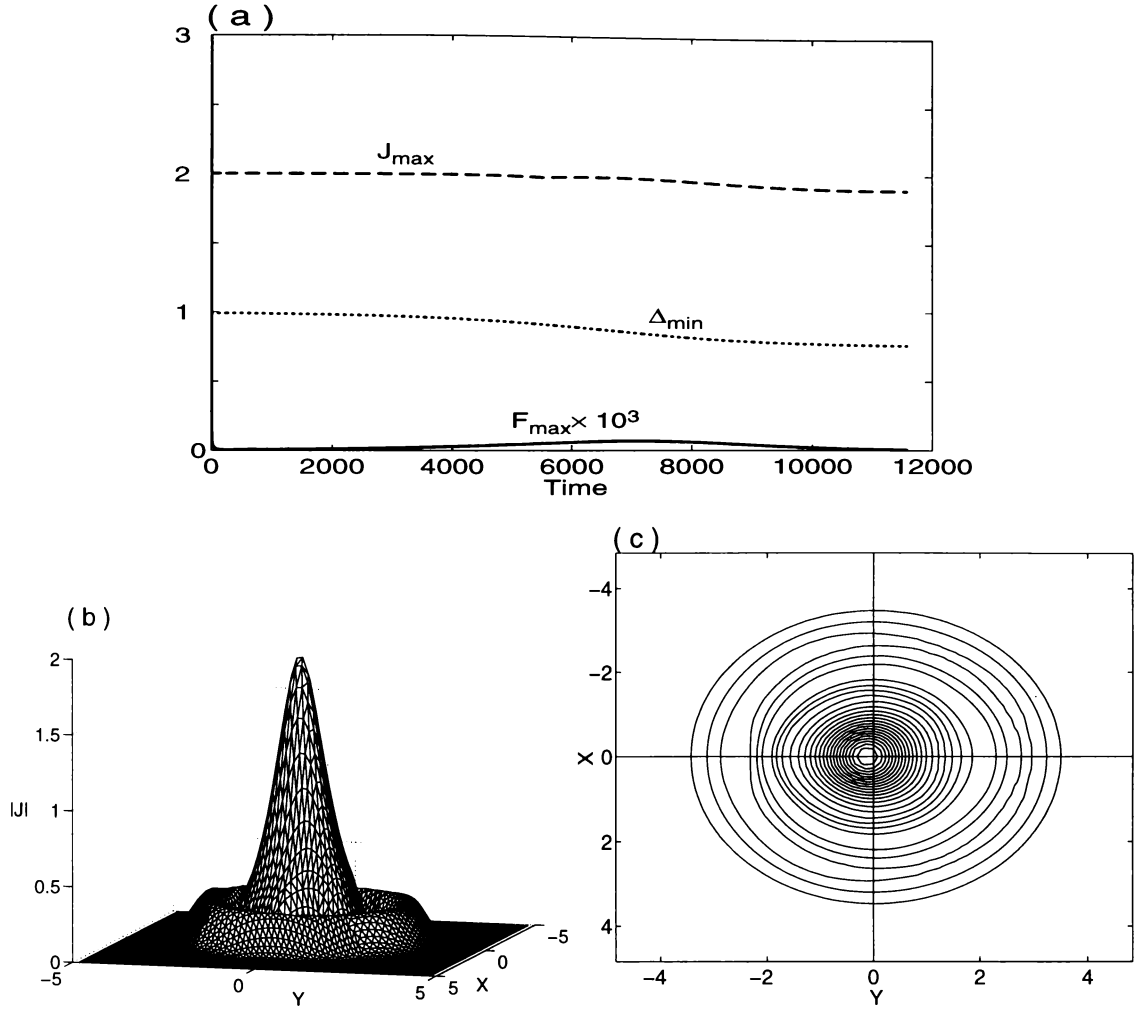

Figure 6.8: Kink of the B_3 field with $\tau = 0.85$ and $\beta = 0.0$.

6.2 The B_4 field

We will see in chapter 7 that a pair of parallel flux tubes whose combined horizontal field is zero at some point, but does not have a neutral point, does not give rise to current sheets while relaxing to equilibrium. Only current concentrations are developed whose intensity increases when the tubes are twisted together. We have also seen (in chapter 5, tube B_2) that a field having a $B_\theta = 0$ line gives rise to a minor current concentration but not a current sheet when the the field kinks and settles to a second helical equilibrium. Here we investigate the nonlinear helical kink of

a field having axial field reversal i.e. a cylinder with $B_z = 0$. Our linear calculations in chapter 3 show that the field B_4 is very weakly unstable to a helical kink. In fact, Robinson [72] mentions that "stable high-β diffuse pinches having similar field configurations are possible and the results compare well with experiment". In view of our experience with weak growth kinks of the other tubes, numerical realization of the helical kink for this tube does not seem feasible. Trial nonlinear calculations confirm this fact. Slight modification of this field however results in a non-equilibrium field that relaxes to a more unstable equilibrium.

As described in chapter 2, the B_4 field is an axially symmetric twisted field with twist k and axial field component, B_z, shown in figure 2.5. The current density of this field is given by

$$\mathbf{J}(r) = \left[0, B'_z, \frac{B_\theta}{r} + B'_\theta\right], \tag{6.1}$$

with

$$B'_z = \begin{cases} \frac{1}{2}\sin(r/2) & \text{if } r \leq 4, \\ 0 & \text{if } r > 4, \end{cases}$$

and

$$B'_\theta = \begin{cases} \frac{1}{2B_\theta}\left(-\frac{2\sin(r)}{r^2} + \frac{1}{2}\sin(r) + \frac{\cos(r)}{r} + \frac{2}{r^3}(1-\cos(r))\right) & \text{if } r \leq 4, \\ -\frac{4}{r^2}B_\theta(4) & \text{if } r > 4, \end{cases}$$

where the prime indicates differentiation with respect to r. Figure 6.9 shows $|\mathbf{J}|$ and B_θ of this field. At $r = 4$ the current is discontinuous but the field is continuous and so this does not represent a sheet.

Unlike all the other fields studied here, the twist $k(r)$ of this field is infinite at $r = \pi$ (see figure 2.5). The horizontal field is thus conveniently defined by

$$B_x = -\frac{y}{r}B_\theta \quad \text{and} \quad B_y = \frac{x}{r}B_\theta$$

with B_θ given by (2.22). Applying a constant twist τ, normally, adds a B_θ component $r\tau B_z$ that is subtracted when defining B_x and B_y in our code, see section 4.2. Defining B_x and B_y as above effectively adds on extra $r\tau B_z$ to B_θ, which means the

initial field is no more in equilibrium and

$$B_\theta = r(k + \tau)B_z. \tag{6.2}$$

When this non-equilibrium field is allowed to relax under helical symmetry with pitch τ, the extra magnetic tension compresses the tube and a new axisymmetric equilibrium is reached. Incidentally, the equilibrium achieved in this way is more unstable to the $m = 1$ kink having pitch τ. Our numerical simulations show that a compressed equilibrium field can easily be achieved only for the τ range [0, 0.5]. Relaxation to a kinked equilibrium is easy only in the narrow band [0.4, 0.5). For smaller τ values more refined grids are necessary to realize a kink while for larger values prohibitively small time steps are needed to achieve a kinked equilibrium. We use the same perturbation (see figure 4.4) to stimulate the kink.

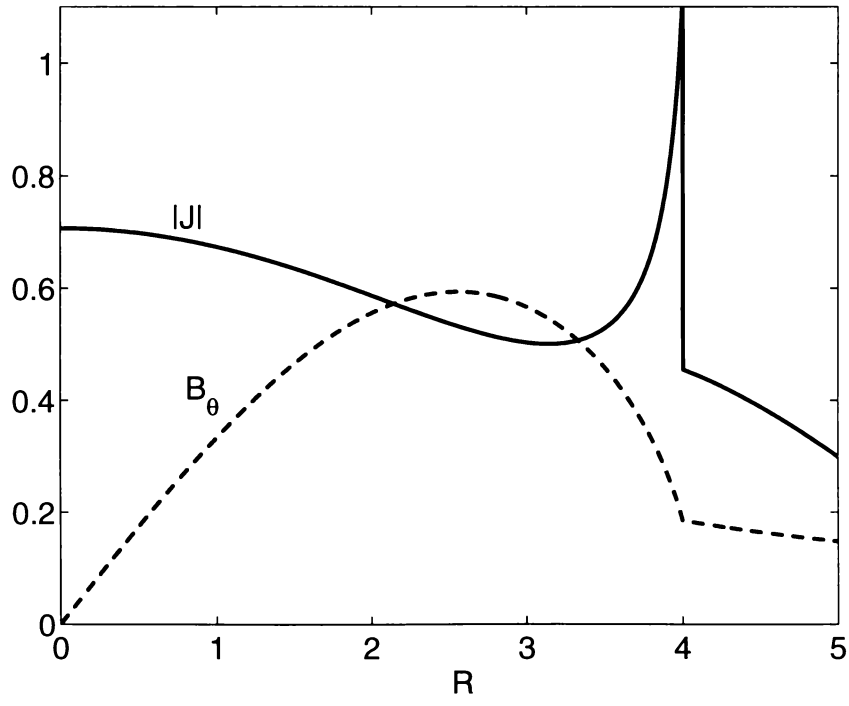

Figure 6.9: $|\mathbf{J}|$ (solid) and B_θ (dashed) of the B_4 field.

Figure 6.10 shows the relaxation process with $\tau = 0.25$ and 0.5 in the left and right columns respectively. In (a) the current grows and settles quickly to a larger value. In (d), on the other hand, $J_{\max}$ grows higher and then decays a little to settle to a

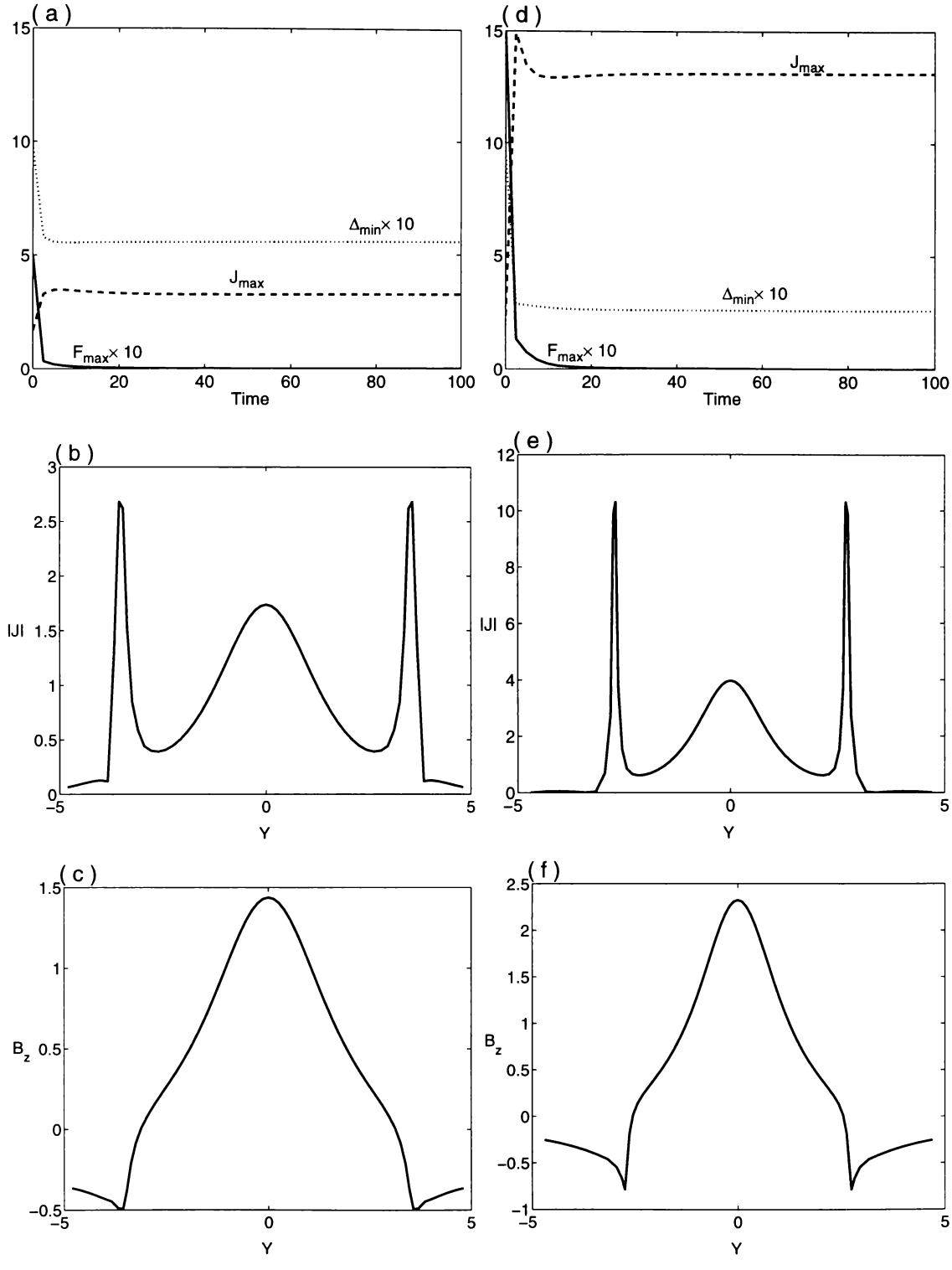

Figure 6.10: Twisting of the B_4 field with $\tau = 0.25$ in the left and 0.5 in the right columns.

larger equilibrium value. It is clear that for a greater τ the relaxation process starts with a higher $F_{\max}$ and hence it is relatively hard to reach equilibrium. Current and axial field are plotted only in the $x = 0$ plane due to axisymmetry. The decay

of $F_{\max}$ is slower and achieving equilibrium requires small time steps. Current and field plots in the left column ((b) and (c)) are at $t = 5000$ and those in the right ((e) and (f)) at $t = 2000$. A greater τ results in larger compression of the field. Doubling the values of τ almost doubles the magnitude of the axial field and increases $J_{\max}$ about four times.

The effect of twist on the current growth is plotted in figure 6.11. The initial discontinuity in current grows very rapidly with τ but this layer does not represent a current sheet, because the field is still continuous. The cusp in B_z, however, gets sharper with τ, as is clear from figures 6.10(c) and (f).

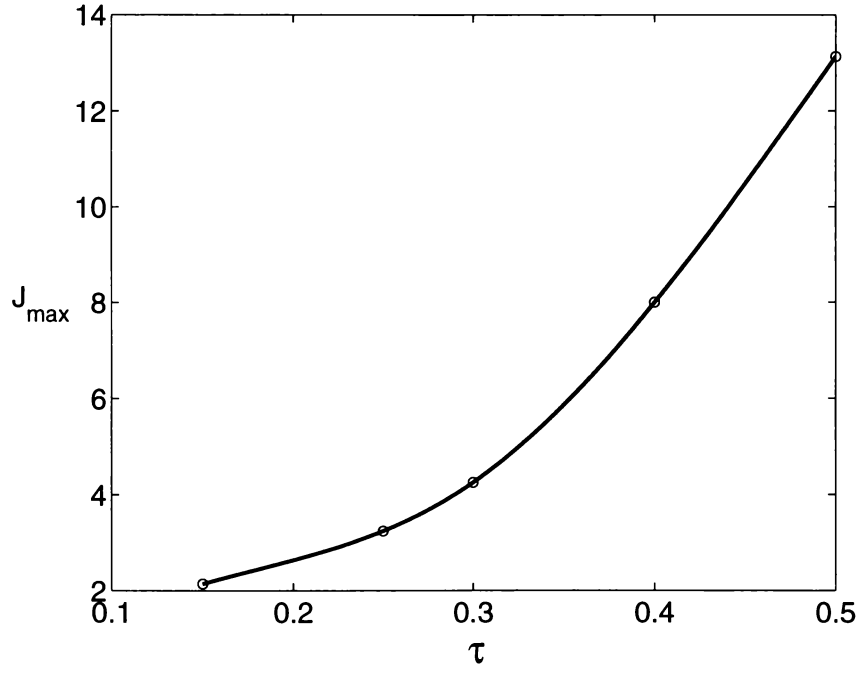

Figure 6.11: Growth of $J_{\max}$ with τ.

To see the effect of plasma pressure on the resulting current density of the compressed field, figure 6.12 shows the current density when $\tau = 0.5$ with $\beta = 0.0$ as a dashed line and $\beta = 0.01$ as a solid line. We see that with $\beta = 0.01$ the resulting $J_{\max}$ is slightly smaller portraying the usual stabilising effect of plasma pressure.

The surface and contour plots of current (and B_z) of the compressed equilibrium field with $\tau = 0.5$, given in figure 6.13, are to be used for comparison with nonlinear

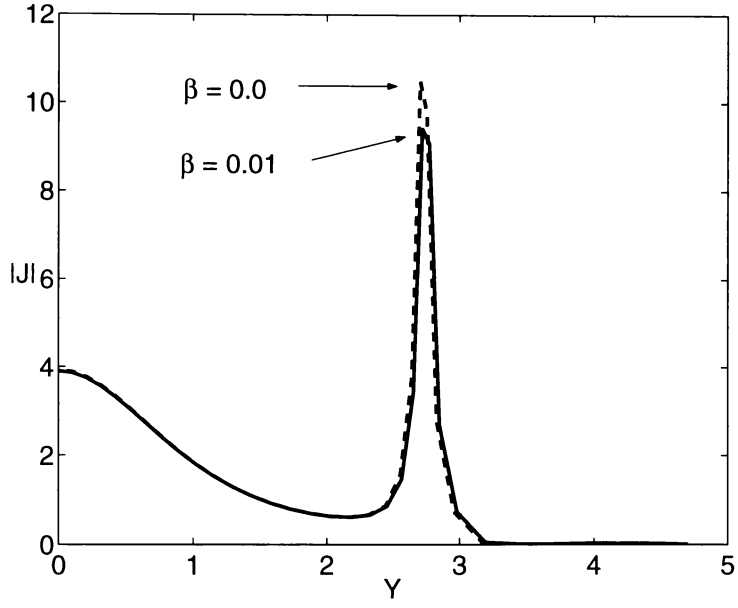

Figure 6.12: $|\mathbf{J}|$ of B_4 field twisted with $\tau = 0.5$ when $\beta = 0$ (dashed) and 0.01 (solid).

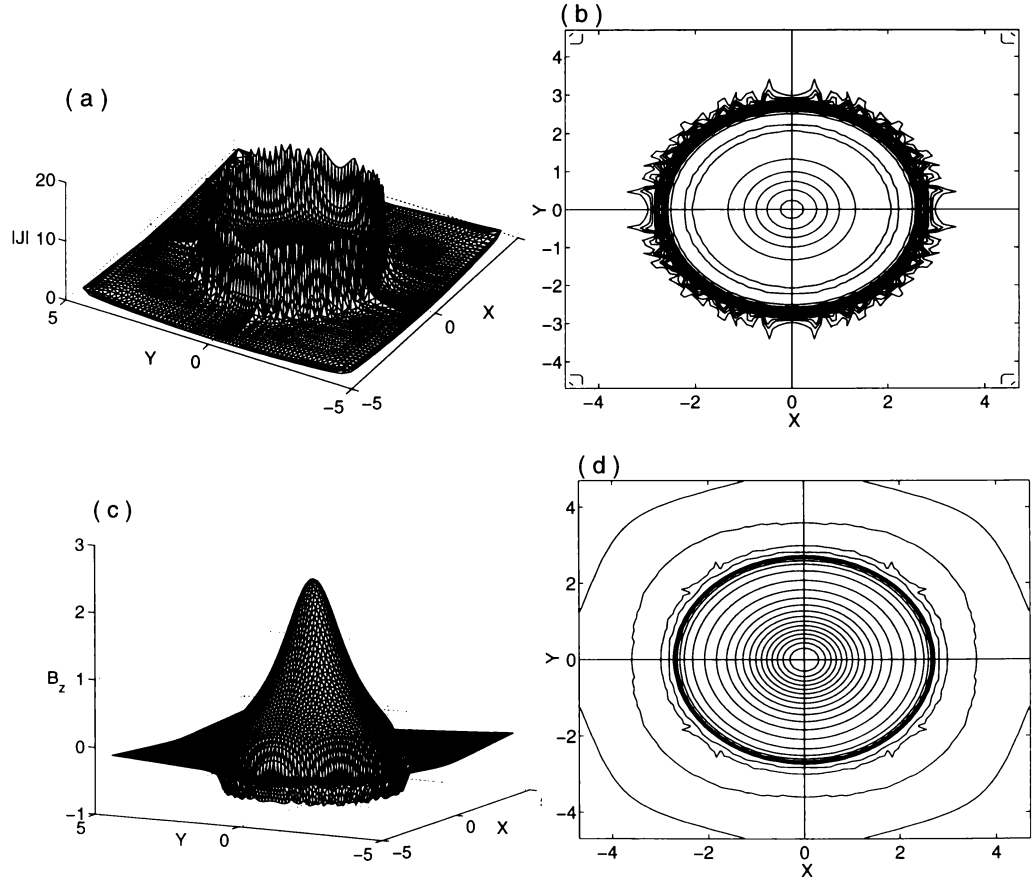

Figure 6.13: $|\mathbf{J}|$ and B_z of the $\tau = 0.5$ equilibrium field when $\beta = 0$.

kink simulations that follow. The jagged wall in the surface plot of $|\mathbf{J}|$ and the noise in the contour plots seem to be mostly due to poor representation of the current discontinuity by our grid and the plotting routines.

Applying a small perturbation, as in the other cases studied earlier, and continuing the calculations with the same τ produce a kink both in the absence and presence

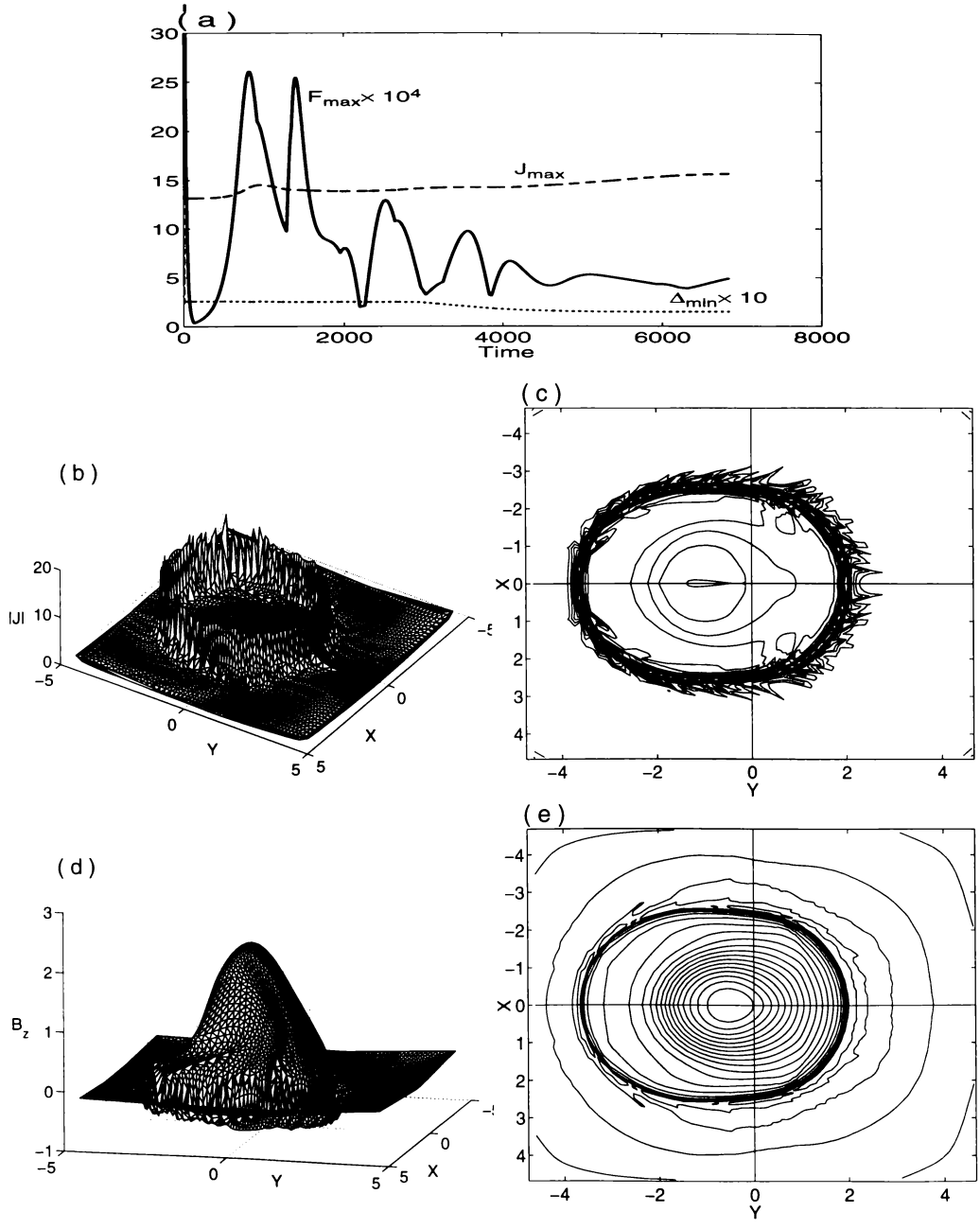

Figure 6.14: Kink in the $\tau = 0.5$ case when $\beta = 0.0$.

of plasma pressure, but achieving a neighboring equilibrium is difficult in the former case. In figure 6.14 are plotted the zero plasma pressure results for the $\tau = 0.5$ case. The oscillatory behavior of $F_{\max}$ and the spiky current structure gives a very unpleasant look but the displaced axis of the tube and growth (and decay) of $F_{\max}$ resemble the previous kink calculations. Current and axial field are plotted at time $t = 7800$ in (b)-(c) and (d)-(e) respectively. The existing current concentration is now deformed and has lost its axial symmetry with slight higher peak on the left.

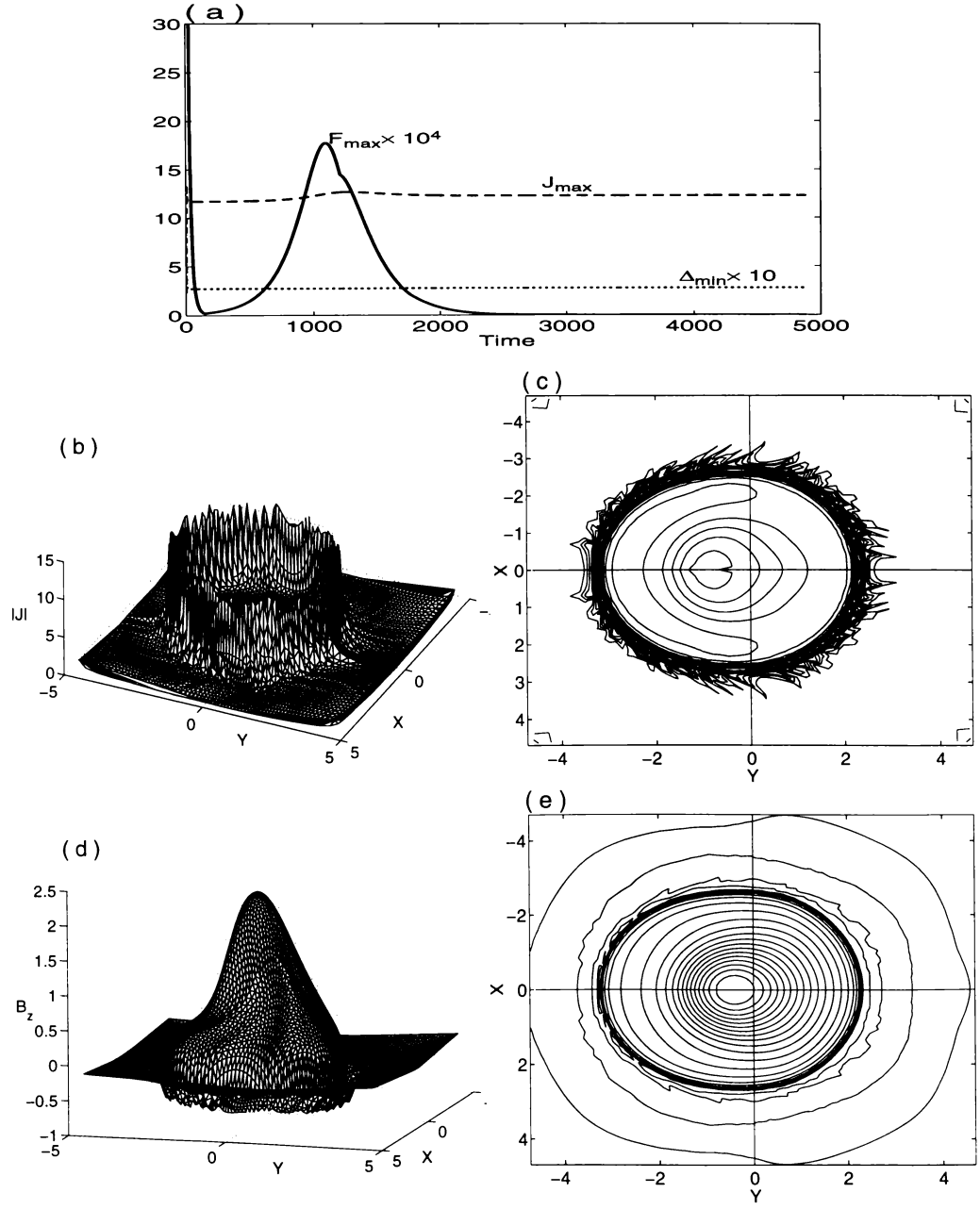

Figure 6.15: Kink in the $\tau = 0.5$ case when $\beta = 0.01$.

The same simulation with a plasma $\beta = 0.01$ gives a smooth development of the kink and relaxation to a neighboring helical equilibrium. This can be seen in the results plotted in figure 6.15. Here the surface and contour plots of current in (b)-(c) and B_z in (d)-(e) are given at $t = 4900$. Though the current profile still remains spiky the relaxation process is now smooth. The kink is weak as usual but development and relaxation is not very slow. For comparison, $|\mathbf{J}|$ and B_z in the plane $x = 0$ are shown in figure 6.16. The solid and dashed lines represent the $\beta = 0.0$ and 0.01 cases respectively. Plasma pressure seems to have reduced the off-axis drift and the current accumulation on the left.

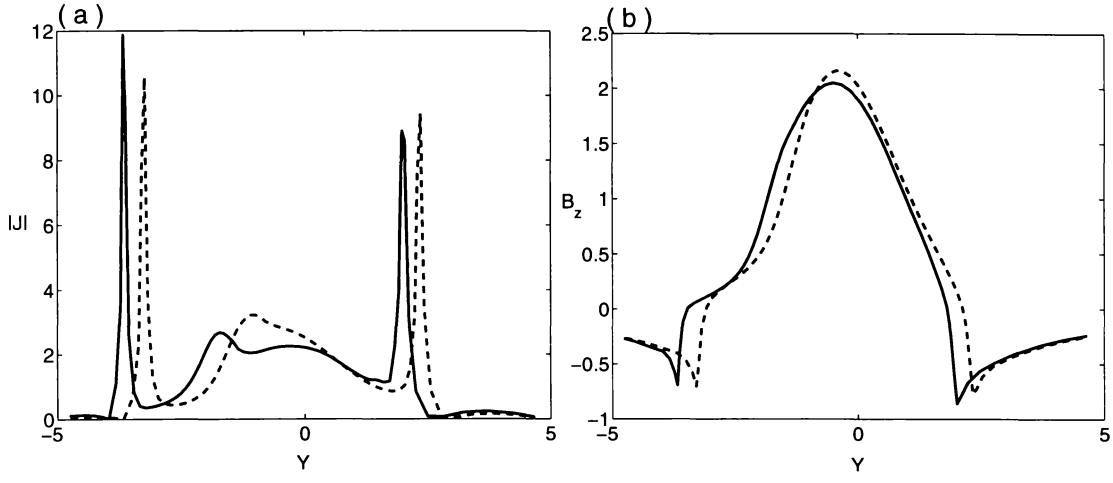

Figure 6.16: Effect of plasma pressure on $|\mathbf{J}|$ and B_z of the $\tau = 0.5$ kink. The $x = 0$ plane view. The solid line represents the $\beta = 0.0$ case and the dashed $\beta = 0.01$.

In contrast to the B_3 tube the current accumulation on the left with the kink is a current concentration and not a sheet. Mesh refinement has no noticeable effect on the current growth anywhere.

Results of the kink with $\tau = 0.4$ are given in figure 6.17. Plasma pressure is zero but still the kink is very weak. Relaxation to a kinked equilibrium is slow and $F_{\max}$ decay is oscillatory. A small plasma pressure smoothes out this kink and calculations with $\beta = 0.01$ does not produce a kink on the standard grid. Instead the corresponding axisymmetric compressed equilibrium field is achieved.

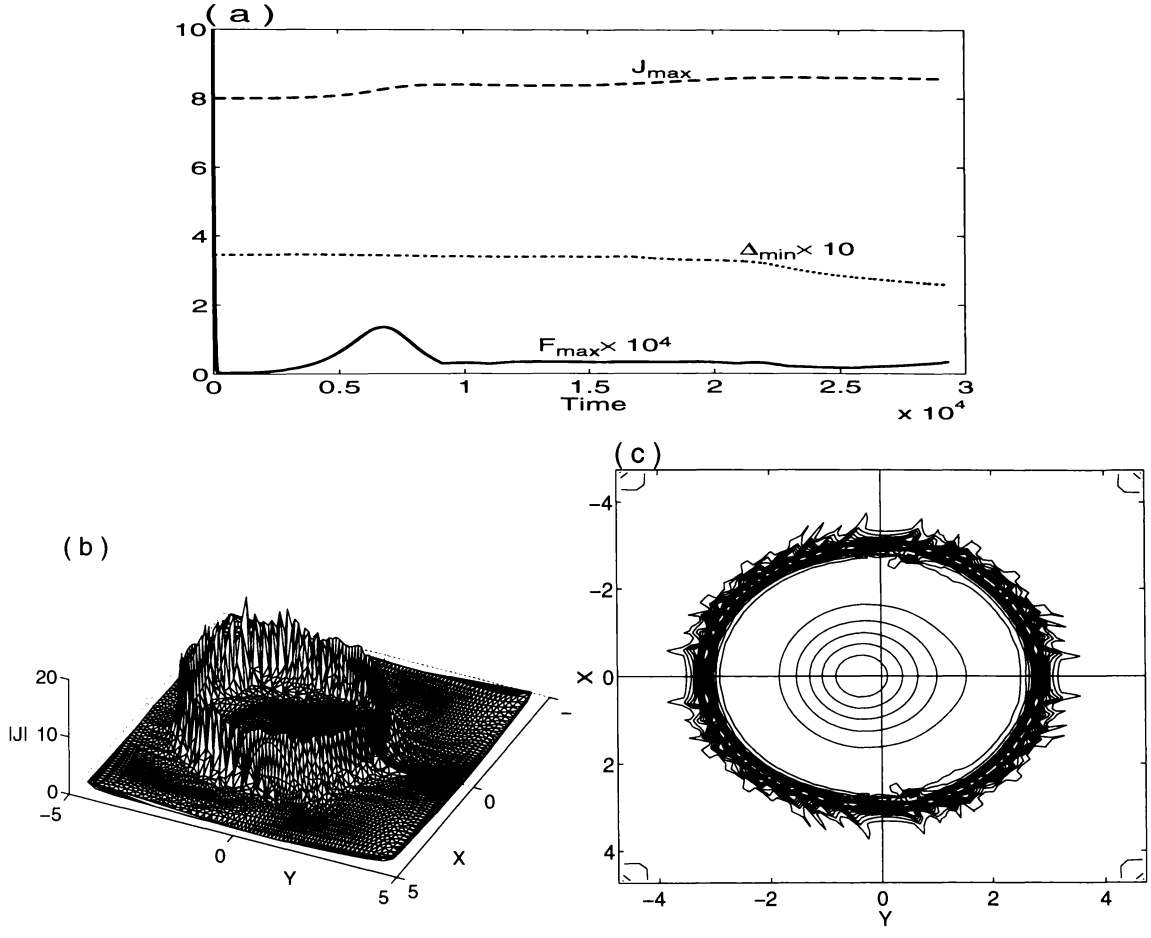

Figure 6.17: The $\tau = 0.4$ kink when $\beta = 0.0$.

When a perturbation is applied to a compressed equilibrium of τ_0 (say) and calculations are carried out with a different pitch value, τ_1, a compressed equilibrium or a kink develops that would have been the result of performing the calculation with twist parameter τ_1. Thus each kinked (and compressed) equilibrium is unique here also. Values of τ greater than 0.5 do produce a kink but relaxation to a kinked equilibrium cannot be achieved especially for much larger values or in the absence of plasma pressure. Smaller values of τ give rise to weaker kinks. For much smaller values either no kink takes place or it is so feeble that it cannot be realized on our standard grid.

Our calculations in this chapter illustrate the formation of a current sheet as a result of the helical kink in the B_3 field. Arber *et al.* [5] were the first to report this

phenomena in a similar flux tube, our local $J_{\max}$ versus N curves complement their findings. Recently Baty [8] has also studied a similar field using a 3-D MHD code and reports reconnection resembling the Sweet-Parker formulation. Our use of helical symmetry reduces the computational effort substantially yet gives a comparable picture of the helical kink and second kinked equilibrium. We show that plasma pressure stabilizes the $m = 1$ kink but does not suppress consequent current sheet formation. We also showed that axial field reversal gives a current concentration but no current sheet is necessarily formed as a result of kink development in such a field.

Chapter 7

Parallel tube interactions

While twisted loops exist in almost all flare sites the composition is normally complex and isolated loops seldom appear to cause energetic flares. Pallavicini [24] reports different kinds of compact flares in the Skylab images and in most cases the observed structure is quite complex, with bundles of loops flaring simultaneously or in succession. In only a few cases is it possible to isolate a simple flaring loop arching between regions of opposite magnetic polarity. Gold and Hoyle [31] were the first to suggest interaction of flux tubes as a possible cause of solar flares. They consider two parallel flux tubes touching each other along a line. The tubes have like currents and thus attract each other at their line of contact. It is argued that if the tubes are kept pressed together for a considerable time they may begin to penetrate each other. This leads to a sudden pinching of the current at the points of contact and subsequent dissipation of the energy associated with that current.

Shearing motion of twin-lobed fields [84, 12] and X-type (and O-type) nulls [52, 23, 70, 17, 16, 53] as causes of magnetic dissipation have been explored by many authors but nonlinear evolution of interacting tubes has received little attention due to the intensive computations required by the three dimensional problem. Parker's widely cited paper on topological dissipation [63] also states that a complicated topology, such as two or more flux tubes wrapped around one another to form a rope,

or braided or knotted flux tubes, is without equilibrium. He studied [65] mutual hydrodynamic forces between neighboring tubes in the convective zone emphasizing that two rising tubes attract each other when they are side by side and repel when one is behind the other.

With Vainshtein [81] Parker investigated the equilibrium requirements for a cluster of twisted flux tubes in a highly conducting fluid and concludes that there is equilibrium only for axial symmetry i.e. only for a single flux tube. Any more complicated cluster of flux tubes is subject to non-equilibrium reconnection of the transverse component of the field. Citing his earlier work [63] and van Ballegooijen [82] he states " In particular, there is in general no equilibrium in any magnetic field topology more complicated than two contiguous parallel flux tubes with opposite twists or with winding of lines of force varying with z (axial displacement) in the same way that the vortex lines in a 2-D flow of ideal fluid wind about each other with the passage of time". Parker [66] illustrates the formation of current sheets due to interaction of an external axial field with a twisted flux tube (and two oppositely inclined twisted tubes) tilted to make an angle θ with the axis. Here the essential ingredient for the formation of current sheets due to continuous deformation of an initially uniform field is argued to be juxtaposition of two different field topologies. Thus it is claimed that "two flux bundles pressed together along their length produce a tangential discontinuity on their common boundary unless one tube is the exact mirror image of the other".

Bogdan [13] studied the mechanical aspect of colliding twisted flux tubes in an inviscid, incompressible conducting gas. He found that flux tubes with opposite twists collide elastically and hence do not interact. They react only with their own kind. Zweibel and Rhoads [89] extended the work of Bogdan by treating the tubes as elastic bodies in the deep convective zone once again assuming incompressible flows. Critical velocities necessary for merging and coalescence are estimated and the validity of Sweet-Parker type reconnection is suggested.

Recently reconnection between two Gold-Hoyle tubes is studied by Kondrashov *et al.* [40] using a 3-dimensional resistive MHD code. Magnetic energy release and relative magnetic helicity are calculated for two different combinations. Similarly reconnection between two attracting flux tubes in the presence of a velocity field is studied by Milano *et al.* [56] using a reduced MHD code. A precursor to reconnection is the existence of current sheets and our aim here is to study combinations of two parallel flux tubes whose interaction may result in current sheet formation.

Sneyd [77] considers coronal flux tubes twisted together as a possible cause of current sheet formation. It is shown that by twisting together two flux tubes, the magnetic tension pulls them together, bringing into contact flux surfaces on which the field may have different orientations, thereby creating a discontinuity in $\mathbf{B}$. Uniform twisting of flux tubes around each other simplifies the analysis under the assumption of helical symmetry. Relaxation to equilibrium of such a configuration is analysed and it is proved that some of the equilibria must contain current sheets; in particular when the following two conditions are satisfied:

(S1) the two constituent flux tubes must have oppositely-directed axial field components ;

(S2) if the magnetic helicities of the tubes have the same sign, the twist τ must also have the same sign.

Nonlinear field evolution studies are needed to illustrate the validity of the findings mentioned above. Tube interactions are three dimensional and require high computational resources but uniformly twisted parallel tubes such as those considered by Sneyd [77], shown in figure 7.1, can be handled conveniently with our helically symmetric code. These tubes as well as the tubes considered by Gold and Hoyle attract each other and the combined field has a neutral point. We will see, in the next chapter, that a current sheet is formed when this field relaxes to equilibrium. We will find that the condition (S1) is necessary and (S2) is sufficient but not nec-

essary. In fact an external twist of any sign gives rise to a current sheet when (S1) is satisfied.

In this chapter we study interaction of two parallel flux tubes whose fields have the same magnitudes ($|\mathbf{B}_1| = |\mathbf{B}_2|$) but may have different directions. We will continue this study in the next chapter, where we deal with the relaxation of tubes whose initial combined field has a neutral point. As in the preceding chapters, $k_i = B_{i\theta}/(rB_{iz})$ denotes the twist of the ith tube and τ is an applied twist that wraps the tubes around each other. Magnetic field interaction and relaxation to equilibrium will be studied in detail. Since we are always dealing with the interaction of two tubes, $a_i = c$ indicates $a_1 = a_2 = c$ etc.

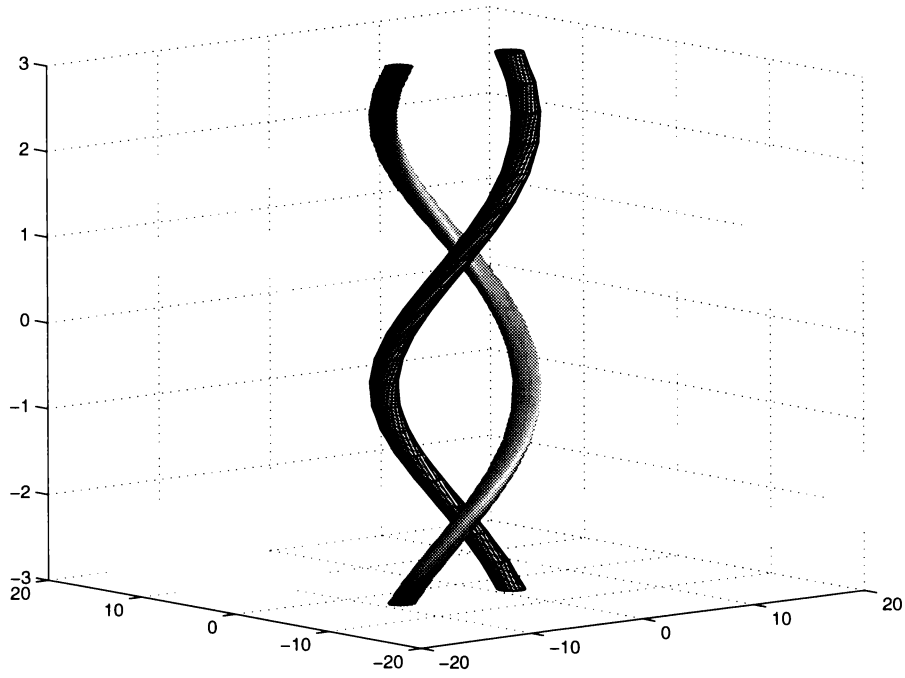

Figure 7.1: Parallel tubes twisted around each other.

We use only Gold-Hoyle tubes due to their simple analytic form and expect similar behavior from other tubes. Formation of current sheets, if any, is illustrated by performing the same calculations with different grid resolutions. The effect of a uniform twist τ on the current profile in each case is illustrated in detail. Plasma pressure is assumed zero since the tubes considered in this chapter do not result in

any current sheet and plasma pressure does not tend to produce a sheet if other conditions are not favorable.

7.1 Parallel Gold-Hoyle tubes

Consider two Gold-Hoyle tubes parallel to the z-axis centered at $(a_1, 0)$ and $(-a_2, 0)$, $a_i > 0$, having fields $\mathbf{B}_1$ and $\mathbf{B}_2$ given by

$$\mathbf{B}_1 = (r_1 k_1 \widehat{\theta} - \widehat{\mathbf{z}}) \frac{b_1}{1 + r_1^2 k_1^2} \quad \text{and} \quad \mathbf{B}_2 = (r_2 k_2 \widehat{\theta} + \widehat{\mathbf{z}}) \frac{b_2}{1 + r_2^2 k_2^2}, \tag{7.1}$$

with $r_1 = \sqrt{x_1^2 + y^2}$, $r_2 = \sqrt{x_2^2 + y^2}$, $x_1 = x - a_1$ and $x_2 = x + a_2$. When $b_1, b_2, k_1, k_2 > 0$ representative field lines are plotted in figure 7.2. Since $B_\theta = rkB_z$, axial and horizontal field components are given by

$$B_{1z} = -\frac{b_1}{1 + r_1^2 k_1^2}, \qquad B_{2z} = \frac{b_2}{1 + r_2^2 k_2^2}, \tag{7.2}$$

$$B_{ix} = -\frac{k_i y b_i}{1 + r_i^2 k_i^2}, \qquad B_{iy} = \frac{k_i x_i b_i}{1 + r_i^2 k_i^2}. \tag{7.3}$$

Both the fields can be written in terms of flux functions $\psi_1(x, y)$ and $\psi_2(x, y)$ as

$$\mathbf{B}_1 = b_1 \nabla \psi_1 \times \widehat{\mathbf{z}} + B_{1z} \widehat{\mathbf{z}} \quad \text{and} \quad \mathbf{B}_2 = b_2 \nabla \psi_2 \times \widehat{\mathbf{z}} + B_{2z} \widehat{\mathbf{z}}, \tag{7.4}$$

when

$$\psi_i = -\frac{1}{2k_i} \ln(1 + r_i^2 k_i^2). \tag{7.5}$$

Each tube being in local equilibrium implies that $\mathbf{J}_i \times \mathbf{B}_i = 0$, and so

$$\mathbf{J}_i = \alpha_i \mathbf{B}_i \tag{7.6}$$

$$\text{with} \quad \alpha_1 = -\frac{2k_1}{1 + r_1^2 k_1^2} \quad \text{and} \quad \alpha_2 = \frac{2k_2}{1 + r_2^2 k_2^2}.$$

Hence (neglecting plasma pressure) the only forces present are $\mathbf{J}_j \times \mathbf{B}_i$ when $i \neq j$. It is clear that $\mathbf{B}_2$ is along the positive y-axis at $(a_1, 0)$ so that $\mathbf{J}_1 \times \mathbf{B}_2$ points along the negative x-axis here. Similarly $\mathbf{B}_1$ is along the negative y-axis at $(-a_2, 0)$ and

$\mathbf{J}_2 \times \mathbf{B}_1$ points along the positive x-axis. The tubes therefore attract each other. The resultant force is given by

$$\begin{aligned}
\mathbf{F} &= \mathbf{J} \times \mathbf{B} = (\mathbf{J}_1 + \mathbf{J}_2) \times (\mathbf{B}_1 + \mathbf{B}_2) = \mathbf{J}_1 \times \mathbf{B}_2 + \mathbf{J}_2 \times \mathbf{B}_1 \\
&= (\alpha_1 - \alpha_2)(\mathbf{B}_1 \times \mathbf{B}_2) \\
&= 2B_{1z}B_{2z}\frac{(r_2k_2 - r_1k_1)[k_1 + k_2 + k_1k_2(r_1^2k_1 + r_2^2k_2)]}{(1 + r_1^2k_1^2)(1 + r_2^2k_2^2)}\widehat{\mathbf{r}}. \qquad (7.7)
\end{aligned}$$

We see that when $\alpha_1 = \alpha_2$ the force between the tubes is zero.

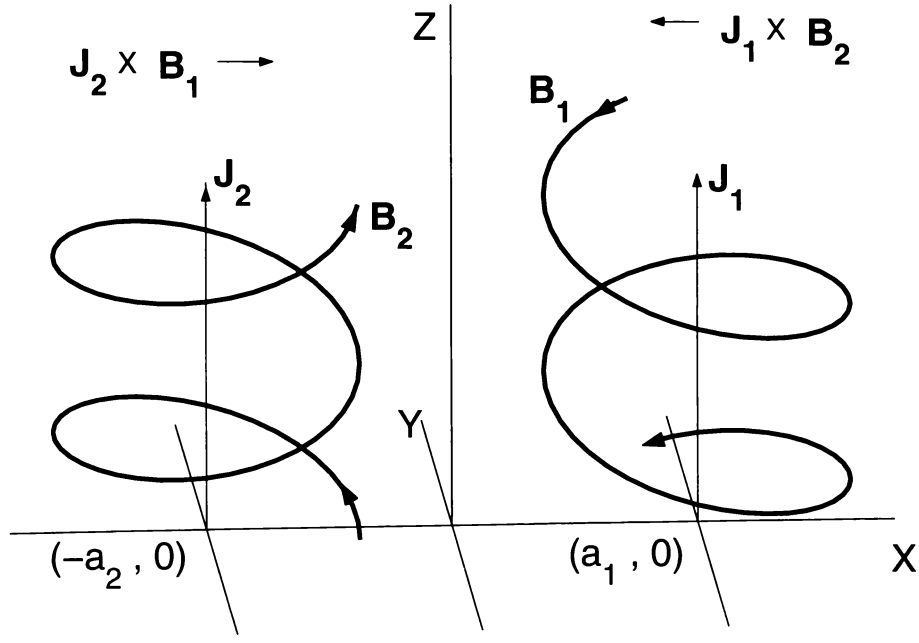

Figure 7.2: Field lines of parallel Gold-Hoyle tubes defined by (7.1) having $k_i, a_i, b_i > 0$.

Figure 7.3 illustrates all possible combinations of two parallel tubes in the plane $z = 0$. A dot at the center of the tube represents current out of page (along the positive z-axis) and a plus sign refers to current into the page. It is clear that the tubes attract each other when the currents have the same sign, i.e. when $B_{1\theta}B_{2\theta} > 0$. In terms of b_i etc. the tubes attract each other when $b_1b_2k_1k_2 > 0$, otherwise they repel. Hence we need to consider only two classes of flux tubes, namely, **attracting** and **repelling** tubes.

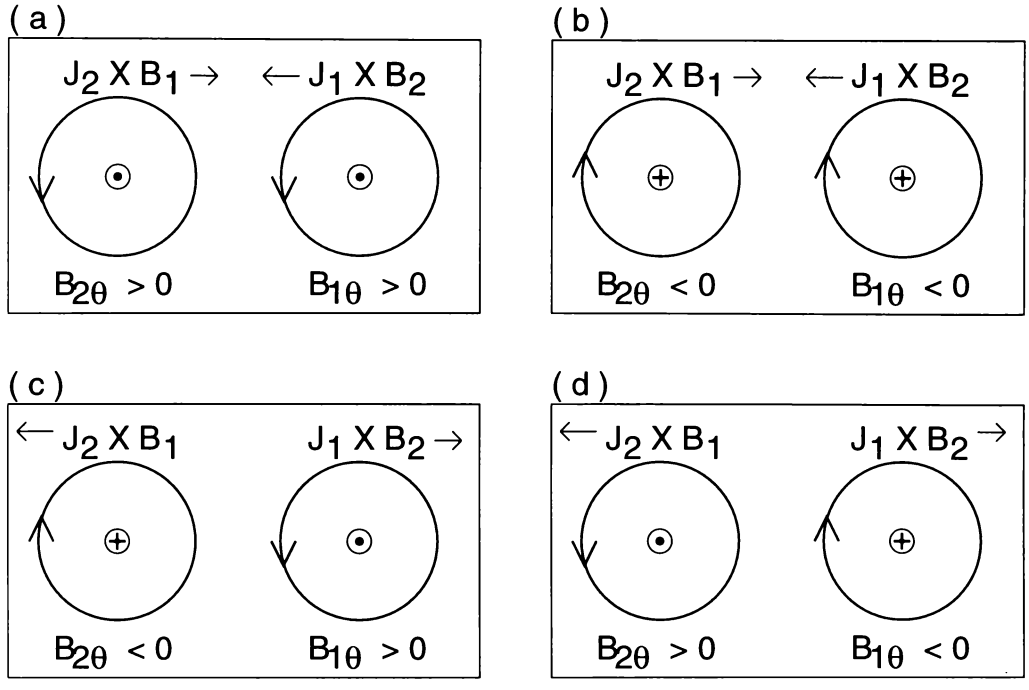

Figure 7.3: Possible combinations of two parallel flux tubes.

Attraction of the tubes will result in field interaction and the combined field will relax to an equilibrium with time. Sneyd [77] studies the attracting tubes of figure 7.2 and finds that when a twist $\tau > 0$ is applied the field develops a current sheet as it relaxes to equilibrium. For a negative twist ($\tau < 0$), however, his argument fails to predict current sheet formation. Our nonlinear relaxation in section 7.3 shows that both positive and negative twists give similar results and a current sheet is formed irrespective of the twist value. No current sheet forms, however, when the initial field contain no neutral point.

Repelling tubes can be forced together only by some external mechanism. Will applying a uniform twist press the tubes against each other to result in current sheet formation? We will address this question in the next section. Let us first look at the existence and location of a neutral point (or null) where all components of the field vanish.

7.1.1 Existence of neutral points

Sneyd [77] mentions that in the case of the tubes of figure 7.2, when $k_1 = k_2 = k$ and $a_1 = a_2 = a$ then $|ka| > 1$ gives an X-type neutral point (X-null) at the origin and two O-type neutral points (O-null) on either side of the origin. When $|ka| < 1$ the two tubes merge together and the field lines are simply closed curves about the origin. Let us consider the tubes defined by (7.1).

To consider a more general combination of tubes, it is clear that in the case where b_1 and b_2 have different signs, even if the tubes attract each other, the axial component of $\mathbf{B} = \mathbf{B}_1 + \mathbf{B}_2$ will not be zero anywhere and so there will be no neutral point. Hence we consider the $b_1 b_2 > 0$ case only. To simplify the case further let $b_1 = b_2 = 1$ (say). A null, if it exists, will lie on the line $y = 0$ between $(-a_2, 0)$ and $(a_1, 0)$ in the $z = 0$ plane. Now

$$B_z = \frac{-1}{1 + r_1^2 k_1^2} + \frac{1}{1 + r_2^2 k_2^2} = 0$$

implies

$$-1 - k_2^2(x^2 + 2a_2x + a_2^2 + y^2) + 1 + k_1^2(x^2 - 2a_1x + a_1^2 + y^2) = 0.$$

Rearranging, this gives

$$A_1(x^2 + y^2) - 2A_2x = A_3,$$

where $A_1 = k_1^2 - k_2^2$, $A_2 = a_1k_1^2 + a_2k_2^2$ and $A_3 = a_2^2k_2^2 - a_1^2k_1^2$. Or

$$\left(x - \frac{A_2}{A_1}\right)^2 + y^2 = \frac{A_3}{A_1} + \frac{A_2^2}{A_1^2},$$

showing that $B_z = 0$ on a circle centered at $\left(\frac{A_2}{A_1}, 0\right)$. Hence on the line $y = 0$ we have $B_z = 0$ at

$$\begin{aligned} x &= \frac{A_2}{A_1} \pm \sqrt{\frac{A_3}{A_1} + \frac{A_2^2}{A_1^2}} \\ &= \frac{A_2}{A_1} \pm \frac{k_1 k_2}{A_1}(a_1 + a_2) \\ &= \frac{a_1k_1 + a_2k_2}{k_1 - k_2} \quad \text{or} \quad \frac{a_1k_1 - a_2k_2}{k_1 + k_2}. \end{aligned}$$

It is clear from (7.3) that on the line $y = 0$ we have $B_x = 0$. The B_y component also vanishes provided

$$\frac{k_1 x_1}{1 + r_1^2 k_1^2} + \frac{k_2 x_2}{1 + r_2^2 k_2^2} = 0.$$

At a neutral point $B_z = 0$ implies

$$\frac{1}{1 + r_1^2 k_1^2} = \frac{1}{1 + r_2^2 k_2^2}$$

and $B_y = 0$ implies $k_1 x_1 + k_2 x_2 = 0$. This gives

$$x = \frac{a_1 k_1 - a_2 k_2}{k_1 + k_2}.$$

Hence the neutral point (when it exists) is at $(x_0, 0)$ where

$$x_0 = \frac{a_1 k_1 - a_2 k_2}{k_1 + k_2}. \tag{7.8}$$

It is clear that this point $(x_0, 0)$ lies between $(-a_2, 0)$ and $(a_1, 0)$ only when both k_1 and k_2 have the same sign. In other words, a neutral point does not exist between repelling tubes. It exists between attracting tubes in the case $b_1 b_2 > 0$.

7.1.2 Types of neutral points

To see what types of neutral points can be expected between two attracting tubes we perform a Taylor series expansion of **B** in the vicinity of the neutral point. Taylor's expansion about x_0 gives

$$\frac{1}{1 + r_1^2 k_1^2} = \frac{1}{1 + k_1^2 (x_0 - a_1)^2} - \frac{2(x_0 - a_1) k_1^2 \delta x}{[1 + k_1^2 (x_0 - a_1)^2]^2} + \cdots$$

where $\delta x = x - x_0$. Neglecting second and higher order terms in δx and taking

$$\delta_1 = \frac{2(a_1 - x_0) k_1^2}{1 + k_1^2 (x_0 - a_1)^2}$$

we have in the vicinity of x_0

$$\frac{1}{1 + r_1^2 k_1^2} = \frac{1 + \delta_1 (x - x_0)}{1 + k_1^2 (x_0 - a_1)^2}.$$

Notice that $\delta_1 \geq 0$ and $|\delta_1 \delta x| < 1$ near x_0. Similarly taking

$$\delta_2 = \frac{2(a_2 + x_0)k_2^2}{1 + k_2^2(x_0 + a_2)^2}$$

we get near x_0

$$\frac{1}{1 + r_2^2 k_2^2} = \frac{1 - \delta_2(x - x_0)}{1 + k_2^2(x_0 + a_2)^2}.$$

Thus in the vicinity of x_0 (when $b_1 = b_2 = 1$)

$$\begin{aligned} B_x &= B_{1x} + B_{2x} \\ &= -y \left\{ \frac{k_1[1 + \delta_1(x - x_0)][1 + (x_0 + a_2)^2 k_2^2]}{[1 + (x_0 - a_1)^2 k_1^2][1 + (x_0 + a_2)^2 k_2^2]} \right. \\ &\quad \left. + \frac{k_2[1 - \delta_2(x - x_0)][1 + (x_0 - a_1)^2 k_1^2]}{[1 + (x_0 - a_1)^2 k_1^2][1 + (x_0 + a_2)^2 k_2^2]} \right\} \end{aligned}$$

and

$$\begin{aligned} B_y &= \frac{(x - a_1)k_1[1 + \delta_1(x - x_0)][1 + (x_0 + a_2)^2 k_2^2]}{[1 + (x_0 - a_1)^2 k_1^2][1 + (x_0 + a_2)^2 k_2^2]} \\ &\quad + \frac{(x + a_2)k_2[1 - \delta_2(x - x_0)][1 + (x_0 - a_1)^2 k_1^2]}{[1 + (x_0 - a_1)^2 k_1^2][1 + (x_0 + a_2)^2 k_2^2]}. \end{aligned}$$

To first order in $x - x_0$ we have $\delta_2 = \delta_1 k_2 / k_1$ and

$$\begin{aligned} \delta_1 &= \frac{2k_1^2 k_2(a_1 + a_2)}{(k_1 + k_2)\left[1 + \frac{k_1^2 k_2^2 (a_1 + a_2)^2}{(k_1 + k_2)^2}\right]}, \\ B_x &= -\frac{A(k_1 + k_2)}{k_1} y \left[k_1 + \delta_1(k_1 - k_2)(x - x_0)\right], \\ B_y &= \frac{A}{k_1}\left[\delta_1(k_1^2 - k_2^2)x^2 + \left\{k_1(k_1 + k_2) - \delta_1 x_0(k_1^2 - k_2^2) - \delta_1(a_1 k_1^2 + a_2 k_2^2)\right\} x \right. \\ &\quad \left. + k_1(a_2 k_2 - a_1 k_1) + \delta_1 x_0(a_1 k_1^2 + a_2 k_2^2)\right], \end{aligned} \tag{7.9}$$

where $A = [1 + (x_0 - a_1)^2 k_1^2]^{-1} = [1 + (x_0 + a_2)^2 k_2^2]^{-1} = \left[1 + \frac{k_1^2 k_2^2 (a_1 + a_2)^2}{(k_1 + k_2)^2}\right]^{-1}$.

Hence for a flux function ψ such that

$$B_x = \frac{\partial \psi}{\partial y} \quad \text{and} \quad B_y = -\frac{\partial \psi}{\partial x} \tag{7.10}$$

we have

$$\begin{aligned} \psi &= -\frac{A}{k_1}\left[\frac{1}{2}(k_1 + k_2)\left\{k_1 + \delta_1(k_1 - k_2)(x - x_0)\right\} y^2 + \frac{1}{3}\delta_1(k_1^2 - k_2^2)x^3 \right. \\ &\quad + \frac{1}{2}\left\{k_1(k_1 + k_2) - \delta_1 x_0(k_1^2 - k_2^2) - \delta_1(a_1 k_1^2 + a_2 k_2^2)\right\} x^2 \\ &\quad \left. + \left\{k_1(a_2 k_2 - a_1 k_1) + \delta_1 x_0(a_1 k_1^2 + a_2 k_2^2)\right\} x\right] \end{aligned} \tag{7.11}$$

For equal equidistant tubes having $a_1 = a_2 = a$, $b_1 = b_2 = 1$ and $k_1 = k_2 = k$ (say) we see that the null lies at the origin (i.e. $x_0 = 0$) and

$$\psi \propto y^2 + (1 - \delta_1 a)x^2$$

with $\delta_1 = 2ak^2/(1 + a^2k^2)$. This shows that flux lines are ellipses and that we have an O-type null at the origin when $|ak| < 1$. When $|ak| > 1$ the flux lines are hyperbolas and there is an X-type null at the origin.

As mentioned earlier, Sneyd [77] has analysed the equal equidistant tubes case in detail and shows that when there is an X-null at the origin, two further O-type nulls exist on either side. To ascertain the existence and types of neutral points we plot in figure 7.4 the initial field lines of two parallel tubes, for different values of k_i. In each case $a_1 = a_2 = 0.3$, $b_1 = b_2 = 0.5$ (except (f) where $b_1 = -0.5$) and the domain is a rectangular box $[-1\ ,\ 1] \times [-1\ ,\ 1]$. In (c) - (f) field lines are shown only in the interior to highlight the corresponding neutral points. Repelling tubes are shown in (a) and further calculations show that the picture remains almost the same (except for direction) even if the magnitudes of the twists k_i are such that $a_i k_i > 1$. The rest of the plots show different combinations of attracting tubes. Figures (b) and (c) show that $a_i k_i < 1$ gives rise to an O-type neutral point whose position depends on the magnitudes of the respective k_i. When $a_i k_i > 1$, see (d), there are three nulls (of $B_H = \sqrt{B_x^2 + B_y^2}$) as shown by Sneyd [77]. A similar situation arises, see (e), even if this inequality holds for either of the tubes. In (f), where $b_1 < 0$, both B_{1z} and B_{2z} are positive so there is no neutral point. However, the tubes attract each other since both $B_{1\theta}, B_{2\theta} > 0$ and B_H has an X-type neutral point at the origin. The point to emphasize in these figures, is that there is always at least one neutral point when two parallel tubes attract each other and have B_z's of opposite sign.

Both tubes when isolated are in equilibrium but the total field is not and will relax to an equilibrium which will depend on the respective twists and field strengths of the tubes. We study this relaxation numerically with our frictional code when a constant twist τ is applied to wrap the tubes around each other, as shown in figure 7.1.

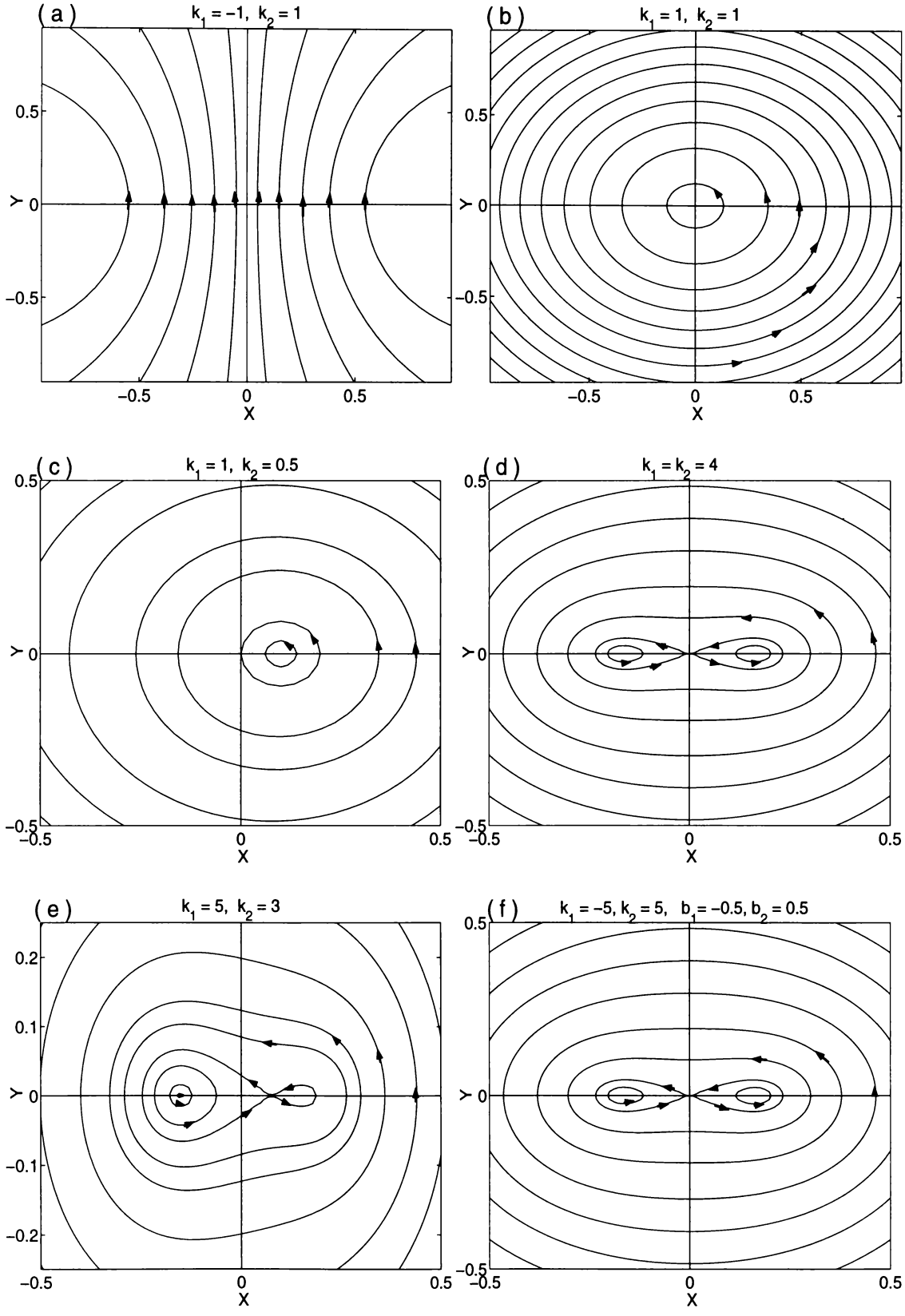

Figure 7.4: Field lines of different combinations of flux tubes.

In the rest of this chapter we study the tubes whose fields are equal in magnitude. The ratios k_1/k_2 and b_1/b_2 do affect the shape and growth of the resulting current sheet but the effect of the external twist τ is almost independent of these parameters. Interactions of tubes with $|\mathbf{B}_1| \neq |\mathbf{B}_2|$ are studied in the next chapter. In sections 7.2 - 7.4 we assume the plasma pressure to be zero; we choose $b_1 = b_2 = 0.5$ (except in section 7.3) and the domain of computation to be $[-1\,,\,1] \times [-1\,,\,1]$. As before, we use the term *current layer*, for a local peak in $|\mathbf{J}|$, until it is clearly diagnosed to be either a current sheet or a current concentration.

7.2 Repelling tubes

As explained earlier (refer figure 7.3) when $B_{1\theta}$ and $B_{2\theta}$ have opposite signs the tubes repel each other. This is equivalent to having $b_1 k_1$ and $b_2 k_2$ of opposite sign. Here we present results for the interaction of repelling parallel tubes and the effect of twist τ on these results.

7.2.1 $\tau = 0$

When $\tau = 0$, figure 7.5 shows results of the nonlinear interaction of tubes having $k_1 = -1$, $k_2 = 1$ in the left and $k_1 = -4$ and $k_2 = 4$ in the right column. The tubes are centered at $a_1 = a_2 = 0.3$ in both the cases. $|a_i k_i| < 1$ in the left and $|a_i k_i| > 1$ in the right column. We plot the initial current profiles in the second row and profiles at $t = 2$ in the third row. The outward movement of all the tubes continues till a pile-up of the current starts near the outer boundaries $x = \pm 1$ just before $t = 2$. This current layer is more pronounced in the left column. Relaxation of tubes having $k_1 = k_2$ but with the sign of b_1 (or b_2) changed gives similar results.

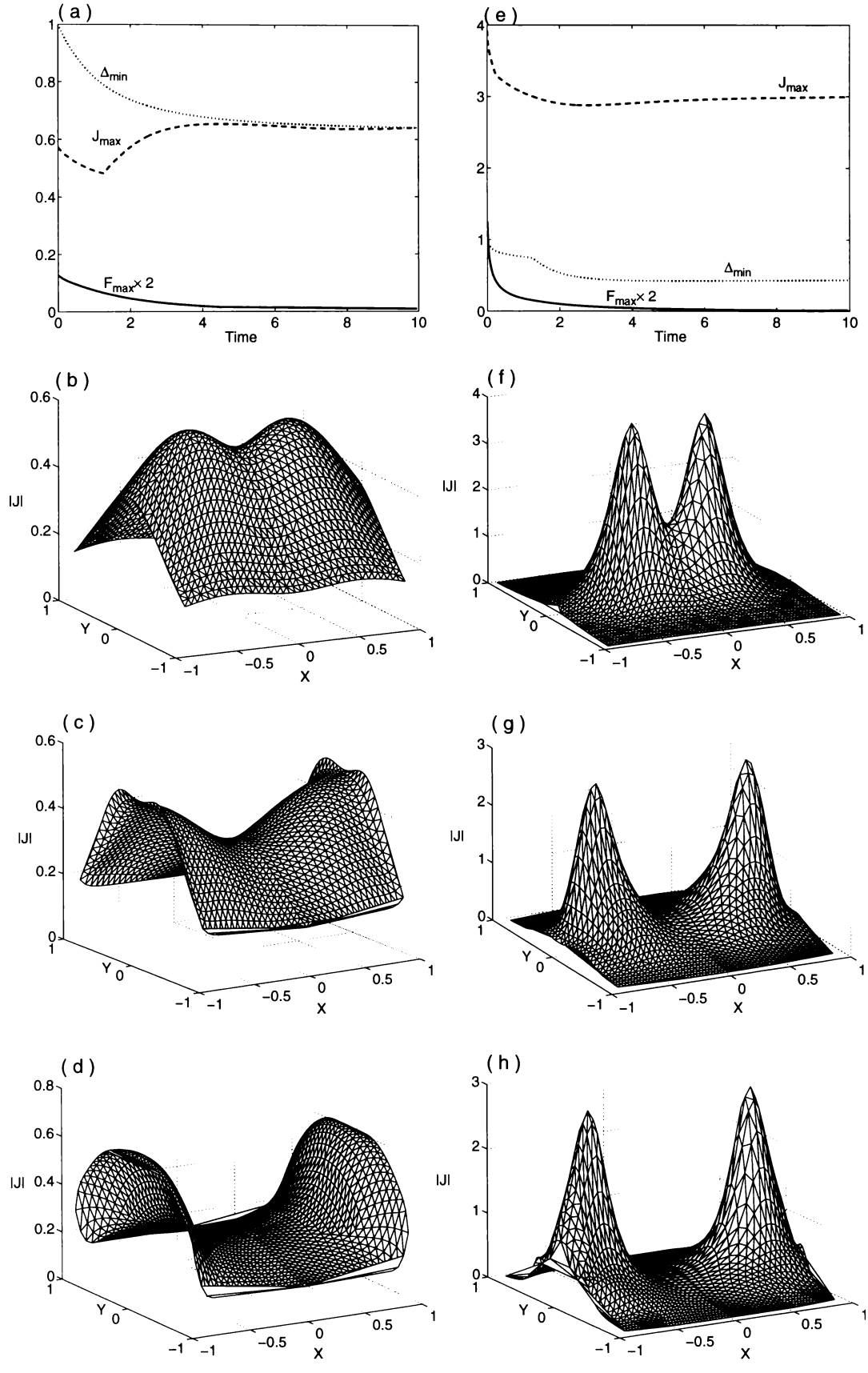

Figure 7.5: Relaxation of repelling tubes. $k_1 = -1$, $k_2 = 1$ in the left and $k_1 = -4$, $k_2 = 4$ in the right column. $b_i > 0$ and $\tau = 0$.

7.2.2 $|\tau| > 0$

One might expect that twisting the tubes together could overcome their natural repulsion, and to see if this is the case we perform numerical calculations with several values of τ. We use the configuration $k_1 = -4$, $k_2 = 4$, having initial current shown in 7.5(f). The effect of a twist $|\tau| = 4.0$ on the initial current is shown in the

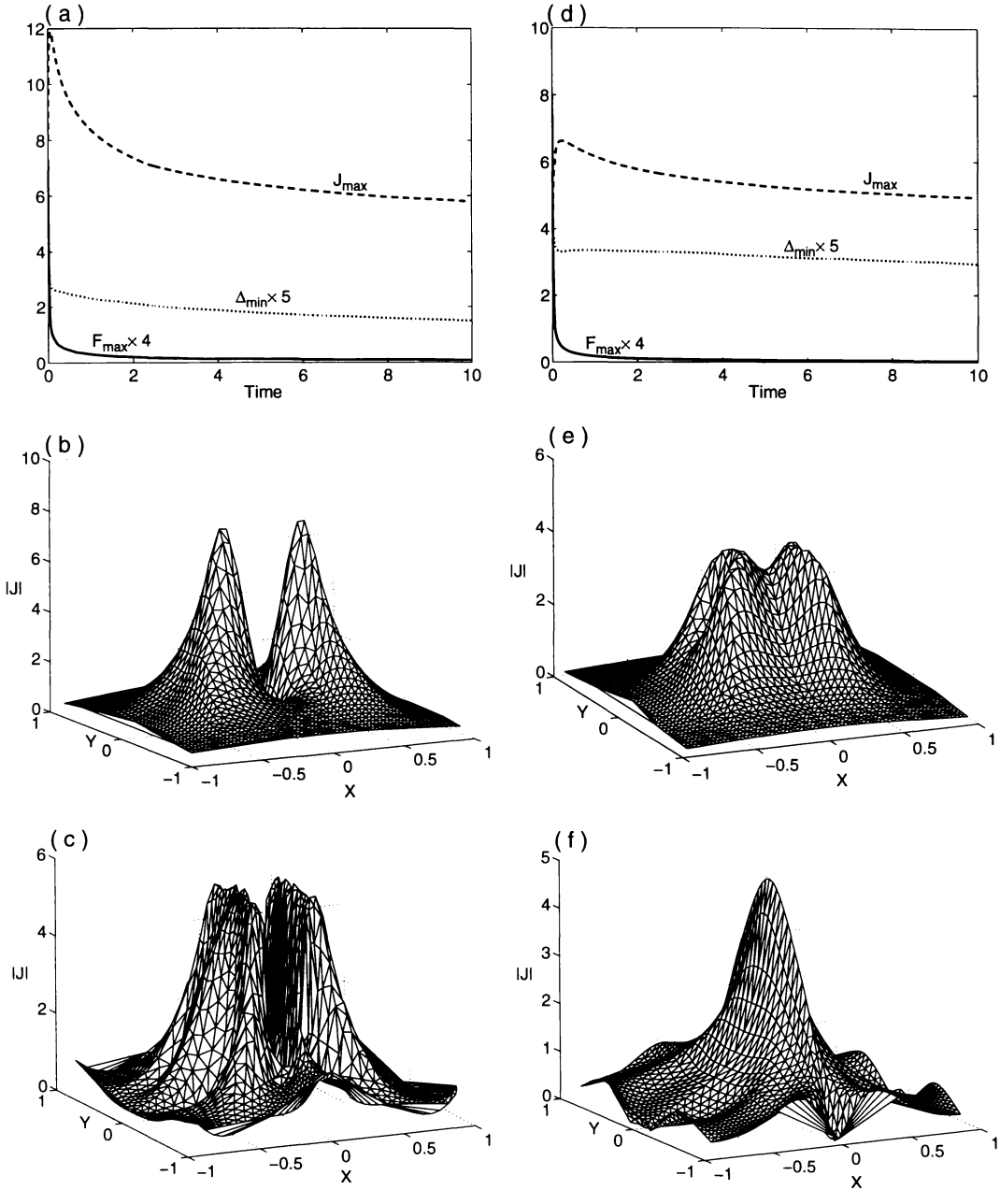

Figure 7.6: Effect of twist on tubes with initial current shown in figure 7.5(f). Twist applied is $\tau = 4$ in the left column and -4 in the right column.

second row of figure 7.6 and after relaxation in the third row. A positive twist $\tau = 4$ is applied in the left column and a negative twist $\tau = -4$ in the right column. The field is squeezed in both cases but quite different deformations of the field result from positive and negative twists. A positive twist seems to fragment the field into two separate layers while a negative twist pinches it resulting in a central layer shown in figure 7.6(f). In both cases $J_{\max}$ grows when the twist is applied (compare figures 7.5(a, e) and 7.6(a, d)) and then decays steadily as the field settles into an equilibrium state. Both the growth and decay are faster in the positive twist case. The outward movement seems restricted in both cases. Further simulations show that the current piles up in layers similar to those in the last row of figure 7.6 whose height and sharpness increase with $|\tau|$.

A positive twist squeezes the tubes together and results in two smaller layers getting closer and taller with increase in twist, but the growth of the layers is slow. A sharper layer results from applying a negative twist. Figures 7.7(a) and (b) show the current profile of the relaxed field with a twist $\tau = -10$ for two resolutions $N = 20$ and 30 in the left and right columns respectively. Compared to figure 7.6(f) the layer has grown and sharpened substantially. The negligible difference in the heights of the peaks, in plots (a) and (b) here, shows that the steepness in B_z, visible in figure 7.7(d), does not represent a true discontinuity. Multiple resolution runs show that the local maximum in $|\mathbf{J}|$ does not grow significantly with mesh refinement, confirming the layer to be a simple current concentration and not a sheet.

Figure 7.8 shows the deformed mesh corresponding to 7.7(a). The movement of nodes towards the origin from all directions indicates that plasma cannot escape from between the flux surfaces to let them approach each other. Hence oppositely directed fields, even if they exist, cannot approach each other to result in a current sheet.

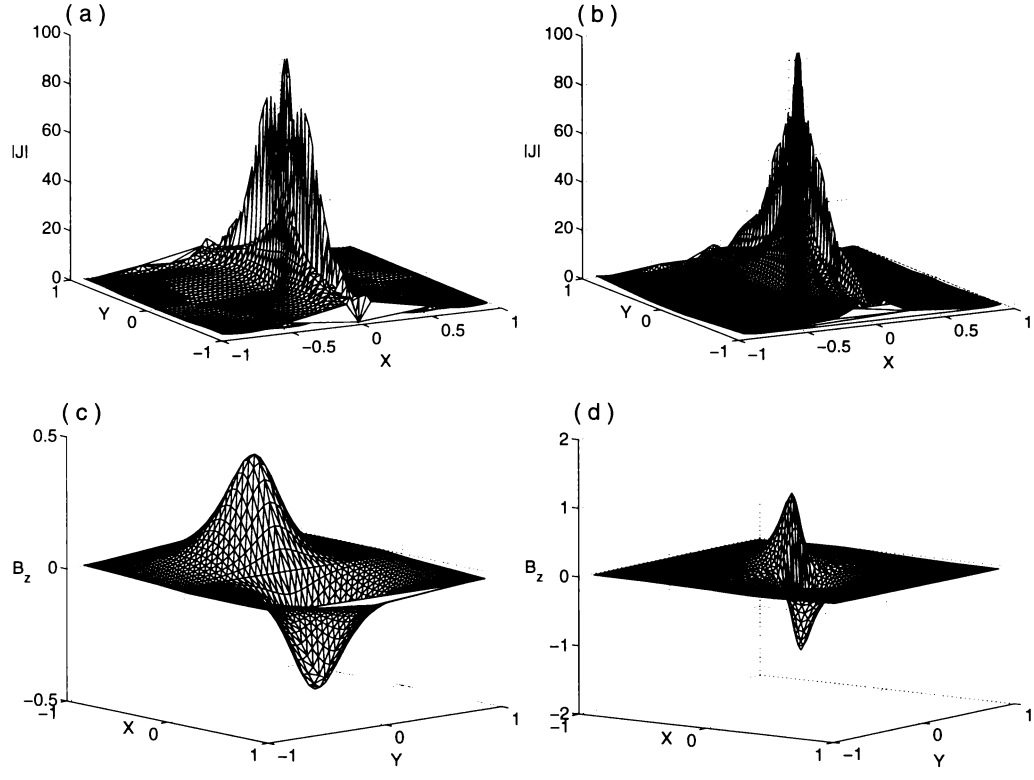

Figure 7.7: First row: Current of the flux tubes having $k_1 = -4$ and $k_2 = 4$ after relaxation with a twist $\tau = -10$. $N = 20$ in the left and 30 in the right. Second row: Initial and final B_z corresponding to (a).

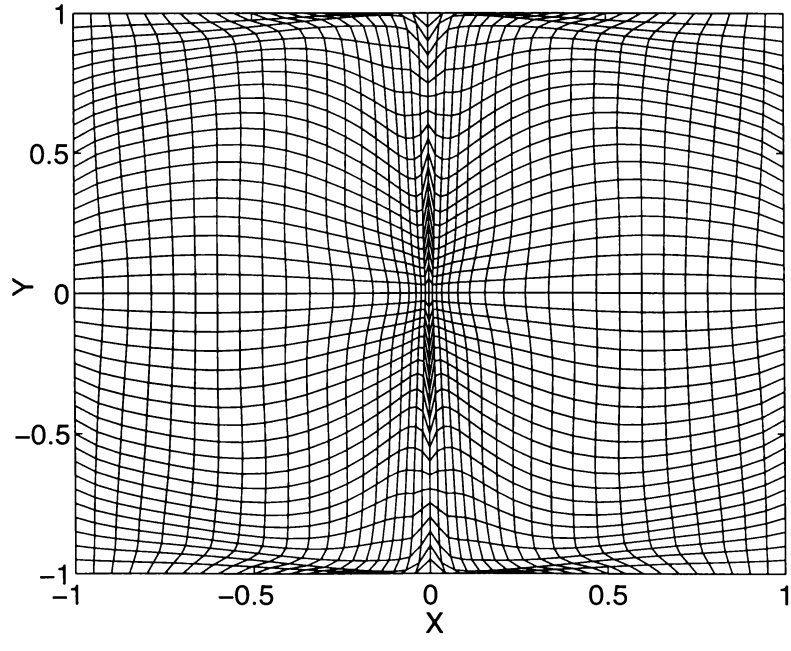

Figure 7.8: Grid corresponding to figure 7.7(a).

The effect of a negative twist on the growth of the current layer when tubes having $k_1 = -4$ and $k_2 = 4$ wrap around each other, is shown in figure 7.9. Increasing the magnitude of τ increases the squeezing and consequently the resulting $J_{\max}$.

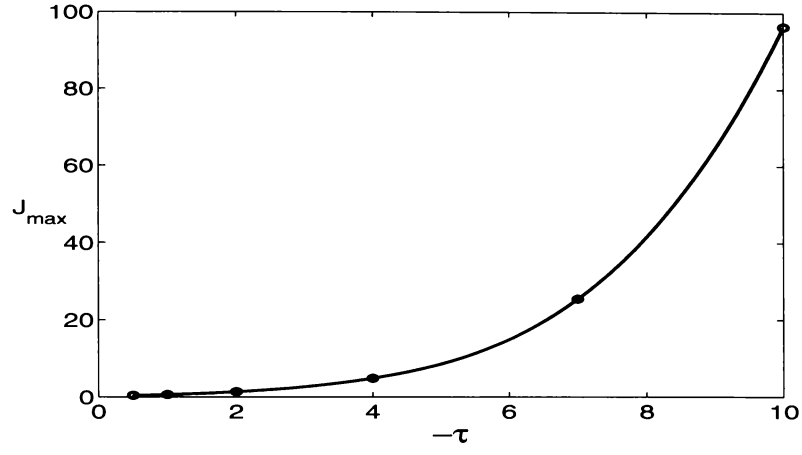

Figure 7.9: Growth of $J_{\max}$ versus -τ on a fixed grid, when repelling flux tubes having $k_1 = -4$ and $k_2 = 4$ are twisted together.

Hence twisting together repelling tubes halts their separation, constrains them to stay together and generates a current concentration at the origin but not a sheet. $J_{\max}$ in the concentration layer grows with twist and after some limiting value of τ the code fails due to lack of resolution.

7.3 Attracting tubes without a neutral point

We have seen in section 7.1 (see figure 7.4) that attracting tubes can give rise to no neutral point, an O-type neutral point or an X-type neutral point, depending on the signs and magnitudes of b_i and k_i. In this section we study nonlinear interaction of attracting tubes with no neutral point. The tubes have $B_{1z} = B_{2z} > 0$ and $B_{1\theta} = B_{2\theta} > 0$ so that $B_z = B_{1z} + B_{2z}$ is everywhere positive but the tubes attract each other because $B_{1\theta}B_{2\theta} > 0$ and the horizontal field vanishes at the origin. We assume zero plasma pressure throughout this section.

7.3.1 $\tau = 0$

Consider relaxation of such fields when no external twist is applied. Figure 7.10 shows the relaxation of tubes having $b_1 = -0.5$, $b_2 = 0.5$ with $k_1 = -1$, $k_2 = 1$ in

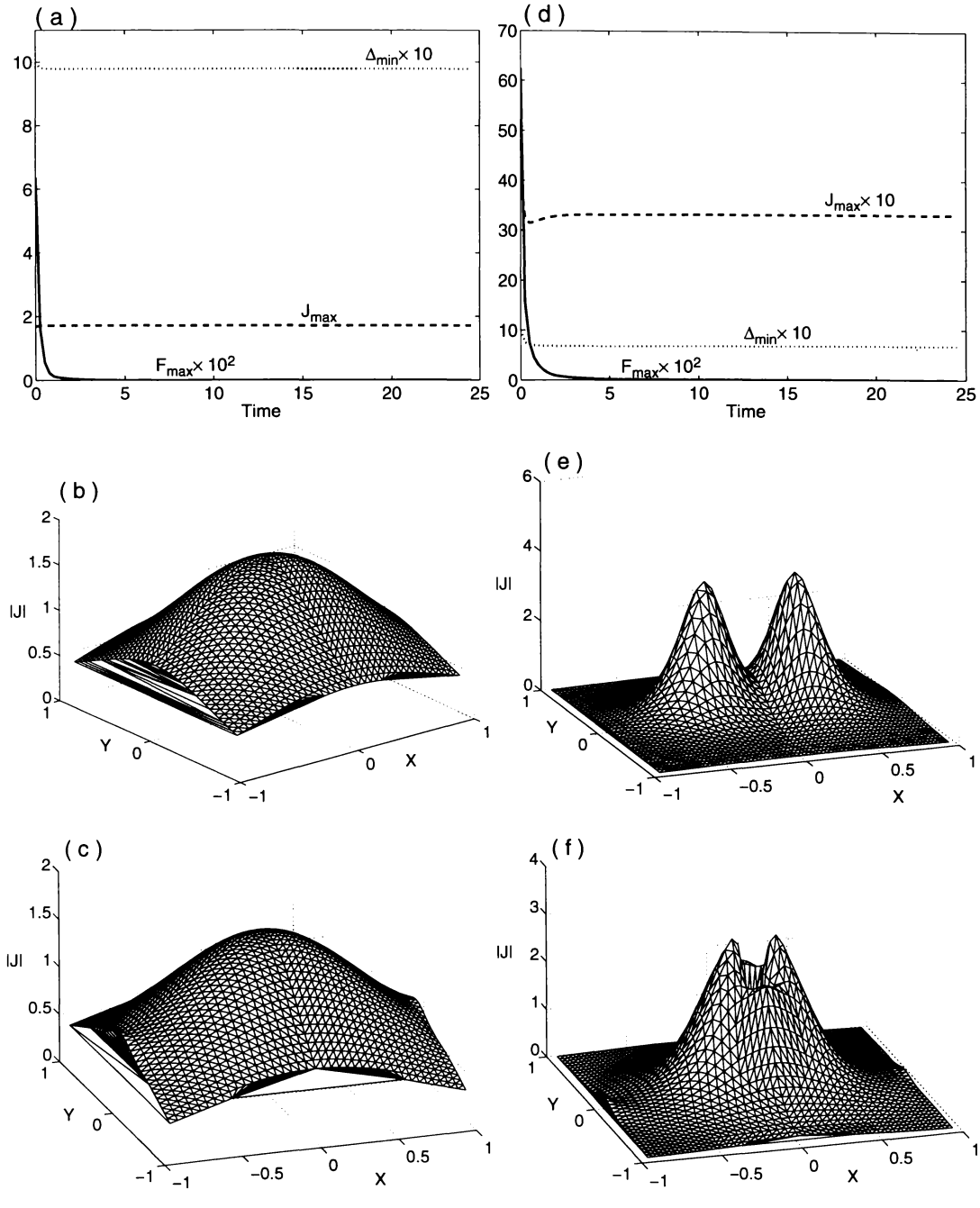

Figure 7.10: Relaxation of attracting tubes having no neutral point. $b_1 = -0.5$, $b_2 = 0.5$ with $k_1 = -1$, $k_2 = 1$ in the left and $k_1 = -4$, $k_2 = 4$ in the right. $a_1 = a_2 = 0.3$ and $\tau = 0$.

the left and $k_1 = -4$, $k_2 = 4$ in the right column. It is clear from figure 7.4 that the initial combined B_H fields of these tubes have an O-type and an X-type neutral point at the origin, respectively, but $B_z > 0$. In the second and third rows are current plots before and after relaxation respectively. Merging of the tubes is more noticeable in the right-hand plots. $J_{\max}$ has slightly increased from 1.684 to 1.71 in the left-hand field while it has decreased from 4.1 to 3.3 in the right-hand field.

7.3.2 $|\tau| > 0$

To see the effect of twist on the merging of tubes we twist together the tubes of the right column of figure 7.10, having $k_1 = -4$, $k_2 = 4$, with several values of τ. Figure 7.11 shows the relaxation with a twist $|\tau| = 4$. The left-hand column corresponds to $\tau = -4$ and the right to $\tau = 4$. The effect of twist on the initial current is shown in the second row. Deformation of the field by the positive twist, compare figure 7.10(e), is quite different than that of the negative twist. In the third row are current plots of the relaxed field. $J_{\max}$ has grown substantially with the positive twist.

To ascertain the nature of $J_{\max}$ growth with a positive twist we carried out simulations with a greater value of twist, $\tau = 10$ on two grids of differing resolutions. Results are plotted in figure 7.12. The left column here represents the simulation on a grid of size $N = 20$ and the right on a grid of size $N = 30$. No significant difference can be noticed in the current profiles. Hence twisting of attracting tubes having no neutral point results in current concentrations when the field relaxes to equilibrium but no current sheet is formed.

Variation of $J_{\max}$ with twist is shown in figure 7.13. As was the case with repelling tubes (see figure 7.9), the current growth is faster than linear. The $J_{\max}$ growth is higher for larger τ but relaxation to equilibrium is harder to achieve.

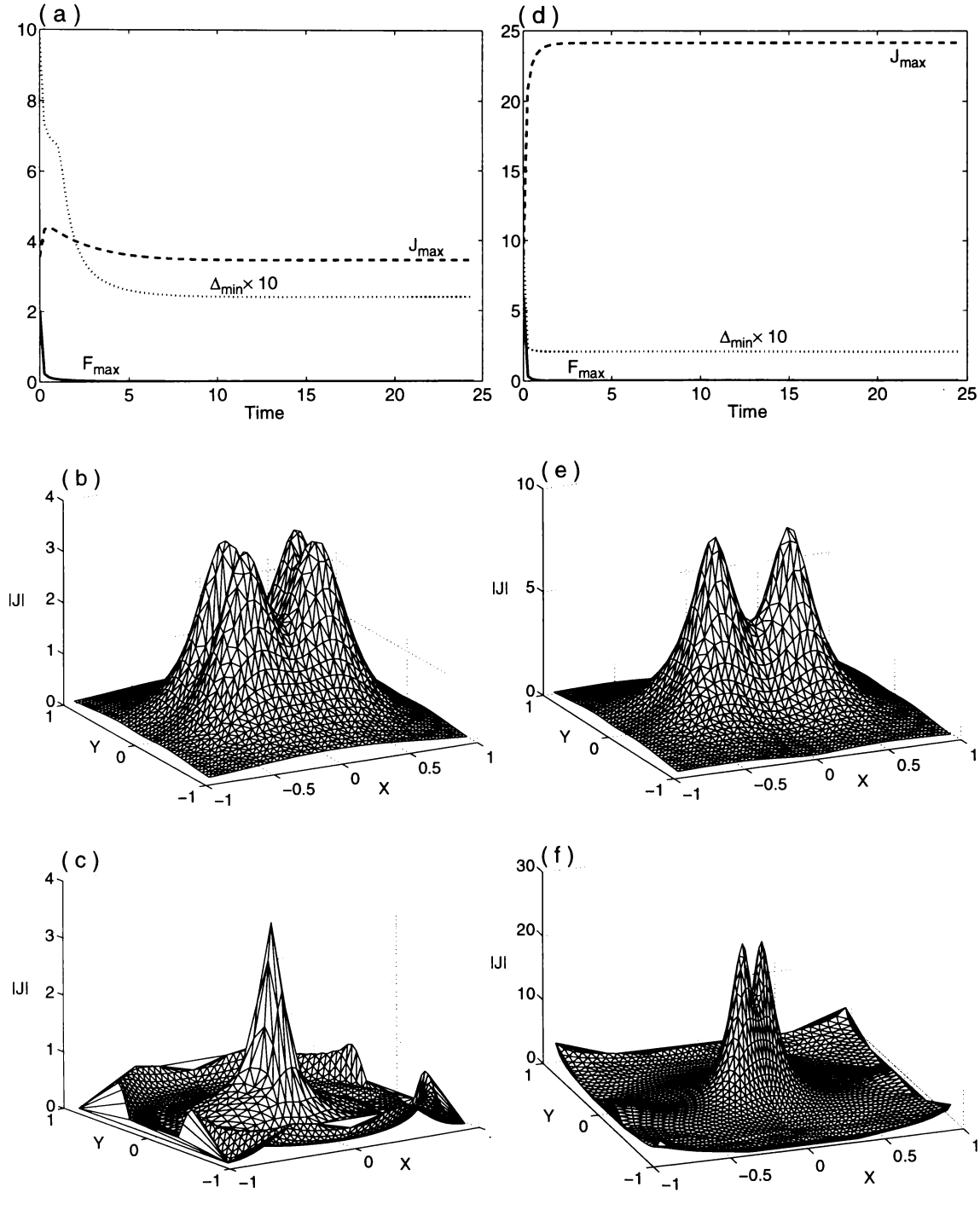

Figure 7.11: Twisting of attracting tubes having no neutral point. $b_1 = -0.5$, $b_2 = 0.5$, $k_1 = -4$, $k_2 = 4$, and $a_1 = a_2 = 0.3$. In the left column $\tau = -4$ and in the right column $\tau = 4$.

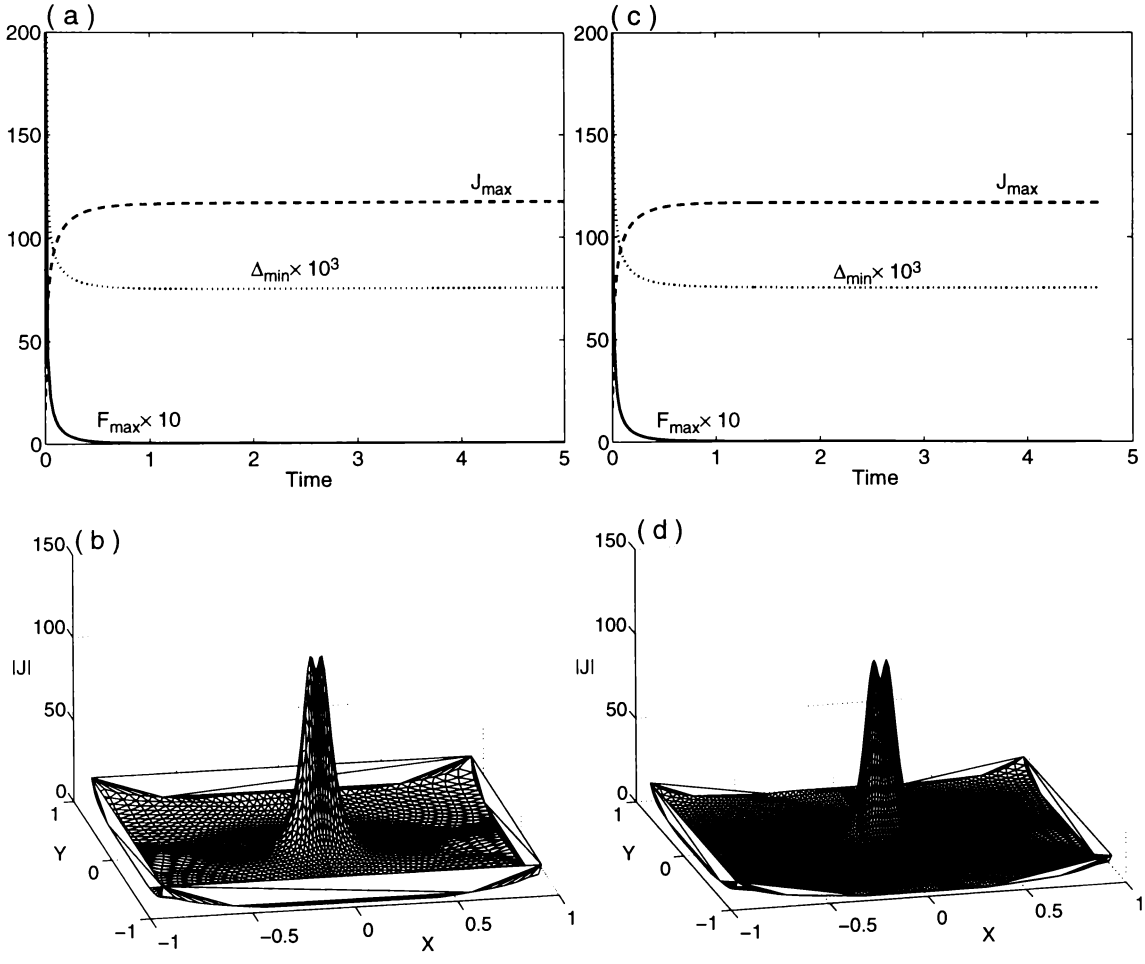

Figure 7.12: Tubes of figure 7.10 with $\tau = 10$. $N = 20$ in the left column and 30 in the right.

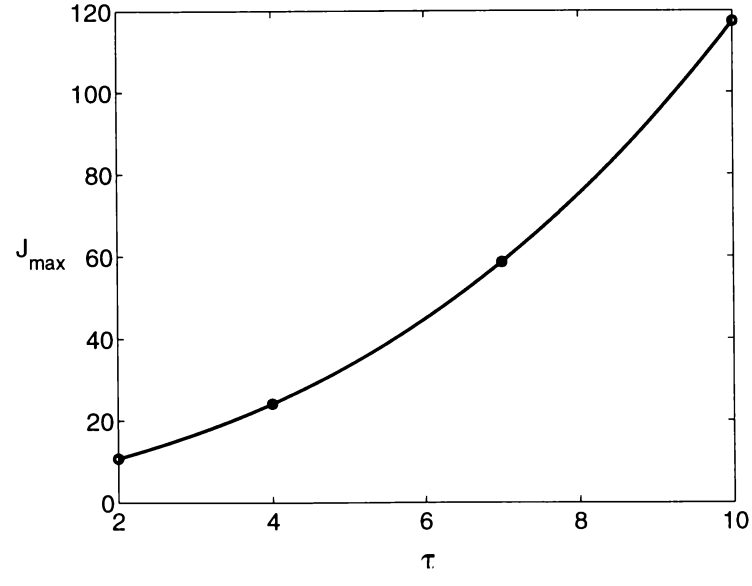

Figure 7.13: Growth of $J_{\max}$ with twist τ when attracting flux tubes without a null, having $k_1 = -4$ and $k_2 = 4$, are twisted together.

Another interesting case is attracting tubes having a uniform axial field. The horizontal component of the field vanishes at the origin while B_z is uniform throughout. When the flow is incompressible, separator reconnection sustained by a strong ribbon of current aligned to the axial field occurs in this case [49]. Our flow, however, is compressible and relaxation of such tubes gives results similar to the case of attracting tubes having $B_z > 0$, studied above. The tubes merge as shown in figure 7.10(d-f) but no current sheet is formed. The axial field piles up between the tubes and magnetic pressure restricts formation of a field singularity. For example, the tubes having a combined field

$$\mathbf{B} = \sum_{i=1}^{2} \Big(- \frac{k_i y b_i}{1 + r_i^2 k_i^2} \hat{\mathbf{x}} + \frac{k_i x_i b_i}{1 + r_i^2 k_i^2} \hat{\mathbf{y}} \Big) + 0.5 \hat{\mathbf{z}}, \tag{7.12}$$

with $a_i = 0.3$, $b_i = 0.5$ and $k_i = 4$, when twisted with $\tau = 5$, result in current similar to that plotted in figure 7.12(b). The resulting pilling up of B_z at the origin is shown in figure 7.14. $J_{\max}$ grows when B_z is weak but only current concentrations are formed whose magnitudes increase with twist.

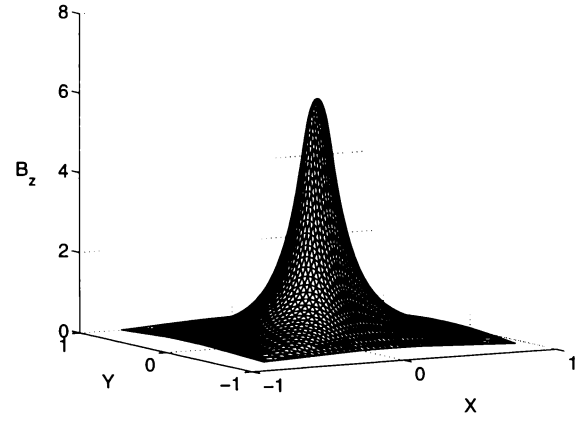

Figure 7.14: B_z of the relaxed field when attracting tubes with initial $B_z = 0.5$ are twisted with $\tau = 5$.

To sum up, the results of this chapter show that in the case of repelling tubes, the tubes move apart as the combined field relaxes to equilibrium and the outward motion can be restricted by twisting them together. In this case only current concentrations results from twisting. Similarly, in the absence of a neutral point, attracting tubes can give rise to current concentrations but not current sheets.

Chapter 8

Tube interactions: fields with neutral points

In this chapter we continue to study parallel Gold-Hoyle tubes but here the initial combined field contains zeros of $B_H = \sqrt{B_x^2 + B_y^2}$ and B_z. Equal tubes are dealt with in detail, to see the effect of grid resolution, twist and plasma pressure. In section 8.1 plasma pressure is assumed zero. The presence of plasma pressure is considered in section 8.2. Various combinations of tubes having $|\mathbf{B}_1| \neq |\mathbf{B}_2|$ are dealt with briefly in section 8.3.

8.1 Equal attracting tubes

In this section we study relaxation of equal parallel flux tubes having neutral points at the origin. Sneyd [77] has shown that twisting of such tubes together results in a current sheet when the combined field relaxes to an equilibrium state. We present here results of numerical simulations to validate this result. We find that current sheets form when the tubes approach each other and the two fields superpose. Twisting enhances the growth of the resulting current sheet in most cases.

8.1.1 $\tau = 0$

Figure 8.1 shows current sheet formation due to superposition of a set of tubes having $k_1 = k_2 = 1$ in the left, and $k_1 = k_2 = 4$ in the right column. As before $b_1 = b_2 = 0.5$ and $a_1 = a_2 = 0.3$ so that $a_i k_i < 1$ on the left and $a_i k_i > 1$ on the right. Thus the field on the left has an O-type neutral point, while that on the right has an X-type neutral point at the origin. The second row shows initial current profiles and the third shows profiles at $t = 0.125$. At this stage a current layer has started to form in the center and the growth is rapid in the right hand field. Afterwards the last row, at $t = 80$, shows that the current peak in the left is twice as high as that on the right. The development in both the cases is quite rapid and we see, in (a) and (e), that after $t \approx 5$ there is very little change in $J_{\max}$.

To show that an O-type neutral point does not necessarily result in higher current, we show in figure 8.2 the relaxation of a second set of tubes. In both cases $b_1 = b_2 = 0.5$ as before but $a_1 = a_2 = 0.6$. The left hand field has $k_1 = k_2 = 1.5$ ($a_i k_i = 0.9$) resulting in an O-type neutral point and on the right $k_1 = k_2 = 2.5$ ($a_i k_i = 1.5$) giving an X-type neutral point at the origin. It is noticeable from plots (a) and (e) that $J_{\max}$ growth starts early in the left hand field but the peak value attained is higher in the right hand field. Initial current profiles are plotted in the second row. The third row shows early stages of the corresponding current build up at the origin at $t = 0.2$, 0.375 in (c) and (g) respectively. The final shapes of the current layers are shown in the fourth row. The width of the layer is larger in (d) but the height is almost double in (h). The dent in the layer, in (h), is due to plotting routine limitations so the current in the plane $x = 0$ is plotted as a thick line overlying the surface plot.

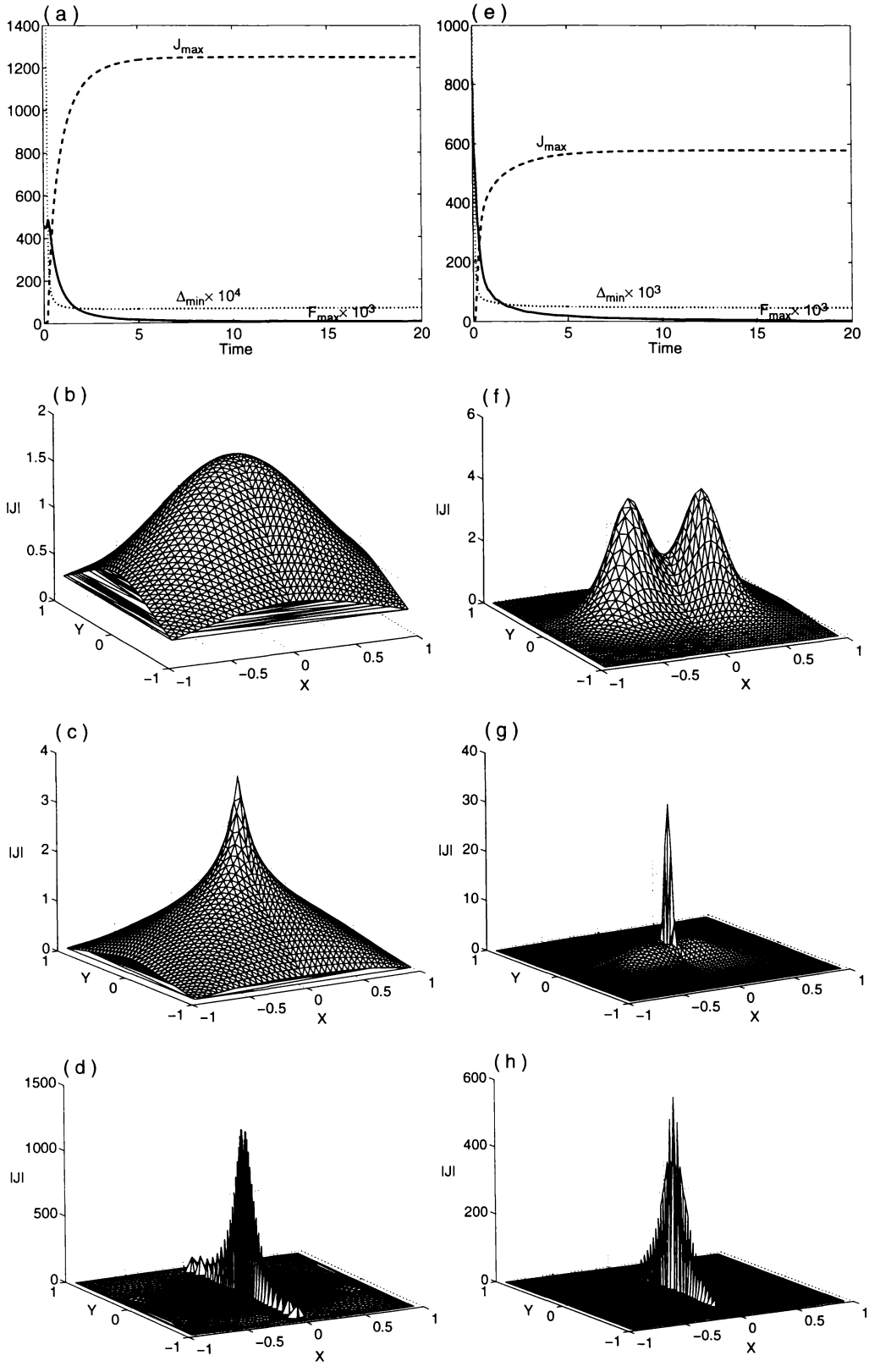

Figure 8.1: Relaxation of attracting tubes with O-type and X-type neutral points. The results in the left column are for tubes with an O-type neutral point, $a_i = 0.3$ and $k_i = 1.0$. Those in the right column have an X-type neutral point and $k_i = 4.0$.

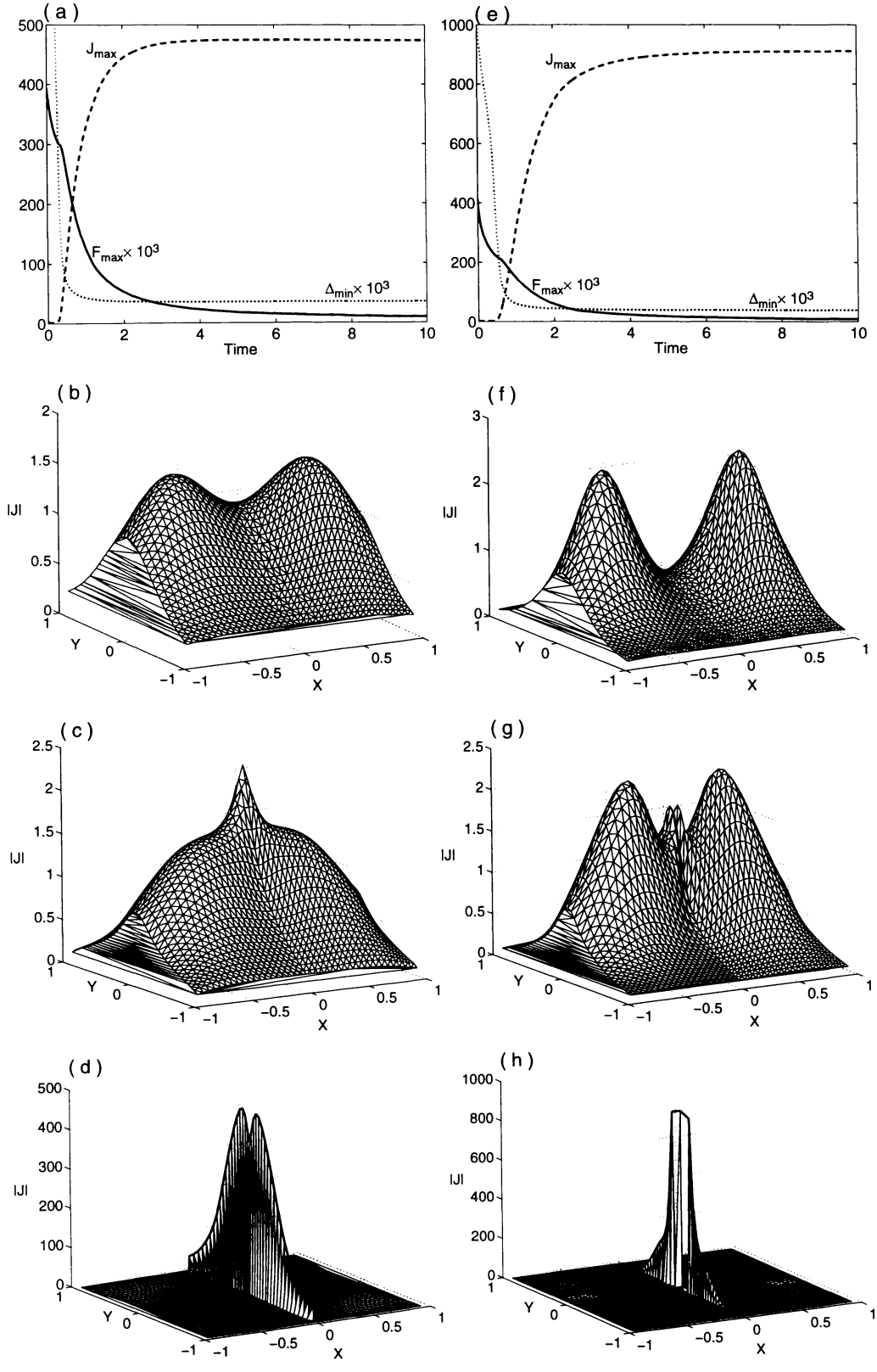

Figure 8.2: Relaxation of attracting tubes with O-type and X-type neutral points. The results in the left column are for tubes with an O-type neutral point, $a_i = 0.6$ and $k_i = 1.5$. Those in the right column have an X-type neutral point and $k_i = 2.5$.

The deformed grid corresponding to figure 8.2(d) is shown in figure 8.3. Since the field is frozen-in to the plasma displacement of a node represents plasma displacement at that location. It is clear that plasma is compressed from each side and is squashed away along the x-axis allowing the oppositely directed field surfaces to meet. Thus formation of a current sheet is feasible along the y-axis.

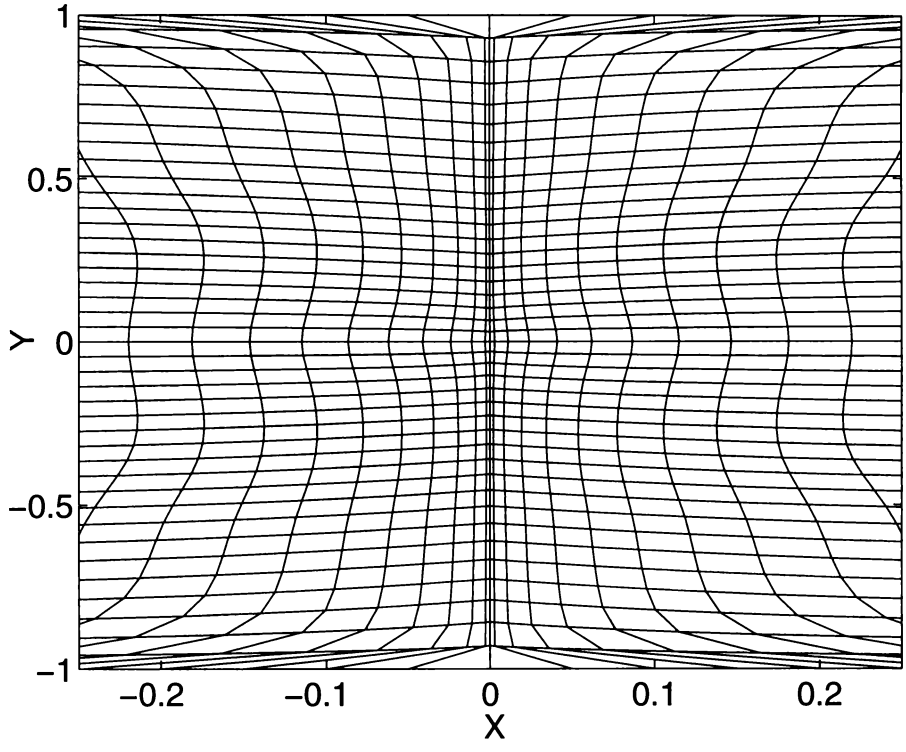

Figure 8.3: Grid corresponding to figure 8.2(d).

The axial fields B_z of all the four cases are plotted in figure 8.4. In the left column are the initial and in the right are the corresponding final B_z surfaces. In the first row are the tubes having $a_1 = a_2 = 0.3$ and $k_1 = k_2 = 1$. In the second row $a_1 = a_2 = 0.3$ and $k_1 = k_2 = 4$, in the third $a_1 = a_2 = 0.6$ and $k_1 = k_2 = 1.5$, and in the last row $a_1 = a_2 = 0.6$ and $k_1 = k_2 = 2.5$. The steep jumps in B_z here and the current layers in figure 8.2 resemble those in figure 7.7. To investigate their true nature we need to carry out relaxation calculations of the same fields with several grid resolutions.

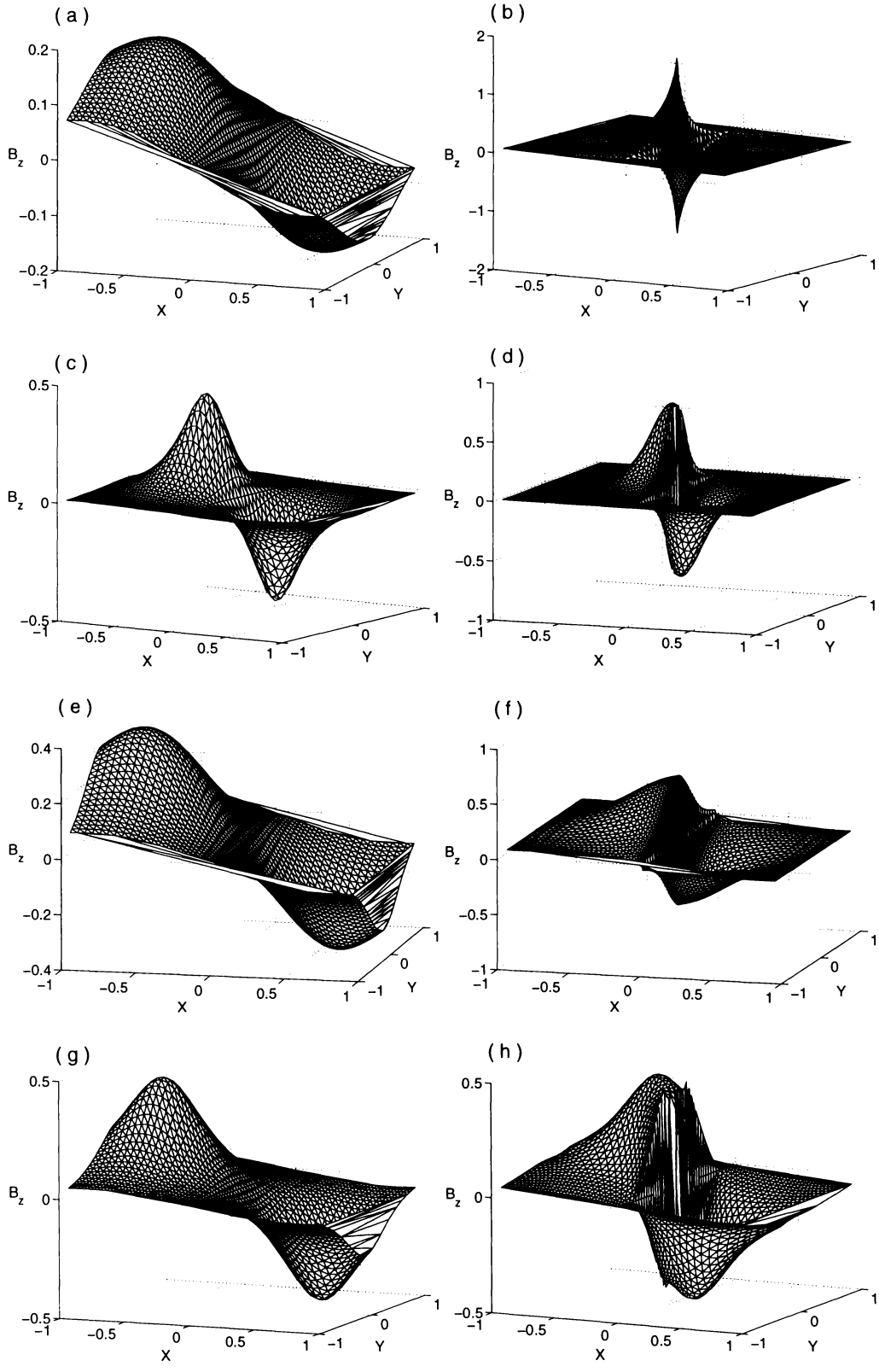

Figure 8.4: Initial and relaxed field B_z. Row 1: $a_i = 0.3$, $k_i = 1$; Row 2: $a_i = 0.3$, $k_i = 4$; Row 3: $a_i = 0.6$, $k_i = 1.5$ and Row 4: $a_i = 0.6$, $k_i = 2.5$.

The growth of J_{max} with mesh refinement is shown in figure 8.5 for all the four combinations discussed above. In all the cases the growth of J_{max} is very fast and represents a true current sheet. J_{max} growth in all these cases is faster than that of the current sheets resulting from the kink of the B_3 field (see figure 6.6).

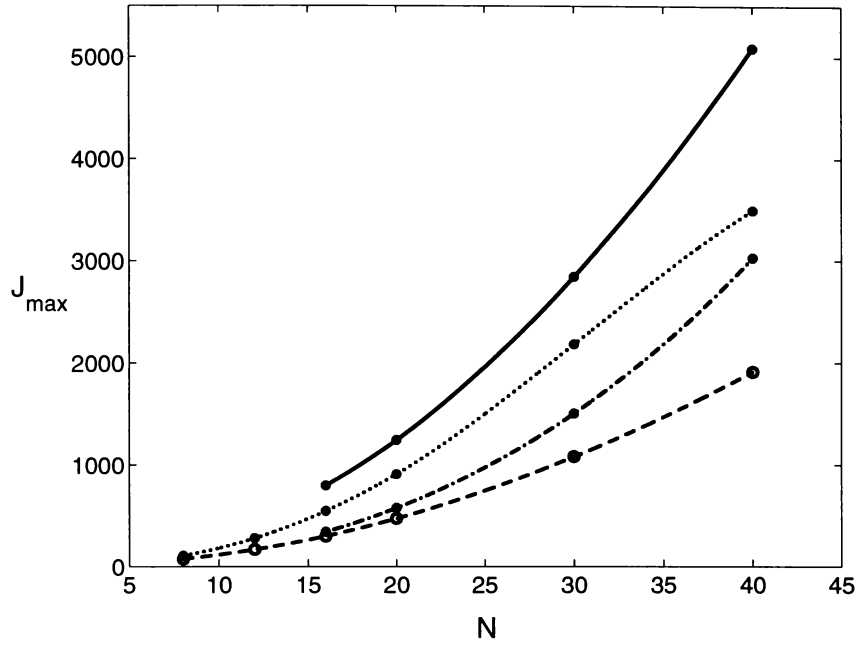

Figure 8.5: Graphs of J_{max} versus N. The solid line corresponds to the tubes with $k_i = 1$, $a_i = 0.3$; the dash-dotted line to the tubes with $k_i = 4$, $a_i = 0.3$; the dashed line to the tubes with $k_i = 1.5$, $a_i = 0.6$ and the dotted line to those with $k_i = 2.5$, $a_i = 0.6$.

Hence interaction of attracting parallel flux tubes having a neutral point results in an equilibrium containing a current sheet. The growth rate of the sheet depends on the field strengths of the respective tubes.

8.1.2 $|\tau| > 0$

We have seen earlier that twisting together of repelling tubes overcomes the repulsive force of the tubes and gives rise to current concentrations. Similarly relaxation of attracting tubes whose combined field has no neutral point results in current concentrations when twist is applied. In the case of attracting tubes having the

combined field with a neutral point however, a current sheet is formed when the field relaxes to equilibrium even in the absence of an external twist, so twisting them together may enhance the current growth.

An important difference between this case and those of sections 7.2 and 7.3 is that now our calculations show that positive and negative twists have the same effect. Hence we consider only positive twist. We present results of several calculations and show that while applying a constant twist enhances the current growth in most cases, sometimes the initial non-equilibrium field deforms so severely that following the relaxation to an equilibrium may not be feasible.

We consider the tubes centered at $a_1 = a_2 = 0.3$ having $k_1 = k_2 = 1$ and $k_1 = k_2 = 4$. Initial current surfaces of both fields are plotted in figures 8.1(b) and 8.1(f) respectively. With a twist $\tau = 2$, the initial phase of relaxation and build

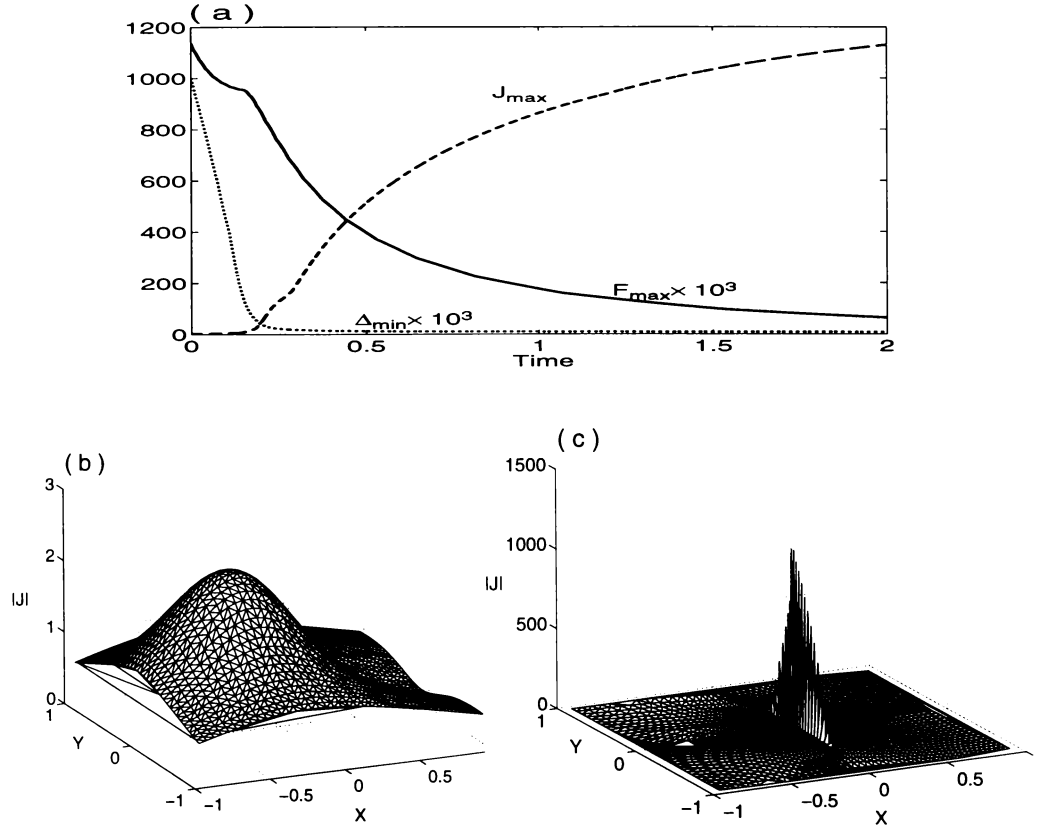

Figure 8.6: Twisting together tubes having $k_1 = k_2 = 1$ with $\tau = 2$.

up of current when $k_1 = k_2 = 1$ are shown in figure 8.6. A current plot just after the twist has been applied is shown in (b) and at $t = 2.0$ in (c). The twist seems to push the field towards the left-hand wall producing a depression on the right. It is clear that equilibrium is still not reached but the current sheet has grown substantially. The Jacobian has become very small ($\Delta_{min} = 0.00859$) and to achieve equilibrium severe time step reduction ($\zeta < 0.0001$) is required.

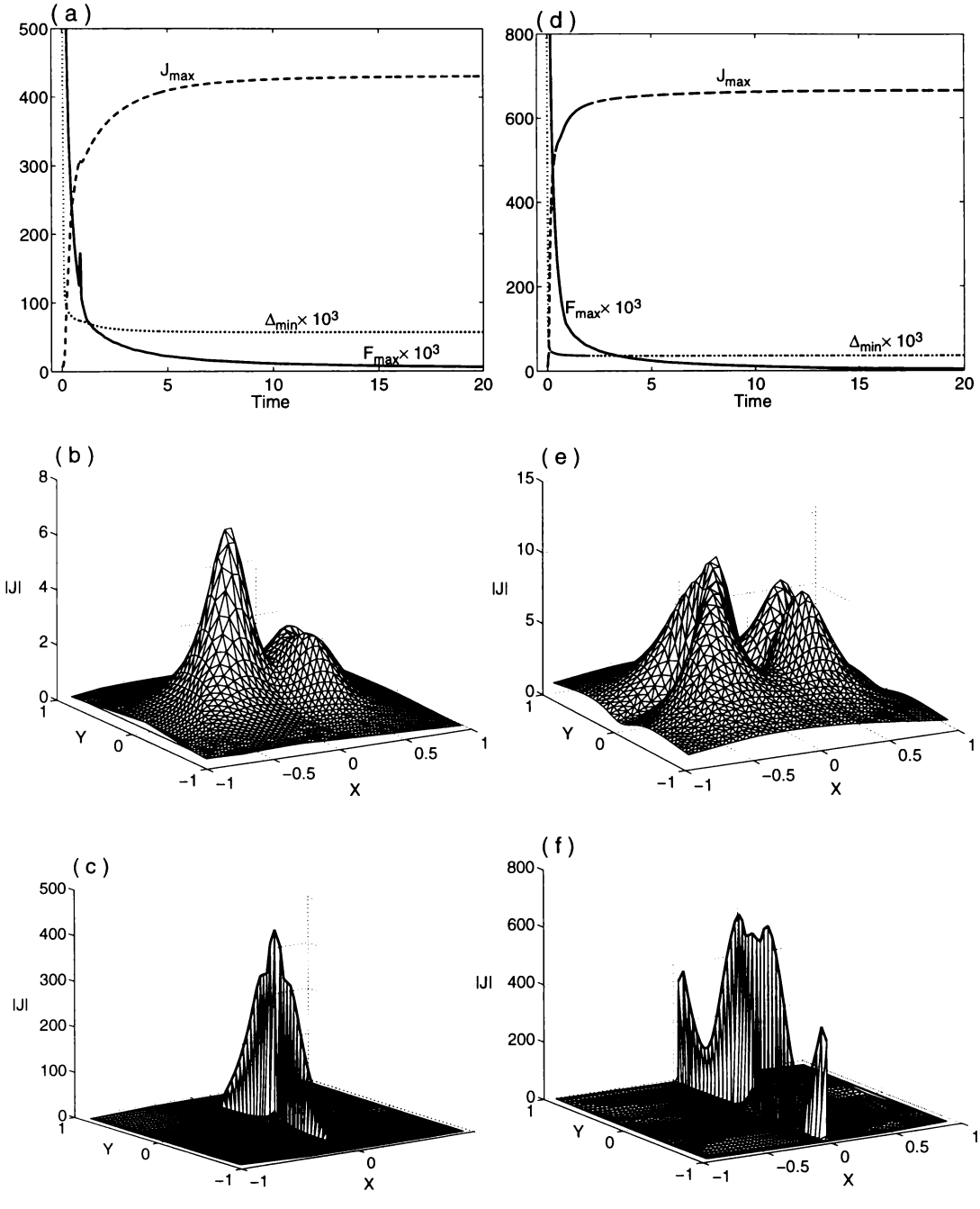

Figure 8.7: Twisting of tubes having $k_1 = k_2 = 4$ with a twist $\tau = 3$ in the left column and $\tau = 7$ in the right column.

The effect of twist on the tubes having $k_1 = k_2 = 4$ is shown in figure 8.7. The twist $\tau = 3$ in the left and $\tau = 7$ in the right column. Here, though the deformation is large with the bigger twist the field is not pushed just to one side (as in figure 8.6(b)) but pinched from both sides, and current sheet development and relaxation to equilibrium is still quite rapid. The bigger the value of the twist the stronger the resulting current sheet and the faster its growth. In figure 8.7(b) and (e) are surface plots of current just after the twist is applied and, (c) and (f) show current surfaces at $t = 12.5$ and 22 respectively.

To see that different combinations of tubes behave differently we plot in figure 8.8 $J_{\max}$ versus τ after relaxation to equilibrium, over a fixed grid, for three pairs of attracting tubes having combined fields with neutral points. The overall behavior is roughly the same but the twist range and $J_{\max}$ growth with τ is different in each case.

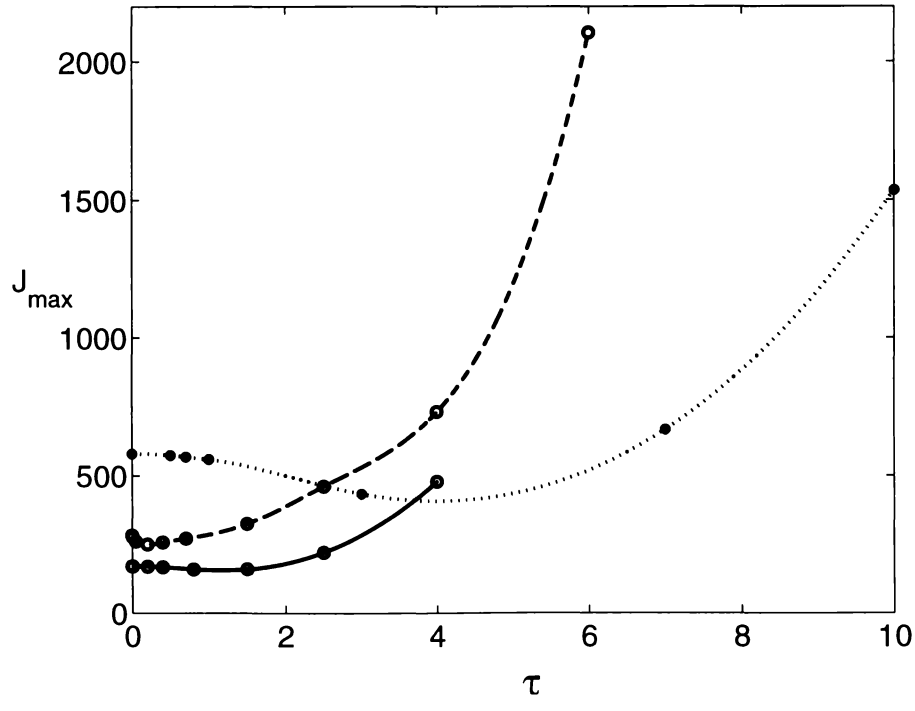

Figure 8.8: $J_{\max}$ variation with τ for tubes having $a_1 = a_2 = 0.6$ with $k_1 = k_2 = 1.5$ as a solid line and $k_1 = k_2 = 2.5$ as a dashed line when $N = 16$. The dotted line represents tubes having $a_1 = a_2 = 0.3$ and $k_1 = k_2 = 4$ when $N = 20$.

Hence twisting together (as shown in figure 7.1) attracting tubes, whose initial combined field has a neutral point, enhances the growth of the current sheet for twists greater than a certain threshold value τ_0 (say) which is different for each configuration. $J_{\max}$ in the sheet increases with $\tau > \tau_0$ and eventually the distortion becomes so high that simulation of the relaxation is not feasible with a reasonable time step.

8.2 The twist and plasma pressure competition

In all the preceding calculations, in this chapter, plasma pressure was neglected but in order to model the solar corona more realistically, we have to include it. Plasma pressure has no tendency to create a current sheet when other conditions are unfavorable. Current sheets may be formed when magnetic flux surfaces, with differently oriented $\mathbf{B}$, are pressed together. As the plasma between the surfaces is compressed pressure will increase, and tend to prevent the surfaces from approaching each other. Thus plasma pressure can be expected to make current sheet formation more difficult. On the other hand, all our preceding calculations show that twisting of tubes together increases $J_{\max}$. Indeed we find that twisting together attracting tubes, whose combined field has a null, overcomes the opposing effect of plasma pressure and current sheets, in the form of circular arcs and line currents, are formed. We consider attracting, parallel, Gold-Hoyle tubes such as were studied in the preceding section. Our results show the opposition of plasma pressure to the formation of a current sheet and the overcoming of this opposition by the twist τ. We give numerical results only for tubes having $a_1 = a_2 = 0.6$, $b_1 = b_2 = 0.5$ and $k_1 = k_2 = 1.5$ since other tubes behave similarly. We have already found that these tubes do give rise to a current sheet when $\beta = 0$ (see figures 8.2(a)-(d)).

8.2.1 $\tau = 0$

With $\tau = 0$, relaxation of these tubes with a finite plasma pressure is shown in figure 8.9. In the left column $\beta = 0.01$ and in the right $\beta = 0.02$. In both cases the

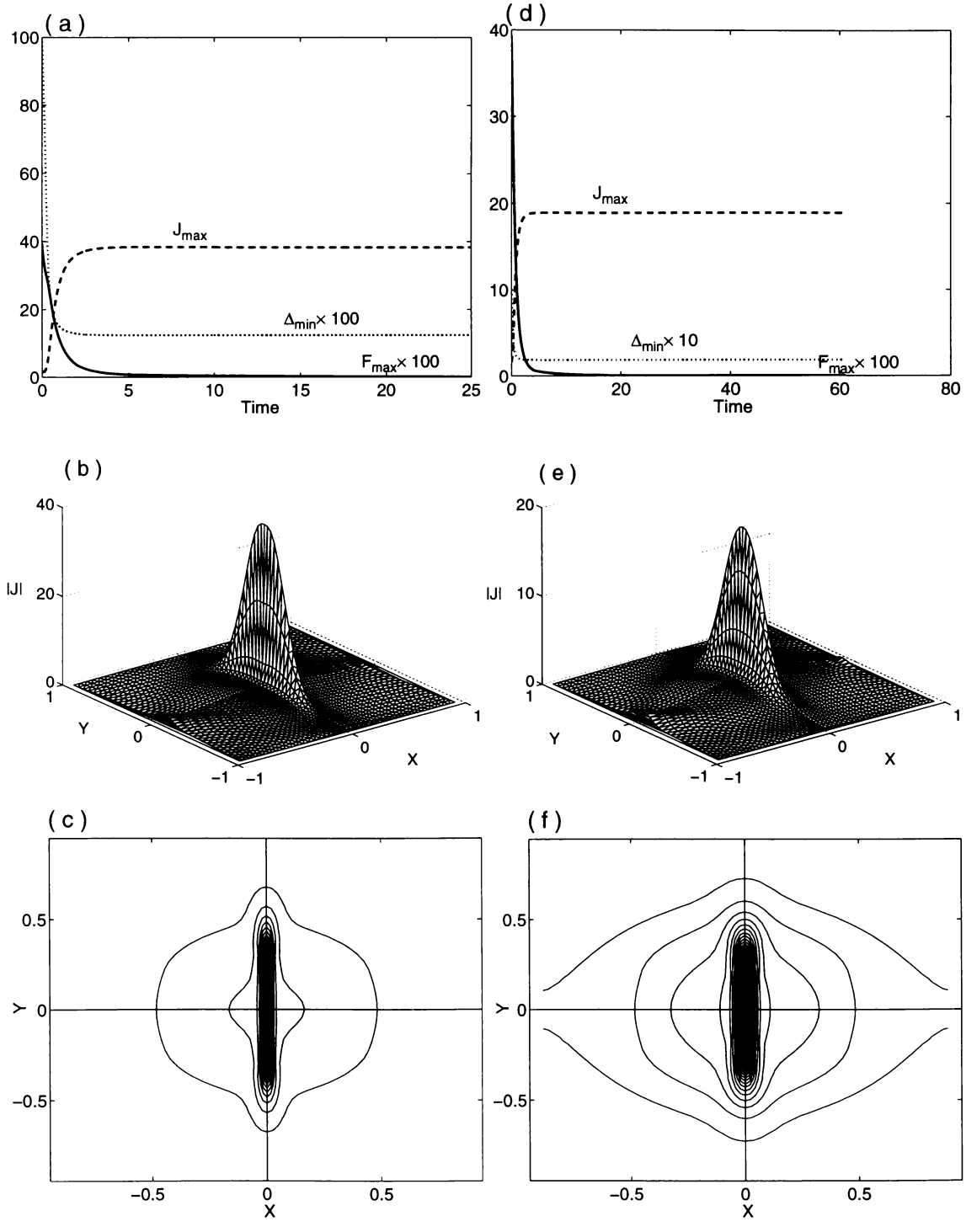

Figure 8.9: Relaxation of tubes having $k_i = 1.5$, $a_i = 0.6$ and $b_i = 0.5$ in the presence of plasma pressure. $\beta = 0.01$ in the left column and 0.02 in the right.

current growth and relaxation is rapid. Due to the smooth nature of the field we can take very large time steps, $\zeta = 20$, compared to those in the preceding cases. Surface plots of $|\mathbf{J}|$ in the relaxed state are given in the second row and the corresponding contour plots in the third row. A region of high plasma pressure, represented by the density plots of figure 8.10, on the y-axis prevents formation of a current sheet. The resulting current layer in both the cases is thick and its peak highly reduced, compare with figure 8.2(d). Doubling β has almost doubled the thickness and halved the height of the layer.

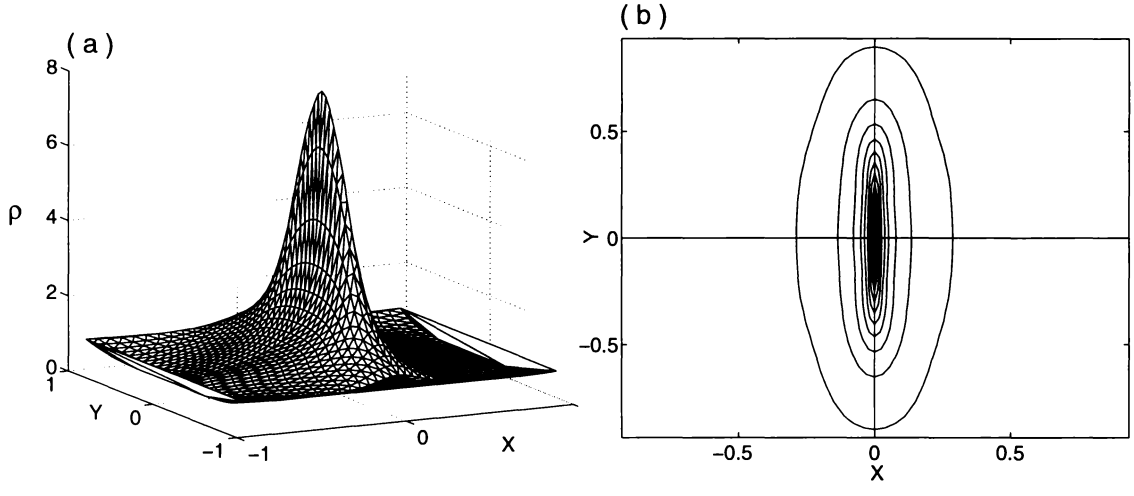

Figure 8.10: Density corresponding to figure 8.9(b)-(c).

Figure 8.11 shows the deformed grid corresponding to figure 8.9(b)-(c). Movement of the nodes from all sides towards the origin shows that there is no way for the plasma to be squeezed out and allow oppositely directed field surfaces to meet. Hence current sheet formation does not seems feasible. Relaxation with several grid resolutions gives the same $J_{\max}$, confirming the absence of a current sheet. Hence the current layer in figure 8.9 represents a concentration and not a sheet.

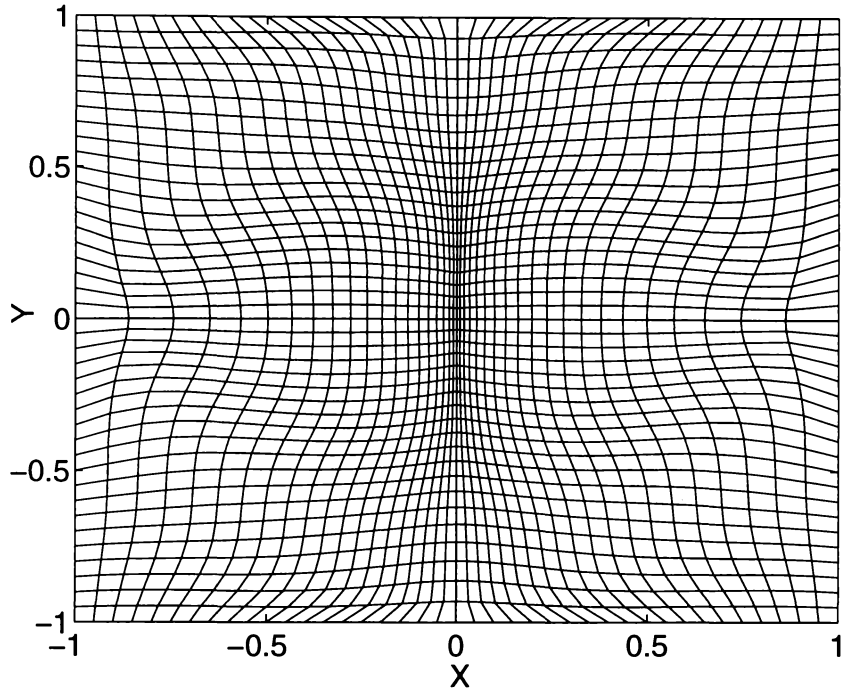

Figure 8.11: Grid corresponding to figure 8.9(b)-(c).

8.2.2 $|\tau| > 0$

With $|\tau| > 0$ the picture changes completely. Twisting the same tubes results in twisting the field in such a way that current layers in the form of circular arcs are formed near the axis of one tube and a current spike near the axis of the other as the field relaxes to equilibrium. Figure 8.12 shows relaxation of these tubes when a twist $\tau = 1$ is applied. The spikes in the surface plots of current are artifacts of the plotting routine. The corresponding contour plots show a smooth current layer in the form of a circular arc at $x = 0.6$ and a small spike at $x \approx -0.6$. As was the case in the preceding section, a negative twist results in the same current profile but just reversed orientation. Twisting the tubes with larger values of τ results in stronger currents and requires smaller time steps.

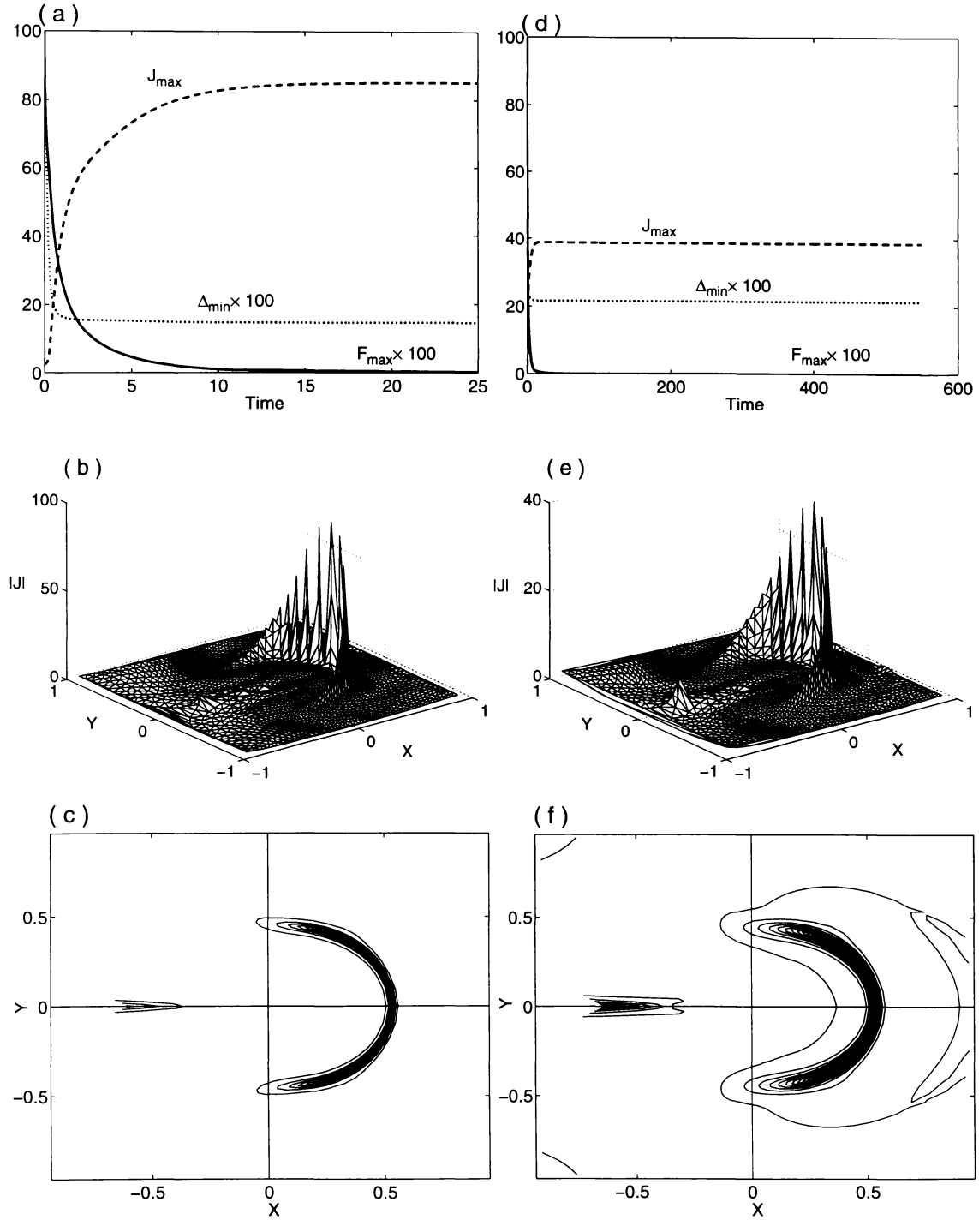

Figure 8.12: Tubes of figure 8.9 when $\tau = 1$.

Figure 8.13 shows the deformed grid corresponding to figure 8.12(b)-(c). Node displacements show that plasma motion outwards along the circular layer may allow oppositely directed field surfaces to meet and form a current sheet. Further simulations on multiple grids show that the circular layer of current is indeed a current

sheet located near the axis of one tube while the spike of current is a line current located near the axis of the second tube.

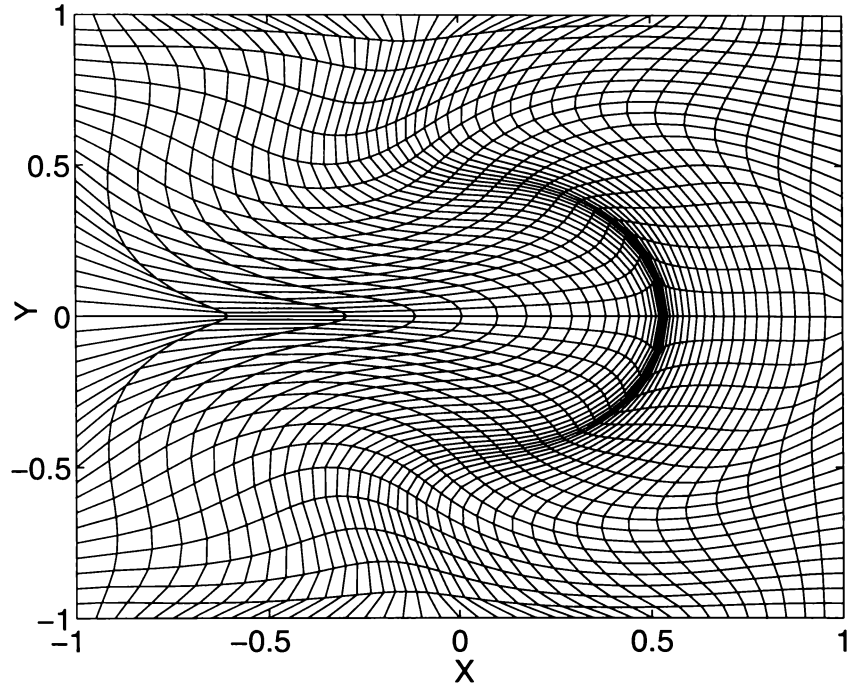

Figure 8.13: Grid corresponding to 8.12(c).

Figure 8.14 shows graphs of $J_{\max}$ versus τ when $N = 20$, a cubic spline has been used to interpolate the data points. A comparison of this figure with 8.8 (solid line)

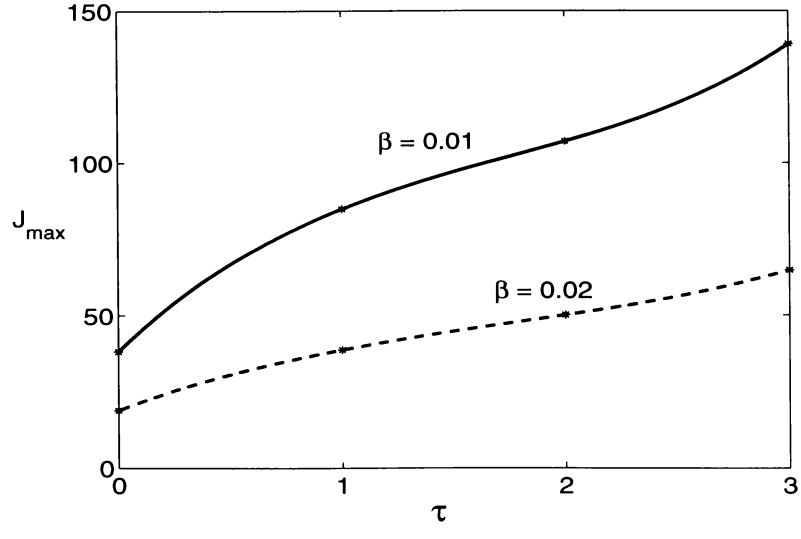

Figure 8.14: $J_{\max}$ growth with τ for tubes of figure 8.9.

shows that while $J_{\max}$ still grows quickly with τ the peak value of $J_{\max}$ is greatly reduced by the plasma pressure.

Figure 8.15(a) shows plots of local $J_{\max}$ versus N in the circular sheet. A logarithmic scale is used for the N-axis since then the graphs are remarkably close to straight lines, indicating that $J_{\max} \propto \log(N)$. The rate of current growth increases with τ. Figure 8.15(b) shows corresponding curves for the line current. Here the current growth is more irregular.

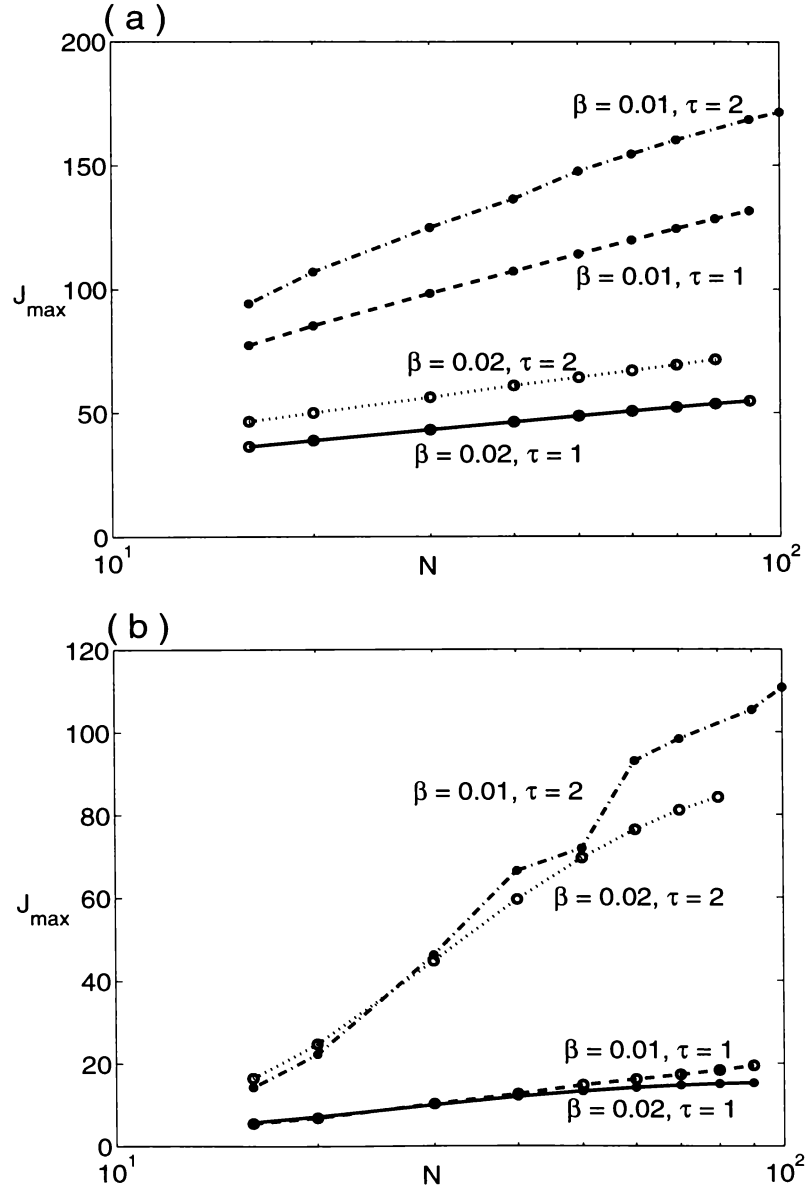

Figure 8.15: $J_{\max}$ growth with N for the sheet (a), and for the line current (b). The tubes are same as in figure 8.9.

For much larger β the sheet becomes highly diffused and with larger twists a secondary line current appears near the first. Figure 8.16 shows plots of $J_{\max}$ in the line currents against N for $\beta = 0.2$. Here also a logarithmic scale is used along the N-axis. When $\tau = 1$, $J_{\max}$ growth is rapid in the line current while for $\tau = 2$ the secondary current grows much faster.

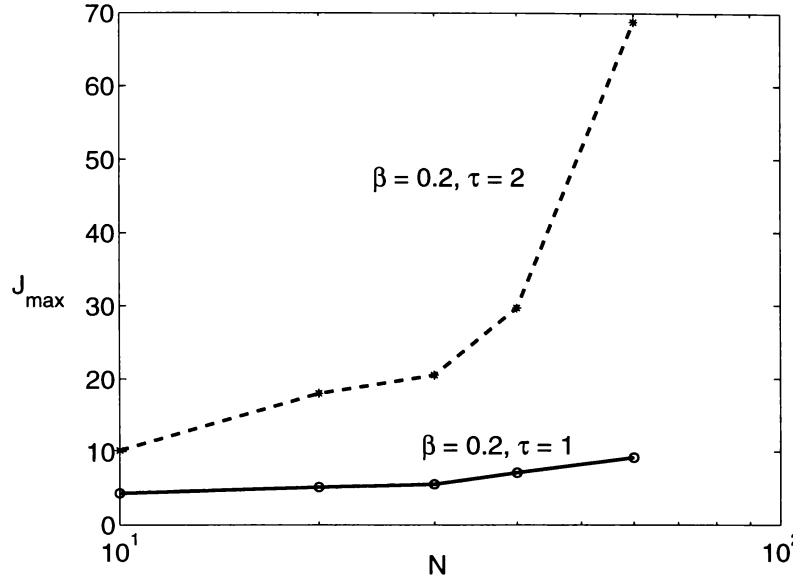

Figure 8.16: $J_{\max}$ in the line current versus N with large β for the tubes of figure 8.9.

This shows that when the tubes attract each other and the combined field has a neutral point, twisting them together overcomes the plasma pressure opposition and gives rise to a current sheet near the axis of one tube and a line current near the axis of the other. In the resulting current sheets $J_{\max}$ grows almost logarithmically with mesh refinement. These sheets are circular arcs similar to those resulting from a kink. In the line currents, on the other hand, $J_{\max}$ grows much faster with N than in the sheets; also it grows faster with τ.

Thus interaction of equal flux tubes, with B_θ's of similar sign but B_z's of opposite sign, produce a current sheet at the origin when $\beta = 0$. The growth rate of the sheet can be enhanced by twisting the tubes together. With $\tau = 0$, plasma pressure prevents current sheet formation but a nonzero twist overcome this tendency

giving rise to a curved sheet and a line current. In the sheet $J_{\max}$ grows almost logarithmically with N while in the line current $J_{\max}$ grows with N much faster for larger τ values.

8.3 Unequal parallel tubes

In this section we give a brief account of tube interactions when $|\mathbf{B}_1| \neq |\mathbf{B}_2|$. The relative magnitudes of repelling tubes and attracting tubes, whose combined field does not contain a null, have little effect on the shape of the relaxed field. Interesting shapes of current sheets result when attracting tubes of differing magnitudes, having a combined field with a neutral point, interact. In this case we have seen earlier (ref. figure 7.4(c), (e)) that the neutral point moves away from the origin. During relaxation a current sheet develops at the location of the neutral point whose shape is highly deformed compared to those studied in the preceding sections. Another interesting situation arises when the combined field of two parallel attracting tubes has a zero of B_z and a zero of $B_x^2 + B_y^2 = B_H^2$ say at different points. In this case $|\mathbf{B}| = 0$ nowhere but a current sheet forms between the two zeros.

We present here numerical simulations for a few pairs of tubes whose combined field has a null not falling on the origin or whose zeros of B_z and B_H do not coincide. In all cases $a_1 = a_2 = 0.3$. We do not apply any twist or plasma pressure here since their effect is similar to that observed in the preceding sections. Due to very small times steps required with a fine mesh, we use a coarse mesh (25×25) in these calculations and hence the results presented here give only a flavor of the actual phenomena.

8.3.1 Tubes having $b_1 = b_2$ and $|k_1| \neq |k_2|$

Attracting parallel tubes with unequal twists k_i, and whose combined field has a neutral point, interact to result in a variety of current sheets. The shape depends on the magnitudes of twists k_1 and k_2. Unequal twists result in $B_{1\theta} \neq B_{2\theta}$ and $B_{1z} \neq B_{2z}$. There is a neutral point, away from the origin, when $B_{1\theta}B_{2\theta} > 0$ and B_{1z}, B_{2z} have opposite signs. A few example interactions of such tubes are given below. In all the cases $b_1 = b_2 = 0.5$ and so B_{1z} and B_{2z} have opposite signs.

Figure 8.17 shows the initial stages of current sheet development resulting from a displaced O-type neutral point in the first row and a displaced X-type neutral point

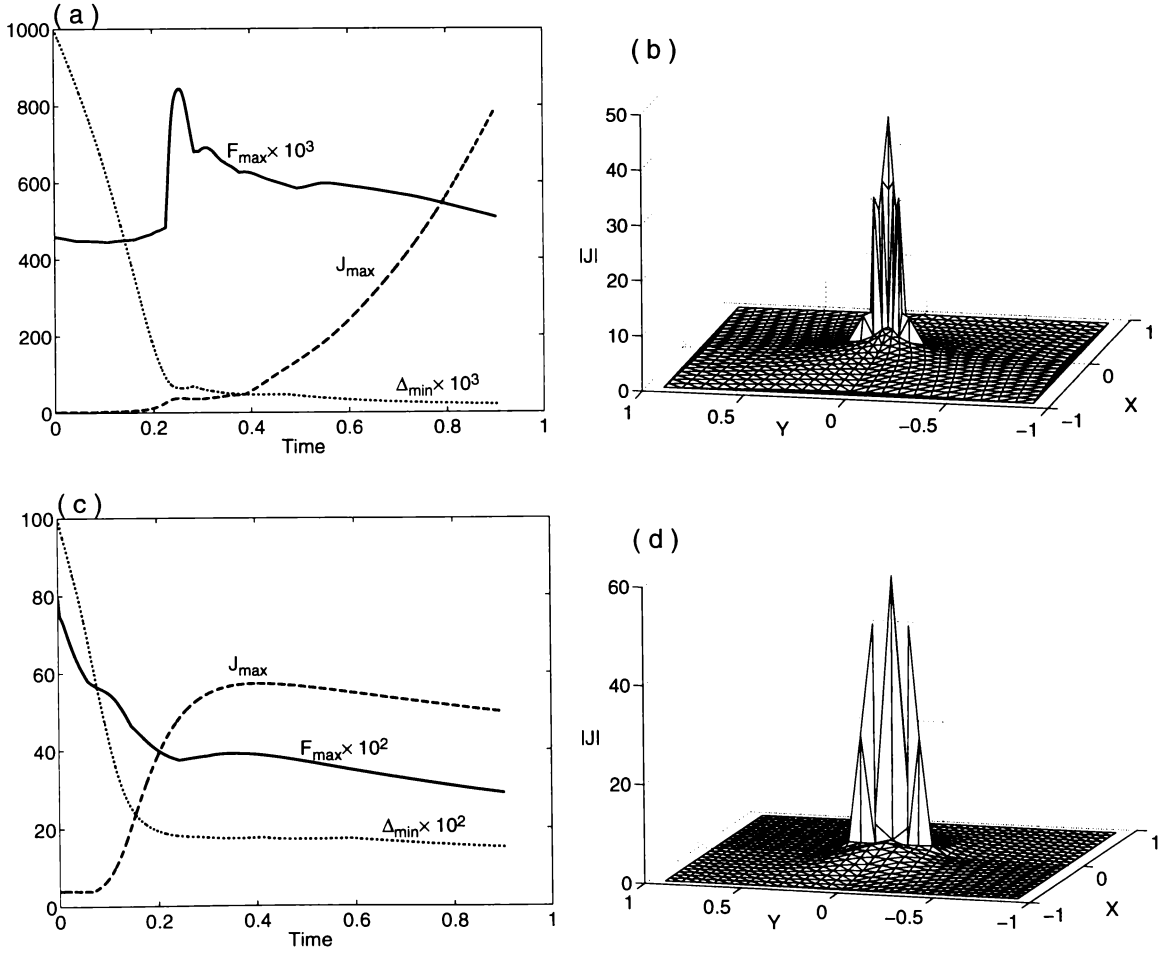

Figure 8.17: Relaxation of unequal parallel tubes having $k_1 = 1.0$, $k_2 = 0.98$ in the first row and $k_1 = 4.0$, $k_2 = 3.98$ in the second.

in the second row on a coarse grid having $N = 12$. The parameters of figure 8.1 are slightly modified to; $k_1 = 1.0$, $k_2 = 0.98$, and $k_1 = 4.0$, $k_2 = 3.98$ in (a)-(b) and (c)-(d) respectively. Current is plotted in (b) and (d) at $t = 0.347$. The shapes of the layers and relaxation processes are completely different from those in figure 8.1.

On a finer mesh the growth is so fast that even with extremely small time steps we could not simulate the relaxation to an equilibrium. A large increase in current on a finer mesh confirms these layers to be current sheets. This need of very small time step does not arise in the presence of plasma pressure, as is mentioned in chapter 4. The sheets in both these cases are curved, develop at the neutral points and move away from origin with time. The more deformed the shape the more intense is the current growth and the more difficult it is to simulate the full relaxation process. Due to the localization of current in the sheets, which are now highly deformed, the current contours are needed to clarify the situation.

The development of curvature and movement of the sheet can be observed more clearly in the contour plots of $|\mathbf{J}|$ shown in figure 8.18. The sharp tip of the dent in the left column represents the site of intense current growth visible in figure 8.17(a). In the left column are plots of the $k_1 = 1.0$, $k_2 = 0.98$ and in the right those of the $k_1 = 4.0$ and $k_2 = 3.98$ configuration. The first row corresponds to $t = 0.208$, the second row to $t = 0.347$ and the third one to $t = 0.903$.

When the difference in k_1 and k_2 is large the neutral point is farther from the origin and the resulting sheet is more deformed. Relaxation of the field is now more difficult to simulate. This fact is illustrated in figure 8.19 where $|\mathbf{J}|$ contours are plotted for tubes having $k_1 = 4.0$ and $k_2 = 2.0$. Figure 8.19(a) shows contours of initial $|\mathbf{J}|$ and (b) at a later time when the sheet is still in the development stage. The sheet is more deformed, compare figure 8.17(f), and the current is more intense here.

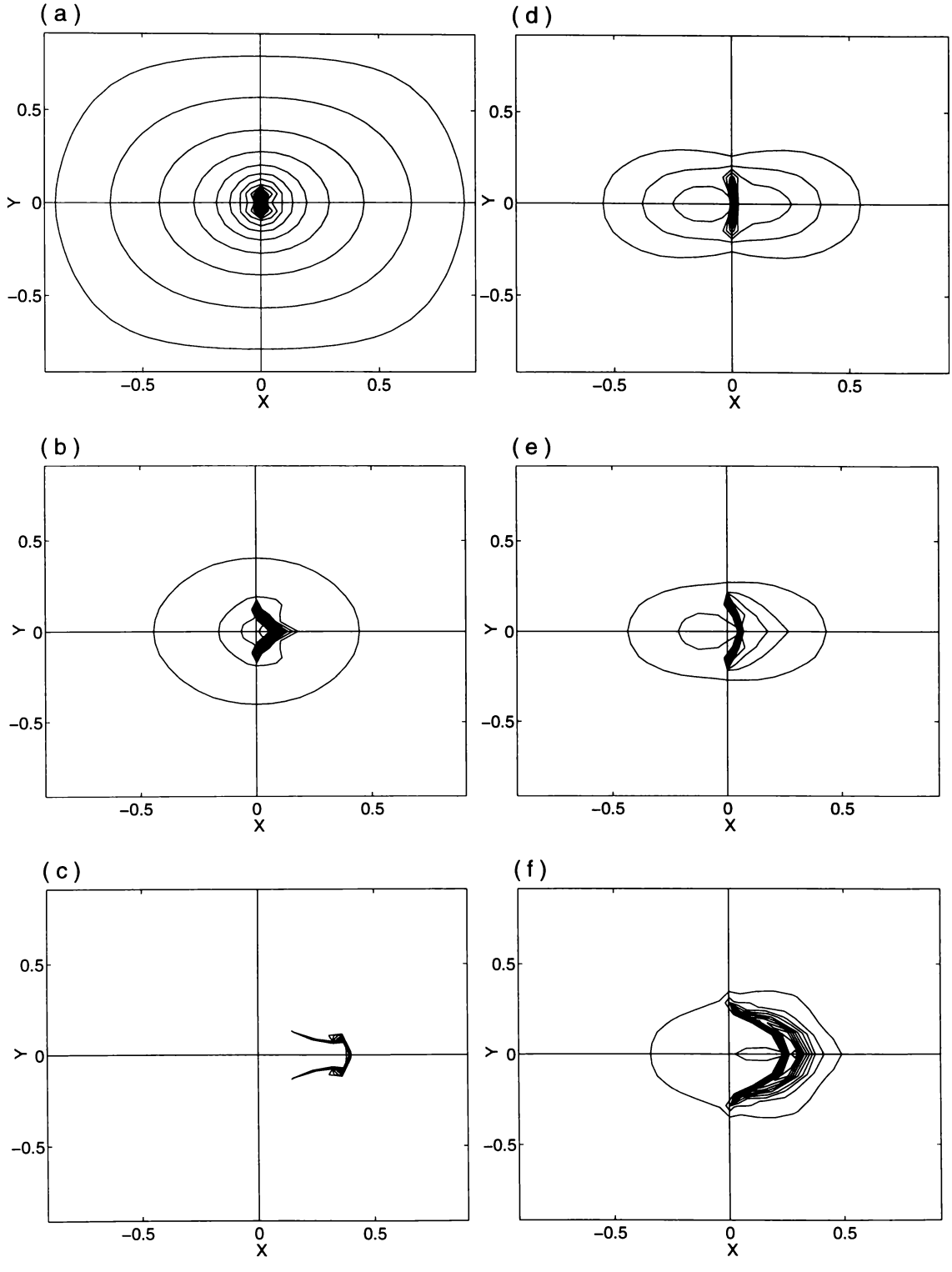

Figure 8.18: Time variation of current sheet position and shape. In the left column $k_1 = 1.0$, $k_2 = 0.98$ and in the right $k_1 = 4.0$ with $k_2 = 3.98$.

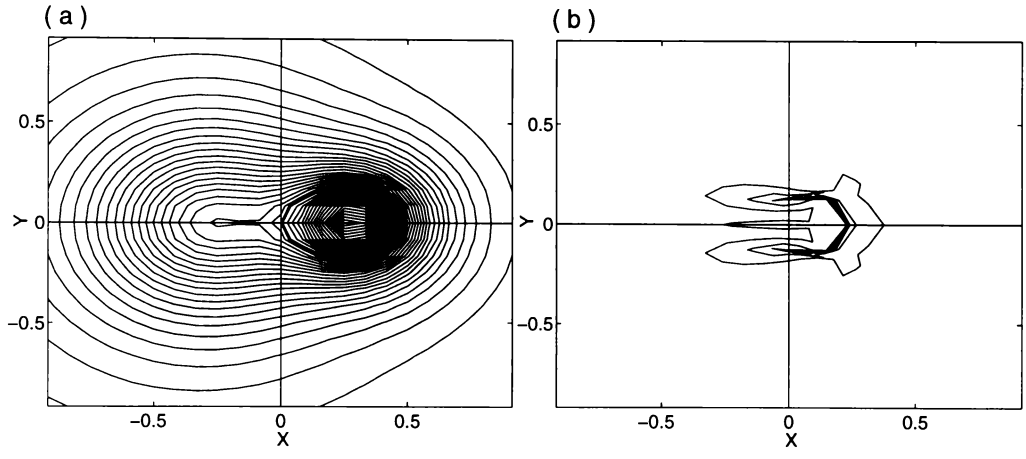

Figure 8.19: $|\mathbf{J}|$ contours at $t = 0$ and 0.347 when the tubes have $k_1 = 4$ and $k_2 = 2$.

8.3.2 Tubes with $k_1 = k_2$ and $b_1 \neq b_2$

Attracting tubes whose combined field has a null but $b_1 \neq b_2$ also give rise to curved current sheets. Deformation of the sheet depends on the ratio b_1/b_2. As was the case in the preceding section, the bigger the difference in b_1 and b_2 the more deformed is the resulting sheet and the more difficult it is to simulate relaxation.

Figures 8.20(a) and (c) show surface plots of current in the initial stage of sheet development for tubes having $k_1 = k_2 = 1$ in the left column and $k_1 = k_2 = 4$ in the right column. In both the cases $b_1 = 0.5$ and $b_2 = 0.48$, so the tubes attract each other and the initial combined field has a neutral point away from the origin. Shapes of the sheets are completely different from those in figure 8.1. In the second row are corresponding contour plots of $|\mathbf{J}|$ showing the deformation of the sheet. Here also the grid is coarse having $N = 12$ only. On a refined mesh the sheet height and hence mesh compression is very large, requiring prohibitively small time steps. Here also the sheet deforms and moves away from the origin as it grows with time.

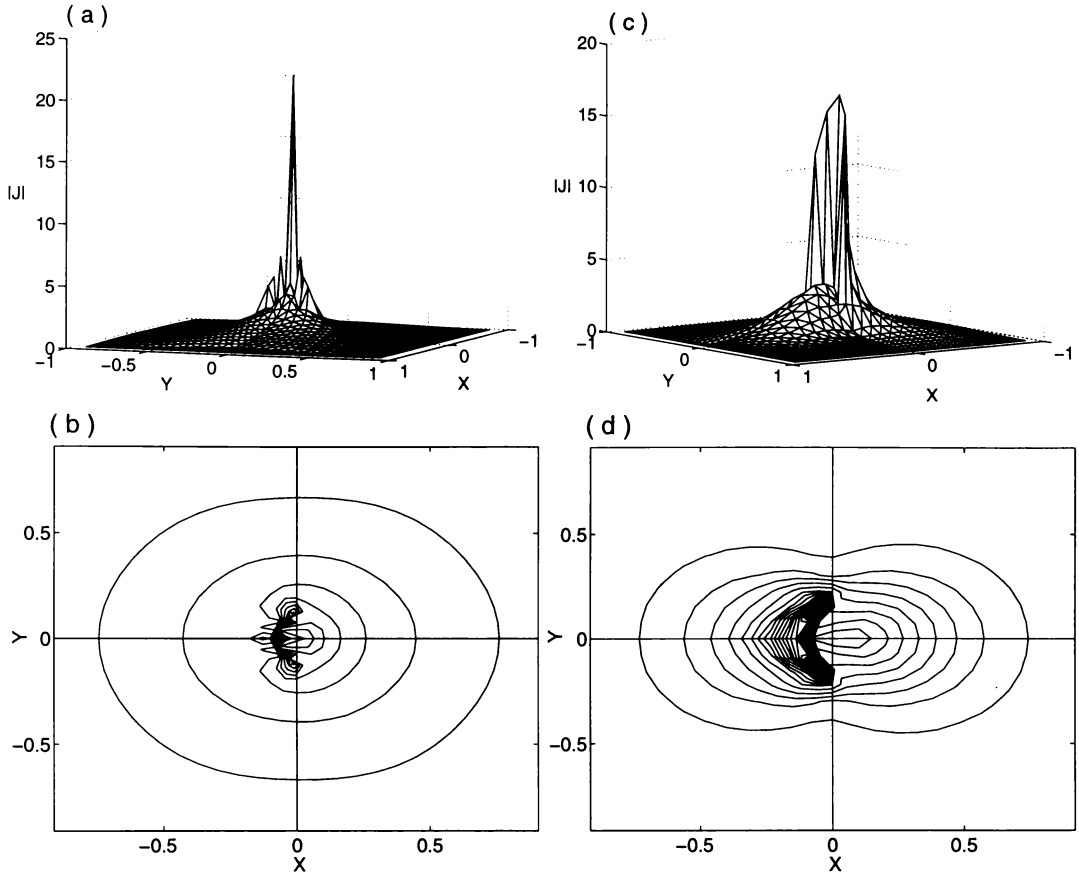

Figure 8.20: Current sheets when $b_1 \neq b_2$. In the left $k_1 = k_2 = 1$ and in the right $k_1 = k_2 = 4$. In both the cases $b_1 = 0.5$ and $b_2 = 0.48$.

To summarize, curved current sheets arise due to interaction of attracting tubes having a neutral point when $|\mathbf{B}_1| \neq |\mathbf{B}_2|$. The bigger the difference the more deformed is the resulting sheet.

8.3.3 Current sheets when $|\mathbf{B}| \neq 0$

When the combined field of two attracting parallel tubes has $B_H = 0$ and $B_z = 0$ at different points, we also see curved current sheets. The initial field has no neutral point and mutual attraction of the tubes brings the two zeros together giving rise to a field singularity. Suppose two parallel tubes have their horizontal field components given by (7.3) with a combined axial field $B_z = \frac{1}{4} - \frac{2}{3}x$. That is

$$\mathbf{B} = \sum_{i=1}^{2} \Big(- \frac{k_i y b_i}{1 + r_i^2 k_i^2} \hat{\mathbf{x}} + \frac{k_i x_i b_i}{1 + r_i^2 k_i^2} \hat{\mathbf{y}} \Big) + \Big(\frac{1}{4} - \frac{2}{3} x \Big) \hat{\mathbf{z}}. \tag{8.1}$$

Here $B_H = 0$ at the origin when $b_1 = b_2$, $k_1 = k_2$ and $b_i, k_i > 0$ but $B_z = 0$ along the line $x = \frac{3}{8} = x_0$ (say). The point $(x_0, 0)$ behaves like a neutral point in that a curved current sheet develops at this point. With time the sheet steepens and this point is dragged towards the origin as the field relaxes to equilibrium. The larger the distance of the $B_z = 0$ line from the origin the more deformed is the resulting current sheet.

Figure 8.21 shows the shapes of the current sheets in the first row for $k_1 = k_2 = 1$, in the second for $k_1 = k_2 = 2$ and in the third row for $k_1 = k_2 = 4$. In the left column are the surface plots of $|\mathbf{J}|$ showing the sheets and in the right column are the corresponding contours at $t = 0.417$. The sheets are located between the initial zeros of B_H (the origin) and B_z (indicated by thick dashed line) fields. It is clear that larger values of k_i result in more deformed current sheets. Here also $J_{\max}$ grows continuously with mesh resolution confirming the sheet to be a true field singularity but, the very small time steps needed to achieve full relaxation make further calculations very difficult.

Our nonlinear simulations in this chapter show that in the absence of plasma pressure, parallel flux tubes whose combined field contain zeros of B_H and B_z interact to produce current sheets. Tubes of differing strengths produce deformed sheets whose growth is rapid. The more rapid the growth of the sheet the more difficult it is to simulate relaxation of the field. When $\tau = 0$, plasma pressure prevents current sheet formation but twisting the tubes together results in a curved sheet and a line current in both of which $J_{\max}$ grows logarithmically with grid resolution when τ is small. For larger τ the line current $J_{\max}$ grows much faster than the sheet $J_{\max}$ with mesh refinement. The resulting current sheets, in this case, are circular in shape when the tubes are of equal strength.

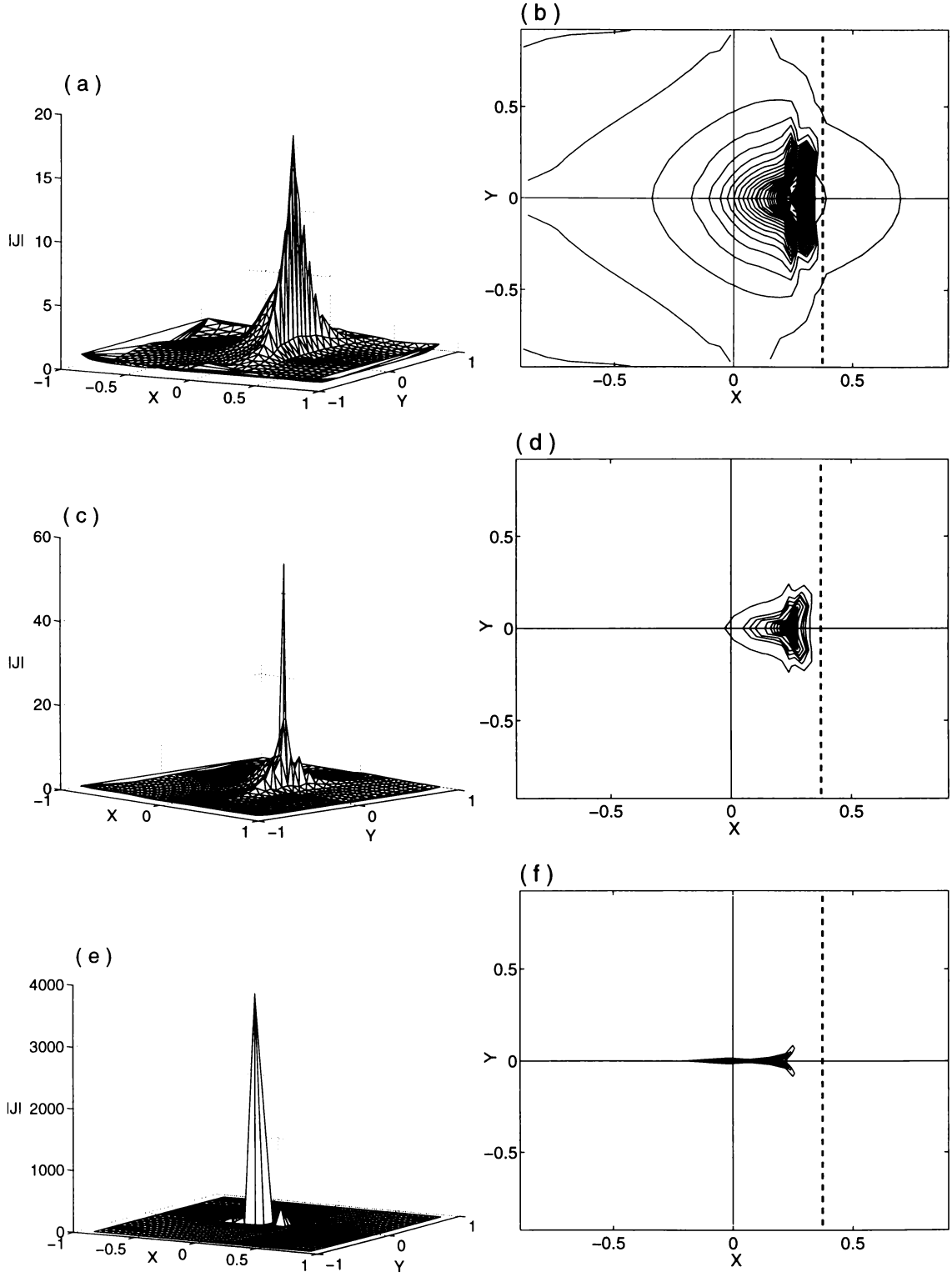

Figure 8.21: In the first row $k_i = 1$, in the second $k_i = 2$ and in the third $k_i = 4$. The dashed thick line represents initial position of $B_z = 0$.

Chapter 9

Conclusions

We have studied two ideal MHD processes capable of generating current sheets in the solar corona. (1) A flux tube in an initial equilibrium may become unstable due to the helical kink instability resulting from twisting of the photospheric footpoints. (2) Two nearby flux tubes may coalesce or wrap around each other. In both cases we assumed the tubes infinitely long and that the field had helical symmetry, so that an effectively two-dimensional numerical code was sufficient to simulate the relaxation to equilibrium.

First we studied the kink instability of an axisymmetric magnetic flux tube, using a helically symmetric magneto-frictional code to allow relaxation to a lower energy state. There are two possible outcomes; a smooth second equilibrium or development of a current sheet. The Gold-Hoyle and B_2 tubes relax to a smooth second equilibrium. This agrees with Lionello *et al.* [46] and contradicts Ng and Bhattacharjee [59] who claim that no smooth equilibrium is possible once an unstable equilibrium is disturbed. For these tubes a twist value τ_0 can be found which gives maximum energy loss. This value represents the pitch of the kink which would develop under no symmetry constraint. The tube B_3, however, develops a current sheet during relaxation whether or not plasma pressure is included. This supports the work of Arber *et al.* [5] who observed current sheets for a similar tube.

Coalescence and twisting of tubes together can also give rise to current sheets. We studied the interaction of parallel Gold-Hoyle tubes and found that attracting tubes, whose initial combined field contained null points of both B_H and B_z may give rise to current sheets. Plasma pressure and twist have vital influence on current sheet formation. When $\tau = 0$, current sheets form as the combined field relaxes to equilibrium only when $\beta = 0$. This feature is completely different from the simple example considered in section 4.4 where plasma pressure could not stop formation of current sheets. When $\tau \neq 0$, however, the tubes are twisted together and current sheets form for all values of β. The growth rate of a sheet is smaller with finite β but increases with twist. The sheet is either curved in the form of a circular arc or in the form of a line current. Thus finite pressure tends to suppress current sheet formation in tube interactions, but twisting the tubes together overcomes this tendency.

A feature of our work is the care taken in differentiating between a current sheet and a simple current concentration. This requires successive computations on systematically refined grids. Steady increase in local $J_{\max}$ with mesh refinement characterises a current sheet. In a current concentration on the other hand, local $J_{\max}$ soon settles to a constant value as the mesh is refined successively.

The current sheets resulting from kinks or interaction of flux tubes found in this thesis may be a plausible solar flare mechanism and could also be a mechanism for coronal heating. Observations do show emergence of groups of flux tubes together and so interaction of the tubes is bound to occur.

This work can be extended in many ways. It would be interesting to give a more precise classification of those flux tubes which kink to form current sheets. The two tubes work can be continued to cater for other (than Gold-Hoyle) parallel tubes. The requirement of helical symmetry in our code seems very restrictive since perfect symmetry can not be found in the solar coronal fields, yet the essential physical mechanisms of current sheet formation should be independent of this constraint. Our results shed light on the basic physical processes involved in current sheet

formation and suggest new mechanisms. Similarly the frictional fluid formulation may not access some equilibrium states and relaxation under realistic conditions may lead to a different equilibrium, but the final equilibrium achieved by our code is guaranteed to be stable. Relaxation of fields with or without formation of current sheets resulting from kinking of, and interaction between, long parallel tubes can be handled satisfactorily. However, the effect of line tying or relaxation of fields having more general geometries will require a more general code. Twisting together and interaction of any number of infinite parallel tubes can be simulated using our code but tubes inclined at different angles will need a three-dimensional extension.

Another important feature to include will be resistivity, to cater for reconnection and energy dissipation. Detailed evolution of current spikes with finite resistivity requires consideration. An estimate of energy released by the current sheets is also important.

An analysis of current sheet diagnostics to estimate $J_{\max}$ growth with mesh refinement is a difficult task. We gave a simple example to show that in current sheets forming at a neutral point one will expect $J_{\max} \propto N^m$, m a real number, but we found some sheets to behave quite differently. $J_{\max}$ variation as $\log(N)$ in the curved current sheets resulting from twisting of attracting tubes in the presence of plasma pressure needs further exploration.

A part of this work will appear in *Geophysical and Astrophysical Fluid Dynamics* Vol. 94, 3-4, 2001, and another paper is in preparation.

Appendix

Taking

$$
\begin{aligned}
s1 \;=\; & \big[-2\hat{\beta} r \lambda^2 (2r^2\lambda + \hat{\beta}\tau^2 r^2 + \hat{\beta} m^2)(mk - \tau)(k^2 r^2 + 1)^4 (\tau r^2 k + m) e^{(2\eta)} \\
& - 2r\lambda (mk - \tau)(k^2 r^2 + 1)^2 (\tau r^2 k + m)(2r^4 k^2 \tau^2 \lambda \hat{\beta} + r^4 k^2 \lambda^2 \\
& + 2r^2 m^2 k^2 \tau^2 \hat{\beta}^2 + 4r^2 m^2 k^2 \lambda \hat{\beta} - 4r^2 m \hat{\beta}^2 k \tau^3 - 4r^2 m \hat{\beta} \lambda k \tau + 2r^2 \hat{\beta}^2 \tau^4 + 4r^2 \hat{\beta} \lambda \tau^2 \\
& + r^2 \lambda^2 + 2k^2 \hat{\beta}^2 m^4 - 4\hat{\beta}^2 k \tau m^3 + 2\hat{\beta}^2 m^2 \tau^2 + 2\hat{\beta} \lambda m^2) e^{(4\eta)} \\
& - 2r(mk - \tau)(\tau^2 r^2 + m^2)(\tau r^2 k + m)(\hat{\beta} k^2 m^2 - 2\hat{\beta} m \tau k + \lambda k^2 r^2 + \lambda + \hat{\beta}\tau^2)^2 e^{(6\eta)} \big] k' \\
& + \lambda^2 (k^2 r^2 + 1)^4 (\lambda^2 k^4 r^6 - 2\lambda k^4 \hat{\beta} r^6 \tau^2 + k^4 \hat{\beta}^2 r^4 \tau^2 m^2 - 2k^3 m r^4 \hat{\beta}^2 \tau^3 \\
& - 12\lambda k^3 \hat{\beta} r^4 m \tau + k^2 r^4 \hat{\beta}^2 \tau^4 + 2r^4 k^2 \tau^2 \lambda \hat{\beta} - 5k^4 r^2 m^4 \hat{\beta}^2 + 10k^3 \hat{\beta}^2 r^2 m^3 \tau \\
& - 14r^2 m^2 k^2 \lambda \hat{\beta} - 8r^2 m^2 k^2 \tau^2 \hat{\beta}^2 + 6r^2 m \hat{\beta}^2 k \tau^3 + 4r^2 m \hat{\beta} \lambda k \tau - 4r^2 \hat{\beta} \lambda \tau^2 \\
& - 3r^2 \hat{\beta}^2 \tau^4 - r^2 \lambda^2 - 9k^2 \hat{\beta}^2 m^4 - 6\hat{\beta} \lambda m^2 - 9\hat{\beta}^2 m^2 \tau^2 + 18\hat{\beta}^2 k \tau m^3) e^{(2\eta)} \\
& + \lambda (k^2 r^2 + 1)^2 (-3\hat{\beta}^2 \tau^6 r^2 - 3\lambda^2 m^2 + 5k^6 r^4 \tau^2 m^4 \hat{\beta}^2 + 5k^2 \hat{\beta}^2 \tau^6 r^4 \\
& - 8\lambda k^5 \hat{\beta} r^6 m \tau^3 - 20k^5 \hat{\beta}^2 r^4 m^3 \tau^3 - 10\lambda^2 k^5 r^6 m \tau + 4k^5 r^2 m^5 \tau \hat{\beta}^2 \\
& - 20\lambda k^5 r^4 m^3 \tau \hat{\beta} + 30k^4 \hat{\beta}^2 r^4 \tau^4 m^2 + 38\lambda k^4 \tau^2 r^4 m^2 \hat{\beta} - 9k^4 \tau^2 r^2 m^4 \hat{\beta}^2 \\
& - 17\lambda k^4 m^4 r^2 \hat{\beta} + 4\lambda k^6 r^6 \tau^2 m^2 \hat{\beta} - k^6 m^6 r^2 \hat{\beta}^2 + 3\lambda k^6 m^4 r^4 \hat{\beta} + 4\lambda k^4 \hat{\beta} r^6 \tau^4 \\
& + 7\lambda k^2 \hat{\beta} r^4 \tau^4 - 5\hat{\beta} r^2 \lambda \tau^4 - 19k^2 \hat{\beta}^2 r^2 \tau^4 m^2 + 36\lambda k^3 \tau m^3 r^2 \hat{\beta} - \lambda^2 k^6 r^8 \tau^2 \\
& + 2\lambda^2 k^6 m^2 r^6 + 2\lambda^2 k^4 \tau^2 r^6 - 5\lambda^2 k^4 m^2 r^4 - 9k^4 m^6 \hat{\beta}^2 + \lambda^2 k^2 \tau^2 r^4 \\
& - 10\lambda^2 k^2 m^2 r^2 - 12\lambda k^2 m^4 \hat{\beta} - 9\hat{\beta}^2 \tau^4 m^2 - 12\lambda \tau^2 \hat{\beta} m^2 + 36k\hat{\beta}^2 m^3 \tau^3 \\
& - 26\lambda k^2 \tau^2 m^2 r^2 \hat{\beta} - 54k^2 \tau^2 m^4 \hat{\beta}^2 + 12km\hat{\beta}^2 \tau^5 r^2 + 12\lambda k \hat{\beta} m \tau^3 r^2 \\
& + 2\lambda^2 k m \tau r^2 + 24\lambda k m^3 \tau \hat{\beta} - 20k^3 m r^4 \hat{\beta}^2 \tau^5 - 28\lambda k^3 r^4 \hat{\beta} m \tau^3
\end{aligned}
$$

$$
\begin{aligned}
&+16k^3r^2\hat{\beta}^2m^3\tau^3+36k^3\tau m^5\hat{\beta}^2-8\lambda^2k^3\tau mr^4-2\lambda^2\tau^2r^2)e^{(4\eta)}\\
&+(mk-\tau)^2(r^2m^2k^2-3m^2+3r^4k^2\tau^2-\tau^2r^2)\\
&(\hat{\beta}k^2m^2-2\hat{\beta}m\tau k+\lambda k^2r^2+\lambda+\hat{\beta}\tau^2)^2e^{(6\eta)}\\
&-\hat{\beta}\lambda^3(k^2r^2+1)^7(r^2\lambda+\hat{\beta}\tau^2r^2+3\hat{\beta}m^2),
\end{aligned}
$$

$$
\begin{aligned}
s2 \;=\; &\big[-2r^3\lambda^3(k^2r^2+1)^3(\hat{\beta}m\tau k^2r^2-r^2k\lambda-2r^2k\hat{\beta}\tau^2-\hat{\beta}m\tau)e^{(2\eta)}\\
&-2r^3\lambda^2(k^2r^2+1)^2(2r^2\hat{\beta}m\tau^3k^2-k\lambda\tau^2r^2-2k\hat{\beta}\tau^4r^2+\hat{\beta}m^3\tau k^2\\
&-\hat{\beta}m\tau^3-k\lambda m^2)e^{(4\eta)}\big]k'\\
&+\lambda^2(k^2r^2+1)^3(3r^2\hat{\beta}^2\tau^4+4r^4k^2\lambda^2-2\hat{\beta}\lambda m^2-3\hat{\beta}^2m^2\tau^2+4k^4r^6\hat{\beta}^2\tau^4\\
&+r^2\lambda^2-3k^2\hat{\beta}^2m^4+6\hat{\beta}^2k\tau m^3+4r^2\hat{\beta}\lambda\tau^2+14r^4k^2\tau^2\lambda\hat{\beta}-2r^2m^2k^2\lambda\hat{\beta}\\
&-2r^2m\hat{\beta}^2k\tau^3-8\lambda k^3\hat{\beta}r^4m\tau+6k^3\hat{\beta}^2r^2m^3\tau-3k^4r^2m^4\hat{\beta}^2+2\lambda k^4\hat{\beta}r^6\tau^2\\
&+3k^4\hat{\beta}^2r^4\tau^2m^2-2k^3mr^4\hat{\beta}^2\tau^3+7k^2r^4\hat{\beta}^2\tau^4-\lambda^2k^4r^6-6km\hat{\beta}^2\tau^5r^4\\
&-8\lambda k\tau^3mr^4\hat{\beta}-12k\tau^3m^3\hat{\beta}^2r^2-2\lambda^2km\tau r^4-8\lambda km^3\tau r^2\hat{\beta}-6km^5\tau\hat{\beta}^2\\
&+6\tau^4\hat{\beta}^2m^2r^2+8\lambda\tau^2\hat{\beta}m^2r^2+8\lambda k^2\tau^4\hat{\beta}r^6+9k^2\tau^4\hat{\beta}^2m^2r^4\\
&+16\lambda k^2\tau^2\hat{\beta}m^2r^4+9k^2\tau^2m^4\hat{\beta}^2r^2+8\lambda k^2\hat{\beta}m^4r^2+6k^4\tau^2m^4\hat{\beta}^2r^4\\
&+6\lambda k^4\hat{\beta}m^4r^4+3k^4m^6\hat{\beta}^2r^2-6k^3m\hat{\beta}^2\tau^5r^6-8\lambda k^3\tau^3mr^6\hat{\beta}\\
&-12k^3\tau^3m^3\hat{\beta}^2r^4-2\lambda^2k^3\tau mr^6-8\lambda k^3\tau m^3r^4\hat{\beta}-6k^3\tau m^5\hat{\beta}^2r^2\\
&+2\lambda k^4\tau^4\hat{\beta}r^8+3k^4\tau^4\hat{\beta}^2m^2r^6+8\lambda k^4\tau^2\hat{\beta}m^2r^6+3k^2\hat{\beta}^2\tau^6r^6+3\lambda^2\tau^2r^4\\
&+2\lambda^2r^2m^2+2\lambda\hat{\beta}m^4+3\hat{\beta}^2\tau^6r^4+2\lambda^2k^4\tau^2r^8+3\lambda^2k^4r^6m^2+5\lambda^2k^2\tau^2r^6\\
&+5\lambda^2k^2r^4m^2+3k^2m^6\hat{\beta}^2+6\lambda\tau^4r^4\hat{\beta}+3\tau^2m^4\hat{\beta}^2)e^{(2\eta)}\\
&+\lambda(k^2r^2+1)^2(3\hat{\beta}^2\tau^6r^2+3r^4\hat{\beta}^2\tau^8+m^4\lambda^2-\lambda^2m^2+4k^2\hat{\beta}^2\tau^6r^4+4k^4\hat{\beta}^2r^4\tau^4m^2\\
&+4\lambda k^4\tau^2r^4m^2\hat{\beta}-k^4\tau^2r^2m^4\hat{\beta}^2-3\lambda k^4m^4r^2\hat{\beta}+4\lambda k^4\hat{\beta}r^6\tau^4+12\lambda k^2\hat{\beta}r^4\tau^4\\
&+5\hat{\beta}r^2\lambda\tau^4-2k^2\hat{\beta}^2r^2\tau^4m^2+8\lambda k^3\tau m^3r^2\hat{\beta}+\lambda^2k^4\tau^2r^6-2\lambda^2k^4m^2r^4-3k^4m^6\hat{\beta}^2\\
&+5\lambda^2k^2\tau^2r^4-\lambda^2k^2m^2r^2-4\lambda k^2m^4\hat{\beta}-3\hat{\beta}^2\tau^4m^2-4\lambda\tau^2\hat{\beta}m^2+12k\hat{\beta}^2m^3\tau^3\\
&-6\lambda k^2\tau^2m^2r^2\hat{\beta}-18k^2\tau^2m^4\hat{\beta}^2-4km\hat{\beta}^2\tau^5r^2+2\lambda^2km\tau r^2+8\lambda km^3\tau\hat{\beta}-8k^3mr^4\hat{\beta}^2\tau^5\\
&-8\lambda k^3r^4\hat{\beta}m\tau^3+4k^3r^2\hat{\beta}^2m^3\tau^3+12k^3\tau m^5\hat{\beta}^2+2\lambda^2k^3\tau mr^4+2\lambda^2\tau^2r^2+4\lambda^2k^2\tau^4r^6
\end{aligned}
$$

$$+4\lambda^2k^2m^4r^2+4\lambda k^2m^6\hat{\beta}+6\lambda\tau^6r^4\hat{\beta}+3\lambda^2k^4m^4r^4+3\lambda^2\tau^4r^4-16\lambda k^3\tau m^5\hat{\beta}r^2$$

$$-12k^3\tau m^7\hat{\beta}^2-4\lambda^2k^3\tau m^3r^4+3\tau^4m^4\hat{\beta}^2+4\lambda^2\tau^2m^2r^2+4\lambda\tau^2m^4\hat{\beta}+10\lambda\tau^4m^2\hat{\beta}r^2$$

$$-12km^5\tau^3\hat{\beta}^2-24\lambda km^3\tau^3r^2\hat{\beta}-4\lambda^2km\tau^3r^4-4\lambda^2k\tau m^3r^2-8\lambda k\tau m^5\hat{\beta}+6\tau^6\hat{\beta}^2m^2r^2$$

$$+4\lambda k^2\tau^6r^6\hat{\beta}+18k^2\tau^6\hat{\beta}^2m^2r^4+24\lambda k^2\tau^4m^2\hat{\beta}r^4+36k^2\tau^4m^4\hat{\beta}^2r^2+\lambda^2k^4\tau^4r^8$$

$$+8\lambda^2k^2\tau^2m^2r^4+24\lambda k^2\tau^2m^4\hat{\beta}r^2+18k^2\tau^2m^6\hat{\beta}^2-8\lambda k^3\tau^5mr^6\hat{\beta}-12k^3\tau^5m^3\hat{\beta}^2r^4$$

$$-4\lambda^2k^3\tau^3mr^6-24\lambda k^3\tau^3m^3\hat{\beta}r^4+6k^4\tau^2m^6\hat{\beta}^2r^2+6\lambda k^4m^6\hat{\beta}r^2+4\lambda k^4\tau^4m^2\hat{\beta}r^6$$

$$+3k^4\tau^4m^4\hat{\beta}^2r^4+4\lambda^2k^4\tau^2m^2r^6+3k^4m^8\hat{\beta}^2+10\lambda k^4\tau^2m^4\hat{\beta}r^4-24k^3\tau^3m^5\hat{\beta}^2r^2$$

$$-12km\hat{\beta}^2\tau^7r^4-16\lambda k\tau^5mr^4\hat{\beta}-24k\tau^5m^3\hat{\beta}^2r^2)e^{(4\eta)}$$

$$+(mk-\tau)(km^5-\tau m^4+2m^3k\tau^2r^2-km^3-2m^2\tau^3r^2+\tau m^2$$

$$+mk\tau^4r^4-3mk\tau^2r^2-\tau^3r^2-\tau^5r^4)(\hat{\beta}k^2m^2-2\hat{\beta}m\tau k+\lambda k^2r^2+\lambda+\hat{\beta}\tau^2)^2e^{(6\eta)}$$

$$+\lambda^3(k^2r^2+1)^6(r^4\hat{\beta}^2\tau^4+r^4\lambda^2+2\lambda\tau^2r^4\hat{\beta}+\tau^2\hat{\beta}^2r^2+2\tau^2\hat{\beta}^2m^2r^2$$

$$+2m^2r^2\hat{\beta}\lambda+\hat{\beta}\lambda r^2+m^4\hat{\beta}^2-m^2\hat{\beta}^2)$$

and

$$\begin{aligned}
dn2 \;=\;& \lambda^2(k^2r^2+1)^4(2r^4k^2\tau^2\lambda\hat{\beta}+r^4k^2\lambda^2+3r^2m^2k^2\tau^2\hat{\beta}^2+4r^2m^2k^2\lambda\hat{\beta}\\
&-6r^2m\hat{\beta}^2k\tau^3-4r^2m\hat{\beta}\lambda k\tau+4r^2\hat{\beta}\lambda\tau^2+r^2\lambda^2+3r^2\hat{\beta}^2\tau^4\\
&-6\hat{\beta}^2k\tau m^3+2\hat{\beta}\lambda m^2+3\hat{\beta}^2m^2\tau^2+3k^2\hat{\beta}^2m^4)e^{(2\eta)}\\
&+\lambda(k^2r^2+1)^2(3k^2\hat{\beta}m^4-6k\hat{\beta}m^3\tau+3k^2\hat{\beta}r^2m^2\tau^2+3\hat{\beta}m^2\tau^2-6\hat{\beta}mk\tau^3r^2\\
&+3\hat{\beta}\tau^4r^2+\lambda r^4k^2\tau^2+2\lambda r^2m^2k^2-2\lambda km\tau r^2+2\lambda\tau^2r^2+\lambda m^2)\\
&(\hat{\beta}k^2m^2-2\hat{\beta}m\tau k+\lambda k^2r^2+\lambda+\hat{\beta}\tau^2)e^{(4\eta)}\\
&+(mk-\tau)^2(\tau^2r^2+m^2)(\hat{\beta}k^2m^2-2\hat{\beta}m\tau k+\lambda k^2r^2+\lambda+\hat{\beta}\tau^2)^2e^{(6\eta)}\\
&+\hat{\beta}\lambda^3(k^2r^2+1)^6(r^2\lambda+\hat{\beta}\tau^2r^2+\hat{\beta}m^2),
\end{aligned}$$

with $\hat{\beta}=\gamma P$ and $\eta=\int_0^r\frac{r^2kk'}{1+r^2k^2}dr$, the coefficients a and b appearing in (2.37) are given by

$$\begin{aligned}
a &= s1/[r(1+r^2k^2)dn],\\
b &= s2/(r^2dn). \qquad (.1)
\end{aligned}$$

References

[1] T. Amari and J.F. Luciani, *Confined disruption of a three-dimensional twisted magnetic flux tube*, Ap. J. **515** (1999), L81.

[2] T. Amari, J.F. Luciani, and P. Joly, *A preconditioned semi-implicit method for magnetohydrodynamics equations*, SIAM J. Sci. Comput. **21** (1999), 970.

[3] S.K. Antiochos, *The topology of force-free magnetic fields and its implications for coronal activity*, Ap. J. **312** (1987), 886.

[4] U. Anzer, *The stability of force-free magnetic fields with cylindrical symmetry in the context of solar flares*, Solar Phys. **3** (1968), 298.

[5] T.D. Arber, A.W. Longbottom, and R.A.M. van der Linden, *Unstable coronal loops: Numerical simulations with predicted observational signatures*, Ap. J. **517** (1999), 990.

[6] G. Bateman, *Mhd instabilities*, MIT Press, Massachusetts, 1978.

[7] G. Bateman, W. Schneider, and W. Grossmann, *Mhd instabilities as an initial boundary-value problem*, Nucl. Fusion **14** (1974), 669.

[8] H. Baty, *Magnetic reconnection in kinked coronal loops*, A&A **353** (2000), 1074.

[9] H. Baty, G. Einaudi, R. Lionello, and M. Velli, *Ideal kink instabilities in line-tied coronal loops*, A&A **333** (1998), 313.

[10] H. Baty and J. Heyvaerts, *Electric current concentration and kink instability in line-tied coronal loops*, A&A **308** (1996), 935.

[11] I.B. Bernstein, E.A. Frieman, M.D. Kruskal, and R.M. Kulsrud, *An energy principle for hydromagnetic stability problems*, Proc. Roy. Soc. London **244** (1958), 17.

[12] M.N. Billinghurst, I.J.D. Craig, and A.D. Sneyd, *Current-sheet formation in two-dimensional coronal fields*, A&A **279** (1993), 589.

[13] T.J. Bogdan, *The turbulent twisted magnetic flux tube gas*, Phys. Fluids **27** (1984), 994.

[14] P. De Bruyne and A.W. Hood, *Simple tests for the ideal mhd stability of line-tied coronal magnetic fields*, Solar Phys. **119** (1989), 87.

[15] R. Chodura and A. Schlüter, *A 3d code for mhd equilibrium and stability*, J. Comput. Phys. **41** (1981), 68.

[16] I.J.D. Craig, *Current sheet formation and dissipation in general x-point topologies*, A&A **283** (1994), 331.

[17] I.J.D. Craig and A.N. McClymont, *Linear theory of fast reconnection at an x-type neutral point*, Ap. J. **405** (1993), 207.

[18] I.J.D. Craig, A.N. McClymont, and A.D. Sneyd, *General methods for determination of the linear stability of coronal magnetic fields*, Ap. J. **335** (1988), 441.

[19] I.J.D. Craig, T.D. Robb, A.D. Sneyd, and A.N. McClymont, *The kink instability in infinite cylindrical flux tubes: Eigenvalues for power-law twist profiles*, Astrophys. Space Sci. **166** (1990), 289.

[20] I.J.D. Craig and A.D. Sneyd, *A dynamical relaxation technique for determining the structure and stability of coronal magnetic fields*, Ap. J. **311** (1986), 451.

[21] I.J.D. Craig and A.D. Sneyd, *An alternating direction implicit scheme for parabolic systems of differential equations*, Computers Math. Applic. **20** (1990), 53.

[22] I.J.D. Craig and A.D. Sneyd, *Nonlinear development of the kink instability in coronal flux tubes*, Ap. J. **357** (1990), 653.

[23] I.J.D. Craig and P.G. Watson, *Fast dynamic reconnection at x-type neutral points*, Ap. J. **393** (1992), 385.

[24] J.L. Culhane and C. Jordan (eds.), *The physics of solar flares*, Proceedings of a Royal Society discussion meeting, Royal Society, London, 1991.

[25] A. Daw, E.E. DeLuca, and L. Golub, *Observations and interpretation of soft x-ray limb absorption seen by the normal incedence x-ray telescope*, Ap. J. **453** (1995), 929.

[26] D.G. Dritschel, *Generalized helical beltrami flows in hydrodynamics and magnetohydrodynamics*, J. Fluid Mech. **222** (1991), 525.

[27] G. Einaudi and G. van Hoven, *The stability of coronal loops - finite - length and pressure - profile limits*, Solar Phys. **88** (1983), 164.

[28] B.J. Foote and I.J.D. Craig, *The linear stability of line-tied coronal magnetic fields*, Ap. J. **350** (1990), 437.

[29] R. Giachetti, G. van Hoven, and C. Chiuderi, *The structure of coronal magnetic loops II: Mhd stability theory*, Solar Phys. **55** (1977), 371.

[30] J.P. Goedbloed and P.H. Sakanaka, *New approach to magnetohydrodynamic stability: I. a practical stability concept*, Phys. Fluids **17** (1974), 908.

[31] T. Gold and F. Hoyle, *On the origin of solar flares*, Mon. Not. R. Astr. Soc. **120** (1960), 89.

[32] A.W. Hood, *Ballooning instabilities in the solar corona: Conditions for stability*, Solar Phys. **103** (1986), 329.

[33] A.W. Hood and E.R. Priest, *Kink instability of solar coronal loops as the cause of solar flares*, Solar Phys. **64** (1979), 303.

[34] A.W. Hood and E.R. Priest, *Magnetic instability of coronal arcades as the origin of two-ribbon flares*, Solar Phys. **66** (1980), 113.

[35] A.W. Hood and E.R. Priest, *Critical conditions for magnetic instabilities in force-free coronal loops*, Geophys. Astrophys. Fluid Dynamics **17** (1981), 297.

[36] L.L. House and M.A. Berger, *The ejection of helical field structures through the outer corona*, Ap. J. **323** (1987), 406.

[37] T.T. Ishii, H. Kurokawa, and T.T. Takeuchi, *Emergence of a twisted magnetic flux bundle as a source of strong flare activity*, Ap. J. **499** (1998), 898.

[38] B.B. Kadomtsev, *Hydromagnetic stability of a plasma*, Reviews of plasma phys. **2** (1966), 153.

[39] L. Kejun and Z. Shuhua, *The observations and analysis of an eruptive prominence*, A&A **126** (1997), 241.

[40] D. Kondrashov, J. Feyman, P.C. Liewer, and A. Ruzmaikin, *Three-dimensional magnetohydrodynamic simulations of the interaction of magnetic flux tubes*, Ap. J. **519** (1999), 884.

[41] M. Kruskal and J.L. Tuck, *The instability of a pinched fluid with a longitudinal magnetic field*, Proc. Roy. Soc. London **245** (1958), 222.

[42] M.J. Landman, *On the generation of helical waves in circular pipe flow*, Phys. Fluids A **2** (1990), 738.

[43] L. Larmore, *A study of the motions of solar prominences*, Ap. J. **118** (1953), 436.

[44] D.D. Lenz, E.E. DeLuca, L. Golub, R. Rosner, J.A. Bookbinder, C. Litwin, F. Reale, and G. Peres, *Long-lived coronal loop profiles from trace*, Solar Phys. **190** (1999), 131.

[45] M.G. Linton, R.B. Dahlburg, G.H. Fisher, and D.W. Longcope, *Nonlinear evolution of kink-unstable magnetic flux tubes and solar δ-spot active regions*, Ap. J. **507** (1998), 404.

[46] R. Lionello, Z. Mikić, and D.D. Schnack, *Magnetohydrodynamics of solar coronal plasmas in cylindrical geometry*, J. Comput. Phys. **140** (1998), 172.

[47] R. Lionello, D.D. Schnack, G. Einaudi, and M. Velli, *Current sheet formation due to nonlinear kink modes in periodic and line-tied configurations*, Phys. Plasmas **5** (1998), 3722.

[48] R. Lionello, M. Velli, G. Einaudi, and Z. Mikić, *Nonlinear magnetohydrodynamic evolution of line-tied coronal loops*, Ap. J. **494** (1998), 840.

[49] Y.E. Litvinenko and I.J.D. Craig, *Flare energy release by flux pile-up magnetic reconnection in a turbulent current sheet*, Ap. J. **544** (2000), 1101.

[50] A.W. Longbottom, G.J. Rickard, I.J.D. Craig, and A.D. Sneyd, *Magnetic flux braiding: Force-free equilibria and current sheets*, Ap. J. **500** (1998), 471.

[51] B.C. Low, *Electric current sheet formation in a magnetic field induced by continuous magnetic footpoint displacement*, Ap. J. **323** (1987), 358.

[52] B.C. Low and R. Wolfson, *Spontaneous formation of electric current sheets and the origin of solar flares*, Ap. J. **324** (1988), 574.

[53] A.N. McClymont and I.J.D. Craig, *Dynamical finite-amplitude magnetic reconnection at an x-type neutral point*, Ap. J. **466** (1996), 487.

[54] Z. Mikić, *Magnetohydrodynamic modeling of the solar corona*, Phys. Fluids B **2** (1990), 1450.

[55] Z. Mikić, D.D. Schnack, and G. van Hoven, *Dynamical evolution of twisted magnetic flux tubes. 1: Equilibrium and linear stability*, Ap. J. **361** (1990), 690.

[56] L.J. Milano, P. Dmitruk, C.H. Mandrini, and O. Gomez, *Quasi-separatrix layers in a reduced magnetohydrodynamic model of a coronal loop*, Ap. J. **521** (1999), 889.

[57] H.K. Moffatt, *Magnetic field generation in electrically conducting fluids*, Cambridge Monographs on Mechanics and Applied Mathematics, Cambridge University Press, Cambridge, UK, 1978.

[58] W.A. Newcomb, *Hydromagnetic stability of a diffuse linear pinch*, Ann. Phys. **10** (1960), 232.

[59] C.S. Ng and A. Bhattacharjee, *Nonequilibrium and current sheet formation in line-tied magnetic fields*, Phys. Plasmas **5** (1998), 4028.

[60] L. Ofman, J.A. Klimchuk, and J.M. Davila, *A self-consistent model for the resonant heating of coronal loops: The effects of coupling with the chromosphere*, Ap. J. **493** (1998), 474.

[61] W. Park, D.A. Monticello, and R.B. White, *Reconnection rates of magnetic fields including the effects of viscosity*, Phys. Fluids **27** (1984), 137.

[62] W. Park, D.A. Monticello, R.B. White, and S.C. Jardin, *Non-linear saturation of the internal kink mode*, Nucl. Fusion **20** (1980), 1181.

[63] E.N. Parker, *Topological dissipation and the small-scale fields in turbulent gases*, Ap. J. **174** (1972), 499.

[64] E.N. Parker, *Cosmical magnetic fields, their origin and activity*, The International Series of Monographs on Physics, Clarendon Press, Oxford, UK, 1979.

[65] E.N. Parker, *Sunspots and the physics of magnetic flux tubes. v. mutual hydrodynamic forces between neighboring tubes*, Ap. J. **231** (1979), 270.

[66] E.N. Parker, *Magnetic reorientation and the spontaneous formation of tangential discontinuities in deformed magnetic fields*, Ap. J. **318** (1987), 876.

[67] A.A. Pevstov and R.C. Canfield, *Reconnection and helicity in a solar flare*, Ap. J. **473** (1996), 533.

[68] E.R. Priest, *Solar magneto-hydrodynamics*, Geophysics and Astrophysics Monographs, vol. 21, D. Reidel Publishing Co., Dordrecht, Holland, Lockheed, Palo Alto, California, USA, 1984.

[69] M.A. Raadu, *Suppression of the kink instability for magnetic flux ropes in the chromosphere*, Solar Phys. **22** (1972), 425.

[70] G.J. Rickard and I.J.D. Craig, *Fast magnetic reconnection and the coalescence instability*, Phys. Fluids B **5** (1993), 956.

[71] P.H. Roberts, *An introduction to magnetohydrodynamics*, Longman, Green and Co., London, UK, 1967.

[72] D.C. Robinson, *High-β diffuse pinch configurations*, Plasma Phys. **13** (1971), 439.

[73] D.M. Rust, *Magnetic helicity, mhd kink instabilities and reconnection in the corona*, Magnetic Reconnection in the Solar Atmosphere, Proc. of Yohkoh Conference (R.D. Bentley and J.T. Mariska, eds.), ASP Conference Series, vol. 111, 1996, p. 353.

[74] P.H. Sakanaka and J.P. Goedbloed, *New approach to magnetohydrodynamic stability: II. sigma-stable diffuse pinch configurations*, Phys. Fluids **17** (1974), 919.

[75] T. Sakurai, *Energy storage and instability in magnetic flux tubes*, Solar and interplanetary dynamics, Proc. of symp., Aug. 27-31, 1979, Cambridge, Mass., D. Reidel Pub. Co., 1980, p. 291.

[76] A.D. Sneyd, *Formation of current sheets by photospheric compression*, Geophys. Astrophys. Fluid Dynamics **70** (1993), 195.

[77] A.D. Sneyd, *Current sheet formation in uniformly twisted magnetic flux tubes*, Geophys. Astrophys. Fluid Dynamics **83** (1996), 135.

[78] A.D. Sneyd and I.J.D. Craig, *Linear mhd stability of infinitely long coronal flux tubes*, Astrophys. Space Sci. **151** (1989), 265.

[79] P.A. Sturrock, *Solar flares*, A Monograph from Skylab Solar Workshop II, Colorado Associated University Press, 1980.

[80] K.C. Tsinganos, *Magnetohydrodynamic equilibrium. III. helically symmetric fields*, Ap. J. **259** (1982), 820.

[81] S.I. Vainshtein and E.N. Parker, *Magnetic nonequilibrium and current sheet formation*, Ap. J. **304** (1986), 821.

[82] A.A. van Ballegooijen, *Electric currents in the solar corona and the existence of magnetostatic equilibrium*, Ap. J. **298** (1985), 421.

[83] R.A.M. van der Linden and A.W. Hood, *A complete coronal loop stability analysis in ideal magnetohydrodynamics. II. force-free cylindrical equilibria*, A&A **346** (1999), 303.

[84] G. Vekstein, E.R. Priest, and T. Amari, *Formation of current sheets in force-free magnetic fields*, A&A **243** (1991), 492.

[85] M. Velli, G. Einaudi, and A.W. Hood, *Ideal kink instabilities in line-tied coronal loops: Growth rates and geometrical properties*, Ap. J. **350** (1990), 428.

[86] B. Vrsnak, V. Ruzdak, and B. Rompolt, *Stability of prominences exposing helical-like patterns*, Solar Phys. **136** (1991), 151.

[87] B.V. Waddell, N.N. Rosenbluth, and D.A. Monticello, *Non-linear growth of the $m = 1$ tearing mode*, Nucl. Fusion **16** (1976), 528.

[88] W.H. Yang, P.A. Sturrock, and S.K. Antiochos, *Force-free magnetic fields: The magneto-frictional method*, Ap. J. **309** (1986), 383.

[89] E.G. Zweibel and J.E. Rhoads, *Magnetic merging in colliding flux tubes*, Ap. J. **440** (1995), 407.

Explanatory notes

A few points noted by the examiners need some clarification as follows:

Page 5 We have mentioned on page 4, in the last paragraph, that rapid changes in the magnetic field **B** can be viewed as discontinuities on the global length scale. More precisely we should say " A current sheet is a true field discontinuity in the context of ideal MHD". In practice the MHD model is invalid over very small length scales.

Page 28 Here it should be made clear that linear instabilities are exponentially growing in time.

Page 71 Our general comment on page 63 " calculated values of E_M (and J_{max}) are shown as thick dots on smooth fitted splines " refers in particular to figure 5.8, 5.13 and 6.6.

Page 79 We mention that the calculations of Arber *et al.* [5] do not show the final equilibrium. In fact their ideal MHD code includes no energy dissipation mechanism, so energy is conserved and equilibrium cannot be achieved. Reconnection takes place in a dynamic setting.